Au25(SR)18 gold thiolate clusters and metal organic frameworks in catalytic transformations

Zahraa Shahin

N°d'ordre NNT : xxx

THESE de DOCTORAT DE L'UNIVERSITE DE LYON
opérée au sein de
l'Université Claude Bernard Lyon 1

Ecole Doctorale ED 206
Ecole Doctorale De Chimie

Discipline : Chimie

Soutenue publiquement le 14/10/2019, par :

Zahraa SHAHIN

$Au_{25}(SR)_{18}$ gold thiolate clusters and metal organic frameworks in catalytic transformations

---

Devant le jury composé de :

JEROME François	Directeur de Recherche CNRS	Université de Poitiers	Rapporteur
TREGUER-DELAPIERRE Mona	Professeure des Universités	Université de Bordeaux	Rapporteure
AMGOUNE Abderrahmane	Professeur des Universités	Université Lyon 1	Examinateur
FATEEVA Alexandra	Maître de Conférences	Université Lyon 1	Examinatrice
DEMESSENCE Aude	Chargée de Recherche CNRS	Université Lyon 1	Directrice de thèse
RATABOUL Franck	Chargé de Recherche CNRS	Université Lyon 1	Co-directeur de thèse
CHIRIAC Rodica	Ingénieure de Recherche CNRS	Université Lyon 1	Co-directrice de thèse

UNIVERSITE CLAUDE BERNARD - LYON 1

Président de l'Université	M. le Professeur Frédéric FLEURY
Président du Conseil Académique	M. le Professeur Hamda BEN HADID
Vice-président du Conseil d'Administration	M. le Professeur Didier REVEL
Vice-président du Conseil Formation et Vie Universitaire	M. le Professeur Philippe CHEVALIER
Vice-président de la Commission Recherche	M. Fabrice VALLÉE
Directrice Générale des Services	Mme Dominique MARCHAND

COMPOSANTES SANTE

Faculté de Médecine Lyon Est – Claude Bernard	Directeur : M. le Professeur G.RODE
Faculté de Médecine et de Maïeutique Lyon Sud – Charles Mérieux	Directeur : Mme la Professeure C. BURILLON
Faculté d'Odontologie	Directeur : M. le Professeur D. SEUX
Institut des Sciences Pharmaceutiques et Biologiques	Directeur : Mme la Professeure C. VINCIGUERRA
Institut des Sciences et Techniques de la Réadaptation	Directeur : M. X. PERROT
Département de Biologie Humaine	Directeur : Mme la Professeure A-M. SCHOTT

COMPOSANTES ET DEPARTEMENTS DE SCIENCES ET TECHNOLOGIE

Faculté des Sciences et Technologies	Directeur : M. F. DE MARCHI
Département Biologie	Directeur : M. le Professeur F. THEVENARD
Département Chimie Biochimie	Directeur : Mme C. FELIX
Département GEP	Directeur : M. F. DE MARCHI
Département Informatique	Directeur : M. le Professeur S. AKKOUCHE
Département Mathématiques	Directeur : M. le Professeur G. TOMANOV
Département Mécanique	Directeur : M. le Professeur H. BEN HADID
Département Physique	Directeur : M. le Professeur J-C PLENET
UFR STAPS	Directeur : M. P.FARGIER
Observatoire de Lyon	Directeur : M. B. GUIDERDONI
Polytech Lyon	Directeur : M. le Professeur E.PERRIN
Ecole Supérieure de Chimie Physique Electronique	Directeur : M. G. PIGNAULT
Institut Universitaire de Technologie de Lyon 1	Directeur : M. le Professeur C. VITON
Ecole Supérieure du Professorat et de l'Education	Directeur : M. le Professeur A. MOUGNIOTTE
Institut de Science Financière et d'Assurances	Directeur : M. N. LEBOISNE

Abstract

This research project reports the synthesis and characterization of new composite materials based on $Au_{25}(SR)_{18}$ thiolate-protected gold nanoclusters (tGNCs), supported over a range of metal organic frameworks (MOFs) and ZrO_2. The synthesized composite materials were tested for catalytic transformations of various substrates.

tGNCs are atomically well defined materials known to be active in oxidation reactions. MOFs nanoparticles are materials suitable for high dispersion of tGNCs. Some MOFs are known to have acidity and can be active as catalysts. Among them, MIL-101 (Cr), UiO-66 (Zr) and ZIF-8 (Zn) were chosen due to their acidic and/or thermal stability properties. The synergy between tGNCs and MOFs has been tested through catalytic conversions of different substrates like glucose, fructose, benzyl alcohol and furfural, involving steps requiring acidic and oxidative features. From this study, $Au_{25}(SG)_{18}$@UiO-66 calcined at 300°C for 12h showed synergy between UiO-66 and the Au Nps for furfural oxidative esterification using base. After the calciation, the Au Nps were of 5.9 nm ± 2.1 nm. Therefore, the size specific properties of tGNCs were not conserved.

In contrast, when deposited on ZrO_2 it was possible to calcine $Au_{25}(SG)_{18}$ nanoclusters at different temperatures to study the ligand and particle size effects for liquid phase oxidation reactions. Thus, the calcination temperature had a significant impact on the catalytic behaviour of these composite materials. A good activity for the oxidation of benzyl alcohol into benzaldehyde in toluene under mild conditions, and of furfural oxidative esterification into methyl-2-furoate, was observed when $Au_{25}(SG)_{18}$@ZrO_2 was fully defunctionnalized at 400°C and reaching 2 nm Au nanoparticles size.

Keywords: Thiolate gold nanoclusters, metal organic frameworks, zirconia, oxidative conversion, partial defunctionalization

Résumé

Ce projet concerne la synthèse et caractérisation de nouveaux matériaux composites à base de nanoclusteurs de thiolates d'or $Au_{25}(SR)_{18}$ (tGNCs), supportés sur divers polymères de coordination (MOFs), ainsi que sur ZrO_2. L'activité catalytique de ces matériaux a été évaluée sur la transformation de différents substrats.

Les tGNCs sont des matériaux atomiquement définis et connus pour être actifs dans des réactions d'oxydation. Les nanoparticules de MOFs sont des matériaux pouvant servir de support pour des tGNCs avec de bonnes dispersions. De plus, certains MOFs sont connus pour avoir des propriétés acides et peuvent être actifs en catalyse. Parmi eux, MIL-101 (Cr), UiO-66 (Zr) et ZIF-8 (Zn) ont été choisis en raison de leurs propriétés acides et/ou de stabilité thermique. La synergie entre les tGNCs et les MOFs a été évaluée à travers la conversion catalytique de différents substrats, tels le glucose, le fructose, l'alcool benzylique et le furfural, impliquant des étapes nécessitant un caractère acide et/ou oxydant. Globalement, il n'a pas été observé d'impact de la présence d'or sur la réactivité de ces substrats, et les tendences catalytiques sont celles obtenues avec les MOFs seuls. Cela est certainement dû à la faible stabilité thermique des MOFs qui empeche une calcination efficace des tNGCs.

Lorsque ces clusters sont déposés sur ZrO_2, il a été possible de les calciner à différentes températures pour étudier l'effet du ligand et de la taille des particules, pour des réactions d'oxydation en phase liquide. Ainsi, il a été montré que la température de calcination a un impact significatif sur le comportement catalytique de ces composites. En conséquence, de bonnes activités pour l'oxydation de l'alcool benzylique en benzaldéhyde dans le toluène et en conditions douces et pour l'esterification oxydante du furfural en furoate de méthyle ont été observées.

Mots-clés: nanoclusteurs de thiolates d'or, polymères de coordination, zircone, oxydation, calcination

Acknowledgments

This thesis was carried out at the Institute of Research on Catalysis and the Environment of Lyon (IRCELYON, France) within the CDFA (Chimie durable: du fondamental à l'application) group. I would like to thank Catherine PINEL, Director of IRCELYON, to have allowed me to perform this work in this laboratory. Thanks to the Allocation de Recherce from UCBL Lyon1.

I express my profound gratitude to Mr François JEROME, CNRS research director within the IC2MP laboratory at Poitiers University, and Mrs Mona TREGUER-DELAPIERRE, Professor at the University of Bordeaux, who accepted to judge my work. I would like to thank Mr Abderrahmane AMGOUNE, Professor at Claude Bernard University-Lyon 1, and Mrs Alexandra FATEEVA, Lecturer at Claude Bernard University-Lyon 1, who honored me by accepting to participate to the jury.

I am very grateful to my thesis director, Aude DEMESSENCE and the co-directors, Franck RATABOUL and Rodica CHIRIAC. Their advices, knowledge, experience in materials synthesis and catalysis, passion for research, and their daily support were the key elements in the success of this project. They allowed me to enrich myself professionally and personally. For that and for the rest, thanks.

My thanks go to Nadine ESSAYEM, who contributed to the scientific quality of my thesis, through her availability and support during several meetings.

My thesis could not have happened without the participation and technical support of Marion ETERNOT and Thibaut CORNIER, technical engineers in the CDFA team. I want to highlight their invaluable help on the laboratory installations. They accompanied me with courage whenever needed. I would also like to thank the scientific services of IRCELYON for the characterization techniques: L. Cardenas (XPS), L. Burel and F. Simonet (TEM), Y. Aizac and F. Bosselet (XRD), N. Cristin and P. Mascunan (ICP-OES).

I would like to thank Anne-Marie Grézaud who helped me with all the administrative procedures, and for all the administration team.

I have spent my last three years with irreplaceable people. Oleksandra VESELSKA, we started our M2 internships and continued our theses together. Thanks for all the scientific discussions and help, and for all the delicious cakes she baked. Thanks to Marwa ABOU-HAMDAN, Lama

OMAR and Ranin ATWI, whom I met at IRCELYON, and will always be among my best friends. They were always there for fruitful discussions, and during the ups and downs.

My thoughts also go to all members of the CDFA team. Lucie, Miguel, Dolores, Roua, Santiago, Amar, Sweta, Antonio, Kamila, Natalia, Bhagyesh, Samira. For the scientific discussions we have had during the frequent team meetings. I would like to thank Laurent, Lorraine, Stéphane, Alexander, Shashank, Noemie, Michèle, for sharing their scientific knowledge.

I want to warmly thank my parents in Lebanon, my sisters (A'laa and Shaimaa) and my brother (Ahmad), for their moral support despite the distance between us.

Infinitive thanks to my lovely husband (Haydar) who was beside me during all the moments, who supported and encouraged me, without him I would not have served for long-term working on the thesis.

Finally, I would like to thank this country. FRANCE, you gave me a lot in the scientific research and personal life. I will consider you like my second country trying to serve you in the future.

List of abbreviations

GNps: Gold nanoparticles

GNCs: Gold nanoclusters

tGNCs: Thiolate gold nanoclusters

MOFs: Metal organic frameworks

TOAB: Teteraoctyl ammonium bromide

HSR: Thiol ligand

HSG: Glutathione

SG: Glutathionate

Capt: Captopril

PET: Phenyl ethyl thiol

ATP: 4-aminothiophenol

MBA: *p*-mercapto benzoic acid

***p*-BBT:** *p*-ter-butyl benzene thiol

Cys: Cysteine

H_2BDC: Terephthalic acid

BDC: Terephtalate

HAP: Hydroxyapatite

PVP: Polyvinylpyrrolidone

BnOH: Benzyl alcohol

Bnald: Benzaldehyde

5-HMF: 5-hydroxymethylfurfural

FF: Furfural

DCM: Dichloromethane

DMF: Dimethyl formamide

DEF: N,N-diethylformamide

SBU: Secondary building unit

MS: Mass spectroscopy

ESI-MS: Electronic spray ionization mass spectroscopy

LDI: Laser desorption ionization

MALDI: Matrix assisted laser desorption ionization

PAGE: Polyacrylamide Gel Electrophoresis

SERS: Surface enhanced Raman spectroscopy

CD: Circular dichroism

PXRD: Powder X-ray diffraction

TGA: Thermogravimetric analysis

IR: Infrared spectroscopy

TEM: Transmission electron microscopy

XPS: X-ray photoelectron spectroscopy

TPD: Temperature programmed desorption

UV-Vis: Ultraviolet-visible spectroscopy

GC: Gas chromatography

HPLC: High performance liquid chromatography

TOF: Turnover frequency

Table of content

General introduction

Gold nanoparticles are known to be effective catalysts in oxidation of a wide range of substrates such as alkenes, alcohols, amines, etc., in mild conditions. Understanding the origin of the catalytic phenomenon at molecular level remains a scientific challenge to be able to optimize the catalyst and its working conditions. However, polydispersity of nanoparticles and the influence of the support are obstacles in understanding different phenomena.

Thiolate-protected gold nanoclusters (tGNCs) are compounds that are atomically defined and have a gold heart (core) less than ~ 2 nm. They are stabilized by thiolate ligands and have the general formula $Au_n(SR)_m$. These compounds have thus aroused a strong interest in catalysis, by the demonstration of high catalytic activities. The particular interests in these materials are the ability to get them pure as molecular species and to know exactely, for some of them, the position of the atoms, thanks to their crystallographic structures solved from single crystal X-ray diffraction.

In heterogeneous catalysis, gold nanoparticles are deposited on a support to be stabilized and to recover the catalyst at the end of the reaction. In addition, the support can be inert or active in catalytic transformations by tailoring its acidity, hydrophobicity or electronic affinity with a substrate. In order to benefit from both, the tGNCs and the supports in catalytic reactions, it is interesting to assemble the tGNCs over a network of hybrid materials nanoparticles that possess, for example, acidity. The presence of acidity, within the support, can enhance the reactivity and selectivity of the species (substrates and products) for a range of reactions, as we performed in this work. In doing so, this kind of composite materials can combine the advantages of supported catalysts (recovery) while having good dispersion and activity. In this work, porous coordination polymers, also called MOFs, were selected for the ability to modulate their functionnality by playing with the metals and the ligands and also for their porosity that brings a low density and implies a good dispersion in a solution.

Thus, the project, in the long-term, is to use the tGNCs, presenting the advantages to have very small sizes (<2 nm) and being atomically well-defined as molecular bricks for the construction of composite materials mixing gold thiolate clusters and hybrid

compounds as the supports. Then, the resulting composite materials were subjected to thermally controlled defunctionalization to study the effect of the presence / absence of the thiolate ligands on the catalytic activities. The support effect and the clusters size upon calcination were evaluated by different catalytic reactions.

The manuscript is divided in five chapters, as follow:

The **first chapter** presents irst, the different types of thiolate-protected gold nanoclusters, their synthesis, structures and physio-chemical properties. It highlights the use of supported $Au_{25}(SR)_{18}$ in heterogeneous catalysis. Second, synthesis of metal organic frameworks nanoparticles and their characteristics that made active in catalysis are described, highlighting the most known types of MOFs (MIL-101, UiO-66 and ZIF-8) in catalysis.

The **second chapter** describes all experimental methods used for the syntheses and characterizations of the catalysts and the performed catalytic tests. Annexes (A, B and C) present at the end of the manuscript describe the routine characterization techniques and analytical methods used for studying the catalysts and the reactional mixtures respectively.

The **third chapter** deals with the detailed synthesis and full characterizations of MIL-101, UiO-66 and ZIF-8. In addition, the use of these MOFs as catalysts for the conversion of sugars and furfural is described.

Chapter four focused on the synthesis of the composite materials based on thiolate-protected gold nanoclusters and MOFs. The characterisations of the synthesized materials are described. The thermal stabilities of the tGNCs and MOFs alone are presented. Then, the controlled defunctionalization of the tGNCs is described to keep the MOFs (support) stable. Finally, the catalytic performance of some composite materials is described, targeting sugars conversion, in addition to benzyl alcohol and furfural transformations under oxidative conditions.

Chapter five describes the synthesis of Au_{25}(SG:Glutathione)$_{18}$ supported over ZrO_2 with defunctionalization at 200°C, 300°C and 400°C. The activity of the non-calcined and the calcined material at different temperatures is described for benzyl alcohol oxidation and furfural oxidative esterification.

Chapter 1

State-of-the-Art

I. **History of gold**

Gold is a sparkling yellow metal very appreciated for its resistance to oxidation. Gold is historically, largely used in jewelry and as a trading reference. Apart from jewelry and its monetary role, the historical use of gold was relatively restricted, because of its high chemical inertness. Despite this apparent inertia, one finds traces of its use since ancient times. It was particularly used in the field of glassware, and more specifically in the dyeing of glasses and ceramics, and in medicinal compositions. It will, however, be necessary to wait for the works of Faraday (1791-1867) to see the first work on gold in chemistry (see below).

II. **Physicochemical properties of gold**

Gold (Au) is a transition metal, belonging to group 11 (IB) of the periodic table and presents the electronic configuration [Xe] $4f^{14}5d^{10}6s^{1}$ (M = 196.97 $g.mol^{-1}$). Its properties are expected to be close to those of platinum and mercury, metals to the left and right of gold in the periodic table. However, it is a unique metal because of its resistance to corrosion and the existence of strong size relativistic effects, notably explaining its coloring.

Gold is a metal that can form alloys with other metals. It can have different degrees of oxidation, the most stable being Au(0), Au(I) and Au(III). We can also find, in some cases, the degree of oxidation (-I) [1] and (+V) [2] as in CsAu and in the ion $[AuF_6]^-$ respectively. Gold is a metal resistant to almost all solvents and acids, with the exception of “aqua regia”, a mixture of two to four volumes of hydrochloric acid and nitric acid respectively, in which gold is oxidized and forms $[AuCl_4]^-$.

III. **Gold nanoparticles (GNps)**

The first study of gold in a nanoparticulate state was done by Faraday, in which gold nanoparticles were described as “solid metallic particles” in an extreme divided state [3]. However, the term colloids was used to describe gold nanoparticles for the first time by T. Graham in 1861 in order to define a class of materials that do not diffuse through a porous membrane. There is, so far, no precise definition in terms of chemical composition or morphology. In general, a colloidal solution is defined as a suspension intermediate between particles larger than a micrometer and true solutions (solution in which the solute (s) is (are) in the state of molecular division in the solvent) [4].

From this definition comes the notion of nanoparticles. Indeed, one term of nanoparticles concerns particulate materials in which at least one dimension is between 1 nm and 100 nm [5], corresponding to the definition of a colloid, whose size is between that of the molecule and the micrometer **Scheme 1-1**. We can get different types of nanoparticles, having different morphologies (rods, spheres, triangles ...) and different sizes. Important criterion to characterize a material is the homogeneity in the size of the synthesized nanoparticles and their surface state. Another parameter, derived from the morphology and size criterion, is the ratio between the surface gold atoms and the total number of atoms. This number, without unit, corresponds to particle dispersion and is of considerable importance in catalysis. It determines the fraction of accessible atoms, those being active in a considered reaction.

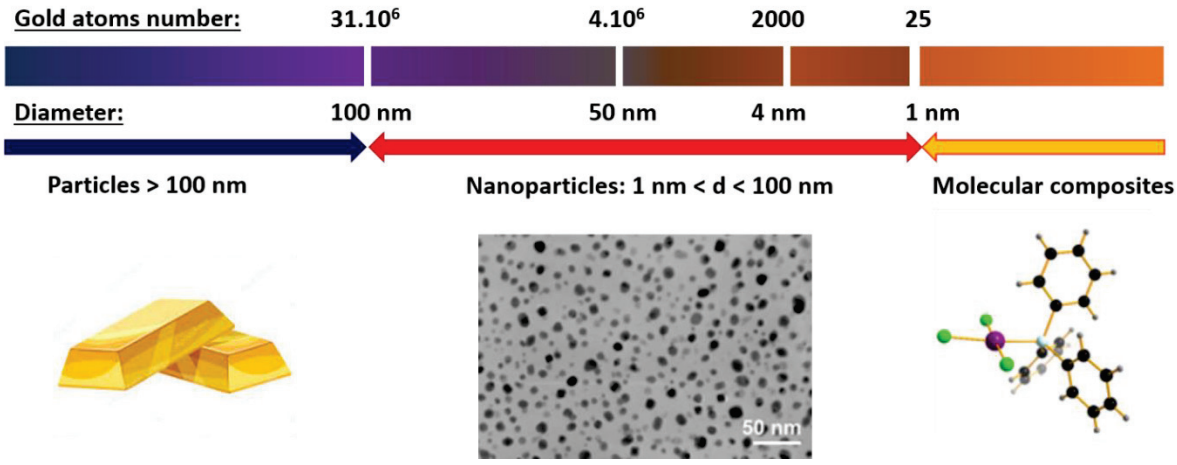

Scheme 1-1 Size scale of gold nanoparticles. Structure of Ph_3PAuCl_3 (from [6]).

The nanoparticles of gold, because of their size, can thus consist of some tens to several thousands of gold atoms. Because of some important catalytic properties under relatively mild conditions [7], and optical features (plasmon resonance, application in SERS) [8], GNps are currently among the most studied materials.

IV. **Gold nanoclusters (GNCs)**

The terms nanoparticles, nanocrystals and nanoclusters (or clusters) are often used to design nanoscale compounds, however, they do not qualify same objects. The term nanoparticle gives only information about the size of the particle, without precision on its crystallinity, whereas the term nanocrystal refers to crystalline nanoparticles. The term cluster refers to an assembly of metal atoms having at least one bond between two metals. However, this term has also been used to describe aggregates of a few tens to many millions of atoms. Thus, we find the terms very small clusters (2 - 20 atoms), small clusters (20 - 500 atoms) and large clusters (500 - 10^7 atoms) [9]. For clarity and to avoid possible confusion due to the lack of unification of the nomenclature concerning these materials, we use here the term nanoclusters to describe particular buildings of size (heart/core) less than ~ 2 nm, or less than about 300 gold atoms.

Gold nanoclusters are thus nanometric-sized compounds with particular properties because of their size. They are atomically defined compounds and are describe with the generic formula Au_nL_m, where n is the number of gold atoms, and m is the number of ligand molecules. The ligands stabilizing the clusters can be neutral (phosphines, as in cluster $Au_{55}[(PPh_3)_{12}Cl_6]$ [10], or anionic (thiolates, chlorides, etc.) [11]. The number of gold atoms is defined and for some of them the crystallographic structure is known, leading to the isolation of specifically structured clusters having size related properties and applications [12, 13]. Nanoclusters stand out to gold nanoparticles, which indeed have a *metallic state* with conduction bands, while nanoclusters exhibit a *molecular state* with discrete energy levels and particular electronic transitions.

Nanoclusters are therefore, situated between *metal complexes* and *gold nanoparticles*. This size domain is interesting to study the size effects on catalytic activities. Obtaining monodispersed nanoparticles is one of the objectives for catalysis, to have a better fundamental understanding of the mechanisms involved. Polydispersity of nanoparticles

is, indeed, a key point on selectivity and activity [14-16].

First studies on gold nanoclusters in 1970s concerned the phosphine protected gold nanoclusters [17-23], followed by thiolate ones [24, 25]. In parallel selenolate [26-29] and acetylene [30, 31] protected gold nanoclusters were also reported.

In our study, we only focused on gold nanoclusters stabilized by thiolate functionalities. The choice to use thiolate derivatives in particular is motivated by the wide range of commercially available ligands, and by their lower toxicity compared to derivatives of selenium or tellurium.

V. **Thiolate-protected gold nanoclusters (tGNCs)**

The generic formula of thiolate-protected gold nanoclusters is $[Au_n(SR)_m]^q$. "n" represents the number of gold atoms, "m" represents the number of coordinating thiolates, and "q" is the charge of the nanocluster. To distinguish gold nanoclusters from coordination oligomers, the ratio gold/ligand must satisfy the condition n > m. In the opposite case (n = m or n < m), the coordination oligomers present "n" atoms of gold with (+I) oxidation state.

The number of gold atoms varies from 10 to more than 300, each having specific number of thiolate ligands, specific structure and properties. tGNCs are characterized by the strong interaction between thiolates and gold. $Au_{25}(SR)_{18}$ was the first tGNC reported as pure species and single crystals were isolated to solve its crystallographic structure. Thus, this cluster is today the most studied and it is presented here, at the level of its syntheses, structures, optical properties and applications (mainly in catalysis) **Scheme 1-2.**

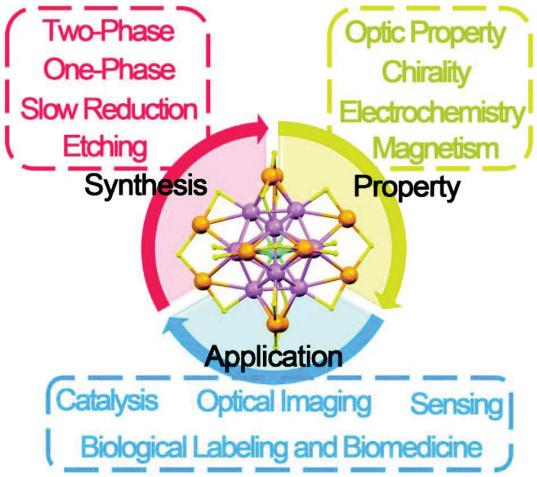

Scheme 1-2 Syntheses, properties, and applications of the $Au_{25}(SR)_{18}$ nanocluster (from [32]).

V.1. Synthesis and purification methods

The synthesis of thiolate-protected gold nanoclusters has been based, to certain extent, on that of small gold nanoparticles (<5 nm). In general, the synthesis of gold nanoparticles is done by bottom-up or top-down approaches. Procedures in the top-down way are based on getting the materials or nanoparticles from a larger set and thus reduce the size of fragments. In the bottom-up way, the principle is to form particles from individual molecules. These two paths have distinct advantages, disadvantages and limitations.

Different ways in optimizing tGNCs synthesis have been known, in which it is possible to differentiate distinct synthetic methods. In the following, we will focus on $Au_{25}(SR)_{18}$ synthetic description.

V.1.1. Direct *in situ* synthesis of tGNCs

Direct synthesis of tGNCs is done in monophasic or biphasic media, where a mixture of polydispersed nanoclusters is obtained, followed by further separation and purification. First reports about tGNCs appeared in 1990s. Protected gold nanoparticles were synthesized in biphasic media of water and toluene, using teteraoctyl ammonium bromide (TOAB) as a transfer agent of gold toward the organic phase. Dodecanethiol (HSR: HS-$C_{12}H_{25}$) was the ligand and sodium borohydride ($NaBH_4$) the reducing agent. The ratio of (Au/HSR, 1/1) was used and the average size of the synthesized mixture was between 1 and 3 nm. The IR spectrum showed that dodecanethiol is a part of the final structure, an

evidence for the protection of gold by thiol ligands [33]. Hence, Brust et al. highlighted three basic steps for tGNCs synthetic procedures:

Phase transfer of gold precursor by TOAB
Au(III) reduction to Au(I) using thiol ligand (HSR)
Au(I) reduction to Au(0) using $NaBH_4$

Polydispersity has been observed on TEM images, meaning that the target of synthesizing a defined type of tGNCs (with homogeneous size) was not achieved. Whetten et al. changed the ratios of the starting materials (Au/HSR, 1/2), and used an excess of the reducing agent ($NaBH_4$) to increase the saturation possibility of gold particles with thiolates. These new conditions did not suppress the polydispersity. However, separation of different types of nanoclusters, within the mixture, was done by cycles of fractional crystallization and each was analyzed by mass spectrometry (MS) [34]. Schaaff et al. discussed after about the details of the synthetic procedure needed to control the purity of homogeneously sized tGNCs. The ratio (Au:/HSR, 1/3) was used as the best molar ratio to purely obtain AuSR complex without neither excess of Au(III) nor of HSR **Figure 1-1**.Then the addition of excess of $NaBH_4$ solution (10 equivalents) very rapidly lead to the reduction of Au(I) to A(0) and a color change into brown-black. In addition, by increasing or decreasing the temperature, tGNCs of bigger or smaller sizes can be obtained, respectively [35].

Step 1: Phase transfer
$HAu^{(III)}Cl_4 + 4[TOA^+][Br^-] \rightarrow [Au^{(I)}Cl_4].3\ [TOA^+]_{tol.} + HBr_{aq.} + [TOA^+][Br^-]_{tol.} + 2Br^-_{aq.}$
Step 2: Reduction by thiol ligand
$[Au^{(I)}Cl_4].3\ [TOA^+]_{tol.} + 3\ RS^{(-II)}H \rightarrow Au^{(I)}SR + RS\text{-}SR + HCl + 3\ [TOA^+][Cl^-] + 2H^+$
Step 3: Reduction by $NaBH_4$
$Au^{(I)}SR + NaBH_4 \rightarrow Au_n(SR)_m$
Total equilibrium equation
$HAu^{(III)}Cl_4 + 4[TOA^+][Br^-] + 3RS^{(-II)}H + NaBH_4 \rightarrow Au_n(SR)_m + RS\text{-}SR + HCl + 3[TOA^+][Cl^-] + 3HBr + [TOA^+][Br^-]_{tol.}$

Figure 1-1 Synthetic equilibrium of tGNCs in biphasic medium.

Arnold et al. showed the first report of using Laser Desorption Ionization (LDI) and Matrix Assisted Laser Desorption Ionization (MALDI) as spectrometric techniques to analyze dodecanethiolate ($^{-}SC_{12}H_{25}$) based tGNCs. However, the irradiation of the sample by laser, broke the Au-S and S-C bonds of the thiolate ligand, and so only Au and S atoms were detected. Their ratio has shown that all gold surface is attached to sulfur. In conclusion, it was not possible to figure out the exact mass and formula of the tGNCs due to their fragmentation [36].

To limit polydispersity, Schaaff et al. used a bulky thiolate ligand (Glutathione: HSG) to reduce the cluster size. The synthesis was done in two steps. During the first, Au(I)SG polymer was obtained, then reduced in a second step with $NaBH_4$ in MeOH:H_2O mixture at room temperature. They obtained a nanocluster mixture with 4.3, 5.6, 8.2 and 10.4 kDa molecular weight (1 kDa = 10^3 g·mol^{-1}). They used Polyacrylamide Gel Electrophoresis (PAGE) for separation and Electrospray Ionization Mass Spectrometry (ESI-MS) for the first time in aqueous solutions (tGNCs with glutathione ligands are soluble in water). After the separation of the different species in the formed mixture, they found that $Au_{28}(SG)_{16}$ was the most abundant species [37, 38]. Negishi et al. used ESI-MS with better resolution to figure out the mass and formula of each single type present in the mixture, without fragmentation issues. The types detected have been: $Au_{10}(SG)_{10}$, $Au_{11}(SG)_{11}$, $Au_{12}(SG)_{12}$, $Au_{15}(SG)_{13}$, $Au_{18}(SG)_{14}$, $Au_{22}(SG)_{16}$, $Au_{22}(SG)_{17}$, $Au_{25}(SG)_{18}$, $Au_{29}(SG)_{20}$, $Au_{33}(SG)_{22}$, $Au_{35}(SG)_{22}$, $Au_{38}(SG)_{24}$, $Au_{39}(SG)_{24}$ [39].

In 2003, Donkers et al. reported the synthesis of $Au_{38}(SC_2H_4Ph{:}PET)_{24}$ through biphasic approach [40]. Its formula was corrected in 2007 to be known as $[Au_{25}(PET)_{18}^{-}][TOA^{+}]$ [41]. This synthesis needed several steps of extraction leading to low $[Au_{25}(PET)_{18}^{-}][TOA^{+}]$ yield. In another approach, Price et al. and Heaven et al. synthesized $[Au_{25}(PET)_{18}^{-}][TOA^{+}]$, by crystallizing it in methanol [42, 43]. In 2008, Zhu et al. published a *kinetically controlled method*, known as *size-focusing methodology*, to synthesize $[Au_{25}(PET)_{18}^{-}][TOA^{+}]$. They decreased the temperature of the first step of [Au(I):SR] formation to 0°C, and allowed the reaction to run for 1h while slowing down the stirring. After this time, the stirring was increased to 1100 rpm and the reducing agent (aqueous solution of $NaBH_4$, 10 eq.) was added all at once, and left for 12 to 24 hours. The crude mixture showed optical behavior related to $Au_{25}(SR)_{18}$ tGNCs without further purification [44]. Signals at 400, 450 and 670

nm were observed (See part V.3.). Later they succeeded in crystallizing the obtained nanoclusters in EtOH with the ratio (EtOH/solubilized cluster solution in toluene, 4/1). Needle like product was obtained in the solution kept in static conditions overnight [45] **Scheme 1-3 a**.

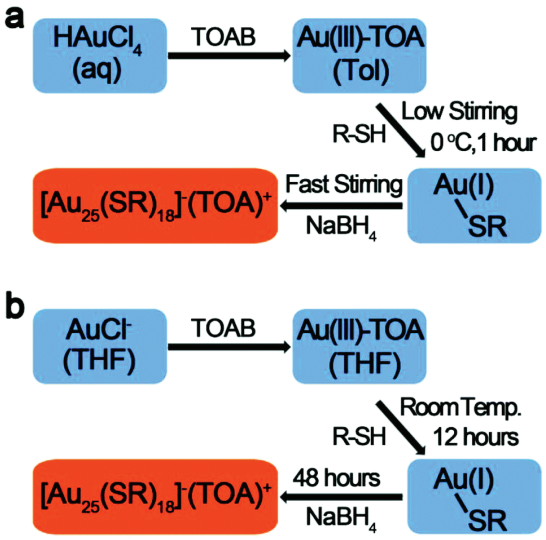

Scheme 1-3 Schematic illustration for the formation of $Au_{25}(PET)_{18}$ nanocluster by (a) kinetically controlled, thermodynamically selective two-phase strategy [44] and (b) one-phase synthetic method [46] (Taken from [32]).

In 2009, Wu et al. optimized the synthesis of $Au_{25}(SR)_{18}$ nanoclusters, with SR = PET and SG. This approach was based on *one phase size focusing method* in THF, improving the purity of the crude mixture, and the yields of $[Au_{25}(PET)_{18}]^q$ and $Au_{25}(SG)_{18}$ [46]. For $[Au_{25}(PET)^-_{18}][TOA^+]$, $HAuCl_4.3H_2O$ has been dissolved in THF, cooled to 0°C during 30min, then PhC_2H_4SH (5eq. to gold precursor) was added slowly under gentle stirring (60 rpm) overnight. Aqueous solution of $NaBH_4$ (10 eq.) was then added while rapid stirring, left at 0°C for 3 h, then at room temperature for 60 h (aging process). Pure $[Au_{25}(PET)^-_{18}][TOA^+]$ was obtained after precipitates removal, solution concentration and washing with EtOH. Synthesis of $Au_{25}(SG)_{18}$, was slightly different, where 11.5 eq. of $NaBH_4$ were used, aging process of 28 h was done, followed by washing with methanol/water mixture (v/v = 4/ 1). In 2010, Parker et al. in a similar monophasic synthesis, have mixed $HAuCl_4.3H_2O$ and TOAB (1/1 molar ratio) in THF for 15 min. PhC_2H_4SH (5eq.) was then added and left stirring (colorless solution). $NaBH_4$ solution was added to the formed Au(I)SR polymeric mixture and slowly stirred for 48 h. Filtration, solution concentration and several washings with methanol gave the pure $[Au_{25}(PET)^-_{18}][TOA^+]$ [47] **Scheme 1-3 b**.

The type of tGNCs synthesized depends on the synthetic conditions. To highlight this sensitivity, the difference between the synthesis of $[Au_{25}(PET)^{-}_{18}][TOA^{+}]$ [44, 45] and $Au_{144}(PET)_{60}$ [48], carried out by Jin and co., is presented below. The differences between both syntheses are the stirring speed during the reduction of Au(III) into Au(I), with an additional thermal treatment step (at 80°C) applied to obtain pure $Au_{144}(PET)_{60}$.

Other types of Au_{25} tGNCs with different ligands were synthesized using *in situ* direct method [32]. Our group at IRCELYON succeeded in synthesizing $Au_{25}(SPhNH_2)_{17}$, pure and in high yield (>75%) [49]. Xie et al. reported the one pot synthesis of Au_{25}(BSA:bovine serum albumin)$_{18}$ [50], and Kumar et al. synthesized $Au_{25}(Captopril)_{18}$ nanocluster having chiral properties [51].

V.1.2. **Ligand exchange method**

Size focusing methodology, through the direct *in situ* synthesis of $Au_n(SR)_m$, leads to variety of tGNCs with wide range of magic numbers. Nevertheless, some magically numbered tGNCs have not been obtained easily using this methodology, but they have been accessible by the *ligand exchange method*, known also as Ligand Exchange-Induced Structure Transformation (LEIST) [52]. Transformation of one stable tGNCs to another, does not mean that the starting one is not stable, it is only being activated under appropriate conditions to be transformed.

In 2002, Woehrle et al. (Hutchison group) reported the synthesis of tGNCs using *ligand exchange method* for the first time, starting from $[Au_{11}(PPh_3)_8Cl_3]$ in organic or biphasic medium [53]. In 2005, Shichibu et al. succeeded for the first time in synthesizing pure $Au_{25}(SG)_{18}$ using Hutchiston method. $[Au_{11}(PPh_3)_8Cl_3]$ was dissolved in chloroform, HSG aqueous solution was added and the reaction proceeded under inert atmosphere (N_2) [54]. This method gave small amount, but with better purity compared to the *in situ* reports. Nevertheless, this method was limited to the use of $[Au_{11}(PPh_3)_8Cl_3]$, proved later by Hutchiston group in 2014. They tried using $[Au_{11}(PPh_3)_7Cl_3]$ having similar structure as the already used $[Au_{11}(PPh_3)_8Cl_3]$, to elaborate $Au_{25}(SG)_{18}$ using the same procedure, but smaller clusters compared to $Au_{25}(SG)_{18}$ were obtained [55].

In 2007, Tracy et al. reported the partial substitution of $Au_{25}(PET)_{18}$ using HSPh (phenyl thiol), HSC_6H_{13} (hexanethiol), HSPEG-biotin (PEG= polyethylene glycol) and *p*-HSPhCOOH

(4-mercaptobenzoic acid, MBA). ESI-MS was used for the analysis and showed the formation of mixed layered clusters having 2 types of thiolate ligands: $Au_{25}(PET)_{18-x}(SR')_x$, where SR' represents the guest ligand [56]. Pure $Au_{25}(S\text{-}C_6H_{13})_{18}$ was synthesized by Zhu et al. [44] and by Devadas et al. [57], then submitted to ligand exchange using pyrene labelled ligand (HS-Py), where $Au_{25}(S\text{-}C_6H_{13})_{17}(S\text{-Py})$ was obtained. In 2008, Shibu et al. exchanged partially the glutathionate ligand within $Au_{25}(SG)_{18}$ using a water-soluble 3-mercapto-2-butanol (MB), adding by that some fluorescence properties to the starting nanocluster [58]. In 2014, Ni et al. reported ligand exchange of $Au_{25}(PET)_{18}$ leading to $Au_{25}(PET)_{16}$(*p*-BBT: *para* ter-butyl benzene thiol)$_2$, in dichloromethane (DCM) during 7 min [59]. Zeng et al. showed kinetic control toward selective formation of tGNCs after ligand exchange process of $[Au_{25}(PET)_{18}^-][TOA^+]$ using *p*-BBT ligand. Au_{28}(*p*-BBT)$_{20}$ was produced when the exchange was conducted at 80°C with 90% yield [60]. Whereas working at 40°C, the production of Au_{20}(*p*-BBT)$_{16}$ was observed [61]. Other types, rather than $Au_{25}(SR)_{18}$ gold nanoclusters, were also used as starting materials to access new tGNCs **Table 1-1**.

Table 1-1 Selected $Au_n(SR)_m$ gold nanoclusters that have been synthesized by ligand exchange method.

Starting cluster (SC)	Produced cluster (PC)	Ratio (L: SC)	T (°C)	Time	References
$Au_{38}(PET)_{24}$	Au_{36}(*p*-BBT)$_{24}$	160:1	80	12 h	[62]
$Au_{38}(PET)_{24}$	$Au_{36}(SC_5H_9)_{24}$	160:1	80	12 h	[63]
$[Au_{23}(S\text{-}c\text{-}C_6H_{11})_{16}]^-[TOA]^+$	$Au_{24}(S\text{-}c\text{-}C_6H_{11})_{20}$	745:1	36	40 h	[64]
$Au_{144}(PET)_{60}$	Au_{133}(*p*-BBT)$_{52}$	370:1	80	4 days	[65]

V.1.3. **Etching**

In an attempt to get pure, smaller and high abundant tGNCs, without further separation steps, new step during tGNCs synthesis have been used. Etching represents a complement step for the already known synthetic procedures. It is based on redispersing the cluster mixture, while heating, in a solution containing a thiol. This triggers the formation of the most thermodynamically stable nanocluster type.

Schaaff et al. formed the Au(I):SR mixture during 30 minutes, then directly quenched the reaction to minimize the polydispersity. The mixture showed abundance of a 14kDa nanocluster. It has been then added to a solution of dodecanethiol at 70°C, leading to the

dominance of 8kDa nanocluster after 15h. Unfortunately, 100% pure monodispersity was not achieved [66]. Until this stage, the important factors to minimize the polydispersity have been:

The molar ratio (Au/SR, 1/3)
The very rapid addition of reducing agent
The quenching of the reaction after short time
Etching step

Price et al. focused on the synthesis of pure tGNCs, based on the work of Brust et al. [33]. They used dichloromethane (DCM) instead of toluene as organic solvent. TOAB was used, and was followed by the reduction with $NaBH_4$ leading to [Au(I):SR]. With an etching step, benzenethiol and hydrogen peroxide were added in THF, then washing was done with acetonitrile, forming pure $[TOA_2Au_{44}(SPh)_{28}]$ [42]. In 2007, the synthesis of $Au_{25}(SG)_{18}$ was optimized with an etching step too. After the synthesis of the polymeric mixture of $Au_n(SG)_m$ according to Negishi et al. procedure [39], the mixture was redispersed in water, HSG was added and heated at 55°C for 12 h. Further, methanol was used to precipitate the pure $Au_{25}(SG)_{18}$ in high yield [67, 68].

V.1.4. **Kinetic control of the reduction step**

Slowing down the kinetics of the reduction step, during tGNCs synthesis, enhances the etching and the yield of the desired product. Reducing agents used in such method were CO (gaseous reducing agent) and $NaBH_4$ (aqueous solution). Their reducing effect is decreased using basic pH media, which inhibits the formation of several types of tGNCs on one hand, and favors the production of specific type of tGNCs depending on the used pH, on the other hand.

Yu et al. reported for the first time the slow reduction method, with CO being the reducing agent, to synthesize Au_{25}(Cysteine=Cys)$_{18}$ [69] and $Au_{25}(SG)_{18}$ [70] nanoclusters. Yuan et al. reported one pot reaction in a gram scale to form pure $Au_{25}(SR)_{18}$ nanoclusters using $NaBH_4$ reducing agent [71, 72].

Regardless the synthetic method, other types of tGNCs have been also synthesized with high purity and are listed in **Table 1-2**. tGNCs gold core sizes range from less than 1nm

[case of $Au_{10}(SR)_{10}$] to 2.9nm [case of $Au_{940\pm20}(SR)_{160\pm4}$].

Table 1-2 Selected types of $Au_n(SR)_m$ thiolate-protected gold nanoclusters synthesized with high purity.

Formula	Thiolate ligand type (SR)	Crystal structure	References
$Au_{10}(SR)_{10}$	$SPhNH_2$	-	[73, 74]
$Au_{20}(SR)_{16}$	SC_2H_4Ph, SCH_2Ph, SPh-tBu (TBBT)	available	[61] [75] [76]
$Au_{24}(SR)_{20}$	SC_2H_4Ph, SCH_2Ph, SCH_2Ph-tBu	available	[64] [76] [77]
$Au_{24}(SR)_{16}$	adamantanethiolate ($SC_{10}H_{15}$)	available	[78]
$Au_{28}(SR)_{20}$	SPh-tBu (TBBT), S-c-C_6H_{11}	available	[60] [79]
$Au_{30}S(SR)_{18}$	S-tBu	available	[80-83]
$Au_{30}(SR)_{18}$	adamantanethiolate ($SC_{10}H_{15}$)	available	[84]
$Au_{38}(SR)_{24}$	PET	available	[85]
$Au_{38}S_2(SR)_{20}$	adamantanethiolate ($SC_{10}H_{15}$)	available	[86]
$Au_{40}(SR)_{24}$	SC_2H_4Ph, SPh-o-CH_3 (*o*-MBT)	available	[87-89] [90]
$Au_{52}(SR)_{32}$	TBBT	available	[90]
$Au_{55}(SR)_{31}$	SC_2H_4Ph	-	[91] [92] [93]
$Au_{64}(SR)_{32}$	S-c-C_6H_{11}	-	[94]
$Au_{67}(SR)_{35}$	SC_2H_4Ph	-	[95]
$Au_{99}(SR)_{42}$	SPh, SPh-p-CH_3	-	[96]
$Au_{102}(SR)_{44}$	4-mercapto benzoic acid (MBA)	available	[97]
$Au_{104}(SR)_{41}$	SPh-m-CH_3	-	[87]
$Au_{130}(SR)_{50}$	SPh-*p*-CH_3 (*p*-MBT), $SCnH_{2n+1}$, SC_2H_4Ph, dithioldurene/SC_2H_4Ph	available	[87, 98-100]
$Au_{137}(SR)_{56}$	SC_2H_4Ph	-	[101]
$Au_{144}(SR)_{60}$	PET	available	[48]
$Au_{246}(SR)_{80}$	*p*-MBT	available	[102]
$Au_{279}(SR)_{84}$	TBBT	available	[103]
$Au_{940\pm20}(SR)_{160\pm4}$	SC_2H_4Ph	-	[104]

V.2. **X- Ray Structure**

To determine their crystal structures, thiolate-protected gold nanoclusters should be obtained in a stabilized crystalline form. Gold nanoclusters are stabilized, like metal complexes, when the valence layers are fulfilled. In such case, the model which explains their stability is the *superatomic complex model*. Orbital molecules in gold nanoclusters arise mainly from 6s orbitals. The stable nanoclusters forms are those having valence electron count equals to: 2, 8, 18, 34, 58, 98, 138 etc [105]. Compounds that respond to this condition (filled valence layer) are called "magic clusters". For tGNCs type $[Au_n(SR)_m]^q$, the number of valence electrons can be calculated according to the following equation [106]:

$$ne = nAu - mS - q$$

An example on that is $[Au_{25}(PET)_{18}]^-$, whose valence electrons count is 8. The stability of some gold nanoclusters is not explained through the superatomic complex model, but rather by the core geometry and ligand stabilization, as for $[Au_{25}(PET)_{18}]^0$, whose valence electron count is equal to 7, but can be isolated in stable form. Rather than stability, structure of nanoclusters has been important to be studied for deeper knowledge in structure-related properties of tGNCs (See section V.3).

As mentioned before, numerous stable tGNCs were synthesized by different synthetic methods, but actually their true structures were not known before 2007. All the work that preceded this date focused on the synthesis, monodispersion and production of tGNCs. A lot of theoretical work was done to determine the structures [107, 108]. The first crystallographically solved structures were for $Au_{102}(MBA)_{44}$ [97] followed by $[Au_{25}(PET)_{18}]^-[TOA^+]$, having decahedral and icosahedral core structures respectively. $Au_{38}(SR)_{24}$ structure was then elucidated too [85], possessing biicosahedral core structure. Other core structures were known, (Face Centered Cubic: FCC [62], Body Centered Cubic: BCC [86], Hexagonal Close Packed: HCP) [109]. As we are interested mainly in $Au_{25}(SR)_{18}$ thiolated-protected gold nanoclusters, the structures of other thiolate nanoclusters and phosphine-protected gold nanoclusters are not detailed below.

$[Au_{25}(SR)_{18}]^q$ tGNCs are atomically defined and stable compounds, for that they are interesting in catalysis. Their thermal stability varies with ligand types and their charge

(q). Comparing aliphatic and aromatic ligands, the nanoclusters stability increases with aliphatic ones [110]. Moreover, three electronic states (q= -1, 0, +1) exist for $[Au_{25}(SR)_{18}]^q$. Under vacuum or inert atmosphere the cluster with q= -1 is the most stable to be isolated, whereas when exposed to O_2, the cluster with q= 0 or +1 is formed. As mentioned in the synthesis part (See part V.1.1.), Heaven et al. succeeded in synthesizing the anionic form of $[Au_{25}(PET)_{18}^-][TOA^+]$ [43]. Akola et al. then predicted its structure theoretically [111]. They reported that it is formed of icosahedral Au_{12} core, having an additional Au atom in the core, and protected by six $[(RS)_3Au_2]$ stapples. Zhu et al. (Jin group) were the first in producing $[Au_{25}(PET)_{18}^-][TOA^+]$ as single crystals [45]. X-ray crystallographic analysis showed that this nanocluster is made of centered icosahedral Au_{12} core having 20 faces, 12 of them are capped by 12 Au atoms as an exterior shell, and encapsulated by 18 thiolate ligands (-SR). Each exterior Au atom has 3 connections with the Au_{13} core face capped by it. One is shorter Au-Au connection (3.02-3.12 Å) and two are longer ones (3.14-3.27 Å). The 18 thiolate ligands have a bridging bonding mode, where each of the exterior 6 Au-Au pairs is bridged by a -SR ligand and connected to two other -SR ligands. X-ray crystallography and NMR analyses revealed that this nanocluster has one equivalent of tetraoctylammonium cation (TOA^+), meaning that it is an anion, $Au_{25}(PET)_{18}^-$ [45].

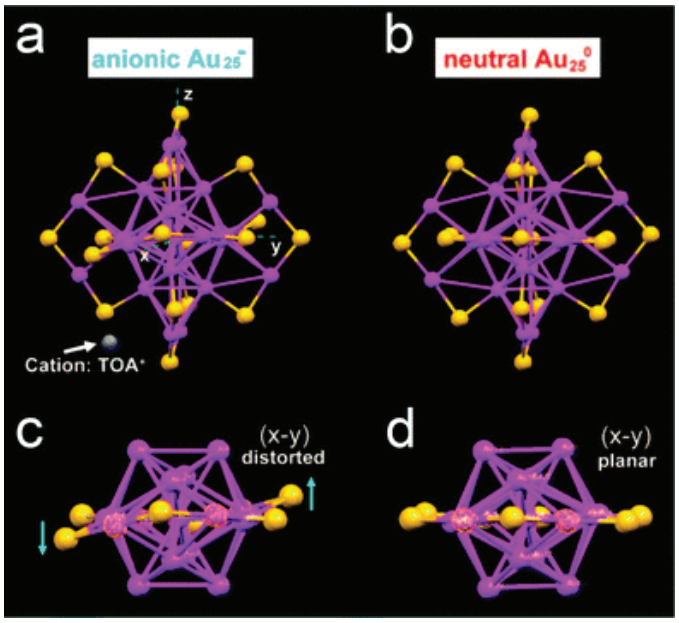

Scheme 1-4 Comparison of the crystal structures of $Au_{25}(PET)_{18}$ with (a, c) anionic and (b, d) neutral charge states. Color legend: purple sphere: Au; orange sphere: S (from [32]).

$Au_{25}(PET)_{18}$ exists also in neutral form. The Jin group highlighted the structural differences between the anionic and the neutral forms. TOA^+ counterion is absent in the neutral form, and the 2 $Au_2(SR)_3$ staple motifs in the xy plane are coplanar **Scheme 1-4 b**. Whereas one sulfur in one staple motif is twisted upward and another sulfur in the other motif is twisted downward in the anionic form **Scheme 1-4 a**. Also the ligands orientations are totally different between the two forms. These differences are suggested to be due to the negative charge or the presence of the bulky counterion TOA^+ [112]. This shows that the stabilization is provided by a geometric factor in the neutral case, which is antagonistic to the electronic stabilization, where the valence electron number is 7.

Other structures have been resolved on single crystals of tGNCs, and correspond to $Au_{38}(SC_2H_4Ph)_{24}$ [85], $Au_{102}(MBA)_{44}$ [97], $Au_{23}(SC_6H_{11})_{16}$ [113], $Au_{24}(SCH_2PhtBu)_{20}$ [77], $Au_{28}(SPhtBu)_{20}$ [60], $Au_{30}S(StBu)_{18}$ [80-83], and $Au_{279}(SR)_{84}$being the largest structure [103].

V.3. Structure related properties

$Au_{25}(SR)_{18}$ thiolate-protected gold nanocluters possess different structure related properties. Their ultrasmall size leads to quantum effects that determines these properties. Optical absorption, electroluminescence and non-linear optical properties, ultrafast electron dynamics, chirality of the gold core, electrochemical and magnetic properties have been detailed in Kang et al. review [32], but only optical absorption properties are highlighted below.

Each type of tGNCs possess unique optical absorption bands that are considered as fingerprints for its composition [38, 66]. Same optical behavior was observed for tGNCs synthesized in the same manner but with different thiol ligands, which pointed out the direct relation between core size/structure and the corresponding optical properties [38]. Depending on the size, the absorption spectrum, related to interband and intraband transitions between HUMO and LUMO, differs **Figure 1-2** [39].

Sample number	Compound
1	$Au_{10}(SG)_{10}$, $Au_{11}(SG)_{11}$, $Au_{12}(SG)_{12}$
2	$Au_{15}(SG)_{13}$
3	$Au_{18}(SG)_{14}$
4	$Au_{22}(SG)_{16}$
5	$Au_{22}(SG)_{17}$
6	$Au_{25}(SG)_{18}$
7	$Au_{29}(SG)_{20}$
8	$Au_{33}(SG)_{22}$, $Au_{35}(SG)_{22}$
9	$Au_{38}(SG)_{24}$, $Au_{39}(SG)_{24}$

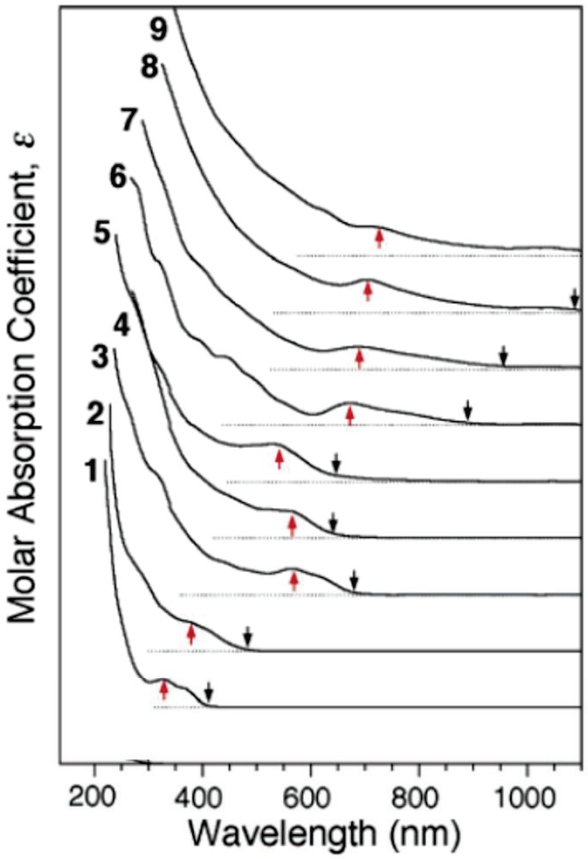

Figure 1-2 Absorption spectra of different thiolate-protected gold nanoclusters in aqueous solution (from [39]).

Nevertheless, the exact reason for optical behaviors was not known before the discovery of the structure of $[Au_{25}(SR)_{18}]^-[TOA^+]$. Its Kohn-Sham orbital energy level diagram published by Jin group **Figure 1-3 (A)**, showed the origin of its three characteristic absorption peaks at 670 nm (a), 450 nm (b) and 400 nm (c) in **Figure 1-3 (B)**:

An intraband transition (sp <- sp) between HOMO-to-LUMO energy levels denoted as (a) related to the peak at 650 nm.

An intraband and interband mixed transitions, (sp <- sp) and (d <- sp) respectively, denoted as (b) related to the peak at 450 nm.

An interband transition (d <- sp) between HOMO-5-to-LUMO energy levels denoted as (c) related to the peak at 670 nm [45].

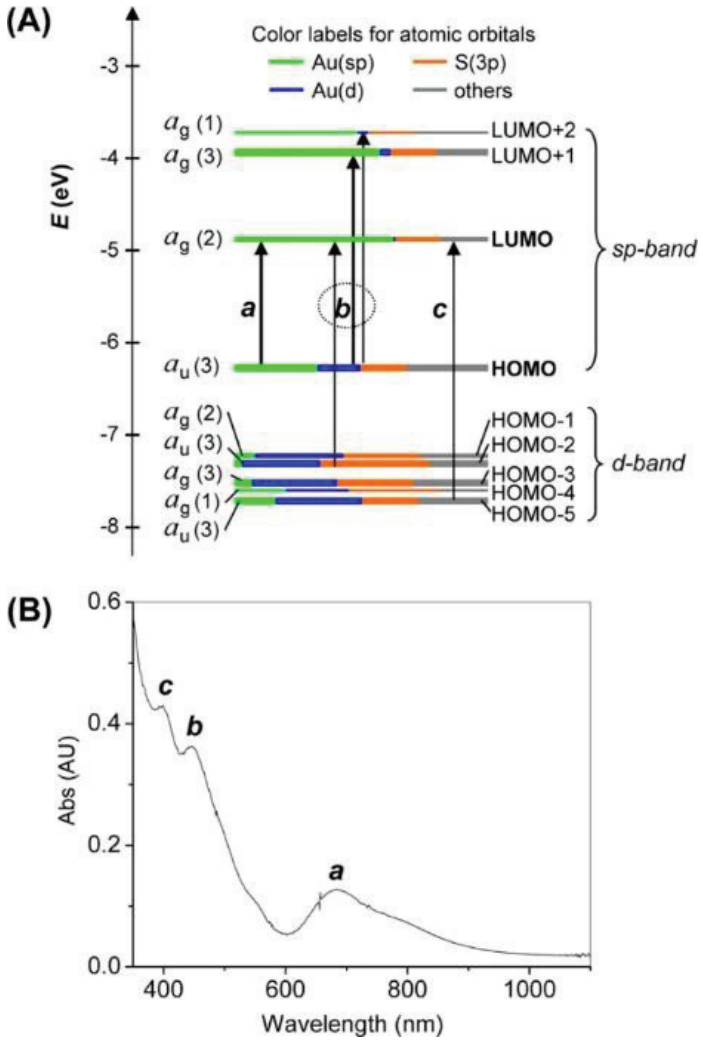

Figure 1-3 (A) Kohn–Sham orbital level diagram for $[Au_{25}(SR)_{18}]^-[TOA^+]$. (B) Peak assignment of the absorption spectrum of $[Au_{25}(SR)_{18}]^-[TOA^+]$ (from [114]).

Thanks to the evolution of the absorption bands, it has been possible to monitor the formation of the most thermodynamic stable tGNCs starting from a crude mixture **Figure 1-4**, as reported by Wu et al. [46].

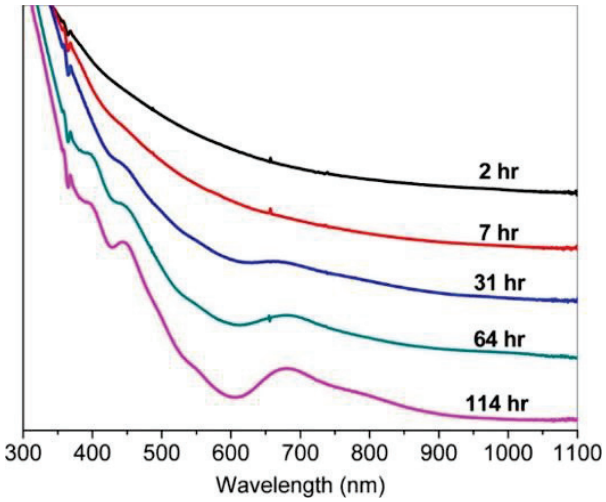

Figure 1-4 Evolution of the UV–vis spectrum of the crude product with aging time. Spectra are vertically shifted for ease of comparison (Taken from [114]).

V.4. **Applications of $Au_{25}(SR)_{18}$ in catalysis**

Bulk gold is known to be inert and non-oxidizable, whereas gold nanoparticles are known to be active in catalysis since the discovery of Haruta in 1987 [7]. $Au_{25}(SR)_{18}$ gold nanoclusters, due to their stability (geometric or electronic), quantum size effects [115-119] and atomically precise structures [116, 120, 121], have shown excellent selective catalytic conversions [122]. $Au_{25}(SR)_{18}$ gold nanoclusters, that are the only tGNCs type discussed in this section, were successfully used for oxidation, reduction [123-126] and photocatalytic [127] reactions (better activity with defunctionalized nanoclusters), coupling [128-131], electron transfer [132] and electrocatalytic [133] reactions (non-defunctionalized nanoclusters were active).

Different factors affect the catalytic behavior of thiolate-protected gold nanoclusters:

Types of ligands: Shorter aliphatic chains allow easier penetration of substrates and so facilitate their interaction with gold atoms enhancing a desired reaction. Aromatic ligands for example, have enhanced 4-nitrophenol reduction due to π – π stacking between the thiolate ligands and the 4-nitrophenol [134].

The functional groups on the ligands: For example, amino functionalities have blocked the 4-nitrophenol reduction reaction due to steric and electronic effects

[134].

Presence or absence of the thiolate ligands: Totally capped clusters $Au_{25}(SC_{12}H_{25})_{18}$ supported over carbon (C) nanosheets have shown no activity in benzyl alcohol oxidation. Nevertheless, partially defunctionalized ones were mostly selective toward benzaldehyde, while the totally defunctionalized $Au_{25}(SC_{12}H_{25})_{18}$@C led to over oxidation toward benzoic acid and its corresponding phenyl-2-benzoate [135]. When the ligands are still present, it is proposed that the active sites are the Au(I) in the staple motif and not the metallic gold in the core. A study showed that O_2 is activated by Au(I) to which in turn is oxidized into Au(III) [136]. Thermal treatments are used to control ligands removal, for partial or complete defunctionalization. But sintering may occur which affects the catalytic properties [137].

Nature of the support: This affects the size of tGNCs after calcination and so affects the catalytic activity. In 2015, Au_{25}(MHA: 6-mercapto hexanoic acid)$_{18}$, supported on various supports: hydroxyapatie (HAP), activated carbon (AC), pyrolyzed graphene oxide (PGO), SiO_2, TiO_2 have been reported for nitrobenzene hydrogenation. After calcination at 300°C, only HAP and TiO_2 prevented the particles sintering, with the best catalytic activity for HAP supporting Au_{25} clusters [138]. This was explained by the strength of interaction between the nanoclusters and the supports, which was assigned to be the strongest with HAP support.

Some oxidation catalytic applications of $Au_{25}(SR)_{18}$ gold nanoclusters are highlighted in the following section.

V.4.1.1. **Benzyl alcohol oxidation**

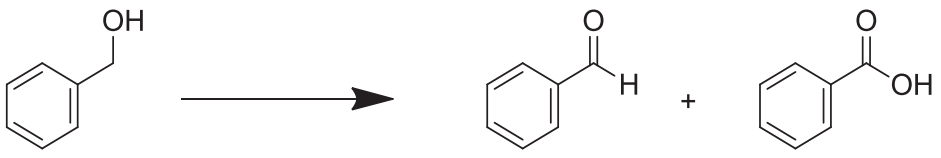

Scheme 1-5 Benzyl alcohol oxidation products

Benzyl alcohol oxidation **Scheme 1-5** is a model reaction used to test the activity of gold nanoparticles. Supported gold nanoclusters have been active in benzyl alcohol oxidation.

Defunctionalization of thiolate gold nanoclusters grafted on different supports is essential for benzyl alcohol selective oxidation into benzaldehyde, benzoic acid or the corresponding ester (depending on the catalyst and reaction conditions). Au_{25}(6-mercaptohexanoic)$acid_{18}$@HAP was defunctionalized either by using tert-butyl hydroperoxide or by calcination at 300 °C and showed, in both cases, incomplete conversion of the benzyl alcohol (46 %) under 5 bar of O_2, at 30 °C and in the presence of a base [139]. Another heterogeneous catalyst, Au_{25}(dodecanethiolate)$_{18}$ deposited on porous carbon nanosheets, has been thermally treated at 500 °C for 4 h and showed full conversion of benzyl alcohol into mostly benzoic acid, under 1 atm of O_2 at 30 °C using a base [135]. In a previous study by our group, $Au_{25}(SPhNH_2)_{17}$@SBA-15, calcined at 400 °C to fully remove the ligands, showed full conversion of benzyl alcohol into benzaldehyde in toluene at 80 °C with a base (Cs_2CO_3) and under atmospheric conditions [140].

V.4.1.2. **Other liquid phase oxidation reactions**

Defunctionalized tGNCs have shown efficiency in styrene [141] and cyclohexane [142] oxidation reactions while non-defunctionalized ones were active toward *trans*-stibene oxidation [143]. More functionalized reactants have been also reported with partially calcined [$Au_{38}(PET)_{24}$@activated carbon], active in glucose oxidation into gluconic acid [144].

V.4.1.3. **CO oxidation**

The activity of gold nanoparticles for CO oxidation was discovered by Haruta and co. in 1987 [7]. In 2012, the activity of thiolate gold nanoclusters was tested for CO oxidation reaction, in an attempt to understand the mechanism and active sites of tGNCs during this transformation.

$Au_{25}(PET)_{18}$ was supported on different oxides (TiO_2, CeO_2, and Fe_2O_3) to study the support effect. It showed that O_2/He pretreatment at 150°C is important to trigger the activity of the composites without removing the thiolate ligands. The reaction was performed at different temperatures, starting from room temperature. $Au_{25}(PET)_{18}$@TiO_2 exhibited no activity, $Au_{25}(PET)_{18}$@Fe_2O_3 showed weak activity even above 120°C, and $Au_{25}(PET)_{18}$@CeO_2 showed 94 % conversion at 80 and 100°C . CeO_2 has been known to be

the best support in CO oxidation. Indeed with this support, CO bound to Au, and interacted with O_2 bound to vacant sites of CeO_2 [145]. Later, $Au_{25}(PET)_{18}@CeO_2$ was calcined at different temperatures to study the ligand effect. Activity started to appear when pretreatements using O_2/He atmosphere at temperature between 150°C and 250°C were carried out. Thus, the activity increased with the increase of temperature, aligning with the increase of the partial defunctionalization of the thiolate ligands. In that case, lattice oxygen interacted with CO on the accessible Au and forms CO_2, then the support compensated the lattice O from atmospheric oxygen. After total calcination, other Au became accessible, and CO and atmospheric O_2 bound at the gold/ceria interface to form CO_2 **Scheme 1-6**. After total calcination, CO oxidation was done at 57°C [145-147].

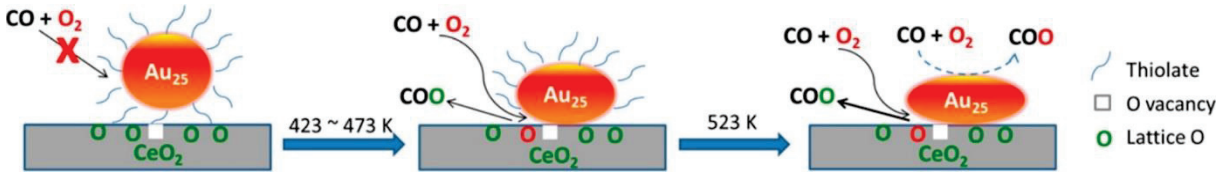

Scheme 1-6 Oxidation Mechanism on intact, partially and fully dethiolated $Au_{25}(SR)_{18}@CeO_2$ (from [146]).

V.5. Application of $Au_{25}(SR)_{18}$ in the formation of composite materials

Combining thiolate-protected gold nanoclusters with another type of material results in multi-functional products having advanced properties. The properties of both may be preserved and synergy could be also observed. In addition, novel properties different than those of the starting materials may appear. Some examples about combining $Au_{25}(SR)_{18}$ with other materials are found in the literature and will be briefly highlighted here.

$Au_{25}(SG)_{18}$ was embedded by MPTS (3-mercaptopropyl)trimethoxy silane) layer, then treated with NaOH (pH= 12) at 60°C for 30 minutes producing $Au_{25}(SG)_{18}@SiO_2$ composite material [148]. Similarly, $Au_{25}(SG)_{18}$ was impregnated on the surface of ZnO semiconductor. Thus, a composite material possessing photocatalytic activity for azobenzene reduction was produced [149]. Another nanocluster, $Au_{25}(BSA)_{18}$, known to have photoluminescence properties [50], was adsorbed on the surface of $Ag@SiO_2$ core-shell nanoparticles, where the formed composite exhibited enhanced fluorescence [150].

$Au_{25}(SG)_{18}$ was very recently combined with porous metal organic framework (ZIF-8: based on Zn(II) metal and 2-methyl imidazolate). The nanocluster was impregnated on the surface and also immobilized inside its pores by 2 different synthetic methods resulting in two different composite materials. Each material showed unique size and photoluminescence properties, as well as specific activity in 4-nitrophenol reduction [151].

The research on composite materials is still in its beginning stages, and it is valuable to go further, especially using metal-organic frameworks as one counterpart beside tGNCs. A part of this thesis was based on synthesizing new composite materials based on different $Au_{25}(SR)_{18}$ nanoclusters beside different metal-organic frameworks, for catalytic applications. In the next part on metal-organic frameworks, different synthetic methods of MOFs Nps are briefly described. Moreover, the characteristics that made MOFs catalytically active are presented. Later, the synthesis, structure and catalytic applications of three, stable, well catalytically known MOFs are highlighted. In this thesis, we focused on UiO-66 (Zr) *[UiO stands for University of Oslo]*, MIL-101 (Cr) *[MIL stands for Matériaux de l'Institut Lavoisier]*, and ZIF-8 (Zn) *[ZIF stands for Zeolitic Imidazolate Frameworks]*, corresponding to M^{4+} carboxylate, M^{3+} carboxylate and M^{2+} imidazolate MOFs respectively, as catalysts and as supports for tGNCs.

VI Metal Organic Frameworks (MOFs)

Metal organic frameworks are stable hybrid materials known also as porous coordination polymers (PCPs). They are constituted of inorganic nodes (metal nodes) and organic linkers connected through coordination bonds **Scheme 1-7**. MOFs are an interesting category in materials science due to their porosity, high surface area, structural and functional tunability and their wide application domains. To date, MOFs registered promising applications in gas storage, heterogeneous catalysis, chemical sensing, and biomedical applications [152-156]. It should be noted that due to these factors and to their ability to be tuned and incorporated different functionalities in the way that suits the desired application, MOFs gained advantages over non- porous and zeolytic compounds. In catalysis, MOFs with high surface area provides large spaces for reactants to penerate and interact with the available active sites [157].

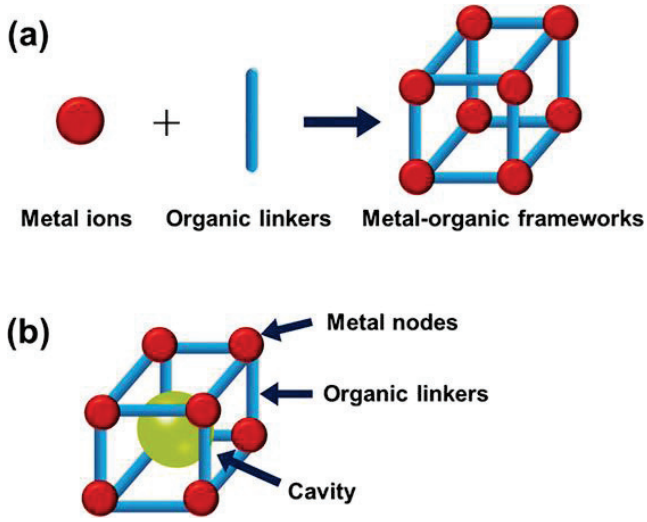

Scheme 1-7 a) Constitution and structure of MOFs. b) Illustration of potential catalytic sites in MOFs (from [158]).

Focusing on their catalytic applications, MOFs are used as heterogeneous catalysts, being possibly recycled and re-used. Designing MOFs with high stability has been a necessary demand. As catalysts, MOFs should not only withstand temperature, but also reactional media (aqueous for example), acidic and basic conditions. MOFs stability is known to align with Pearson's hard/soft, acid/base (HSAB) theory [159]. Based on HSAB theory, the high-valent metal ions with high charges (hard metal centers: Ti^{4+}, Zr^{4+}, Al^{3+}, Fe^{3+} and Cr^{3+}) form strong bonds with hard ligands mainly oxo ligands. While low-valent metal ions with lower charges (soft metal centers: Zn^{2+}, Cu^{2+}, Ni^{2+}, Mn^{2+} and Ag^{+}) form strong bonds with soft ligands mainly imidazolates, pyrazolates, triazolates and tetrazolates. In addition to the strong bond between a metal center and an organic linker, MOFs stability may be also related to the length of the linker [160] and to surface hydrophobicity [161].

VI.1. **Synthetic approaches for metal-organic frameworks nanoparticles**

Different combinations between metals and ligands have been achieved and resulted in the formation of numerous stable MOFs [162]. Nevertheless, in order to serve as a support for heterogeneous catalysis, nanoparticles of MOFs, easy to disperse in a solution, have to be synthesized. Two key-steps during MOFs synthesis are important to get MOFs Nps and are highlighted below.

VI.1.1. **Rapid nucleation**

LaMer model describes fast nucleation and early stage stop of crystallization as a key-step in the formation of Nps. This occurs using high concentration of reactive monomers, higher than the nucleation concentration. Thus, numerous nuclei form by burst nucleation, followed by rapid growth termination through the depletion of all precursors.

Acceleration of nucleation started with Sun et al. who modulated the reactants concentration of H_2PtCl_4 and *p*-phenyldiamine at room temperature in aqueous solution and formed 300 nm spherical coordination polymers Nps [163]. Oh et al. created "initiation solvent" method, where an antisolvent (non-polar), ex. diethyl ether or pentane, was slowly added to the polar precursors solution, resulting in the precipitation of spherical microparticles of size ranging between 190 nm and 2 µm [164]. Deprotonation of acidic ligands was shown to accelerate nucleation too as reported by Rieter et al. resulting in 58 nm ± 8 nm spherical particles [165]. All these methods decreased the size but did not eliminate polydispersity. In other approaches, under soft synthetic conditions (time and temperature), the microwave-assisted synthesis and the ultrasound synthesis have been considered as the best approaches in the synthesis of crystalline MOFs Nps.

Microwave-assisted synthesis leads to produce uniform temperature that exceeds the solvent boiling point, and generate high pressure that accelerates nucleation, followed by fast consumption of the produced nuclei resulting in crystalline MOFs Nps. Li et al. synthesized ZIF-7 membranes, using this approach, at 100 °C in DMF with 40 nm to 140 nm size [166].

Ultrasound (US) approach is based on the generation of local hot spots of high temperature and pressure, enhancing nucleation and rapid nuclei depletion through high heating and cooling rates. The US synthesis of MIL-53 was reported by Haque et al. in 35 min resulting in well crystallized Nps (size is not indicated) [167].

VI.1.2. **Coordination modulation**

Coordination modulation is based on the use of a non-bridging modulator (monocarboxylic acids) that affects the nucleation and growth rates of a desired crystal, and as a consequence the size and shape of the targeted product. Coordination

modulators bind to specific facets of the SBU (secondary building unit) and blocks the growth in the binding direction, so controls the size and the morphology which will be dependent on the modulator concentration **Scheme 1-8**.

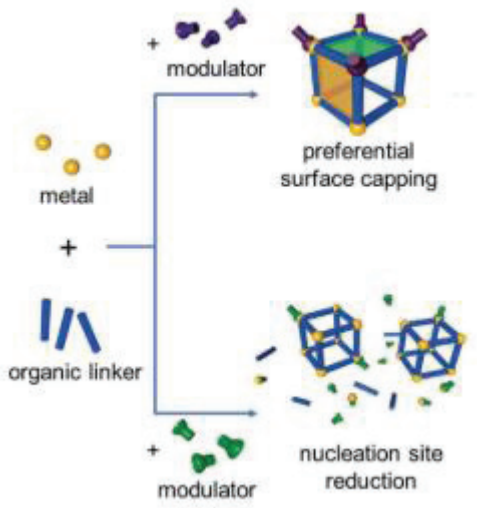

Scheme 1-8 Schematic representation of coordination modulation impacting the nanoparticles shape and size (from [168]).

The activity of the monocarboxylates (modulators) that are able to replace dicarboxylate linkers in the secondary building unit of MOFs is concentration dependent. If the concentration of the monocarboxylates is high, they will bind to metal ions and this hardens the binding of dicarboxylates, and so decreases the nucleation rate leading to bigger crystals. Small crystals are obtained when using low modulator concentration, where the rate of nucleation will not be affected and the modulators will be slowly replaced by the bridging dicarboxylate linkers to build the framework. In addition, the terminal attachment of the monocarboxylates, blocks the growth due to the absence of another carboxylate group leading to small crystals. This was reported in 2011 by Schaate et al., who added 5 equivalents of acetic acid (modulator), with respect to the $ZrCl_4$ precursor, during the synthesis of UiO-66 and obtained small crystals with 95 nm diameter [169]. Whereas when 30 equivalents of acetic acid were used in a previous report, bigger UiO-66 crystallites were formed (1-2 µm) [160]. Another example for coordination modulation was reported for HKUST-1 (Cu(II)-trimesate MOF) Nps, where different concentrations of dodecanoic acid (from 0.234 to 1.188 M) were used, varying the results from nanoscale octahedra, to micrometer-sized cuboctahedra, then reaching

micrometer-sized cubes of HKUST-1 particles [170].

VI.2. Factors behind the efficiency of MOFs in catalysis

Regardless the huge number of well known MOFs in the literature, they are not all suitable to trigger catalytic conversions. MOFs efficiency in catalysis is related to their metal and ligand nature, structure and size, porosity, and chemical functionalities (incorporation of several active sites, covalently or through coordination interactions). Some examples concerning these properties are described in this section.

VI.2.1. Metal vacancies acting as Lewis acids or bases

VI.2.1.1. Lewis acid MOFs

Some low valent [HKUST-1 (Cu)] and high valent [MIL-100 (Sc) (M(III)-trimesate MOF) and UiO-66 (Zr)] MOFs have unsaturated metal centers (UMCs) that act as Lewis acid sites. These UMCs are generated upon thermal activation where solvent molecules (H_2O for example) directly coordinated to metals are eliminated as in the case of (HKUST-1) [171] and MIL-100 (Sc) [172]. Thanks to their Lewis acid properties, HKUST-1 was active in α-pinene isomerization and MIL-100 (Sc) showed high activity in carbonyl ene reaction. MIL-101 (Cr) also has Lewis acid character generated after removal of 2 solvent molecules directly connected to 2 Cr metals within the Cr-trimer constituting this MOF [173]. Solvent removal upon thermal treatment through dehydroxylation was the case of UiO-66. The loss of 2 H_2O molecules from $Zr_6O_4(OH)_4$ resulted in Zr_6O_6. This created Lewis acid properties of UiO-66 that was then active in citronellal cyclization into isopulegol [174].

VI.2.1.2. Lewis base MOFs

Lewis base properties is related to alkaline earth metals based MOFs. Mg_3(PDC:3,5-pyrazoledicarboxylate)$(OH)_3(H_2O)_2$ is an example. This MOF showed activity in aldol condensation reaction [175].

VI.2.2. Brønsted acidic characters in MOFs

Brønsted acidity can be introduced through encapsulation of Brønsted acid molecule in the MOFs pores, ligation of Brønsted acid functions to unsaturated metal sites or to the covalent linked ligands.

These characters can be added to MOFs directly during their synthesis, or post-synthetically (modifications after the MOFs synthesis).

VI.2.2.1. **Encapsulation of of Brønsted acid molecule in MOFs pores**

Keggin-type polyoxometallate was encapsulated in MIL-101 (Cr) [176] in one pot synthesis, and the resulted complex has been reported to be active in 5-HMF production starting from glucose or fructose [177]. Postsynthetic guest molecule introduction was reported when mixing MIL-101 (Cr) with H_2SO_4 and H_3PO_4 encpsulating them in the pores (catalysis application was not mentioned) [178].

VI.2.2.2. **Ligation of Brønsted acid functionalities to unsaturated metal sites**

Upon synthesis, some MOFs have hydroxyl groups bridging metal atoms and are the source of Brønsted acidity, as in MIL-101 (Cr) [173]. Due to that, activity in Diels-Alder reaction has been reported [179]. By post synthetic pathways, Brønsted acidity was introduced into UiO-66 after mixing it with a DMF solution containing oxalic acid, and the latter bound to metal vacancies in UiO-66. The resulting product was able to capture ammonia, SO_2, NO_2 and octane from a gas stream, with higher efficieny than non-modified UiO-66 [180].

VI.2.2.3. **Covalently bound Brønsted acid functionalities to MOFs ligands**

During a direct MOFs synthesis, an acid precursor is introduced with the MOFs precursors (metal and ligand), as it was the case of MIL-101 (Cr) with $–SO_3H$ groups. The resulted product was active in cellulose hydrolysis [181]. Postsynthetically, MIL-100 (Fe) was mixed with aqueous solution of CF_3COOH, this protonated some carboxylate functional groups binding to Fe metals and formed -COOH free groups. The product was active in Diels-Alder reaction [179].

VI.2.3. **Brønsted basic characters**

Brønsted basicity can be introduced through ligation to unsaturated metal sites or covalent link to the ligands. These characters can be added to MOFs directly during their synthesis, or post-synthetically (modifications after the MOFs synthesis).

VI.2.3.1. **Ligation of Brønsted base functionalities to unsaturated metal sites**

It has been performed through post-synthetic modifications. Ethylene diamine has been introduced into MIL-101 (Cr) through ligation to the unsaturated metal sites. The formed complex was active in Knoevenagel condensation of benzyl alcohol and melanonitrile in hexane at 80°C [182].

VI.2.3.2. **Covalently bound Brønsted base functionalities to MOFs ligands**

IRMOF-3 showed Brønsted base properties when directly synthesized from $Zn(NO_3)_2$ and modified terephthalic acid (2-aminoterephthalic acid) [183]. Post synthetic modifications were applied on MIL-101 (Cr) for direct amination of the aromatic rings. The ligands were nitrated by reduction, producing amino functionalized MIL-101 [184]. It has been reported to be active in Knoevenagel condensation of benzyl alcohol and melanonitrile in toluene at 80°C [185].

For more details concerning Lewis and Brønsted acid/base functionalized MOFs, comprehensive reviews are available [186, 187].

VI.2.4. **Immobilized metal nanoparticles**

MOFs are in general functionalized with metal Nps for catalytic activities. Metal Nps or metallic precursors can be imbedded within the pores (M/MOF) or supported on the surface (M@MOF) of MOFs. One key step to synthesize MNps in or on MOFs is the stability of the MOFs under the synthetic conditions applied. Moreover, controlling the path of the MNps (in the pores or on the surface) is dependent on the size of the precursors used with respect to the accessible windows of the MOFs pores. In general, confirming the confinement of metals within the pores without their presence on the surface is complicated. One normally considers that small size distribution of metal nanoparticles means that they are all in the MOFs pores, while when bigger size distribution is observed, the possibility of being outside the pores increases.

Surface anchored metallic precursors were fewly reported. An example, by Long group, showed the coordination of $[Cr(CO)_6]$ on the surface of MOF-5 through the phenyl ring of the ligand [188]. Then, Chavan et al. reported the coordination of $[Cr(CO)_3]$ onto UiO-66 [189]. Recently, HfO_2 and TiO_2 were observed to coat the surface of UiO-66 after the

attempts to perform metal exchange (exchange of Zr with Hf or Ti) in a post-synthetic modification approach [190].

Mostly metal Nps are reported to be inside the MOFs pores. This has been reported to be done using chemical vapor deposition (CVD), wetness impregnation, sol-gel polycondensation, grinding and constructing the MOFs in the presence of metallic precursors. The following review describes metal immobilization in MOFs and shows different applications from adsorption to catalysis [191, 192]. Here, some metal/MOFs systems with catalytic activities are highlighted [193].

Pd was loaded into the pores of MOF-5 by wet impregnation using $Pd(acac)_2$ in chloform, followed by reduction. The BET surface area of MOF-5 decreased from 2885 $m^2.g^{-1}$ to 958 $m^2.g^{-1}$, confirming the encapsulation of Pd metal Nps inside the pores. Pd/MOF-5 was active in styrene hydrogenation [194]. In the same synthetic approach, Pd was encapsulated in MIL-101, where its BET surface area decreased from 2367 $m^2.g^{-1}$ to 2046 $m^2.g^{-1}$. The particles size was 1.5 nm. Pd/MIL-101 showed complete styrene hydrogenation in 7h, while it reached 80% with Pd/MOF-5 after the same time interval [195]. Pd encapsulation within the pores of MIL-101 (Cr), functionalized with ethylenediamine, using $[PdCl_4]^{2-}$ precursor produced 2 nm to 4 nm Pd nanoparticles. Pd/MIL-101 was active in Heck reaction [182]. Besides, microwave assisted synthesis was used to prepare also Pd/MIL-101 systems. $Pd(NO_3)_2$ precursor was added to aqueous solution of MIL-101 along with hydrazine as a reducing reagent. The mixture was placed in a microwave reactor of 1000 W power for 1 min. Particles of 2 - 3 nm size were encapsulated within the pores, and also others of 4 - 6 nm were localized on the surface. The formed system was active in CO oxidation [196]. Iridium was deposited in and on UiO-66 having $–NH_2$ groups and showed 3.5 nm to 9 nm particles size. This complex was active in aromatic hydrogenation [197].

For Au Nps supported in or on MOFs, some examples are described. Au Nps were located within the pores of UiO-66 though having 5 nm size, according to Zhu et al. [198]. An interesting paper for Liu et al. showed different synthetic approaches for Au Nps in or on MIL-101. Depending on each synthesis, Au Nps were obtained in different sizes. Only deposition-precipitation method showed particles < 2 nm and these were supposed to be inside the pores, while when bigger particles were obtained, they were located on the

surface of MIL-101 [199]. Same explanation for Au Nps deposited in/on ZIF-8. Smaller particles < 2 nm were located inside pores while the bigger ones were reported to be outside. The formed complex of Au Nps and ZIF-8 was active in CO oxidation[200].

VI.2.5. **Hydrophobicity**

Hydrophobicity can be tuned in MOFs too, enhancing their stability in humid environment and making them active in different domains. Hydrophobicity can be introduced during MOFs synthesis using specific ligands. ZIF-8 is a famous example in this topic having a methyl group on the imidazolate. Hydrophobicity can be also introduced through post-synthetic modifications, by introducing fluorinated groups to the ligand as the case of F_nNU-1000 (perfluorinated pyrene-based linkers of $Zr_6(\mu_3\text{-}OH)_4(\mu_3\text{-}O)_4(OH)_4(H_2O)_4$ MOF). Hydrophobic coating membranes is another method, this was the case of MIL-101 coated with silica. These factors are described in details along their applications in the following review for whom is interested [201].

VI.3. **Synthesis and structure of UiO-66 (Zr), MIL-101 (Cr) and ZIF-8 (Zn)**

UiO-66 (Zr), MIL-101 (Cr) and ZIF-8 (Zn) are known to have high thermal stabilities, in addition to various characters that made them interesting materials to be used in catalytic transformations. They were reported as successful catalysts themselves or after being impregnated with noble metals. As indicated before, the work of this thesis was based on using these MOFs as catalysts and as supports for tGNCs. For that, their structure, syntheses and their major characteristics that made them successfull in catalysis are discussed in this part.

VI.3.1. **UiO-66**

UiO-66 was firstly reported by Cavka et al. in 2008 [160]. It has a 3D structure, composed of octahedral metallic nodes made of 6 Zr atoms forming the $[Zr_6(\mu_3\text{-}O)_4(\mu_3\text{-}OH)_4]^{12+}$ clusters known as the secondary building unit (SBU). The octahedra arrange themselves in a face-centered cubic arrangements connected by terephthalates. Each Zr_6 cluster is connected to 12 similar neighboring clusters leading to the 3D porous network **Scheme 1-9**. The network has octahedral and tetrahedral cages of 9 Å and 7 Å respectively, connected by triangular windows of 6 Å.

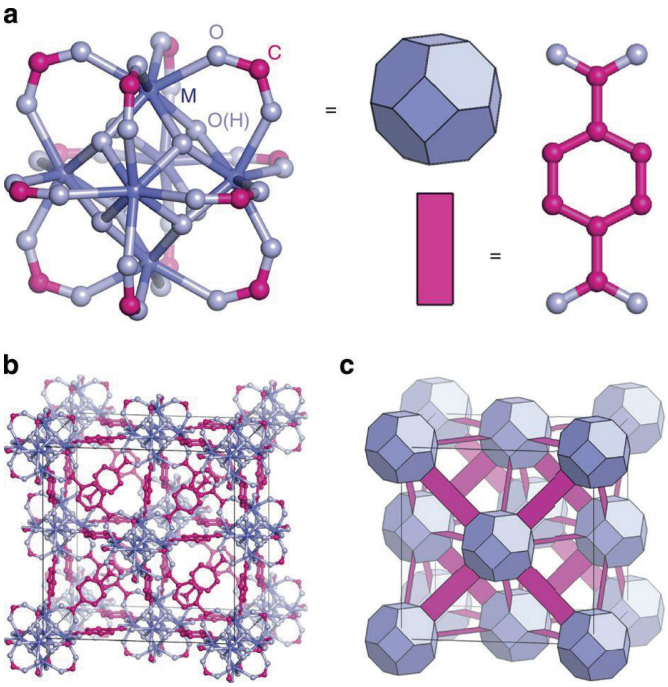

Scheme 1-9 (**a**) The building unit of UiO-66 connected by terephthalate linkers: Zr (dark purple), O (light purple) and C (magenta). (**b**) The building blocks adopt face-centred-cubic arrangement. (**c**) A simplified polyhedral representation of **(b)** (from [202]).

The solvothermal synthesis of UiO-66 has been based on mixing $ZrCl_4$ and H_2BDC in DMF (N,N-dimethylformamide) at 120°C during 24h, followed by several cycles of DMF washing then drying at room temperature. It has been reported to be stable up to 300°C, with octahedral particles size of 1-2 µm and a surface area of around 1200 m^2/g [160]. Different modulators were used to optimize the particle size. 5 equivalents of acetic acid [169] and 10 equivalents of benzoic acid [203] with respect to $ZrCl_4$ resulted in 95 nm – 100 nm UiO-66 particles. In 2014, Li et al. reported a microwave assisted synthesis leading to 250 nm particles having 1500 m^2/g surface area [204]. Functionalized UiO-66 (Zr) derivatives can be obtained by direct synthesis using functionalized BDC ligands: $-NH_2$, $-NO_2$, -Br etc. These functionalities have been introduced without affecting the thermal and chemical stability of UiO-66 [205].

As discussed earlier, its Lewis acidic properties, in addition to Brønsted acid and base ones in modified UiO-66, beside active encapsulated metal Nps in or on UiO-66, made this MOF active in esterification and oxidation catalytic reactions [206].

VI.3.2. **MIL-101**

MIL-101 is one of the most known trivalent metal based MOFs. Férey and co. established the early work with high valent metals in MOFs synthesis and reported the MIL series with three metal types, Al^{3+}, Fe^{3+} and Cr^{3+}, named MIL-53 (terephthalate) [207], MIL-100 (trimesate) [208] and MIL-101 (terephthalate) [173]. MIL-101 is a 3D network composed of Cr trimers connected by μ_3-O and 3 terephthalates. Depending on the synthetic conditions, one Cr is connected to -F or -OH anions, and the two other Cr are connected to two solvent molecules (Lewis acid character of the metal upon thermal elimination) [173]. This results in the SBU $Cr_3(\mu_3\text{-}O)(OH)(H_2O)_2(BDC)_3$ clusters. The SBU organize themselves to form supertetrahedra, which lead in turn to the formation of two mesoporous cages (29 Å and 34 Å diameters) having two accessible microporous windows (12 and 16 Å) **Scheme 1-10**.

MIL-101 is a stable MOF of a surface area superior to 4000 $m^2.g^{-1}$. The solvothermal synthesis consists of mixing the chromium salt with H_2BDC in water in the presence of hydrofluoric acid (HF), and placed in an autoclave at 220°C for 8h [173]. Microwave-assisted synthesis was used to form nanoparticles of MIL-101. $Cr(NO_2)_3{\cdot}9H_2O$ and terephthalic acid were mixed in water in the presence of HF at 210°C in less than 1 h. When crystallization time was 40 min the particle size was 40-80 nm giving broad peaks in PXRD whereas when increasing the crystallization time, the particle size increased [209]. In 2009, HF free microwave synthesis was reported by Demessence et al., where 22 ± 5 nm MIL-101 particles were obtained at 200°C in 1 min [210].

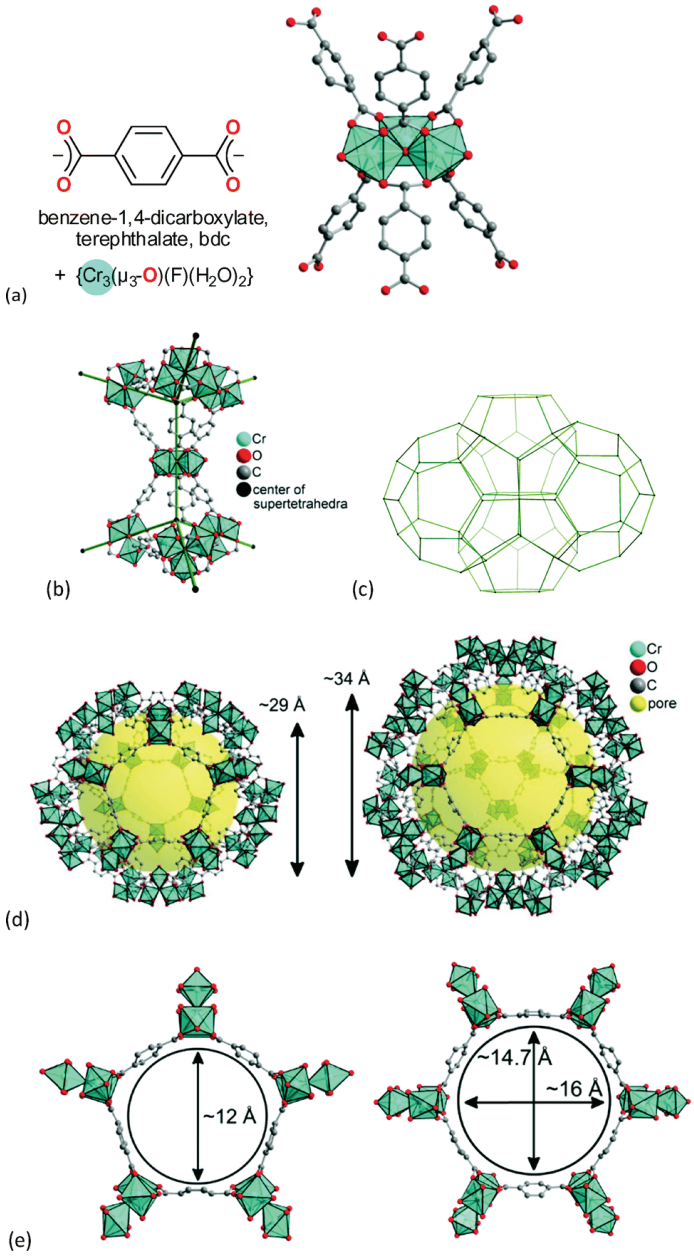

Scheme 1-10 (a) Ligand and metal building blocks in the trinuclear $Cr_3(\mu_3\text{-}O)(O_2C\text{-})_6(F/OH)(H_2O)_2$ building unit; (b) supertetrahedra; (c) mesoporous zeotypic network; (d) small cage with pentagonal windows and large cage with pentagonal and hexagonal windows; (e) dimensions of pentagonal and hexagonal cage window apertures (from [211]).

Due to its Lewis acid character and Brønsted acid functionalities in its derivatives, in addition to the active metals deposited in MIL-101, it has been widely used in catalysis. Examples on reactions with MIL-101 based catalysts, cyanosilylation of aldehyde, oxidative cleavage of alkenes and oxidation of aromatic alcohols etc [212].

VI.3.3. **ZIF-8**

Yaghi and co. were the first to introduce imidazolates into MOF chemistry [213]. ZIF-8, a common imidazolate microporous MOF, is formed by tetrahedral Zn atoms, where each Zn is connected to two 2-methylimidazolate (HMeIm), forming the SBU $Zn(MeIM)_2$. The latter arranges itself by four and six- ZnN_4 clusters membered ring with internal cavities of 11.6 Å diameter, connected by 3.4 Å windows [213] **Scheme 1-11.**

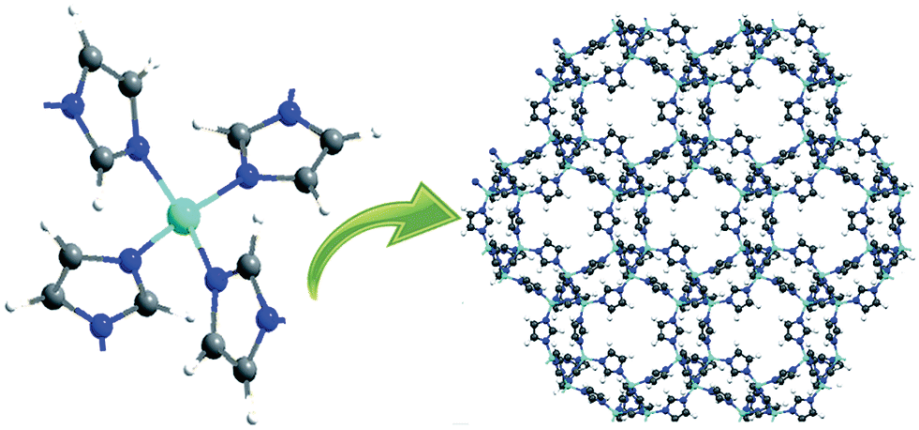

Scheme 1-11 Secondary building unit and crystal structure of ZIF-8 (Zn: cyan; C: grey; H: white and N: blue) (from [214]).

ZIF-8 has a BET surface area between 1100 and 1400 $m^2.g^{-1}$. It was firstly synthesized in DMF, using 2-methylimidazole and $Zn(NO_3)_2{\cdot}4H_2O$ as precursors, at 85°C for 72 h [215]. Later, Lai group published for the first time the aqueous phase synthesis of ZIF-8 which took place within minutes leading to nanocrystals of 85 nm size [216]. Sonochemical [217], electrochemical [218] and mecanochemical syntheses [219] were also reported. TGA shows that ZIF-8 is stable up to 550°C under N_2 atmosphere. In boiling water it is stable for almost 7 days, due to the bond strength between the metal and the ligand and its hydrophobic characteristics because of the presene of methyl groups.

Different metals were supported using ZIF-8 crystals leading to composites with Pd, Pt, Ag or Au metallic sites, each having specific characteristics and applications. ZIF-8 and its funtionalized derivatives have been used for catalytic applications including reduction, condensation and oxidation reactions [220].

VI.4. **UiO-66, MIL-101 and ZIF-8 in catalysis**

In this part, the use of UiO-66, MIL-101 and ZIF-8 based catalysts specifically for biomass transformations and for benzyl alcohol oxidation reactions are discussed. For other catalyzed reactions using these MOFs intact or their derivatives, comprehensive reviews are available [187, 211].

VI.4.1. **UiO-66, MIL-101 and ZIF-8 for transformations of biomass**

In general, non-functionalized MOFs show poor activity in biomass-based transformations. Modifications introducing Brønsted acid functionalities or impregnated metals (Pd, Pt and Ru) give active materials. Examples of MIL-101-SO_3H, UiO-66-SO_3H, Pd supported MIL-101, Pd supported UiO-66-NH_2, Ru supported UiO-66 catalyzing biomass transformations have been reviewed [211, 221]. In this section the use of intact UiO-66, MIL-101 and ZIF-8 will be highlighted through examples.

UiO-66 nanoparticle (≤ 100 nm), showed 92.7 % yield of ɣ-valerolactone (GVL) in the catalytic hydrogen transfer of ethyl levulinate in isopropanol (being the hydrogen source) **Scheme 1-12**, at 200°C for 2 h [222]. This result was of higher selectivity compared to that using ZrO_2 as catalyst (62% 5 GVL after 4h at 150°C) [223]. In general Zr based catalysts were widely used for this transformation, as $Zr(OH)_4$ [224] and Al_7Zr_3 [225].Thanks to Lewis acid properties of UiO-66 and its high surface area that was supposed to increase the interaction between the substrates and the active sites resulting in comparable and some times better activities of the already mentioned catalysts.

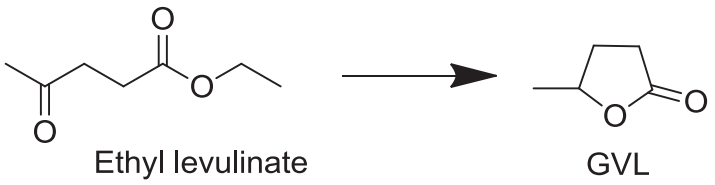

Scheme 1-12 Transformation of ethyl levulinate to GVL using UiO-66.

MIL-101 was reported to be active in glucose isomerization into fructose in water at 100°C during 24 h. 22 % conversion with 12.6 % fructose yield were obtained [226]. Glucose dehydration was also reported using MIL-101 (Cr) into 5-HMF (5-hydroxymethyl furfural). Solvent mixture of THF: H_2O / 39: 1 was found to be necessary to stabilize the

formed 5-HMF. The reaction was conducted at 130°C for 24 h but less than 2 % yield of 5-HMF was detected **Scheme 1-13**. MIL-101-SO_3H, with Brønsted acidity, showed, as expected, better activity and yielded 29 % of 5-HMF under the same conditions. However, conducting the reaction in pure water resulted in rapid production of 5-HMF with uncontrolled polymerization of the formed species leading to humins (unsoluble black precipitates). Humins deactivate the catalyst and block its recovery [227, 228].

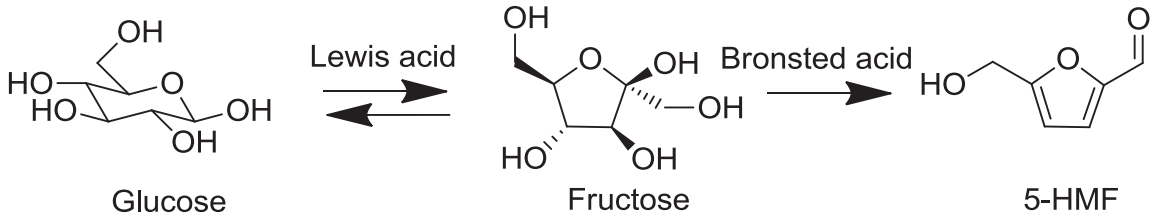

Scheme 1-13 Glucose conversion using MIL-101 and its derivative.

Starting from xylose, at 170°C during 3 h, 49 % of furfural can be obtained in 10 ml of water/toluene mixture (3 ml/ 7 ml) **Scheme 1-14**. Unfortunately after several cycles the MIL-101 activity decreased due to the stability loss. Efforts to enhance its stability by modifications using octadecyltrichlorosilane, increased the activity and 56 % furfural was obtained with stable activity up to 8 cycles [229].

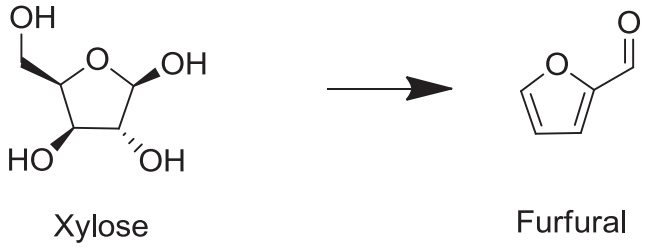

Scheme 1-14 Xylose transformation into furfural using MIL-101 and its derivative.

ZIF-8 has been applied to sugar conversion into lactic acid derivatives. Firstly reported by Murillo et al. in 2016, ZIF-8 nanoparticles (150 nm) were able to form 35 % of methyl lactate by transformation of sucrose in methanol at 160°C for 24 h. This conversion is due to the Zn Lewis acidic properties necessary for such transformation [230].

VI.4.2. **Gold supported MOFs for alcohol oxidation reactions**

MOFs have served as supports for various metals (Au, Pd, Pt, Ru, Cu and others) eading

to functional composite materials. The deposition of the particles can be inside the MOF pores or at the surface of the particles, depending on the synthetic method [191, 192, 231]. In this part, only gold nanoparticles supported on MOFs (Au@MOFs), more precisely Au@UiO-66, Au@MIL-101 and Au@ZIF-8, will be highlighted, with application to alcohol oxidation [193].

MOFs, to be active in alcohol oxidation reactions, should have metal vacancies and so Lewis acid character. The only intact MOF (without postsynthetic modifications) that was able to trigger such transformation is $Cu_3(BTC)_2$ (BTC: benzenetricarboxylate), having Cu^{2+} centers. The reaction was conducted at 75°C in acetonitrile with TEMPO (2,2,6,6-tetramethylpiperidine-1-oxyl), an initiator, Na_2CO_3 base and atmospheric O_2 as the oxidant. The best activity was registered for benzyl alcohol (primary alcohol) oxidation into benzaldehyde (90 % yield), within 22 h [232]. UiO-66, MIL-101 and ZIF-8 alone have never been reported for such transformations despite having required acid character. Otherwise, these MOFs supporting metal nanoparticles showed good activity at this level. The beginning of gold nanoparticles supported on MOFs was done by with Haruta and co. in 2008. They studied Au@MIL-53 system, having 1.5 nm ± 0.7 nm particle size and being at the outer surface of MIL-53. It was synthesized by solid grinding followed by H_2 reduction [233]. After, the use of Au supported UiO-66, MIL-101 and ZIF-8 systems was also reported.

Au/UiO-66 composite was synthesized by mixing UiO-66 in dry *n*-hexane with aqueous Au precursor solution, then reduced with $NaBH_4$ aqueous solution, resulting in 5 nm Au nanoparticles located within the pores of UiO-66. It was then used for benzyl alcohol oxidation in free solvent conditions. Benzyl alcohol, Au@UiO-66 and K_2CO_3 were mixed at 80°C, under O_2 flow during 10 h, leading to the formation of 53.7 % benzaldehyde [198] **Scheme 1-15**.

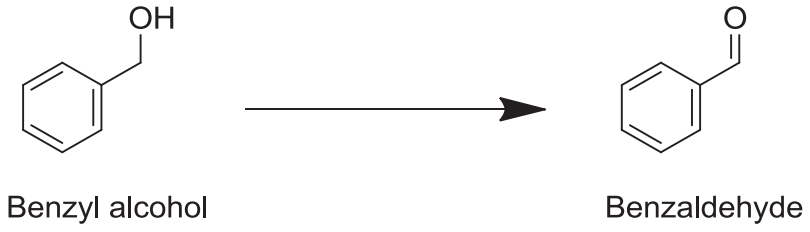

Scheme 1-15 Benzyl alcohol oxidation using Au Nps supported UiO-66.

Au/UiO-66 catalyst, synthesized by impregnation-reduction method with H_2 being the reducing agent resulted to 3-5 nm particles size embedded within the pores of UiO-66. This catalyst showed high efficieny in furfural oxidative esterification toward methyl-2-furoate in methanol at 140°C in 4h, under 3 bar O_2 and with a base for complete selectivity toward methyl-2-furoate. It should be noted that synergy between Au Nps and UiO-66 was highlighted, where UiO-66 was observed to transform furfural into the corresponding acetal and hemi-acetal, which in turn is transformed into the ester by the oxidation power of Au Nps [234].

Li et al. showed the deposition of Au over MIL-101 by different techniques: colloidal deposition with polyvinylpyrrolidone (PVP), impregnation and deposition-precipitation. The best method was colloidal deposition with PVP leading to average particles size of 2 nm located inside the pores. They used $HAuCl_4$, PVP and $NaBH_4$ in the synthesis followed by MIL-101 addition. The composite formed showed very nice oxidation activity toward different alcohols in toluene at 80°C and 1 atm O_2 pressure using H_2O or any type of base [199]. The conversion and selectivity were > 99 %. This activity is due to high dispersion of Au within the MIL-101 pores, showing synergy between Au and MIL-101. The latter has pore sizes that allow the easy access of reactants and products diffusion.

Au@ZIF-8 composite was reported for alcohol oxidation by Corma et al. in 2010. Au Nps were encapsulated inside the pores of ZIF-8 using a volatile gold precursor [Au(CO)Cl], and then 2 bars H_2 at 100-130°C was apply to trigger gold reduction. The obtained nanoparticles were 3.2 nm in size. Benzyl alcohol oxidative esterification was targeted in methanol, under pure oxygen pressure (0.5 MPa) leading to 81.2 % conversion and 98.2 % selectivity toward methyl benzoate (ML) at 80°C during 24 h [189] **Scheme 1-16**.

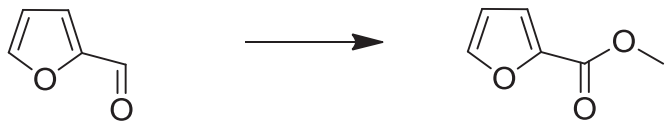

Furfural Methyl-2-fuorate

Scheme 1-16 Furfural oxidative esterification in methanol using Au Nps supported ZIF-8.

VII. **Conclusion, positioning of the project and objectives**

Literature review of tGNCs and MOFs has been presented. Synthesis, types, structures, physical properties and catalytic applications of both types of materials have been described. Based on what preceeded, the objectives of the thesis have been chosen as following:

- Synthesis of new composite materials that couple the advantages of tGNCs and MOFs for catalytic transformations. In the tGNC@MOF materials the clusters are the active species for oxidation reactions and the MOFs as nanoparticles may have two roles: (i) a light support for the dispersion of gold clusters and (ii) an active catalytic species with the presence of Lewis acid sites.

- With those multifunctional catalysts cascade catalytic reactions can be expected, that is why complex transformations of the sugars are studied in the manuscript. In addition, model reactions were chosen to identify the catalytic activity of each component, to deduce after the possible synergy between tGNCs and MOFs. For that MOFs alone were tested for catalysis, and an in-depth study with a composite material using an oxide as a support, tGNC@ZrO_2, allowed to evaluate the catalytic activity of the clusters without MOFs.

To reach these ultimate objectives the study has been divided as follows:

- Three clusters, $Au_{25}(SG)_{18}$, $Au_{25}(Capt)_{18}$ and $Au_{25}(SC_6H_4NH_2)_{18}$, were chosen to study their thermal stability and their different affinity with the support depending on their external organic functions (1 or 2 -COOH, -NH_2 or nothing).

- Three 3D porous MOFs, UiO-66, MIL-101 and ZIF-8, were chosen as supports and studied as catalysts in the transformation of biomass derivatives (glucose, fructose and xylose), due to their Lewis acidity.

- Formation of composite materials with the tGNCs and the 3 selected MOFs (UIO-66, MIL-101 and ZIF-8) **Scheme 1-17**. Their catalytic activity was evaluated through two model reactions: (i) benzyl alcohol oxidation and (ii) furfural

oxidative esterification. Further, the transformation of biomass derivatives was also tested.

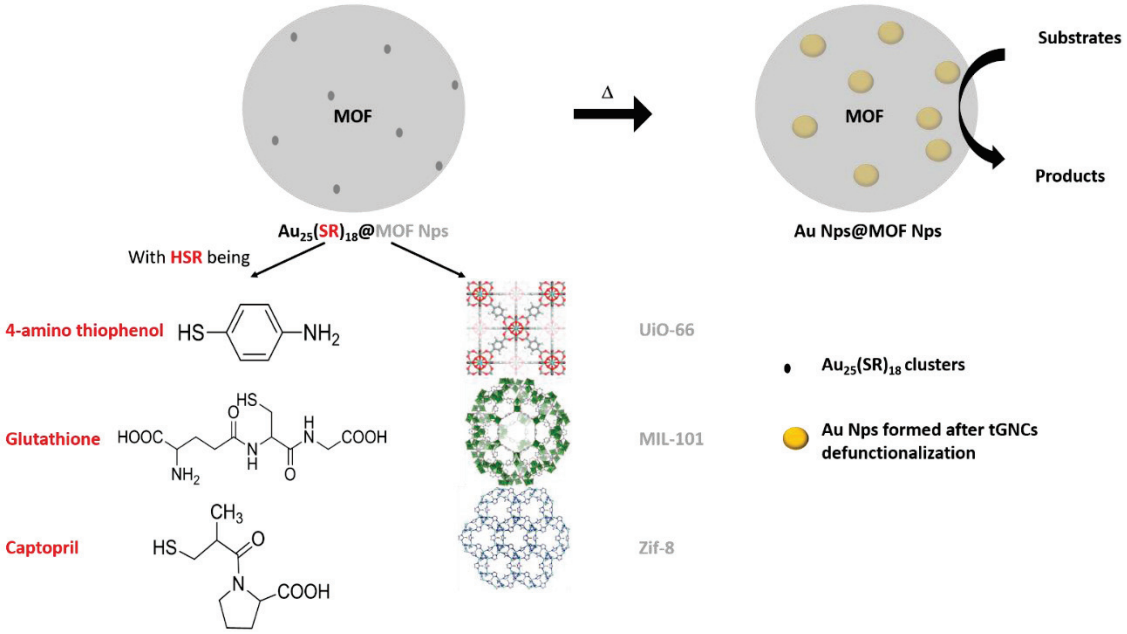

Scheme 1-17 Composite materials tGNCs@MOF Nps (before calcination) and the produced Au Nps @MOF Nps catalysts (after calcination).

- Formation of the composite material $Au_{25}(SG)_{18}@ZrO_2$ with in-depth gradual defunctionalization **Scheme 1-18**. It was catalytically tested in benzyl alcohol oxidation and furfural oxidative esterification.

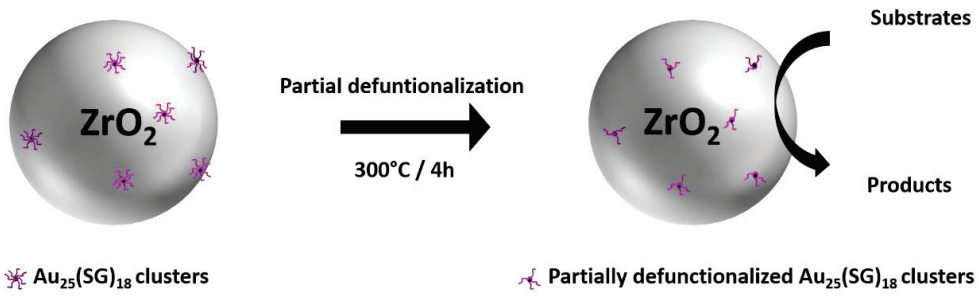

Scheme 1-18 $Au_{25}(SG)_{18}@ZrO_2$ Nps before and after partial defunctionalization for catalytic applications.

Chapter 2

Experimental Part

I. Preparation of different materials

The starting compounds are described in annex A.

I.1. **Preparation of metal organic frameworks nanoparticles**

Syntheses of UiO-66, MIL-101 and ZIF-8 were performed based on known procedures.

I.1.1. **UiO-66**

$ZrCl_4$ (2.75 mmol, 640 mg) and terephthalic acid: H_2BDC (2.85 mmol, 473 mg) were added to 40 ml DMF in a 250 ml glass vial capped with Teflon. Benzoic acid (27.6 mmol, 3.36 g) was added and all were dissolved using an ultrasonic bath during 5 min. The mixture was kept in a preheated oven at 120°C for 30h under static conditions. Suspension was collected after cooling to room temperature and centrifuged at 10000 rpm for 15 min. Three times washings using DMF were performed to remove the excess of ligand, followed by other three times washings by MeOH at 4000 rpm (10 min/cycle) [203]. The white product obtained (75% yield), corresponding to UiO-66 nanoparticles, was dried at room temperature and activated at 150°C under vacuum (12h) before use.

I.1.2. **MIL-101**

By hydrothermal synthesis

In the hydrothermal approach [235], $Cr(NO_3)_3{\cdot}9H_2O$ (15 mmol, 6 g) was dissolved in 80 mL H_2O. Terephthalic acid (15 mmol, 2.5 g) was added and the mixture was heated at 220 °C for 8 h (480 min). The green solid obtained was filtered and purified using soxlet extraction during two consecutive nights: one night using DMF and the other using MeOH. Finally, MIL-101 (Cr) was dried under vacuum at 150 °C for 12 h.

By microwave assisted synthesis

$Cr(NO_3)_3.9H_2O$ (5.2 mmol, 2g) was dissolved in 10 ml H_2O in a 30 ml microwave tube. H_2BDC (5.2 mmol, 833 mg) was added. The microwave-assisted synthesis was done in an Anton Paar microwave (monowave 400) equipped with an auto sampling holder (MAS 24), at 200°C during 1 min. The temperature increased within 4 min from 25°C to 200°C and was held at 200°C for 1 min before the cooling step. The formed precipitates were separated by centrifugation at 11000 rpm for 15 min. Soxlet extraction was done during two consecutive nights: one night using DMF and the other using MeOH [210]. The obtained green product (30% yield), corresponding to MIL-101 nanoparticles, was dried at room temperature and activated at 150°C under vacuum before use.

I.1.3. ZIF-8

$Zn(NO_3)_2.6H_2O$ (1.23 mmol, 365 mg) was dissolved in 25 ml MeOH. 2-methylimidazole (9.84 mmol, 806.88 mg) was dissolved in 25 ml MeOH. Both solutions were mixed at room temperature followed by stirring at 1000 rpm for 30 min. Centrifugation was done at 11000 rpm for 10min, then repeated 3 times while washing with 50 ml EtOH [216]. The product (50% yield), corresponding to ZIF-8 nanoparticles, was dried at room temperature overnight and activated at 150°C under vacuum before using.

I.2. Preparation of ZrO_2 nanoparticles

ZrO_2 nanoparticles were obtained from $Zr(OH)_4$, calcined at 550°C (2°C.min^{-1}) for 5h. Mixed-phase ZrO_2 was obtained (monoclinic and tetragonal phases).

I.3. Preparation of thiolate-protected gold nanoclusters

Three types of $Au_{25}(SR)_{18}$ thiolate gold nanoclusters have been synthesized according to published procedures. For $Au_{25}(SG)_{18}$ some modifications were done to obtain the cluster with high purity.

I.3.1. $Au_{25}(SG)_{18}$ based on Glutathione ligand (HSG)

$HAuCl_4.3H_2O$ (0.252 mmol, 99.2 mg) was dissolved in 50 ml MeOH using 100 ml round-bottom flask in an ice bath. Glutathione: HSG (1 mmol, 307.1 mg) was added, and the mixture was stirred at 1500 rpm for 30 min. Sodium borohydride ($NaBH_4$) aqueous

solution (2.513 mmol in 12.5 ml cold H_2O) was added rapidly followed by vigorous stirring for 1 h. Centrifugation at 11000 rpm for 10 min, repeated 3 times while washing with 50 ml of MeOH. The obtained mixture was dried under vacuum, then dissolved in 12.5 ml H_2O, and the flask was placed at 55°C in an oil bath. HSG (0.5 mmol) was then added and left for 4 h stirring at 60 rpm. Filtration was done to remove insoluble by-products. 20 ml of MeOH were added to precipitate the $Au_{25}(SG)_{18}$ nanoclusters. Centrifugation at 11000 rpm for 10 min, repeated 3 times for washing with 50 ml of MeOH, resulted in the product (40% yield) that was dried at room temperature overnight [68].

I.3.2. $Au_{25}(Capt)_{18}$ based on Captopril ligand (Capt)

$HAuCl_4.3H_2O$ (0.202 mmol, 79.5 mg) was dissolved in 10 ml MeOH using 100 ml round-bottom flask and placed in ice bath. Tetraoctylammonium bromide: TOAB (0.229 mmol, 125.2 mg) was added followed by stirring at 1000 rpm for 20 min. Captopril aqueous solution (1 mmol, 5 ml H_2O) was added rapidly followed by stirring at 1100 rpm for 30 min. Sodium borohydride ($NaBH_4$) aqueous solution (1.953 mmol in 5 ml cold H_2O) was added rapidly followed by vigorously stirring at 1500 rpm. Stirring was then slowed down to 60 rpm for 16 h. Centrifugation at 11000 rpm was done to remove insoluble byproducts. The solution mixture was evaporated on a rotavap at 50°C, followed by drop to drop ethanol (EtOH) addition until precipitates were observed. Centrifugation was done at 11000 rpm for 10min, repeated 3 times, for washing with 50 ml of MeOH. The resulting product (50% yield) was dried at room temperature overnight [51].

I.3.3. $Au_{25}(SC_6H_4NH_2)_{18}$ based on 4-aminothiophenol ligand

Sublimated 4-aminothiophenol (1.056 mmol, 132.2 mg) was dissolved in 20 ml cold THF using 100 ml round-bottom flask placed in an ice bath. $HAuCl_4.3H_2O$ (0.528 mmol, 208 mg) solution in 20 ml THF, and lithium borohydride 2 M in THF (1.1 ml) solution in 20 ml THF, were added simultaneously with controlled addition rate of 60 $ml.h^{-1}$, while stirring at 400 rpm. The mixture was transferred into 250 ml round-bottom flask and left stirring at 300 rpm at room temperature for 5 h. The solution was evaporated on a rotavap. The resulting solid was dispersed in EtOH and centrifuged at 11000 rpm during 10min. Centrifugation was repeated 3 times for washing with 50 ml of EtOH. The product (75% yield) was dried at room temperature overnight [49].

I.4. **Preparation of composite materials**

Table 2-1 reports the conditions of syntheses of different composite materials, based on different thiolate gold nanoclusters and different supports.

In a simple deposition method, $Au_{25}(SR)_{18}$ was dissolved in a suitable solvent. The support was then added as a powder. The mixture was stirred at 400 rpm for specific time **Table 2-1**. The product, $Au_{25}(SR)_{18}$@support, was filtered and dried at room temperature. After the deposition, the solution with the tGNCs that was dark brown turned to a brighter color, or was totally decolorized, pointing out the good interaction of the tGNCs with the supports. It should be noted that when DMF was the solvent used during the deposition, washing with MeOH was performed to remove coordinated DMF.

Calcination at different temperatures (200°C, 300°C and 400°C) was done under air with rate of 10°C.min^{-1} in the case of MOFs and 2°C.min^{-1} in the case of ZrO_2, and left at the chosen temperature for 4 or 12h.

Table 2-1 Conditions of composite materials syntheses

Composite material	m support (mg)	% Au	% Au_{tGNC}	m tGNC (mg)	Solvent: volume (ml)	Stirring (rpm)	Time (h)	Washing
$Au_{25}(SG)_{18}$@UiO-66	100	1	47.1	2.2	H_2O:10	400	2	-
$Au_{25}(SC_6H_4NH_2)_{18}$@UiO-66	100	1	69	1.5	DMF:10	400	2	MeOH
$Au_{25}(SG)_{18}$@MIL-101	100	1	47.1	2.2	H_2O:10	400	2	-
$Au_{25}(Capt)_{18}$@MIL-101	100	1	58.1	2.2	H_2O:10	400	2	-
$Au_{25}(SC_6H_4NH_2)_{18}$@MIL-101	100	1	66	1.5	DMF:10	400	2	MeOH
$Au_{25}(SC_6H_4NH_2)_{18}$@ZIF-8	100	1	66	1.5	DMF:10	400	2	MeOH
$Au_{25}(SG)_{18}$@ZIF-8	100	1	47.1	2.2	H_2O + EtOH: 3 + 7	400	2	-
$Au_{25}(SG)_{18}$@ZrO_2	500	1	47.1	10.6	H_2O:10	400	0.25	-

II Catalytic tests protocol

Table 2-2 reports the conditions used for the catalysis of different substrates using different catalysts.

II.1. Sugar transformation

Catalytic evaluation was carried out in a 50 ml autoclave, with the following conditions: Sugar (0.5w%t) was dissolved in water or iPrOH (30ml) without the use of base. The reactions were conducted air, O_2 or argon, at temperatures 120°C or 140°C, while stirring at 700 rpm. The reactions were monitored by regular samplings (0.5 mL) that were diluted 2 times in standard butyric acid solution (1 g/kg in H_2O) and were analyzed immediately by high performance liquid chromatography.

II.2. Benzyl alcohol oxidation in toluene

Catalytic evaluation was carried out in a two-neck 100 mL round-bottom flask equipped with a condenser and a magnetic stirrer, benzyl alcohol (BnOH, substrate, 1 mmol), cesium carbonate (Cs_2CO_3, base, 3 mmol), toluene (solvent, 20 mL) and gold-based catalyst (2 µmol Au) were stirred at 400 rpm at 80 °C under atmospheric air pressure, while connecting the flask to a reflux. The reactions were monitored by regular samplings (0.2 mL) that were diluted 2 times in the standard dodecane solution (1 wt % in toluene) and were analyzed immediately by gas chromatography.

II.3. Furfural (or furfuryl alcohol or benzyl alcohol) oxidative esterification in methanol

Catalytic evaluation was carried out in a 50 ml autoclave, with the following conditions: Substrate (0.36 mmol, 35 mg), methanol (28 mL), catalyst (40 mg having 0.2 mg of Au, 1 µmol), O_2 (6 bar), 100 °C, 700 rpm. The reactions were monitored by regular samplings (0.5 mL) that were diluted 2 times in standard butyric acid solution (1 g/kg in MeOH) and were analyzed immediately by gas chromatography. The reactions were intentionally performed in the absence of a base, except some tests performed using Na_2CO_3 (0.33 mol equiv./furfural, 75 mg).

Gold content and pressure conditions were fixed after studying the influence of Au amount and O_2 in the absence of base. Unless noted, the reactions were performed with the catalyst obtained after calcination at 400 °C of the supported $Au_{25}(SG)_{18}$. The amount of introduced catalyst corresponded to a ratio 0.57 wt% of Au.

Table 2-2 Conditions of the catalysis using different substrates.

Substrate: catalytic device	Solvent:volume (ml)	Substrate wt%	Base	Catalyst:µmol of Au	T (°C)	Atmosphere:P (bar)	Stirring (rpm)
Glucose: reactor	H_2O:30	0.5	no	**MIL-101:** 0 **$Au_{25}(SR)_{18}$@MIL-101 (with and without calcination):** 2	120-140	Air or Argon:30 O_2:6	700
Fructose: reactor	H_2O:30	0.5	no	**MIL-101:** 0 **$Au_{25}(SR)_{18}$@MIL-101 (with and without calcination):** 2	120-140	Air or Argon:30 O_2:6	700
Xylose: reactor	H_2O:30	0.5	no	**MIL-101:** 0 **$Au_{25}(SR)_{18}$@MIL-101 (with and without calcination):** 2	120-140	Air or Argon:30 O_2:6	700
Xylose: reactor	iPrOH:30	0.5	no	**MIL-101:** 0 **$Au_{25}(SR)_{18}$@MIL-101 (with and without calcination):** 2	120-140	Air:30	700
Benzy lalcohol: round bottom flask	Toluene:20	0.6	Cs_2CO_3	**$Au_{25}(SR)_{18}$@MIL-101 (with and without calcination):** 2 **$Au_{25}(SR)_{18}$@UIO-66 (with and without calcination):** 2 **$Au_{25}(SR)_{18}$@ZrO_2 (with and without calcination):** 2	60-80	ambient	700
Benzyl alcohol: reactor	MeOH:30	0.1	no	**$Au_{25}(SR)_{18}$@ZrO_2 (with and without calcination):** 1	100	O_2:6	700
Furfural: reactor	MeOH:30	0.1	no	**$Au_{25}(SR)_{18}$@ZrO_2 (with and without calcination):** 1	100	O_2:6	700

Chapter 3

Metal organic frameworks as heterogeneous catalysts

UiO-66, MIL-101 and ZIF-8, as well as their derivatives, have been widely used as heterogeneous catalysts principally due to their acidity and high thermal stability.

The total acidity of these non-modified MOFs has been reported in the literature based on NH_3-TPD (temperature-programmed desorption) analysis. UiO-66 has total acidity that ranges between 1.81 and 11.62 $mmol.g^{-1}$ depending on the synthetic method [236]. MIL-101, synthesized by a hydrothermal method, showed a total amount of acidic sites equals to 2.91 $mmol.g^{-1}$ [237]. ZIF-8 was reported to have 0.675 $mmol.g^{-1}$ of total acidity [238]. UiO-66, MIL-101 and ZIF-8 are stable in the solid phase up to 500°C, 280°C and 400°C respectively, under continuous heating conditions (TGA experiments).

According to the literature, sugar transformations using MOFs did not proceed much in water [226-228]. For that, we decided to re-investigate and study, under green conditions, different sugars transformations using mainly MIL-101 as heterogeneous catalyst. UiO-66 and ZIF-8 have been tested on glucose transformation. This chapter shows the catalytic activity of MIL-101 through the conversion of glucose, fructose and xylose. As a first indication, we can say here that isomerization of each tested sugar was the dominant mechanism favored by MIL-101. Isomerization of glucose was also dominant with UiO-66 and ZIF-8. MIL-101, UiO-66 and ZIF-8 were also tested for other transformations of biomass based substrates into valuable products. Furfural oxidative esterification in MeOH was targeted. Transformation of furfural into its corresponding 2-(dimethoxymethyl) furan was observed **Scheme 3-1**.

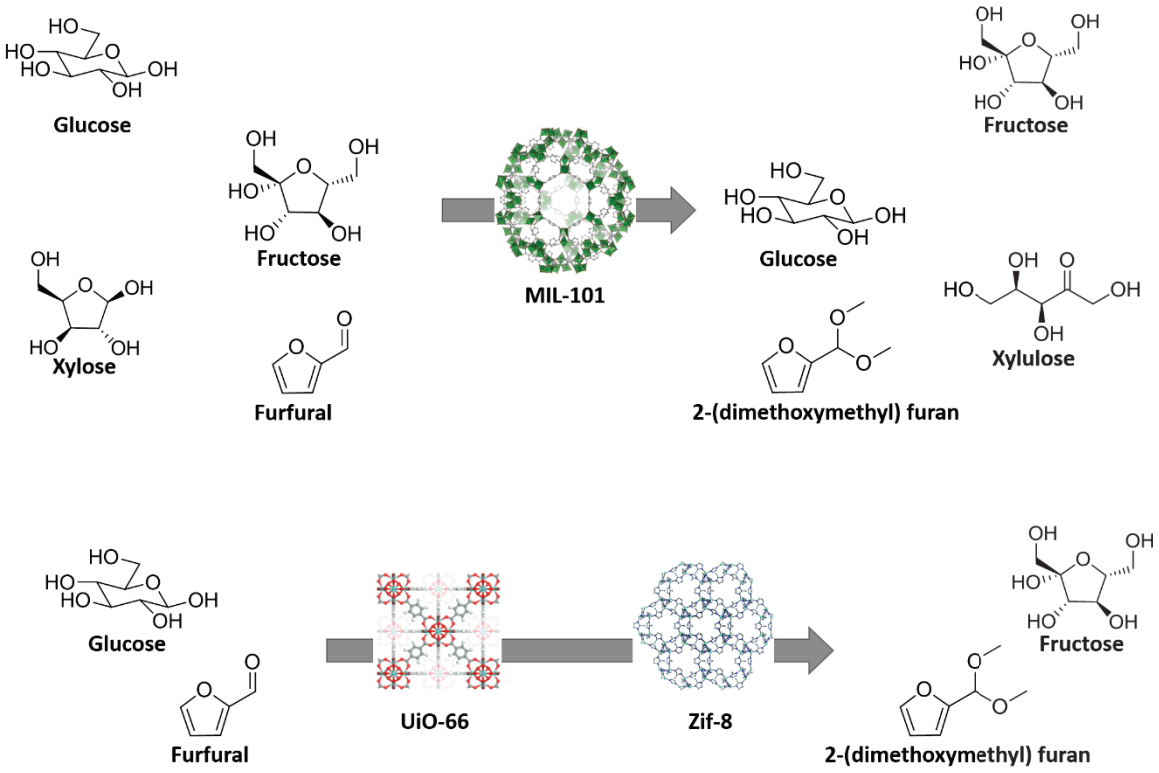

Scheme 3-1 Substrates and their corresponding products when catalyzed by MIL-101, UiO-66 and ZIF-8.

I. MIL-101 as catalyst

I.1. Synthesis

Synthesis of MIL-101 was carried out by hydrothermal and microwave approaches, aiming to form nanoparticles of MIL-101. Both approaches were carried out according to reported procedures, with some modifications (detailed procedures in **Chapter 2**). Neither protic acids nor monocaroxylic acids (modulators) were used to keep the surface free.

To differentiate MIL-101 samples synthesized by each methods, **MIL-101$_{XX}$** naming format has been used, where: XX= HT (Hydrothermal) or MW (Microwave).

The synthesized MIL-101 samples were characterized by PXRD, TEM, N_2 adsorption, TGA, TGA-µGC, IR, and TPD-NH_3.

I.2. Catalyst characterization

Powder XR diffractograms of **MIL-101$_{MW}$** and **MIL-101$_{HT}$** showed superimposable reflections with those of the simulated MIL-101 pattern, indicating the efficiency of both synthetic approaches. Moreover, the Bragg reflections of both synthesized materials were broader compared to the reference one **Figure 3-1.**

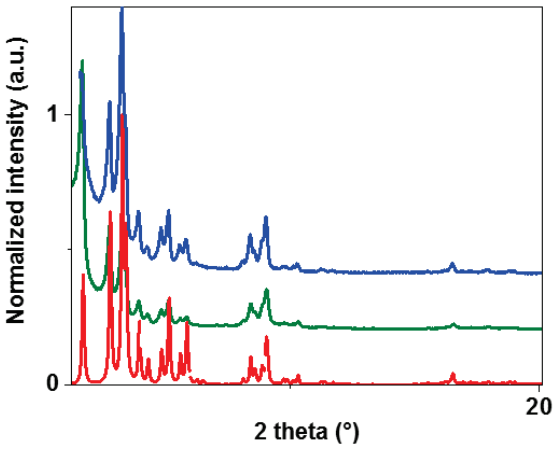

Figure 3-1 Powder X-ray diffraction patterns of MIL-101 synthesized by hydrothermal approach(blue), by microwave-assissted method (green) and compared to a reference sample (red).

SEM and TEM images were used to characterize precisely the particle size distribution of both MIL-101 samples. Almost 250 particles were measured in both cases. The average particle size of **MIL-101$_{MW}$** was 92 nm ± 30 nm, whereas that of **MIL-101$_{HT}$** was 106 nm ± 30 nm. There is no big difference at the level of particles size for nanoparticles obtained in both cases **Figure 3-2**.

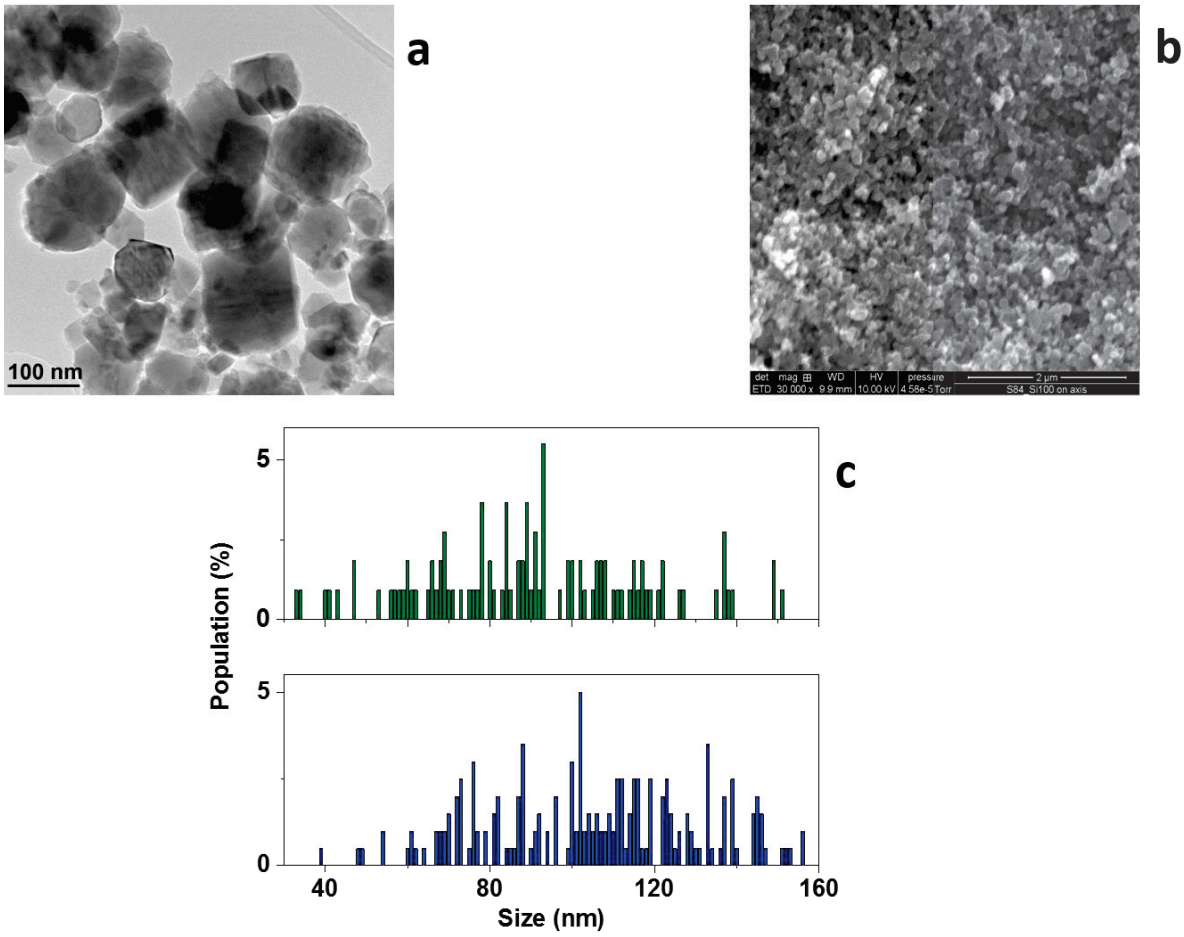

Figure 3-2 (a) TEM image of MIL-101$_{MW}$ (b) SEM image of MIL-101$_{HT}$ (c) Size distribution of MIL-101$_{MW}$ (green) and MIL-101$_{HT}$ (blue).

The main difference between both synthetic approaches was at the level of the BET surface area, determined by N_2-adsorption analysis. Higher surface area was observed for **MIL-101$_{MW}$**, 2700 $m^2.g^{-1}$, compred to 1600 $m^2.g^{-1}$ for **MIL-101$_{HT}$** **Figure 3-3**. This means that some residual molecules are present in the **MIL-101$_{HT}$** or that the pore openings are blocked.

TGA analysis showed similar curves of weight loss for both samples. The general formula of MIL-101(Cr) is $[Cr_3(\mu_3\text{-}O)(OH)(H_2O)_2(BDC)_3].xH_2O$. Without taking into consideration the H_2O molecules, the theoretical weight loss of the organic part of MIL-101 (Cr) between 200 and 400°C corresponds to 66 %, with 34 % of inorganic part corresponding to Cr_2O_3 at the end of the TGA analysis. First mass loss (around 100°C) corresponds to solvent loss and was more pronounced in **MIL-101$_{MW}$**. With excluding water content, one finds: 69.0 % weight loss in **MIL-101$_{MW}$** and 69.0 % in **MIL-101$_{HT}$**. These values are close to the

theoretical ones indicating that quite pure MIL-101(Cr) samples were formed, by both methods. From these data, they are stable up to 280°C under continuous heating conditions (25°C-800°C/10 °C.min^{-1}/Air/50 ml.min^{-1}) **Figure 3-4**.

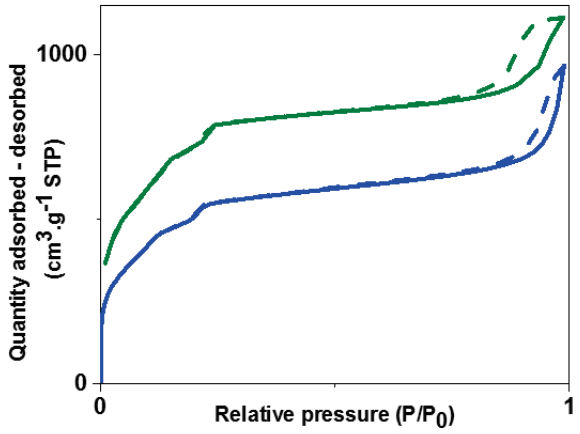

Figure 3-3 N_2 adsorption (line) and desorption (dashes) isotherms at 77 K of MIL-101$_{MW}$ (green) and MIL-101$_{HT}$ (blue).

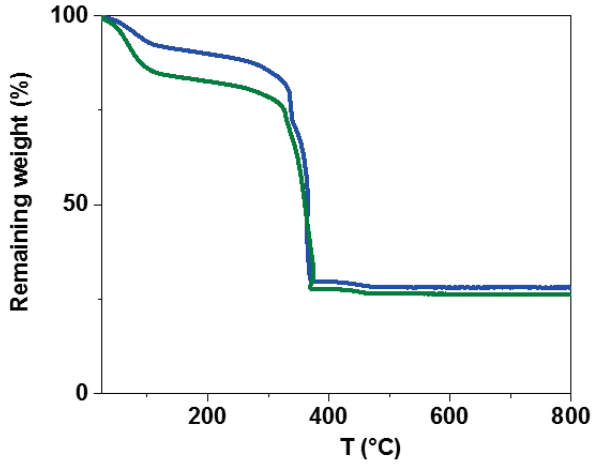

Figure 3-4 TGA thermograms for remaining weight percentage for MIL-101$_{MW}$ (green) and MIL-101$_{HT}$ (blue).

To prove the efficiency of the thermal activation and the absence of MeOH or DMF molecules, MIL-101$_{MW}$ was analyzed by TGA coupled with µGC. The analysis did not show peaks related to MeOH or DMF, meaning that washing and desorption for activation were successful. **Figure 3-5** shows that the weight loss of MIL-101 before 134 °C is accompanied with water release (MIL-101 captures moisture from air). Therefore, the 2 vacancies

(Lewis acid sites) on Cr are not coordinated to solvents other than H_2O. For that desorption was repeated directly before catalytic tests to ensure the elimination of H_2O. After 134 °C in **Figure 3-5** around 3 % of organic part is lost. This aligned with the release of CO_2 (CO_2 values were multiplied by 5 to increase the visibility of its evolution curve). This observation is related to decomposition of terephthalic acid that may be present at the surface of the MOF (indeed, it is shown in **Chapter 4** that MIL-101 was stable upon isothermal studies up to 200 °C for 12 h).

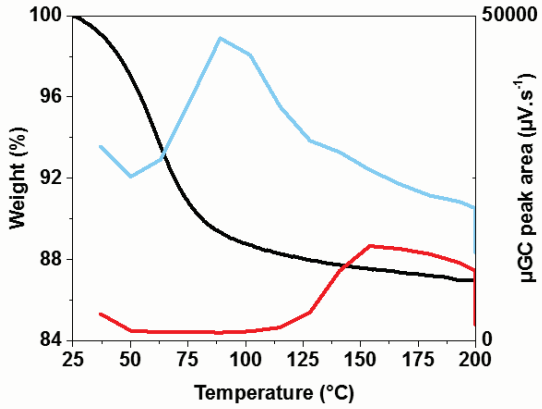

Figure 3-5 Coupled TGA-µGC results. TGA thermogram of MIL-101 (black) up to 200°C (10 °C.min^{-1}). Emitted water vapor (blue) and emitted CO_2 (red).

The IR analysis showed similar spectra for **MIL-101$_{MW}$** and **MIL-101$_{HT}$** **Figure 3-6 a**. In the 1800 cm^{-1} region, the symmetric (υ_s) and assymmetric (υ_{as}) bands at 1280 cm^{-1} and at 1680 cm^{-1}, respectively, are typical of non coordinated C(O)OH bonds of terephthalic acid. In MIL-101(Cr) samples, these bands approached from each other leading to bands at 1400 cm^{-1} and 1625 cm^{-1}, respectively **Figure 3-6 b**. These bands correspond to coordinated C(O)O with chromium. In addition, IR indicated the absence of terephthalic acid.

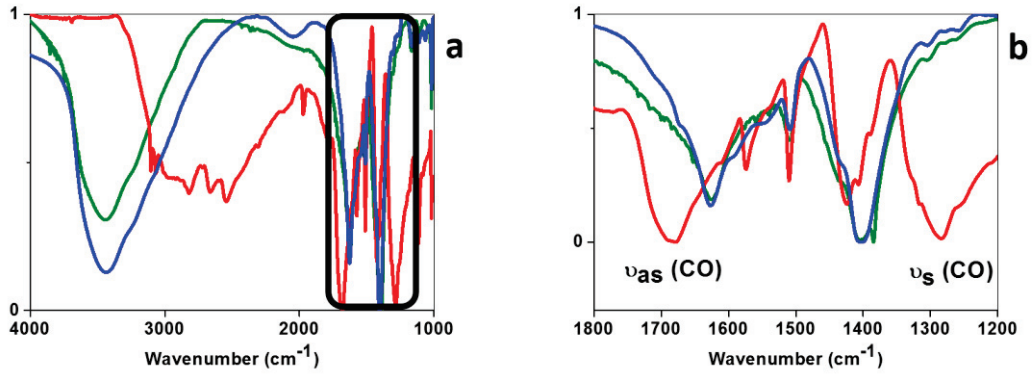

Figure 3-6 (a) IR spectra of terephthalic acid (red), MIL-101$_{MW}$ (green) and MIL-101$_{HT}$ (blue). (b) Zoom in the 1200-1800 cm^{-1} region.

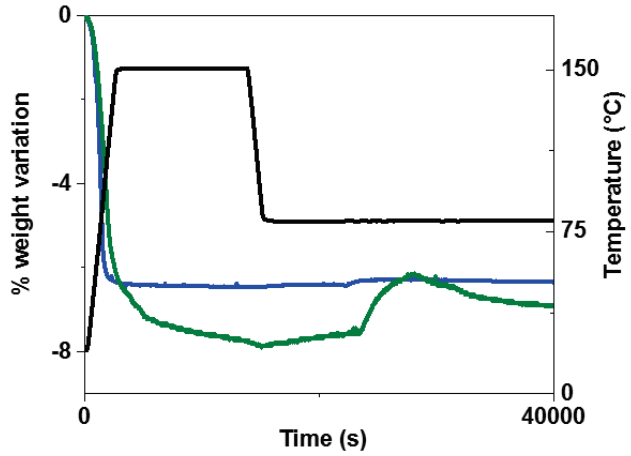

Figure 3-7 TPD-NH$_3$ curves of MIL-101$_{MW}$ (green) and MIL-101$_{HT}$ (blue) with temperature ramp (black).

TPD of NH$_3$ was performed to determine the total acidity of both samples. **MIL-101$_{MW}$** showed 0.4 mmol.g^{-1} adsorbed quantity of NH$_3$, while **MIL-101$_{HT}$** adsorbed 0.19 mmol.g^{-1} **Figure 3-7**. In general, it is known that the total acidity of a MOF is affected by the ligand/Cr molar ratio and the synthesis temperature [236]. In the present work, the molar ratio ligand/Cr = 1 and the same temperature of 220 °C were used, in both the hydrothermal and the microwave approaches. The only difference was the heating source (oven or microwave), that induced a higher SA of the sample obtained from microwave. So the lower acid site density in **MIL-101$_{HT}$** can be explained by some pore blocking or by the presence of larger partices that are more difficult to be activated. The presence of defects or missing linkers in MIL-101 synthesized by microwave method can also justify

the higher SA and total acidity.

Based on all what preceeded, the microwave-assisted method appeared to be very interesting for the synthesis of MIL-101catalyst. It saves time and energy, and results in better characteristics of surface area and acidity of MIL-101 nanoparticles.

I.3. Catalytic activity

The catalytic features were assessed through the conversion of different sugars. Oxidative conditions were applied to trigger activity of metal moieties present in **MIL-101$_{MW}$**. No base was used because the MIL-101 was not stable under basic conditions. In the presence of air or pure O_2 at different temperatures, no oxidation resulting products were observed. Instead, isomerization was the dominant transformation, due to Lewis acidity of MIL-101 under the applied conditions. Another assessement for the activity of MIL-101 was for the furfural oxidative esterification. Oxidative conditions (6 bars of pure O_2) and 100 °C were used. No oxidation related products were observed and only 2-(dimethoxymethyl) furan was observed from the beginning of the reaction. (See **Chapter 2 part III** for detailed catalytic tests conditions)**.**

I.3.1. Glucose conversion

The target from the conversion of glucose was the production of gluconic acid with the composite materials, thus the evalulation of the catalytic activity of the MIL101 itself was done first. This acid is important because it is widely used as food additive and in the production of medicines and biodegradable polymers [239]. Working in water, under 30 bar of air or 6 bar of pure O_2, no products resulting from oxidation reactions were detected. When using 30 bar of argon as reactional atmosphere, same results as with air and O_2 were observed. Therefore, there was no effect of the atmosphere. The initial concentration of glucose was fixed to be 0.5 wt % in 30 ml of H_2O. The catalyst quantity was varied but had no effect on the reactional results. For that, constant amount of chromium sites within **MIL-101$_{MW}$** was fixed to ($n_{Glucose}$ used/10). The amount of MIL-101 corresponding to be 0.1 mmol of chromium sites was 40 mg. The only factor that played pronounced role and led to the formation of fructose and 5-HMF (**Scheme 3-2**), was the temperature. Tests were done at 120 °C and 140 °C.

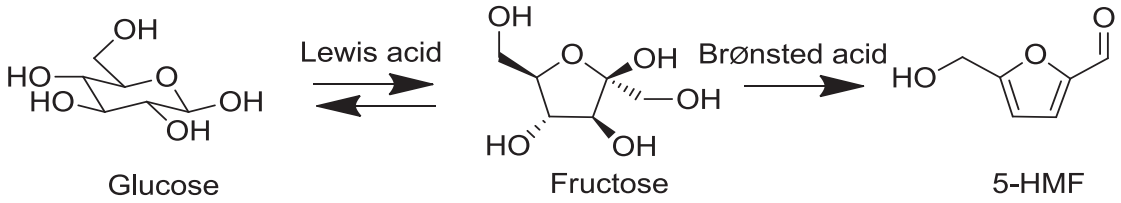

Scheme 3-2 Glucose conversion using MIL-101$_{MW}$.

Figure 3-8 shows the chromatograms of the reactional mixture of glucose transformation after 24 h at 120 °C and 140 °C respectively. The peak at 8.5 min is related to glucose, the one at 9.8 min is attributed to fructose and the one after 32.5 min is for 5-HMF. Two peaks appeared also at 20.5 min and 22.8 min, those were not identified. But they are not related to reactional products, because they also appeared when testing the stability of MIL-101 under the reactional conditions without any substrate. They may result from the partial dissociation of the terephthalic acid, as proven from TGA-µGC analysis described before. They are not related to MeOH or DMF, because these were not detected with TGA-µGC.

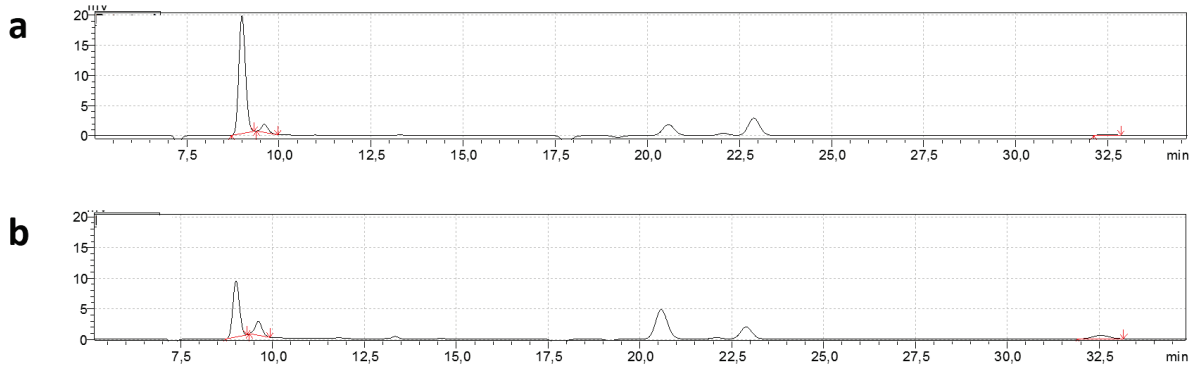

Figure 3-8 HPLC chromatograms of the reactional mixture of glucose transformation using MIL-101$_{MW}$ at (a) 120 °C and (b) 140 °C.

At 120°C, 5 % of glucose was converted into fructose (3 %) and 5-HMF (1.8 %) without using the catalyst. Using **MIL-101$_{MW}$**, the conversion of glucose increased into 18%, producing fructose (10 %) and 5-HMF (2 %) **Figure 3-9 (a) and (b)**. At 140 °C, 12 % of glucose were converted into fructose (3 %) and 5-HMF (9 %) without catalyst. Whereas when **MIL-101$_{MW}$** was used, the conversion of glucose increased to 55 %, producing fructose (20 %) and 5-HMF (10 %) **Figure 3-9 (c) and (d)**. At both temperatures, when **MIL-**

101$_{MW}$ was used, traces (<2 %) of formic acid, acetic acid and lactic acid were detected.

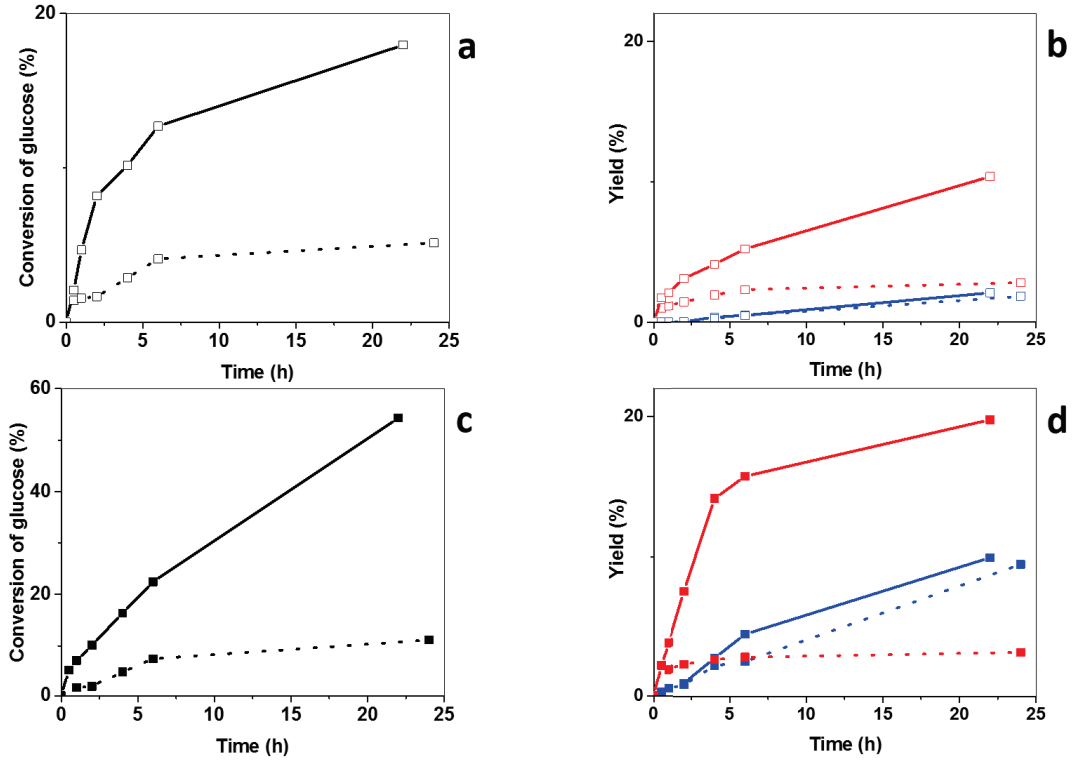

Figure 3-9 (a) and (c) present the conversion of glucose (black) with and without catalyst at 120 °C and 140 °C respectively. (b) and (d) present the yields of fructose (red) and 5-HMF (blue) obtained with and without catalyst at 12 0°C and 140 °C respectively. Dotted lines (no catalyst), solid lines (with catalyst).

When using **MIL-101$_{MW}$** as catalyst, the conversion did not correspond to the sum of the obtained products at 120 °C and 140 °C. The reason was the formation of humins. Humins are non-soluble black precipitates mainly formed due to the polymerization of small molecules (as sugars and 5-HMF) and their formation is favored in pure water. Humins have been supposed to affect the active sites of the catalyst by poisoning, decreasing the activity of **MIL-101$_{MW}$**.

These results indicated, that **MIL-101$_{MW}$** is active, and its activity is temperature dependent. No oxidation reactions were observed making this material an inert support for oxidation of glucose. Isomerization of glucose towards fructose was dominant with traces of 5-(hydroxymethyl) furfural (5-HMF) detected too as a result of dehydration reaction. This aligned with the already reported MIL-101, as a catalyst for glucose isomerization at 100 °C in water, where 22 % conversion and 12.6 % fructose yield with

no 5-HMF were observed [226]. So the higher the temperature is, the higher the conversion and products yield. Fructose was then tested as initial substrate in an attempt to assess the formation of 5-HMF because it is known to be more reactive towards the 5-HMF formation.

I.3.2. **Fructose conversion**

Scheme 3-3 presents the reaction of fructose that took place, resulting in glucose and 5-HMF.

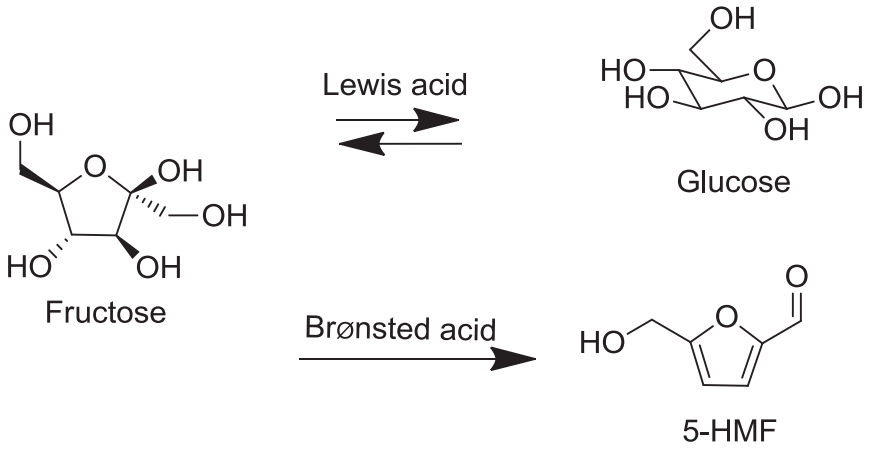

Scheme 3-3 Fructose conversion using MIL-101$_{MW}$.

Figure 3-10 presents the chromatograms of the reactional mixture after 24 h at 120 °C and 140 °C. Again the peaks at 20.5 min and 22.8 min were observed.

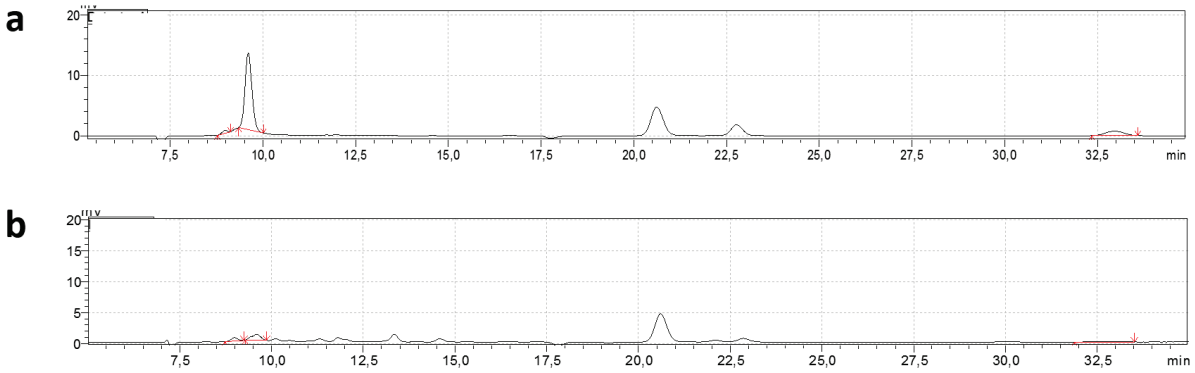

Figure 3-10 HPLC chromatograms of the reactional mixture of fructose transformation in water using MIL-101$_{MW}$ at (a) 120 °C and (b) 140 °C.

At 120 °C, 11 % of fructose were converted into glucose (1 %) and 5-HMF (9 %) without

using a catalyst. Using **MIL-101$_{MW}$**, the conversion of fructose increased to 25 %, producing 4 % of glucose and 11 % of 5-HMF **Figure 3-11 (a) and (b)**. At 140 °C, 65 % of fructose were converted into glucose (1.0 %) and 5-HMF (12 %) without a catalyst, while with **MIL-101$_{MW}$**, 90 % of fructose were converted into glucose (6 %) and 5-HMF (8 %) in 4 h. Untill the end of the reaction (24 h), the percentage of the produced glucose and 5-HMF decreased to 4 % and 1 % respectively **Figure 3-11 (c) and (d)**. At 140 °C both products are not stable in the presence of MIL-101 and undergo side reactions, probably uncontrolled polymerisations. Traces (<2 %) of formic acid, acetic acid and lactic acid were detected. Humins were also observed at both temperatures when using **MIL-101$_{MW}$**.

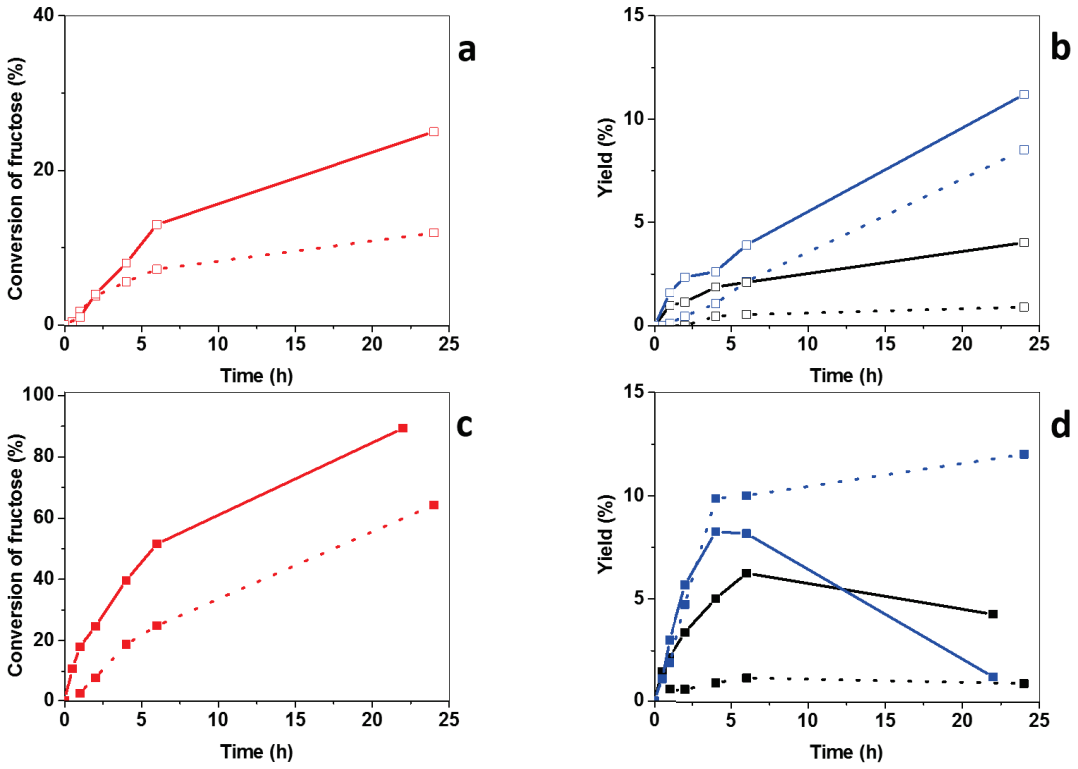

Figure 3-11 (a) and (c) present the conversion of fructose (red) with and without catalyst at 120 °C and 140 °C, respectively. (b) and (d) present the yields of glucose (black) and 5-HMF (blue) obtained with and without catalyst at 120 °C and 140 °C respectively. Dotted lines (no catalyst), solid lines (with catalyst).

As a conclusion, due to its Lewis acid sites, from the Cr(III) metals, **MIL-101$_{MW}$** had the ability to only isomerize the reactants when catalyzing the conversion of glucose and fructose. The presence of Brønsted acid sites, that could originate from uncoordinated terephthalic acids, was limited as indicated by the limited yields of 5-HMF.

To go further, the reactivity of C-5 sugar (xylose) in water was also performed. Moreover, tests on xylose in isopropanol (iPrOH) were also performed.

I.3.3. **Xylose conversion**

Scheme 3-4 shows xylose conversion to xylulose (its isomer) which in turn was transformed to furfural (FF).

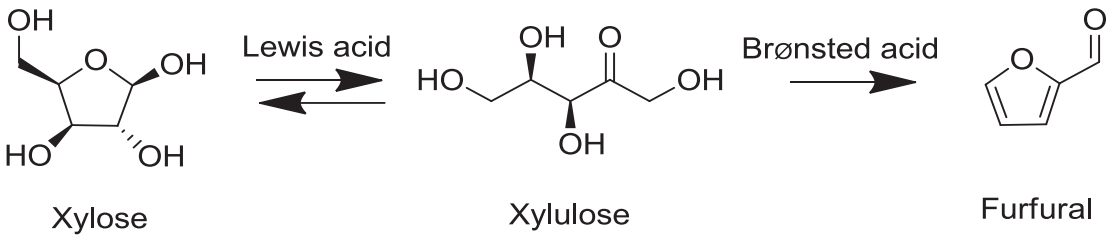

Scheme 3-4 Xylose conversion using MIL-101$_{MW}$.

I.3.3.1. **In H_2O**

Figure 3-12 shows the chromatograms of the reactional mixture of xylose transformation in water after 24 h at 120 °C and after 6 h and 24 h at 140 °C. Peak at 9.5 min is related to xylose, at 9.8 min to xylulose and after 54.5 min to FF. It is clear that 2 peaks at 20.5 min and 22.8 min appeared too.

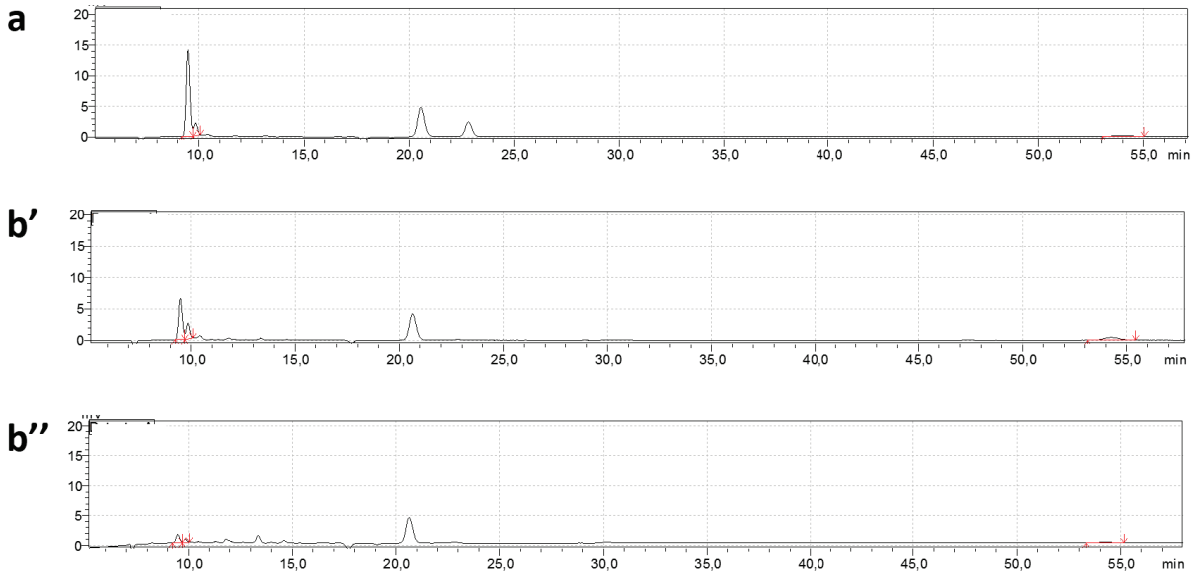

Figure 3-12 HPLC chromatograms of the reactional mixture of xylose transformation in water using MIL-101$_{MW}$ at (a) 120 °C, (b') 140 °C after 6 h and (b'') 140 °C after 24 h.

At 120°C, xylose showed 7 % conversion with isomerization to 2.2 % xylulose that gave

1 % furfural (FF) without any catalyst. When using **MIL-101$_{MW}$**, the conversion of xylose increased into 30 %, producing 15 % of xylulose and 2.5 % furfural in 24 h **Figure 3-13 (a) and (b)**. At 140 °C, 34 % of xylose were converted into 1.8 % xylulose and 12 % FF without catalyst. With **MIL-101$_{MW}$**, the conversion of xylose increased to 93 %, producing 12 % of xylulose after 4 h. The latter decreased with time and reached 2.4 % after 24 h. FF reached a maximum of 8 % during the first 6 h and then decreased to 2.3 % at the end of the reaction **Figure 3-13 (c) and (d)**. Humins were also observed as a black precipitates [228].

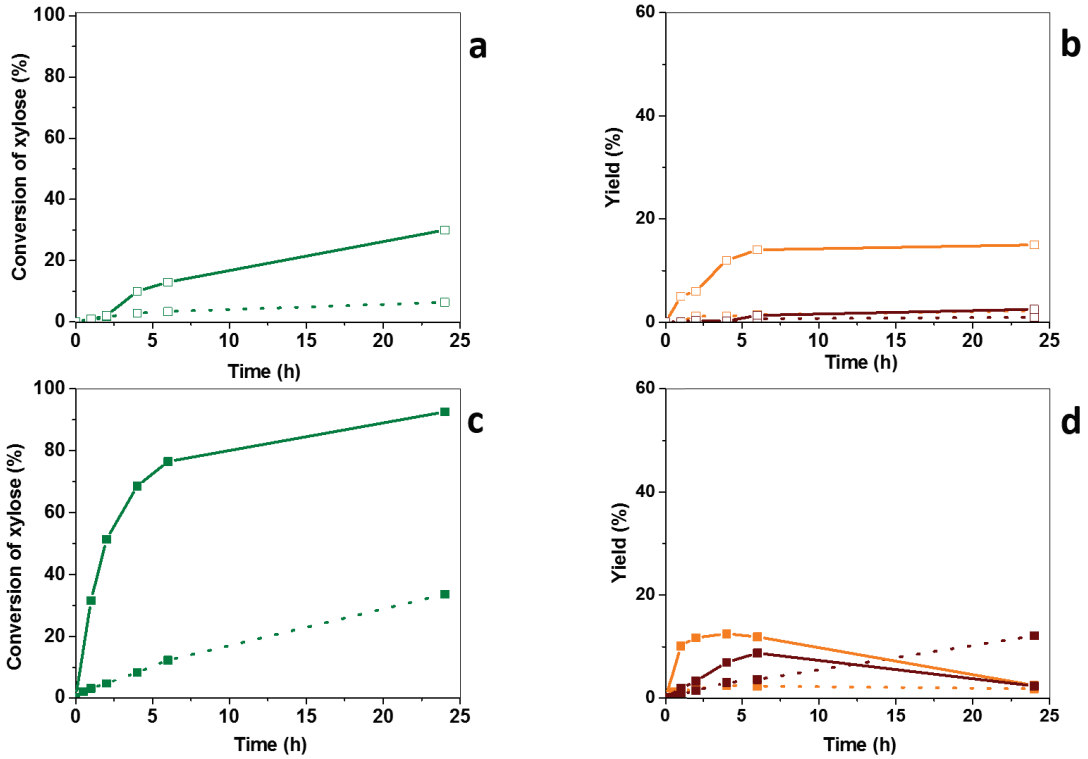

Figure 3-13 (a) and (c) present the conversion of xylose (green) with and without catalyst at120 °C and 140 °C respectively. (b) and (d) present the yields of xylulose (orange) and furfural (wine) obtained with and without catalyst at 120 °C and 140 °C respectively. Dotted lines (no catalyst), solid lines (with catalyst).

Under similar conditions, **MIL-101$_{MW}$** also isomerized xylose into xylulose in water, reinforcing the presence of Lewis acid sites that are responsible to such activity, as the case of glucose and fructose. Limited formation of furfural is related to the lack of Brønsted acid sites, pointing out that there is no uncoordinated carboxylic acids in the MOF. These results align with some reports that were based on the used of Lewis acid catalysts to trigger xylose isomerization in water. MIL-101 showed similar capacity to isomerize xylose in H_2O at 120 °C compared to tin based zeolite Sn-β (60 % xylose

conversion and 27 % xylulose formation at 100 °C) [240], while it was better than zeolite Sn-MFI (18 % xylose conversion and 8 % xylulose formation at 80 °C) [241].

Humins formation due to the small molecules (sugars, 5-HMF and FF) may be limited in different medium other than water. Indeed this was the case when using a mixture of H_2O:THF, the formation of 5-HMF was stabilized and the humins formation limited [227]. Based on this fact, we tried alcoholic medium (2-propanol: iPrOH), in an attempt to decrease humins formation, limit the active sites posining of the catalyst, and test if xylose transformation will be enhanced.

I.3.3.2. **In iPrOH**

Figure 3-14 presents the chromatograms of the reactional mixtures when tests were done in iPrOH. At 120 °C, xylose showed 11 % conversion producing only xylulose (8 %) when no catalyst was used. When using **MIL-101$_{MW}$**, the conversion of xylose increased to 80 %, producing 40 % of xylulose and 0 % of furfural **Figure 3-15 (a) and (b)**. At 140 °C, 41 % of xylose were converted into xylulose (16 %) with no catalyst. With **MIL-101$_{MW}$**, the conversion of xylose went up to 90 %, producing only xylulose, 45 % in 6 h, which then deacreased to 24 % after 24 h **Figure 3-15 (c) and (d)**.

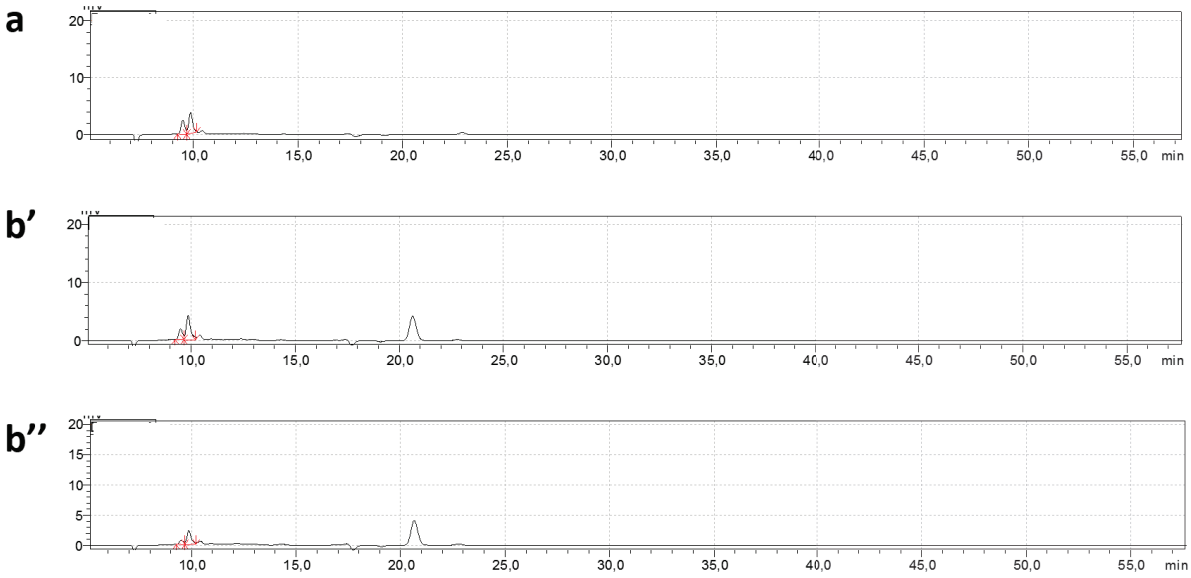

Figure 3-14 HPLC chromatograms of the reactional mixture of xylose transformation in 2-propanol using MIL-101$_{M.W.}$ at (a) 120°C, (b') 140°C after 6 h and (b'') 140°C after 24 h.

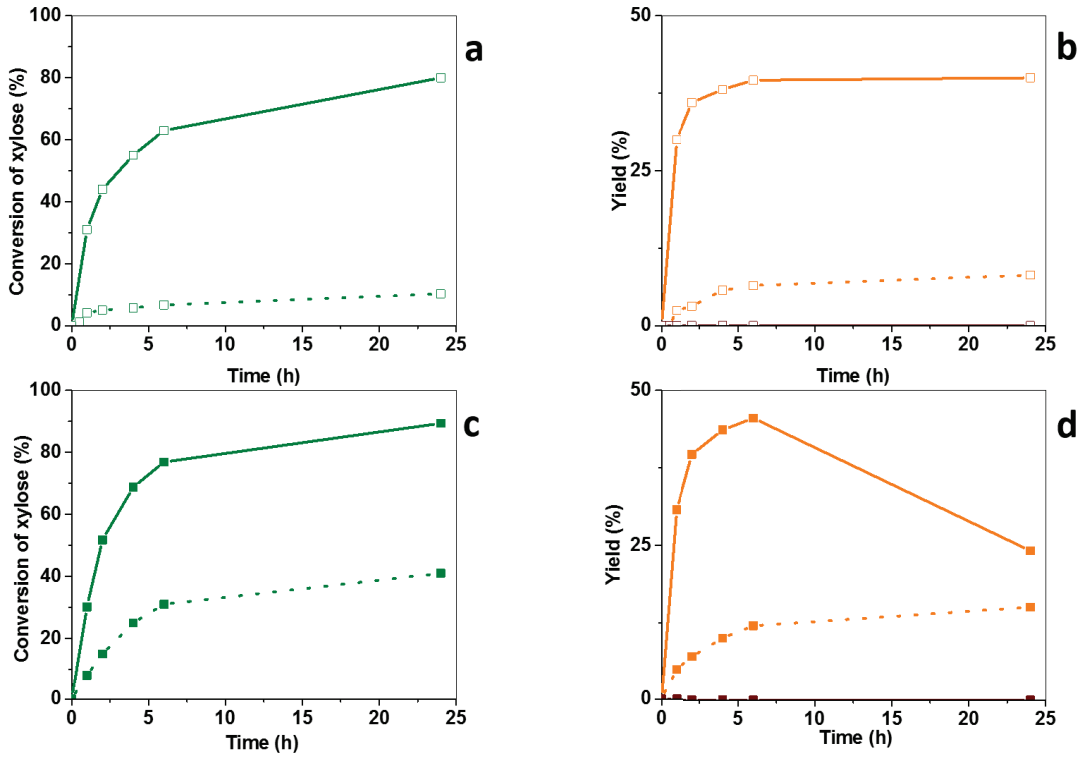

Figure 3-15 (a) and (c) present the conversion of xylose (green) with and without catalyst at 120 °C and 140 °C respectively. (b) and (d) present the yields of xylulose (orange) and furfural (wine) obtained with and without catalyst at 120 °C and 140 °C respectively. Dotted lines (no catalyst), solid lines (with catalyst).

Therefore, the best activity of **MIL-101$_{MW}$** was registered for the conversion of xylose in iPrOH. Only xylulose, the isomer of xylose, was produced in iPrOH at 140 °C with 45 % yield after 6 h. This is an important transformation which is the key-step for furfural production starting from xylose. Although the selectivity was not 100 %, no byproducts were observed. Humins were not observed, indicating that no side polymerization in iPrOH as in water. Compared to literature, xylose isomerization was reported to be done in 2 steps using alcoholic medium (methanol) then water. Methanol forms methyl xyluloside, then hydrolysis using water results in xylulose. The final xylose conversion was 62 % and xylulose yield 47 % after 1h reaction at 100 °C. The catalyst was zeolite-Y (H-USY) having both brønsted and Lewis acid characters [242]. This means that for only Lewis acid based catalyst (MIL-101), the selective isomerization of xylose to xylulose is interesting.

I.3.4. **Furfural conversion**

Since alcoholic medium seemed to be more suitable for better selectivity of MIL-101 during xylose transformation where no humins were observed, another assessement for

MIL-101 activity on smaller molecule (furfural) transformation was done in alcohol solution **Scheme 3-5**.

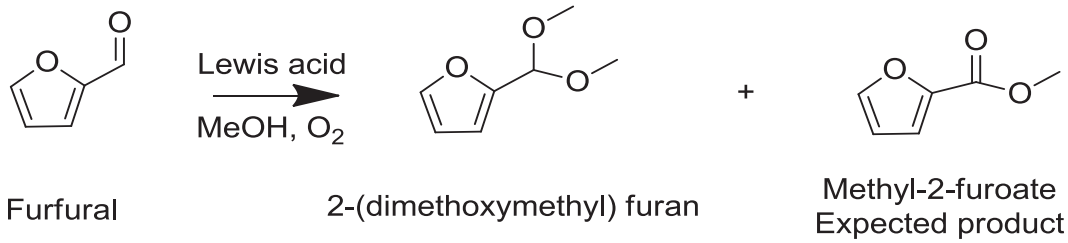

Scheme 3-5 Furfural conversion in MeOH using MIL-101$_{MW}$ as catalyst.

The conversion of furfural (0.1 % wt in 44 ml MeOH), was tested at 100 °C under 6 bars of O_2 and 40 mg MIL-101$_{MW}$ (For detailed conditions, see **Chapter 2**). The conversion of furfural was parallel to the formation of 2-(dimethoxymethyl) furan. Conversion of furfural reached a maximum of 75 % with 100 % of selectivity to 2-(dimethoxymethyl) furan after 1 h reaction and remained constant till the end of the reaction **Figure 3-16**.

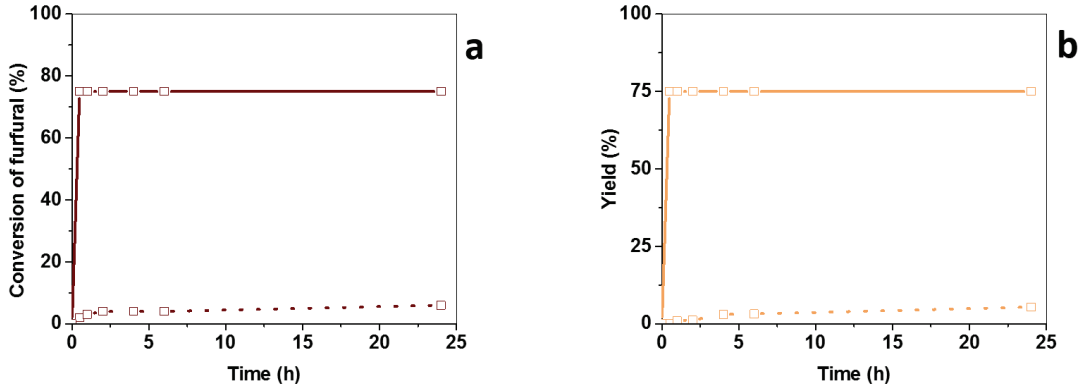

Figure 3-16 (a) presents the conversion of furfural (wine) with and without catalyst at 100 °C. (b) presents the yields of 2-(dimethoxymethyl) furan (orange) obtained with and without catalyst. Dotted lines (no catalyst), solid lines (with catalyst).

Figure 3-17 shows the chromatogram after 6 h of reaction time, clearly representing the peaks related to dodecane (internal standard used), furfural and 2-(dimethoxymethyl) furan at 6.7 min, 14 min and 17.7 min, respectively.

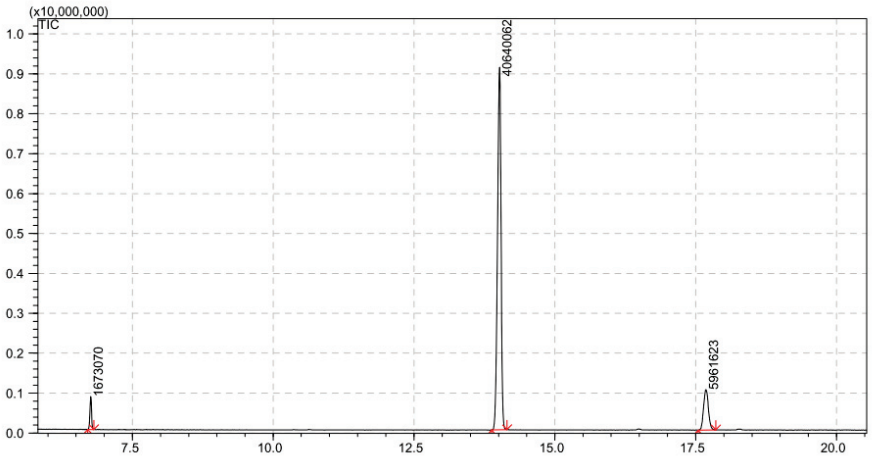

Figure 3-17 GC chromatogram of the reactional mixture of furfural transformation in m using MIL-101$_{MW}$.

Here, there was no effect of O_2 since no oxidative esterification products was observed. The reaction was limited to a simple acetalisation of the furfural. MIL-101 failed again in oxidative transformations, where the expected methyl-2- furoate was not obtained. This transformation is already well known with gold based catalysts (see **Chapter 5 part II** for more examples concerning this reaction), but fewly reported with MOFs. One report appeared recently and highlighted the activity of Au Nps/UiO-66 for this transformation (as discussed in **chapter 1 part VI.4.2.**) [234]. This report showed that UiO-66 alone was able to transform furfural into the corresponding acetal and hemiacetal only, but no oxidation products were produced without gold. The activity of UiO-66 is supposed to be related to its Lewis acidity, same as the case of MIL-101 is this work.

II. UiO-66 as catalyst

II.1. Synthesis

The synthesis of UiO-66 has been performed according to the procedure described in **Chapter 2**.

II.2. Catalyst characterization

The characterization of UiO-66 was realized using PXRD, SEM, N_2 adsorption, TGA, IR, and TPD-NH_3.

PXRD showed that the synthesized UiO-66 had similar pattern to that of the simulate

pattern.Two extra peaks were observed for the synthesized UiO-66 at 6° and 12° respectively. The peaks of the synthesized UiO-66 were broader than in the referenced pattern, pointing out the formation of small crystallites **Figure 3-18**.

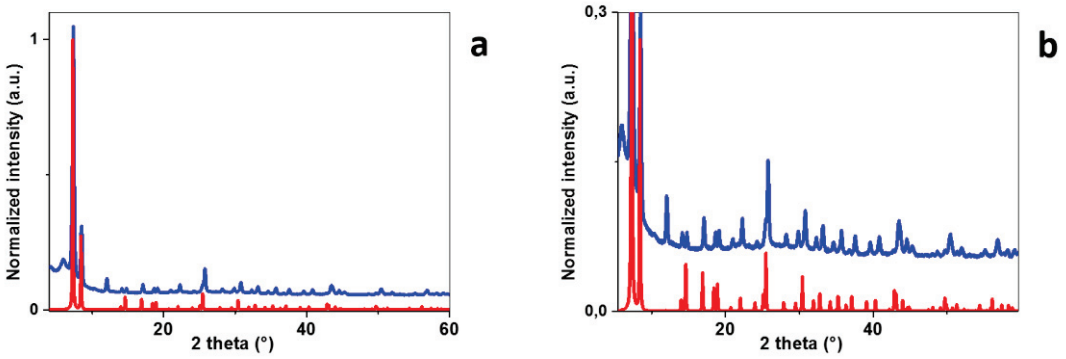

Figure 3-18 (a) Powder X-ray diffraction patterns of UiO-66 synthesized by solvothermal approach (blue), and the simulated pattern (red). (b) zoomed version.

The average particle size of the synthesized UiO-66 from TEM images was 88 nm ± 20 nm **Figure 3-19**.

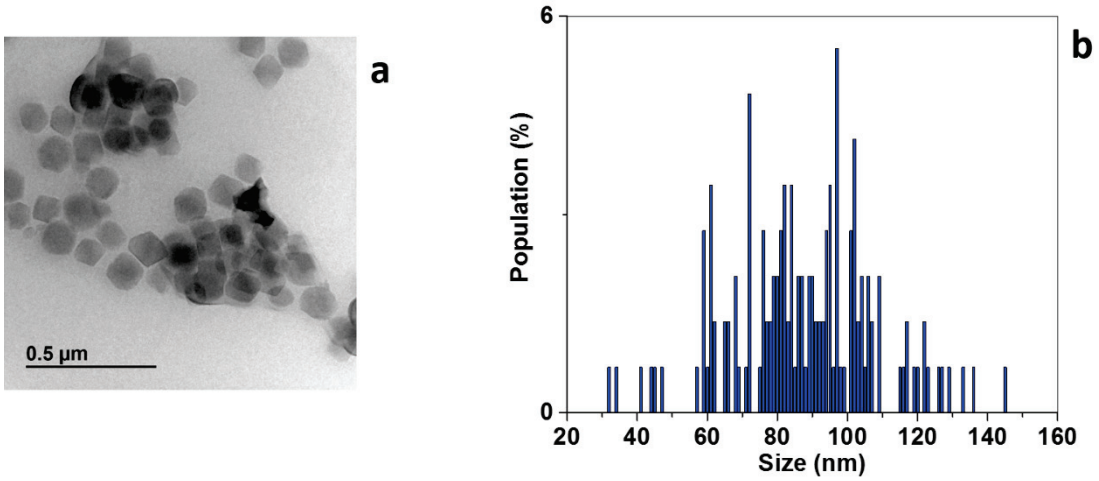

Figure 3-19 (a) TEM image of UiO-66 and (b) its size distribution.

The BET surface area was 1450 $m^2.g^{-1}$. The isotherm is typical of a microporous material with the presence of mesopores originating from the interparticular space, and so pointing out the formation of nanoparticles **Figure 3-20**.

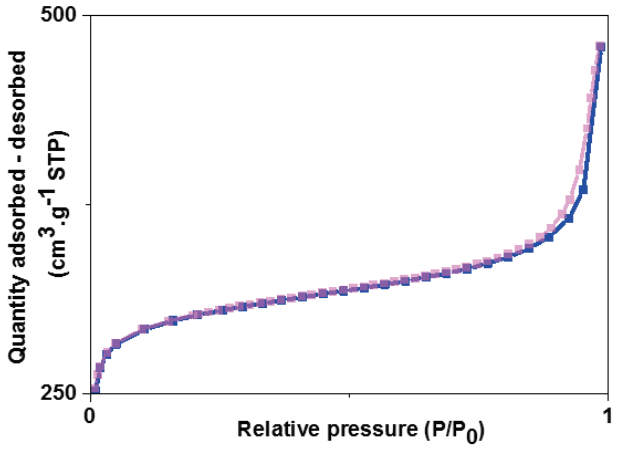

Figure 3-20 N_2 adsorption (blue) and desorption (pink) isotherm of UiO-66.

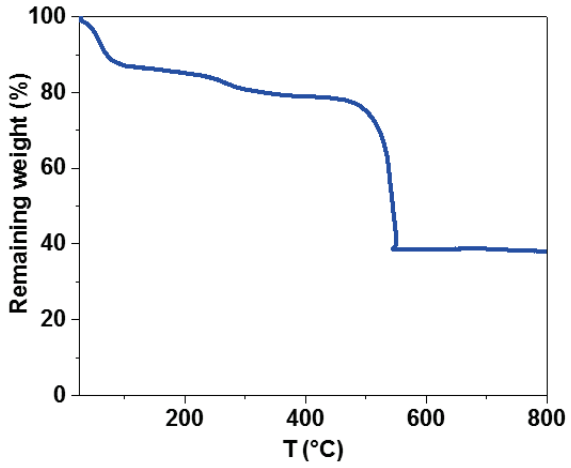

Figure 3-21 TGA thermogram for remaining weight percentage for UiO-66.

TGA analysis showed first step weight loss (12 %) around 100 °C corresponding to the adsorbed water loss. Another weight loss (8 %) was observed up to 200 °C, corresponding to coordinated water or solvent molecules (DMF or MeOH), being incorporated within the UiO-66 structure. Ligand loss and UiO-66 decomposition started around 500 °C, confirming the high thermal stability of this MOF, in the solid state, under continuous heating (25 °C-800°C/10 °C.min^{-1}/Air/50 ml.min^{-1}). The theoretical remaining percentage without taking into consideration the solvent content is 44.5 %. In the synthesized case, the remaining weight percent was 46 % corresponding to ZrO_2 **Figure 3-21**.

As the case of MIL-101, also UiO-66 showed the symmetric band at 1280 cm^{-1} and

asymetric band at 1680 cm^{-1} of non-coordinated C(O)OH bonds of terephthalic acid approached and fused with neighboring bands resulting in new bands at 1400 cm^{-1} and 1680 cm^{-1} respectively **Figure 3-22**. This confirms the presence of coordinated carboxylate and the absence of uncoordinated carboxylic acid functions of the ligand.

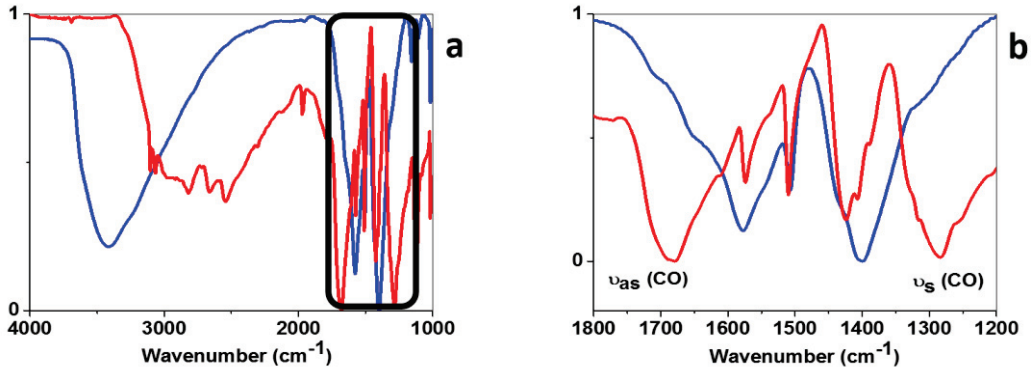

Figure 3-22 (a) IR spectra of terephthalic acid (red) and UiO-66 (blue). (b) Zoomed region (1200-1800 cm^{-1}).

TPD-NH_3 analysis showed the adsorption of a 1.2 $mmol.g^{-1}$ of NH_3 by UiO-66 **Figure 3-23**, being higher than the already mentioned value related to MIL-101 (0.4 $mmol.g^{-1}$).

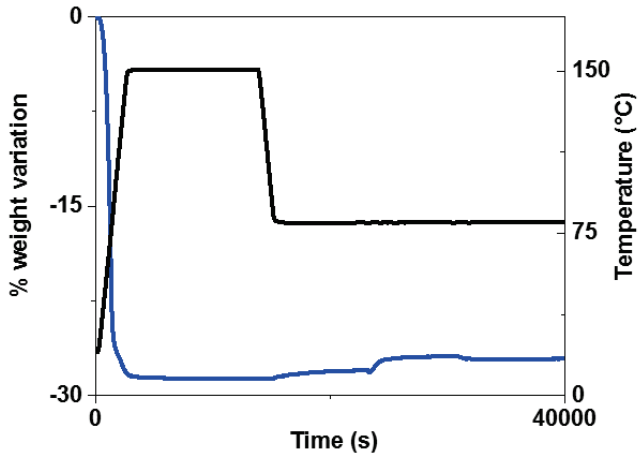

Figure 3-23 TPD-NH_3 of UiO-66 (blue) and temperature program (black).

II.3. Catalytic activity

UiO-66 was tested for glucose conversion in H_2O at 140°C and for furfural oxidative esterification in MeOH at 100°C.

II.3.1. **Glucose conversion**

At 140°C, 12 % of glucose were converted into fructose (3 %) and 5-HMF (9 %) without using the catalyst. Using UiO-66, the conversion of glucose increased to 80 %, producing fructose (9 %) and 5-HMF (2 %) after 24 h. The conversion with UiO-66 was higher than with MIL-101 (55 %), while fructose and 5-HMF yields were lower. Again the peaks at 20.5 min and 22.8 min appeared as in the case of MIL-101, ensuring the hypothesis that they are related to terephthalic acid within the MOFs. Humins also appeared which justifies the high conversion **Figure 3-24**.

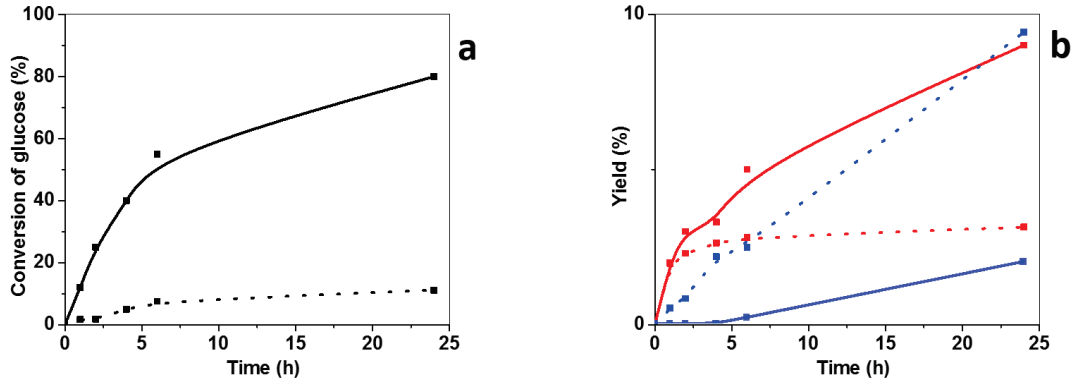

Figure 3-24 (a) presents the conversion of glucose (black) with and without UiO-66 at 140 °C. (b) presents the yields of fructose (red) and 5-HMF (blue) obtained with and without catalyst at 140°C. Dotted lines (no catalyst), solid lines (with catalyst).

II.3.2. **Furfural conversion**

For furfural oxidative esterification, 75 % conversion and 100 % selectivity toward 2-(dimethoxymethyl) furan was obtained after 30 min from t_0 (the time at which the temperature reached 100 °C) **Figure 3-25**. Here also, no oxidation products were observed. UiO-66 ability to perform acetalization of furfural is related to its Lewis acidity, as reported in [234], and similar to the MIL-101 case.

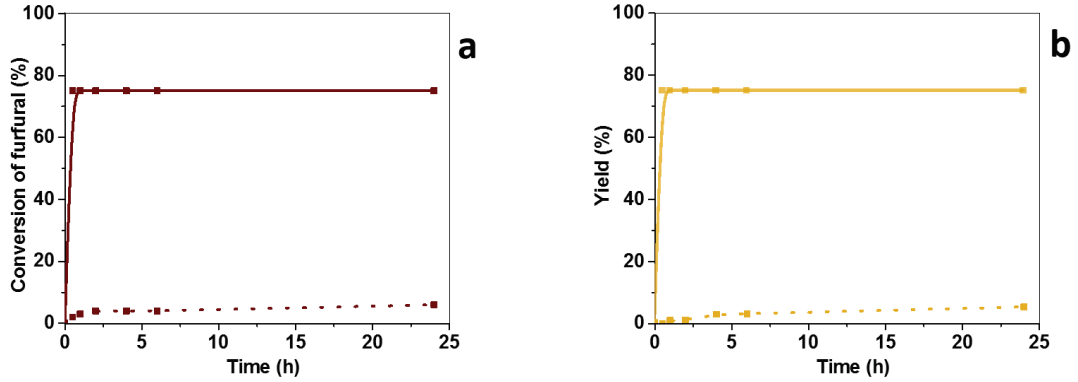

Figure 3-25 (a) presents the conversion of furfural (wine) with and without UiO-66 at 100 °C. (b) presents the yields of 2-(dimethoxymethyl) furan (orange) obtained with and without catalyst. Dotted lines (no catalyst), solid lines (with catalyst).

III. ZIF-8 as catalyst

III.1. Synthesis

The synthesis of ZIF-8 has been done according to the procedure described in **Chapter 2**.

III.2. Catalyst characterization

The characterization of this MOF was realized using PXRD, SEM, N_2 adsorption, TGA, IR, and TPD-NH_3.

PXRD showed that the ZIF-8 had similar pattern to that of the simulated file. The peaks were broader than the reference pattern **Figure 3-26**.

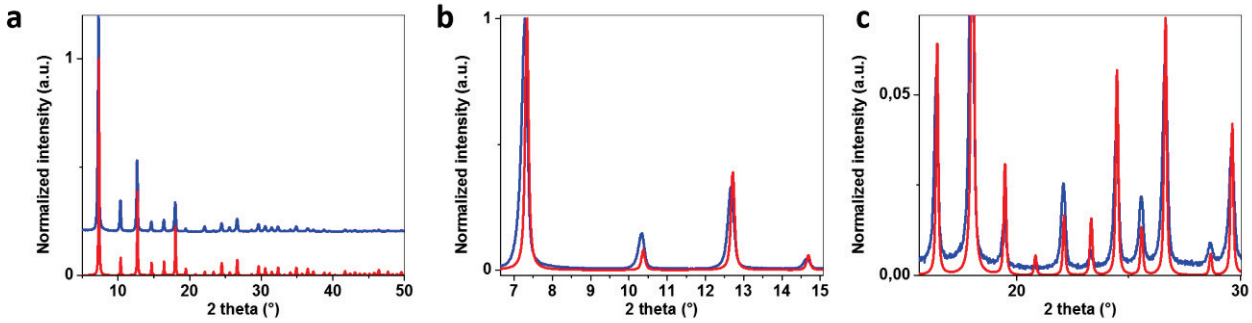

Figure 3-26 (a) Powder X-ray diffraction pattern of ZIF-8 synthesized by solvothermal approach (blue), and the simulated pattern (red). (b) and (c) are zoomed versions.

The average particle size of the synthesized ZIF-8 was 44 nm ± 8 nm **Figure 3-27**.

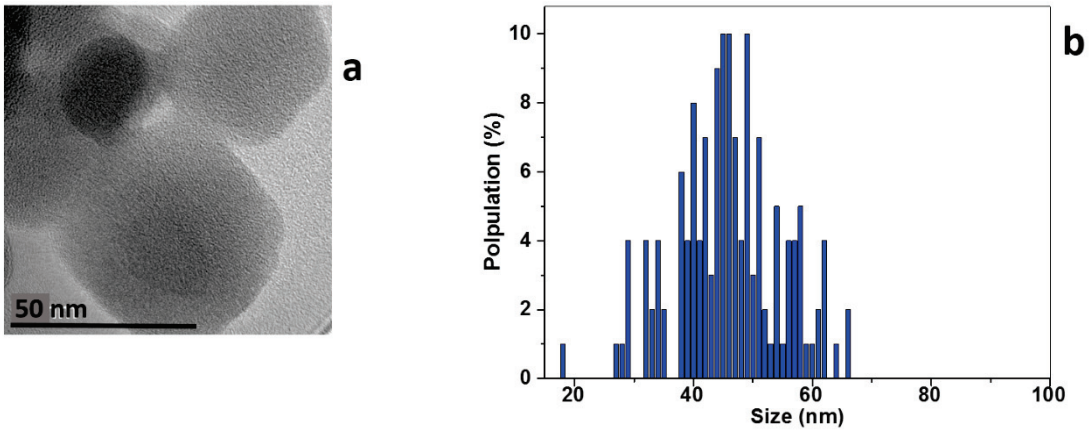

Figure 3-27 (a) TEM image of ZIF-8 and (b) its size distribution.

Type I nitrogen sorption isotherm was observed indicating the microporous nature of the synthesized ZIF-8 **Figure 3-28**. The BET surface area was 1300 $m^2.g^{-1}$ with a micropore volume of 0.609 $cm^3.g^{-1}$.

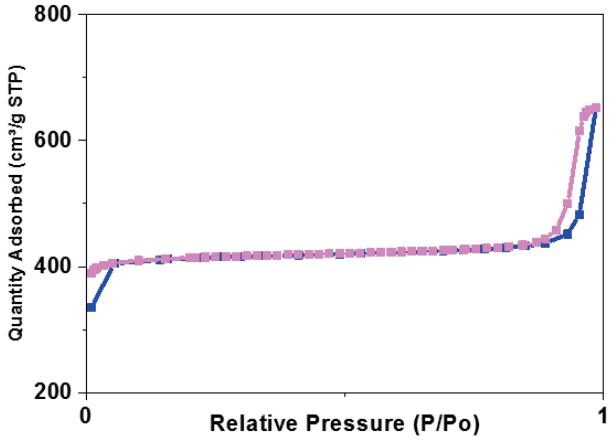

Figure 3-28 N_2 adsorption (blue) and desorption (pink) isotherms of ZIF-8.

TGA analysis showed that ZIF-8 is first hydrophobic without the departure of water molecules and second stable up to 400 °C under continuous heating (25 °C-800 °C/10

°C.min^{-1}/Air/50 ml.min^{-1}). The weight loss started after 400 °C. The theoretical remaining percentage is 35.7 %. For the synthesized material, the remaining weight percent was 35.3 % corresponding to ZnO **Figure 3-29**.

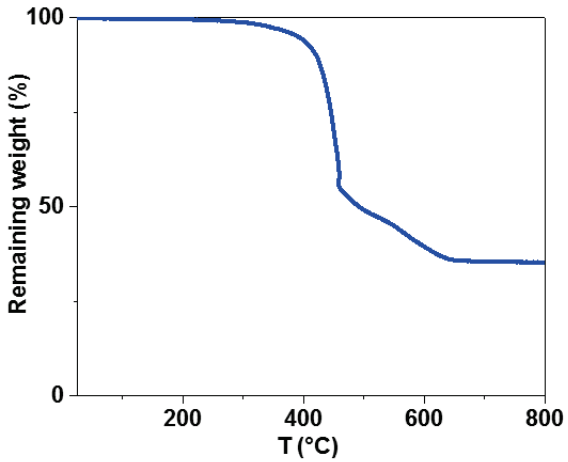

Figure 3-29 TGA thermogram for remaining weight percentage for ZIF-8.

IR spectrum of ZIF-8 showed common C-H stretching bands with the IR spectrum of free 2-methylimidazole at 2930 cm^{-1} and 3100 cm^{-1}. These bands correspond to C_{sp3} and C_{sp2} aliphatic and aromatic C-H vibrations within 2-methylimidazole unit. N-H vibration band corresponding to the secondary amine in 2-methylimidazole is observed at 3200 cm^{-1}. This band is absent in the IR spectrum of ZIF-8, an evidence about the coordination between Zn^{2+} and 2-methylimidazolate. ZIF-8 showed a band around 3400 cm^{-1} corresponding to OH groups present (probably due to MeOH) **Figure 3-30 b**. The bands between 1350- 1550 cm^{-1} correspond to the vibration of the aromatic ring. The bands between 950 - 1350 cm^{-1} correspond to in plane bending of the ring, whereas those < 800 cm^{-1} are related to the out of plane bending **Figure 3-30**.

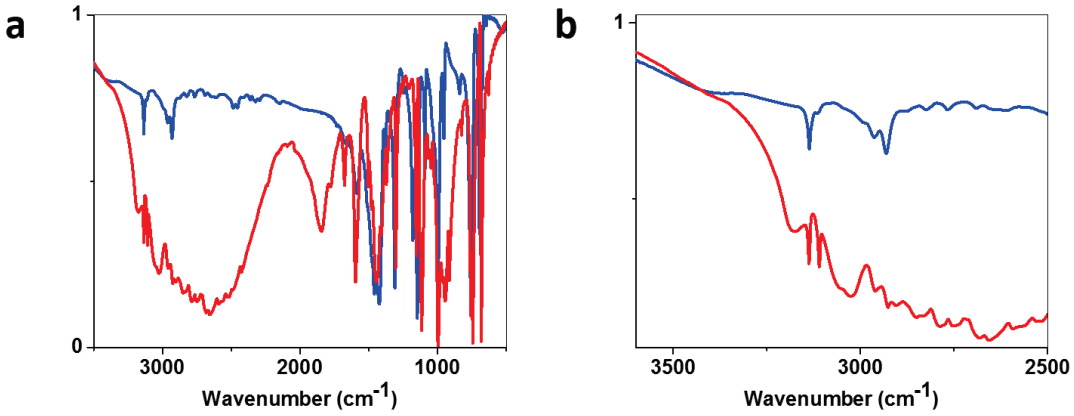

Figure 3-30 (a) IR spectra of 2-methylimidazole (red) and ZIF-8 (blue). (b) zoomed version.

NH_3-TPD showed no increase in mass, meaning that no adsorption of NH_3 occurred on ZIF-8. This means that no Lewis nor Brønsted acidity is present in the synthesized ZIF-8.

III.3. **Catalytic activity**

As UiO-66, ZIF-8 was tested for glucose conversion in H_2O at 140 °C and for furfural oxidative esterification in MeOH at 100 °C.

III.3.1. **Glucose conversion**

At 140 °C, 12 % glucose was converted into fructose (3 %) and 5-HMF (9 %) without using the catalyst. Using ZIF-8, the conversion of glucose was 65 %, producing fructose (5 %) and 5-HMF (2 %) after 24 h **Figure 3-31**. The peaks at 20.5 min and 22.8 min were not seen in HPLC chromatograms, because of the absence of terephthalic acid in this MOF. Humins also appeared.

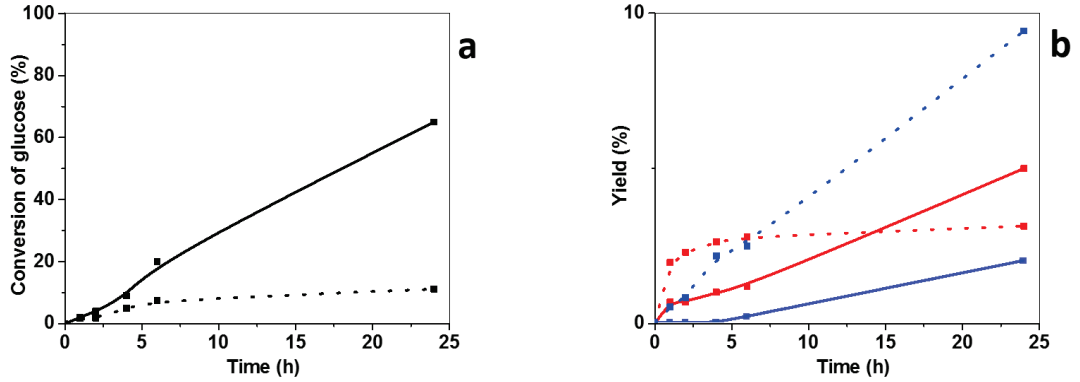

Figure 3-31 (a) presents the conversion of glucose (black) with and without ZIF-8 at T140 °C. (b) presents the yields of fructose (red) and 5-HMF (blue) obtained with and without catalyst at 140 °C. Dotted lines (no catalyst), solid lines (with catalyst).

III.3.2. **Furfural conversion**

For furfural conversion, 65 % conversion and 100 % selectivity toward 2-(dimethoxymethyl) furan was obtained after 24 h **Figure 3-32**. The reaction was still limited to acetal formation. However, the transformation proceeded much slower compared to MIL-101 and UiO-66 due to the lack of acidity of ZIF-8 material.

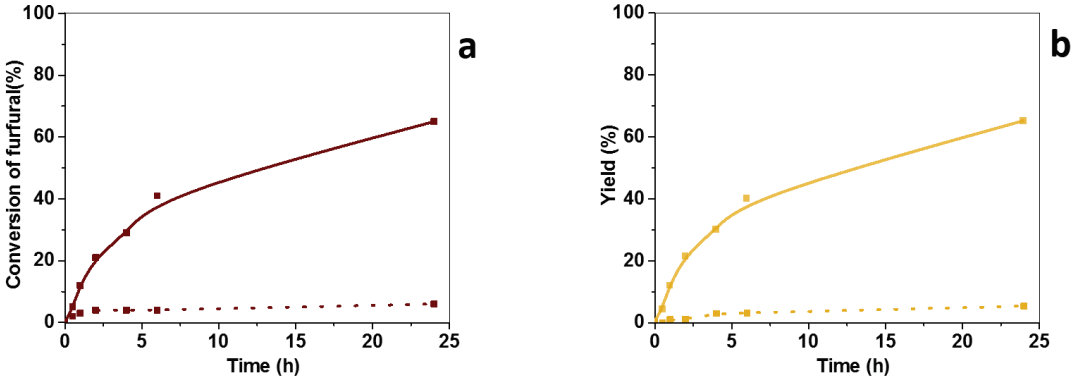

Figure 3-32 (a) presents the conversion of furfural (wine) with and without ZIF-8 at 100 °C. (b) presents the yields of 2-(dimethoxymethyl) furan (orange) obtained with and without catalyst. Dotted lines (no catalyst), solid lines (with catalyst).

It is worth to point, after all these catalytic tests, the stability of the MOFs. Even when humins were collected with the catalyst after sugars conversion, PXRD and N_2 adsorption always proved the stability of MIL-101, UiO-66 and ZIF-8.

IV. **Conclusion**

This study indicates that non-postsynthetically modified MOFs present a certain activity for sugar transformation, and furfural acetalisation. It appeared difficult to draw definite trends, on the impact of the metal present in MOF (Cr, Zr, Zn), and on the acidity of the materials. Nevertheless, the probably Lewis acid character of MIL-101 and UiO-66 allowed fast acetalization of FF with methanol, and some activity for glucose isomerization. The metallic moieties in all these MOFs do not promote oxidation reactions.

Based on these facts, those three MOFs were used as supports for thiolate gold nanoclusters, in order to generate a synergy between both counterparts on sugar transformation reactions.

Chapter 4

Thiolate gold nanoclusters supported over metal organic frameworks for catalytic applications

I. Introduction

Thiolate gold nanoclusters possess a well-defined number of Au atoms and have size specific chemical and physical properties, different from bulk gold. They are stable in solution and in solid states. Different types of $Au_{25}(SR)_{18}$ are known to be catalytically active. Because of their homogeneity in size and known structures, different than gold nanoparticles, it has been interesting to use tGNCs as catalysts to relate their size with a precision at the atomic scale to their catalytic activities. The core of this project has been based on mixing tGNCs with MOFs, the latter being also possibly catalytically active, to figure out if a synergy exists between both counterparts for catalytic applications and ultimately for cascade reactions.

This chapter shows the synthesis and characterization of three types of $Au_{25}(SR)_{18}$ tGNCs: Au_{25}(SG:Glutathione)$_{18}$, Au_{25}(Capt:Captopril)$_{18}$ and Au_{25}(ATP:4-aminothiophenol)$_{18}$. These tGNCs have been supported over MIL-101, UiO-66 and ZIF-8. Various non-calcined and calcined composite materials were prepared. The use of different MOFs and different tGNCs aimed to assess, the support effect and the thiolate ligand effect at the level of tGNCs size homogeneity and catalytic behavior of the composite materials. Fundamentally, in-depth understanding of the mode of interaction between both counterparts is of high importance.

For most of the catalytic reactions reported in the literature, tGNCs have to be defunctionalized through calcination to be active in catalysis, thus thermal studies on both

tGNCs and MOFs have been done to find the best calcination conditions. Sugars and benzyl alcohol oxidations have been targeted to test the oxidation properties of tGNCs supported over MIL-101, combined with the catalytic activity of the latter. For composite materials based on UiO-66 and ZIF-8 supports, they were catalytically tested for furfural oxidative esterification.

II Thiolate gold nanoclusters

The synthesis of three types of $Au_{25}(SR)_{18}$, each possessing a different thiolate ligand, was done based on already described procedures in **Chapter 2**. HSR = glutathione, captopril or 4-aminothiophenol. The characterizations of the synthesized tGNCs were done by using different techniques: PXRD, UV-Vis and TGA.

II.1. PXRD

The PXRD of the synthesized $Au_{25}(SR)_{18}$ exhibited an intense reflection at low angle, corresponding to a center-to-center distance between two clusters by applying the Bragg's law. This distance has been in good agreement with the expected size of $Au_{25}(SR)_{18}$, knowing that the Au_{25} core is estimaned to be equal to 1 nm. In addition, a broad reflection at high angle has been observed for each $Au_{25}(SR)_{18}$ type, corresponding to the ultra-small Au_{25} gold core and confirms the absence of large gold nanoparticles or bulk gold **Figure 4-1**.

For $Au_{25}(SG)_{18}$ an intense reflection has been observed at 4.9° corresponding to a center-to-center distance of 1.76 nm. For $Au_{25}(Capt)_{18}$, the peak has been located at 5.75° corresponding to a center-to-center distance of 1.92 nm. $Au_{25}(ATP)_{18}$ showed a peak at 4.49° corresponding to a center-to-center distance of 1.7 nm. It is known that the size of the clusters follows the size of the ligands. When the cluster size increases, the low angle peak is shifted toward higher angles. The low angle peak in the three cases is thin and intense, indicating the homogeneity in size of the obtained products. Broad peaks at 37°, 38° and 38.4° corresponded to the gold core of $Au_{25}(SG)_{18}$, $Au_{25}(Capt)_{18}$ and $Au_{25}(ATP)_{18}$ respectively.

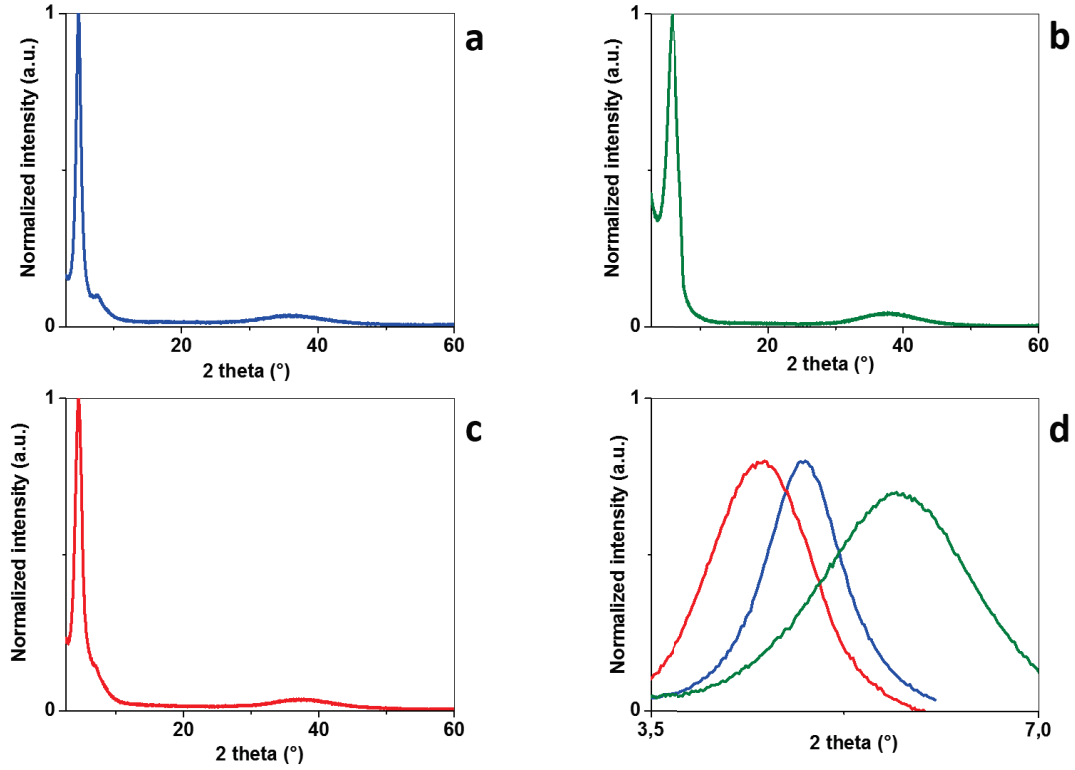

Figure 4-1 PXRD patten of (a) $Au_{25}(SG)_{18}$, (b) $Au_{25}(Capt)_{18}$ and (c) $Au_{25}(ATP)_{18}$. (d) Zoomed low angle region for superimposed PXRD patterns of the synthesized tGNCs.

II.2. **UV-Vis**

The characterization of the tGNCs by UV–vis spectroscopy is important, because $Au_{25}(SR)_{18}$ clusters exhibit two absorption bands corresponding to their typical discrete electronic transitions.

For $Au_{25}(SG)_{18}$ and $Au_{25}(Capt)_{18}$ the two absorption peaks have been centered at 450 and 650 nm. For $Au_{25}(ATP)_{18,}$ the peaks have been observed at 470 and 710 nm **Figure 4-2**. This shift when ATP is the ligand, has been also observed in one case when phenylethylthiolate was replaced by thiophenolate [243]. The absence of a peak at 520 nm indicates that no plasmon resonance phenomenon is observed, meaning that no big gold nanoparticles are present.

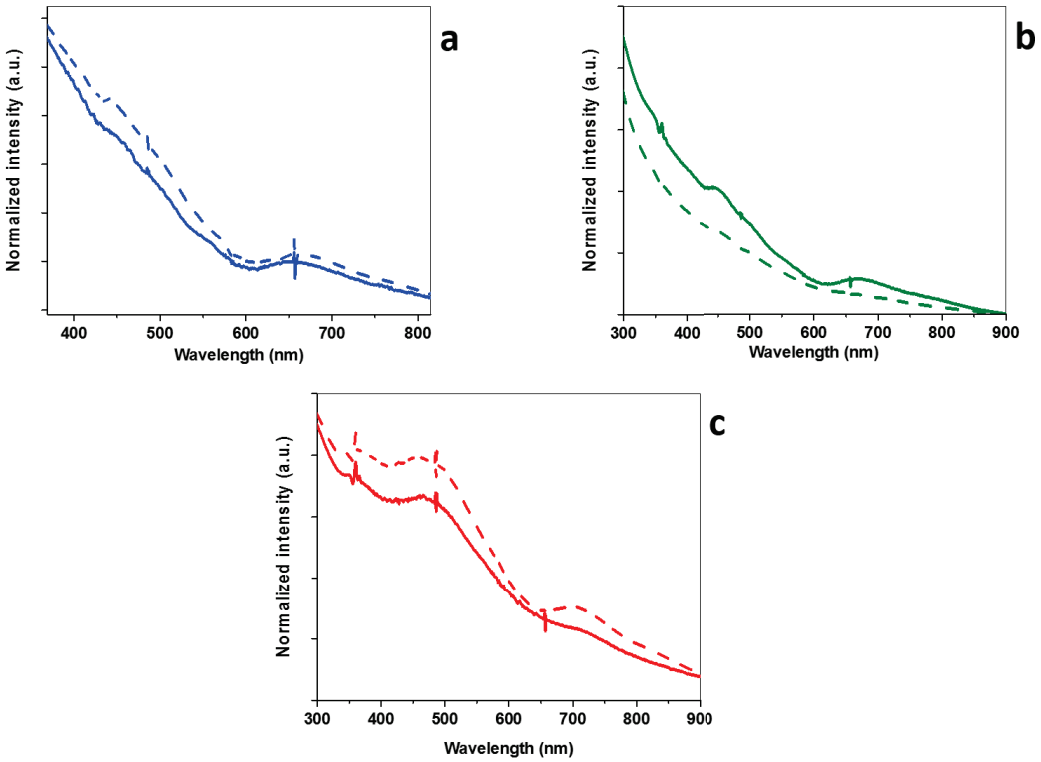

Figure 4-2 UV-Vis spectra during synthesis (dashed line) and after purification (solid line) of (a) $Au_{25}(SG)_{18}$, (b) $Au_{25}(Capt)_{18}$ and (c) $Au_{25}(ATP)_{18}$.

II.3. **TGA**

Thermal studies of the materials were done by TGA under air and dynamic conditions of temperature (10 °C.min^{-1}), on pure $Au_{25}(SG)_{18}$, $Au_{25}(Capt)_{18}$ and $Au_{25}(ATP)_{18}$ tGNCs **Figure 4-3**.

TGA curves of the tGNCs showed a first gradual weight loss before 200 °C corresponding to the evaporation of water molecules. This weight loss corresponded to 6.5 % in the case of $Au_{25}(SG)_{18}$ and $Au_{25}(Capt)_{18}$ and to 1.0 % for $Au_{25}(ATP)_{18}$. Then, other gradual weight losses happened for the three tGNCs up to 500°C.

For $Au_{25}(SG)_{18}$, 48.0 % of the total weight were lost up to 500 °C and the remaining gold was 46.0 %. The actual percentage of glutathione lost, without taking into consideration the solvent content, was 51.0 % close to the theoretically calculated value (53.0 %). This slight difference may be due to the early decomposition of the molecules before 200 °C or to the presence of impurities such as bigger clusters or molecular species.

For $Au_{25}(Capt)_{18}$, 36.0 % of the total weight were lost up to 800 °C and the remaining

gold was 58.0%. The actual percentage of captopril lost, without taking into consideration the solvent content, was 40.0 % not far from the theoretically calculated value (43.0 %).

For $Au_{25}(ATP)_{18}$, 33.0 % of the total weight were lost up to 600 °C and the remaining gold was 66.0 %. The actual percentage of ATP lost, without taking into consideration the solvent content, was 33.0 % very close to the theoretically calculated value (34.0 %).

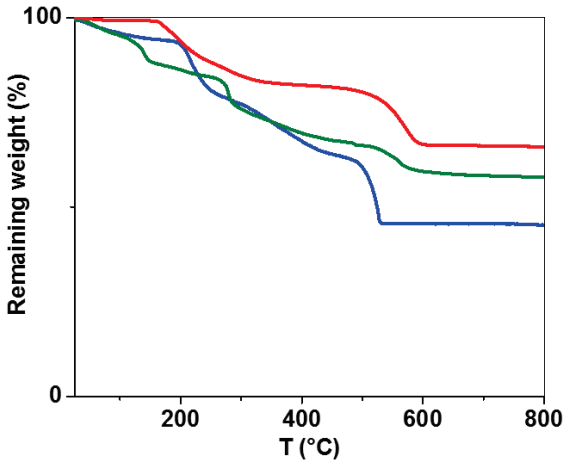

Figure 4-3 TGA thermograms of $Au_{25}(SG)_{18}$ (blue), $Au_{25}(Capt)_{18}$ (green) and $Au_{25}(ATP)_{18}$ (red) done under air with a rate of 10 °C.min^{-1}.

Therefore, under air and with continuous heating, complete defunctionalization of $Au_{25}(SG)_{18}$, $Au_{25}(Capt)_{18}$ and $Au_{25}(ATP)_{18}$ is reached at 500 °C, 600 °C and 600 °C respectively.

III Composite materials

A composite material is a combination of two or more materials, each possessing its own functionality. The chemical, physical and catalytic behaviors of both counterparts may be idealy retained in the newly formed composite, or altered leading to new characteristics.

In this project, the production of composite materials composed by $Au_{25}(SR)_{18}$ and MOFs has been targeted. Syntheses were done using a deposition method and were considered as 2 pots syntheses, because $Au_{25}(SR)_{18}$ and MOFs were synthesized apart, then used together to elaborate the $Au_{25}(SR)_{18}$@MOF composite materials. Readers can refer to

chapter 2 for more details about the synthetic conditions.

To simplify the names of the composite materials, a specific nomenclature was followed. Two capital letters are used, the first one for the MOF followed by the second one for the thiolate ligand within the used $Au_{25}(SR)_{18}$. For example, **(MG)** corresponds to **M**IL-101 supporting $Au_{25}(SG)_{18}$ clusters based on **g**lutathione ligand. The table below summarizes the synthesized composites and their corresponding symbols **Table 4-1**.

Table 4-1 Nomenclature of the synthesized composite materials.

Composite material	Nomenclature within the text
$Au_{25}(SG)_{18}$@MIL-101	(MG)
$Au_{25}(Capt)_{18}$@MIL-101	(MC)
$Au_{25}(ATP)_{18}$@MIL-101	(MA)
$Au_{25}(SG)_{18}$@UiO-66	(UG)
$Au_{25}(ATP)_{18}$@UiO-66	(UA)
$Au_{25}(SG)_{18}$@ZIF-8	(ZG)
$Au_{25}(ATP)_{18}$@ZIF-8	(ZA)

Following the syntheses, the composite materials were characterized using PXRD, ICP and TEM.

III.1. PXRD

PXRD diffractograms of all composite materials were similar to the PXRD diffractograms of their related MOFs before tGNCs deposition **Figure 4-4**. Indeed the observed peaks referred to the reflections of MIL-101, UiO-66 and ZIF-8, meaning that:

(i) The $Au_{25}(SR)_{18}$ nanoclusters were well integrated within the MOFs matrix

(ii) No bulk gold was observed (absence of bulk gold peaks at high angles)

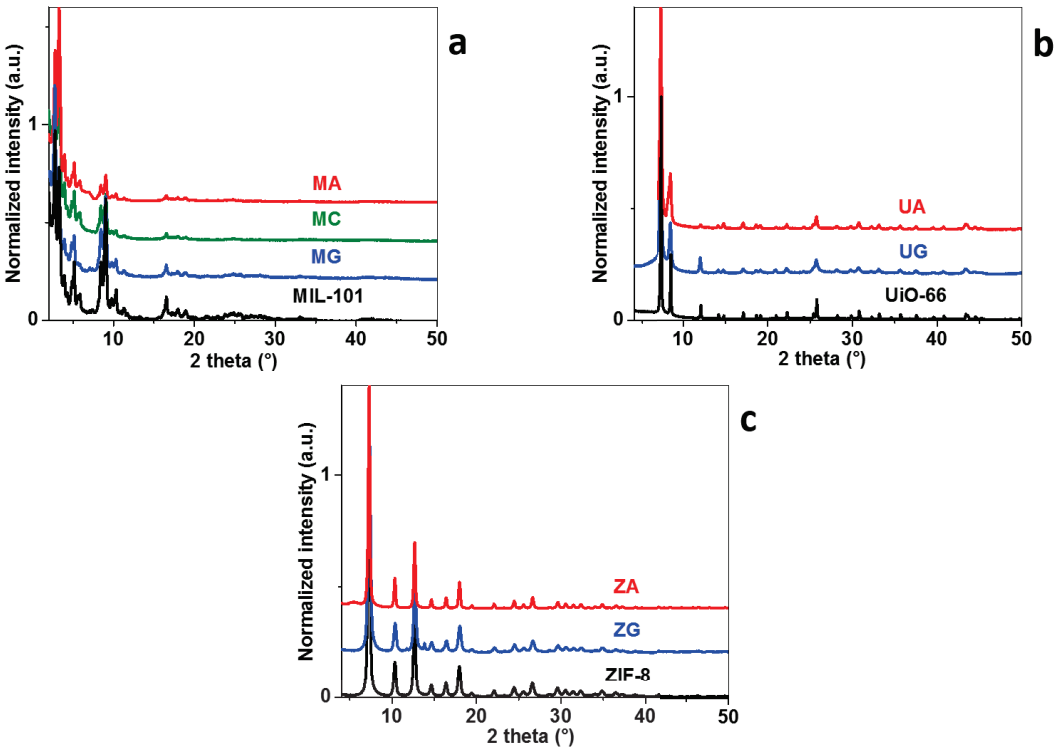

Figure 4-4 PXRD diffractograms of composite materials and their corresponding MOF support. (a) Composites with MIL-101 support, (b) with UiO-66 support and (c) with ZIF-8 support.

III.2. **ICP analysis**

Different gold contents (wt %) were detected within the synthesized composite materials **Table 4-2**. These values allowed the determination of the total gold quantity per 1 g of MOF. It should be noted that the targeted Au (wt %) was 1 %.

Table 4-2 ICP analysis for Au amount within composite materials based on different MOFs and $Au_{25}(SR)_{18}$ nanoclusters, per 1 g of the used MOF.

$Au_{25}(SR)_{18}$@MIL-101	**Au content (wt %)**	**µmol of Au per 1 g of MOF**
(MG): $Au_{25}(SG)_{18}$@MIL-101	0.3	15.2
(MC): $Au_{25}(Capt)_{18}$@MIL-101	0.6	30.4
(MA): $Au_{25}(ATP)_{18}$@MIL-101	0.5	25.4
(UG): $Au_{25}(SG)_{18}$@UiO-66	0.9	45.7
(UA): $Au_{25}(ATP)_{18}$@UiO-66	0.5	25.4
(ZG): $Au_{25}(SG)_{18}$@ZIF-8	0.99	50
(ZA): $Au_{25}(ATP)_{18}$@ZIF-8	1.1	54.3

From the experiments the gold content varies between 0.3 % for (MG) to 1.1 % for (ZA).

These differences may be explained by the different modes of interaction or affinities between $Au_{25}(SR)_{18}$ and MOFs. It can be assigned to electrostatic, hydrogen bonding or Van der Waals interactions. Such interactions may be related to ligand (of clusters) – ligand (of MOFs) or ligand (of clusters) – metal (of MOFs) interactions, or maybe both.

Comparing **(MG)**, **(UG**) and **(ZG)**, it was noticed that the total amount of $Au_{25}(SG)_{18}$ used was adsorbed on the corresponding MOF in the case of **(UG)** and **(ZG)**, but it was not the case for **(MG).** MIL-101 and UiO-66 have both terephthalates as ligands, but the adsorption of $Au_{25}(SG)_{18}$ was not the same. This means that the MOFs ligands are not the sites adsorbing the tGNCs. This is also validated by **(ZG)** who has 2-methyl imidazolates ligands and showed same behavior as **(UG**). **(MA)** and **(UA)** showed similar gold contents of 0.5 wt%, meaning that the amino ligand has a weak interaction with the supports. Another difference between the three MOFs is the metal centers, (Cr^{3+}) in MIL-101, (Zr^{4+}) in UiO-66 and (Zn^{2+}) in ZIF-8. Maybe the adsorption ability of these MOFs toward $Au_{25}(SG)_{18}$ having carboxylic acid groups is also related to ligand – metal interactions.

When comparing **(MA)**, **(UA)** and **(ZA)**, one notices that complete $Au_{25}(ATP)_{18}$ adsorption was on ZIF-8 only. 4-aminothiophenol within $Au_{25}(ATP)_{18}$ does not have carboxylatic acids, but has phenyl ring. Maybe π-π stacking between the phenyl ring of ATP ligands and the imidazolate rings favored this interaction. Rather, it seems more ligand – ligand interactions.

Comparing **(MC)**, **(MG)** and **(MA)** shows also differences in the Au amounts from different tGNCs on the same MOF type.

Based on what preceeded, the adsorption of thiolate-protected gold nanoclusters depend on the nature of the MOF as well as on the thiolate ligands functional groups. Which is still not clear, is wether the interaction of $Au_{25}(SR)_{18}$ is directed toward the metallic or organic parts of the used MOFs, or both. In depth studies on several samples should be carried out to bring some solid proofs. Difference of solubility of the clusters during the washing may also explain the variation of gold loadings.

III.3. **TEM**

TEM images have been taken to assess the size distribution of $Au_{25}(SR)_{18}$ supported over

MOFs. Through TEM images only the metallic part of tGNCs can be visualized, and not thiolate linkers. It should be noted that, all images were taken rapidly, because both tGNCs and MOFs are not stable under the microscopic beam. tGNCs can undergo defunctionalization, move and sinter, while MOFs degrade. MOFs nanoparticles were important at this level to optimize the tGNCs distribution and minimize the probabilities of moving and sintering. $Au_{25}(SR)_{18}$ nanoclusters have been located at the surface of MOFs. They can not be located inside the MOFs pores because their sizes are bigger than the accessible windows of each MOF.

The sizes of $Au_{25}(SG)_{18}$, $Au_{25}(Capt)_{18}$ and $Au_{25}(ATP)_{18}$ based on Bragg's law calculation from the low angle PXRD are 1.76 nm, 1.92 nm and 1.7 nm respectively. Their sizes when deposited on MOFs were as following: $Au_{25}(SG)_{18}$ within **(MG)**, **(UG)** and **(ZG)** showed a an average size of 1.4 nm ± 0.3 nm, 1.8 nm ± 1.8 nm and 1.8 nm ± 1.76 nm, respectively. $Au_{25}(ATP)_{18}$ within **(MA)**, **(UA)** and **(ZA)** showed an average size of 1.6 nm ± 0.5 nm, 1.7 nm ± 0.7 nm and 1.5 nm ± 0.4 nm, respectively. The average size of $Au_{25}(Capt)_{18}$ within **(MC)** was 1.3 nm ± 0.9 nm **Figure 4-5**, **Figure 4-6** and **Figure 4-7**.

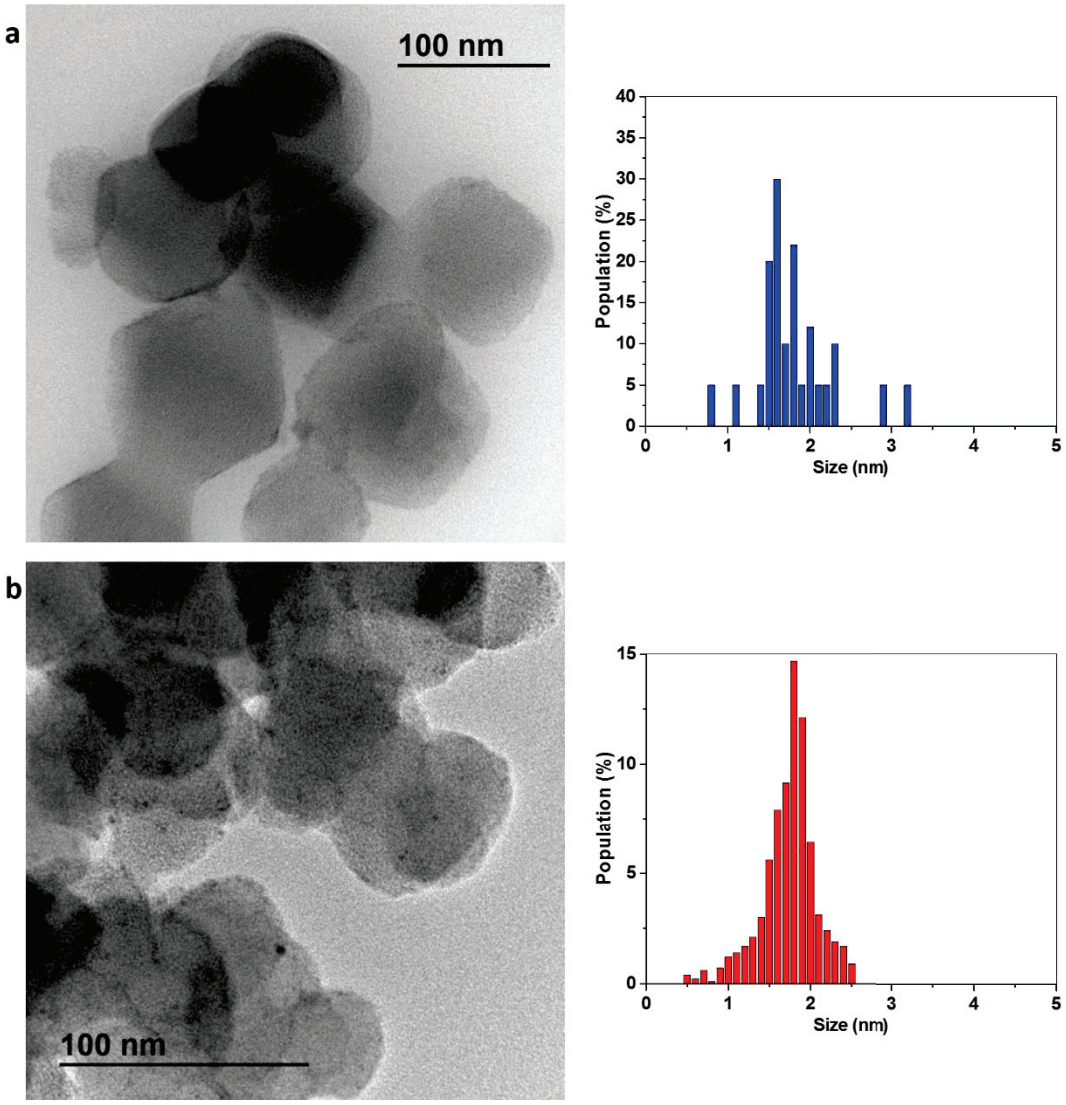

Figure 4-5 TEM image and size distribution of $Au_{25}(SR)_{18}$ supported on UiO-66. (a) **(UG)** and b) **(UA)**.

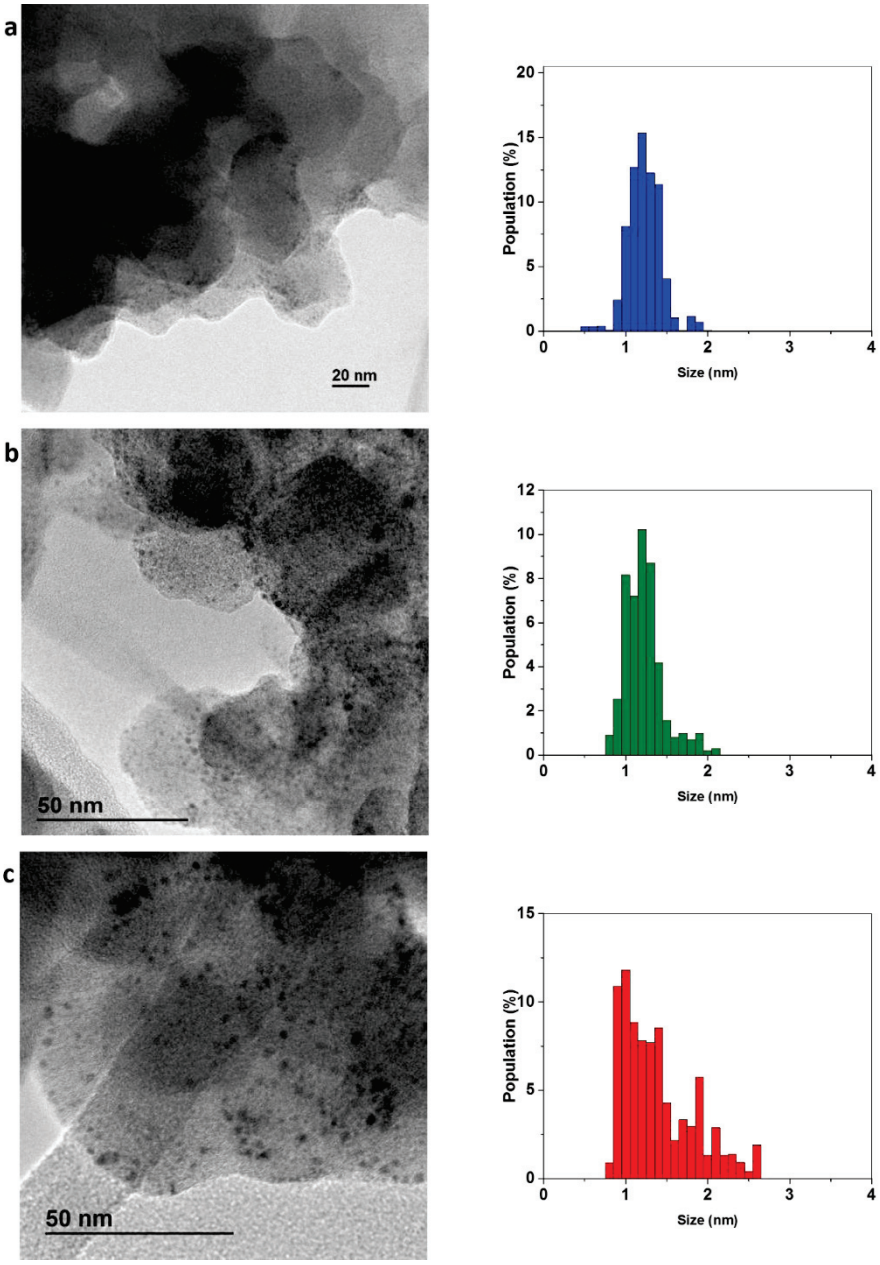

Figure 4-6 TEM images and size distributions of $Au_{25}(SR)_{18}$ supported on MIL-101. (a) **(MG)**, (b) **(MC)** and (c) **(MA)**.

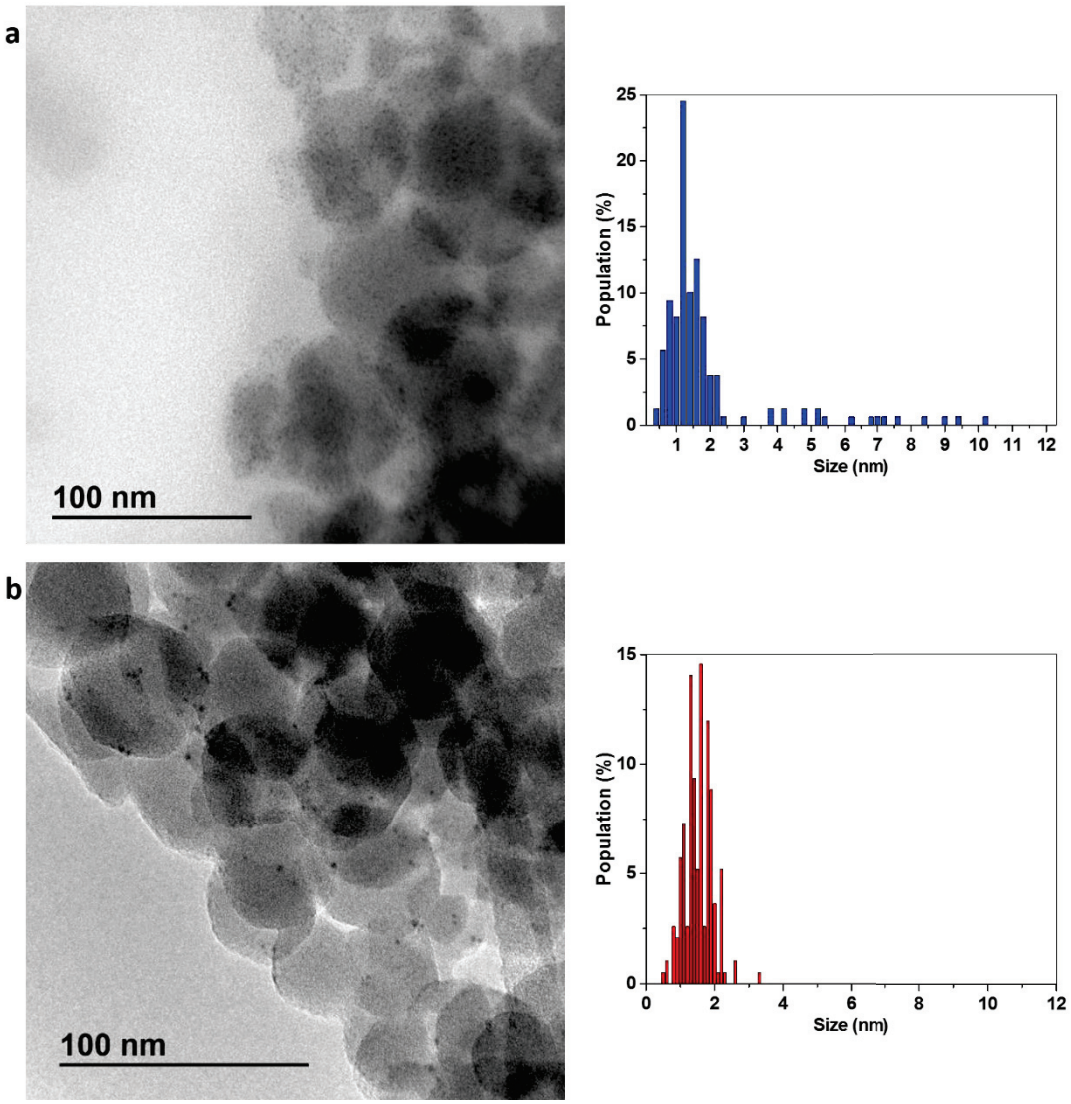

Figure 4-7 TEM image and size distribution of $Au_{25}(SR)_{18}$ supported on ZIF-8. (a) **(ZG)** and (b) **(ZA)**.

IV Isothermal studies for the stabilities of $Au_{25}(SR)_{18}$ and MOFs

Isothermal studies on MOFs and clusters individually were performed at constant temperatures 200 °C, 300 °C and 400 °C (10 °C.min^{-1}) for 12 hours under air, in order to simulate the calcination procedures. The percentages presented in the following correspond to the weight percentage of the organic part removed.

IV.1. MIL-101

In the case of MIL-101, following the isotherm analysis at 200 °C, 300 °C, and 400 °C, the final loss reached 15.0 %, 63.5 % and 66.0 %, respectively, corresponding to water loss at

200°C, and almost complete removal of the ligand at 300 °C and at 400 °C (solvent not excluded). It is interesting to note that the complete decomposition at 300 °C and 400 °C is reached after almost 1 h of heating **Figure 4-8**. Therefore, thermal treatments of the composite materials based on MIL-101 as a support can be done only at 200 °C to avoid the decomposition of MIL-101.

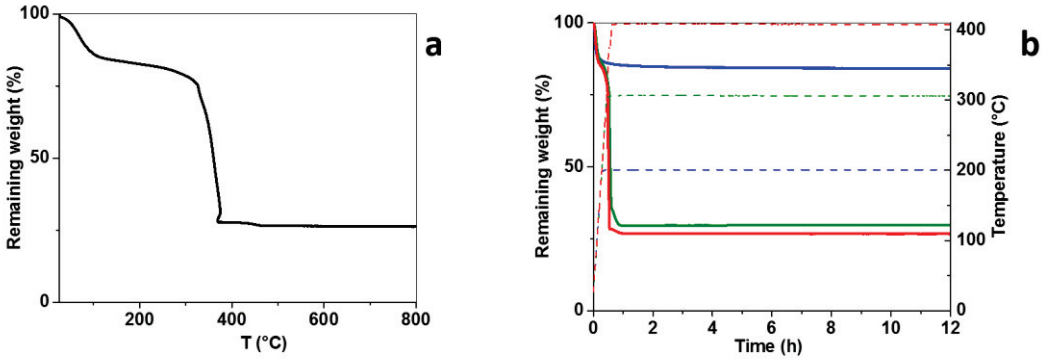

Figure 4-8 (a) TGA experiment on MIL-101 under air at 10 °C.min^{-1}. (b) Isotherm experiments on MIL-101 under air at 200 °C (blue), 300 °C (green) and 400 °C (red) for 12 h. Solid lines represent the weight (%) and dotted lines represent the heating ramp.

Figure 4-9 shows the X-ray diffractograms corresponding to **MIL-101$_{200}$, MIL-101$_{300}$ and MIL-101$_{400}$** calcined at 200°C (12 h), 300 °C (4 h) and 400 °C (12 h) in an oven with 10°C.min^{-1}, respectively. PXRD of **MIL-101$_{200}$** showed that MIL-101 is stable. PXRD of **MIL-101$_{300}$** showed that the peaks of the MOF are still there, though in the TGA showed complete decomposition. Maybe this is related to the air flow during the TGA analysis, and shorter heating time in the oven. The diffractogram corresponding to Cr_2O_3 was observed in the case of **MIL-101$_{400}$**, meaning that total decomposition of MIL-101 occurred, aligning with the isothermal TGA studies.

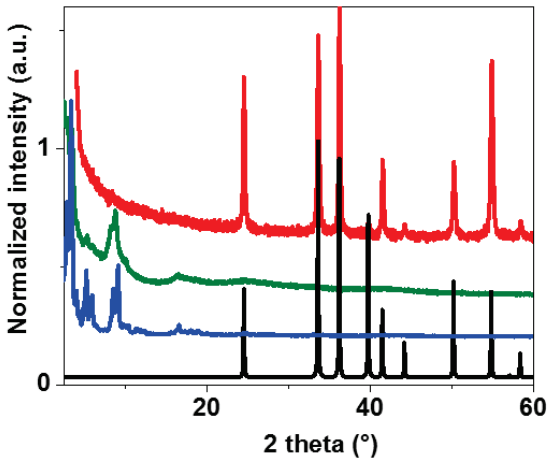

Figure 4-9 PXRD diffractograms of **MIL-101$_{200}$** (blue), **MIL-101$_{300}$** (green), **MIL-101$_{400}$** (red) and the simulated PXRD diffractogram of Cr_2O_3 (black).

IV.2. **UiO-66**

In the case of UiO-66, following the isotherm analyses at 200 °C, 300 °C, and 400 °C for 12 h, the final loss reached 16.0 %, 19.0 % and 55.5 %, respectively, corresponding to water loss and maybe some coordinated DMF molecules at 200 °C and 300 °C (solvent not excluded). Complete ligand removal was observed at 400 °C **Figure 4-10**.

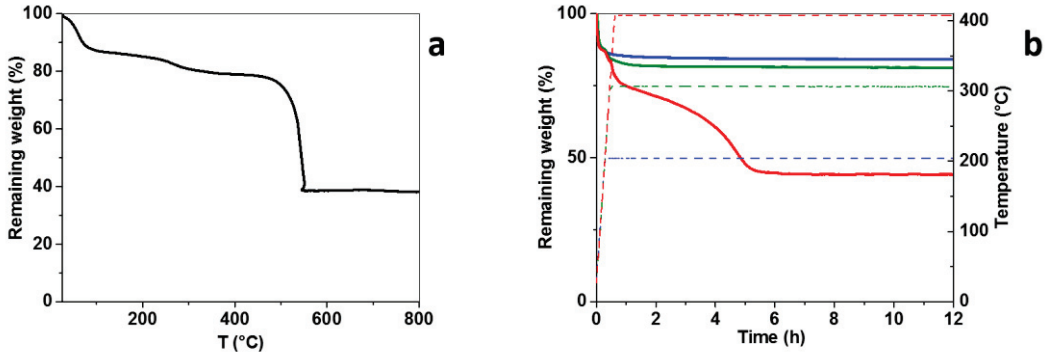

Figure 4-10 (a) TGA experiment on UiO-66 under air at 10 °C.min^{-1}. (b) Isotherm experiments on UiO-66 under air at 200 °C (blue), 300 °C (green) and 400 °C (red) for 12 h. Solid lines represent the weight (%) and dotted lines represent the heating ramp.

For further verifications of these results, UiO-66 was calcined at 200 °C, 300 °C and 400 °C under air for 12 h with a ramp of 10 °C.min^{-1} in an oven. **Figure 4-11** shows the powder X-ray diffractograms corresponding to **UiO-66$_{200}$, UiO-66$_{300}$ and UiO-66$_{400}$** calcined at 200

°C, 300 °C and 400 °C, respectively. PXRD of **UiO-66$_{200}$** and **UiO-66$_{300}$** did not change proving their thermal stability, whereas loss of cristallinty and amorphization without formation of an oxide was observed for **UiO-66$_{400}$.** Therefore, thermal treatments of the composite materials based on UiO-66 as a support can be done at 200 °C and up to 300 °C.

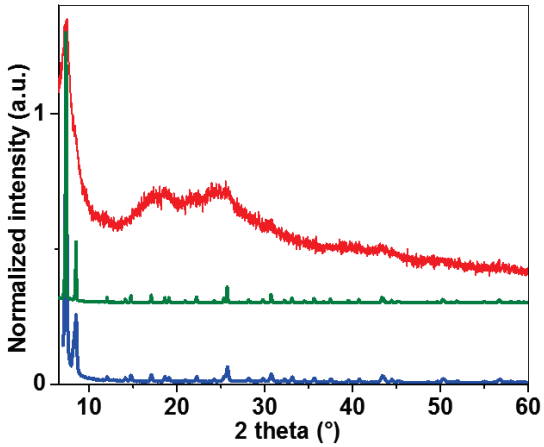

Figure 4-11 PXRD diffractograms of **UiO-66$_{200}$** (blue), **UiO-66$_{300}$** (green) and **UiO-66$_{400}$** (red).

It should be noted that the N_2 adsorption at 77 K for **UiO-66$_{400}$** gave a BET surface area of 550 $m^2.g^{-1}$, indicating the partial decomposition of UiO-66 and the formation of a still porous and amorphous compound.

IV.3. **ZIF-8**

In the case of ZIF-8, following the isotherm analyses at 200 °C, 300 °C, and 400 °C, the final loss reached 4.0 %, 6.5 % and 41.0 %, respectively, corresponding to some solvent loss at 200 °C and 300 °C and complete decomposition at 400 °C **Figure 4-12**.

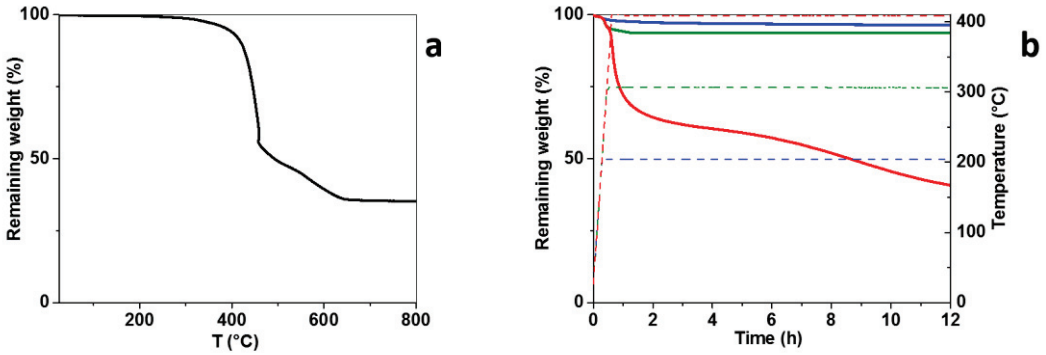

Figure 4-12 (a) TGA experiment on ZIF-8 under air at 10 °C.min^{-1}. (b) Isotherm experiments on ZIF-8 under air at 200 °C (blue), 300 °C (green) and 400 °C (red) for 12 h. Solid lines represent the weight (%) and dotted lines represent the heating ramp.

For further verifications of these results, **ZIF-8** was calcined at 200 °C, 300 °C and 400 °C under air for 12 h with a ramp of 10°C.min^{-1} in an oven. **Figure 4-13** shows the powder X-ray diffractograms corresponding to **ZIF-8$_{200}$, ZIF-8$_{300}$ and ZIF-8$_{400}$** calcined at 200 °C, 300 °C and 400 °C respectively. **ZIF-8$_{200}$** and **ZIF-8$_{300}$** were stable, whereas total decomposition was observed for **ZIF-8$_{400}$** and resulted in the formation of hexagonal ZnO (zinc oxide). Therefore, thermal treatments of the composite materials based on ZIF-8 as a support can be done also at 200 °C and 300 °C to avoid ZIF-8 decomposition.

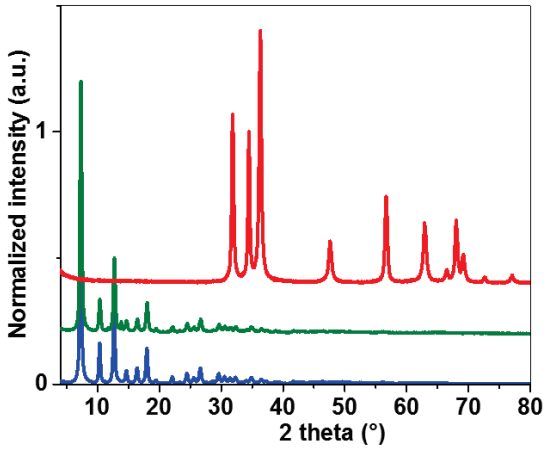

Figure 4-13 PXRD diffractograms of **ZIF-8$_{200}$** (blue), **ZIF-8$_{300}$** (green) and **ZIF-8$_{400}$** (red).

IV.4. $Au_{25}(SG)_{18}$

In the case of $Au_{25}(SG)_{18}$, following the isotherm analysis at 200 °C, 300 °C, and 400 °C, the final loss reached 17.0 %, 40.0 % and 52.9 %, respectively, corresponding to partial calcination at 200 °C and 300 °C, and almost complete removal of the ligand at 400 °C **Figure 4-14** (solvent excluded). It is interesting to note that the complete calcination of the ligands at 400 °C is reached after almost 3 h of heating, suggesting that a heating ramp of at least 3 hours is required to completely remove the glutathione molecules from the gold cluster.

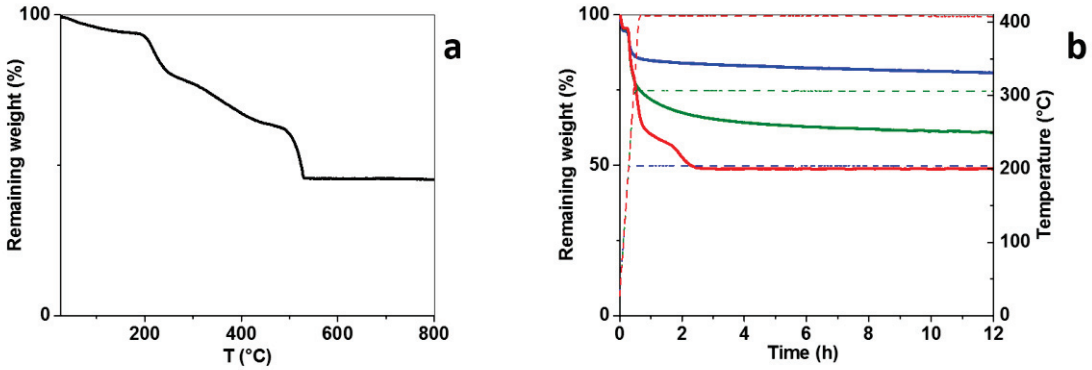

Figure 4-14 (a) TGA experiment on $Au_{25}(SG)_{18}$ under air at 10 °C.min^{-1}. (b) Isotherm experiments on $Au_{25}(SG)_{18}$ under air at 200 °C (blue), 300 °C (green) and 400 °C (red) for 12 h. Solid lines represent the weight (%) and dotted lines represent the heating ramp.

IV.5. $Au_{25}(Capt)_{18}$

In the case of $Au_{25}(Capt)_{18}$, following the isotherm analyses at 200 °C, 300 °C, and 400 °C, the final loss reached 20.0 %, 26.0 % and 31.0 %, respectively, corresponding to partial calcination at 200 °C, 300 °C and at 400 °C **Figure 4-15**. The total weight loss corresponds to 36.0 %. This means that for the complete calcination of the ligands in $Au_{25}(Capt)_{18}$, higher temperatures are needed.

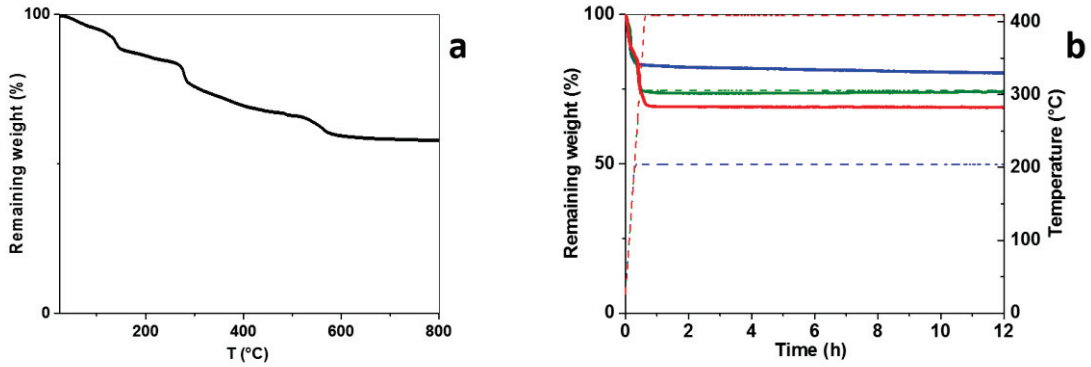

Figure 4-15 (a) TGA experiment on $Au_{25}(Capt)_{18}$ under air at 10 °C.min^{-1}. (b) Isotherm experiments on $Au_{25}(Capt)_{18}$ under air at 200 °C (blue), 300 °C (green) and 400 °C (red) for 12 h. Solid lines represent the weight (%) and dotted lines represent the heating ramp.

IV.6. $Au_{25}(ATP)_{18}$

In the case of $Au_{25}(ATP)_{18}$, following the isotherm analyses at 200 °C, 300 °C, and 400 °C, the final loss reached 12.0 %, 18.0 % and 31.5 %, respectively, corresponding to partial calcination at 200 °C and 300 °C, and complete removal of the ligand at 400 °C. The complete calcination of the ligands at 400 °C is reached after almost 3 h of heating, suggesting that a heating ramp of at least 3 h is required to completely remove the glutathione molecules from the gold cluster **Figure 4-16**.

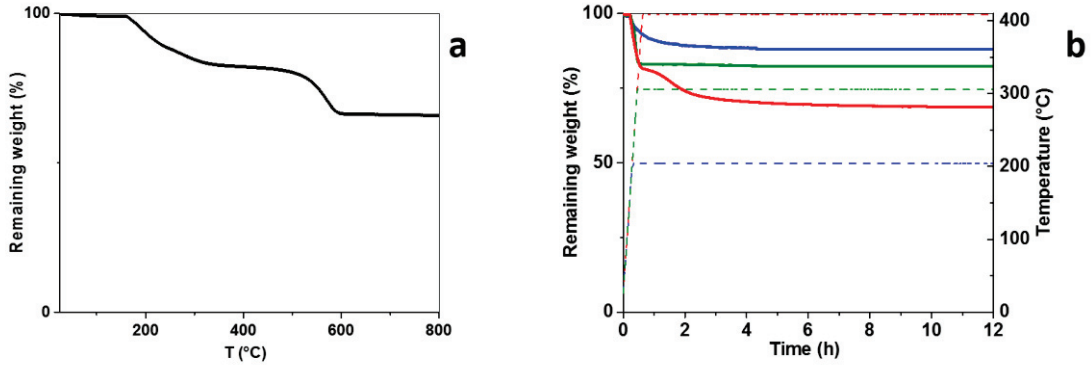

Figure 4-16 (a) TGA experiment on $Au_{25}(ATP)_{18}$ under air at 10 °C.min^{-1}. (b) Isotherm experiments on $Au_{25}(ATP)_{18}$ under air at 200 °C (blue), 300 °C (green) and 400 °C (red) for 12 h. Solid lines represent the weight (%) and dotted lines represent the heating ramp.

According to the described thermal studies, it was not possible to defunctionalize totally the $Au_{25}(SR)_{18}$ without decomposing the MOFs, because the tGNCs required a

temperature equals or higher than 400 °C for complete defunctionnalization. To keep the MOFs intact, calcination can be done under air, 10 °C.min^{-1} for 12 h at a maximum temperature of 200 °C in the case of MIL-101 and 300 °C in the case of UiO-66 and ZIF-8. Therefore, in all cases the partial defunctionalization of tGNCs is only possible.

V Thermally treated composite materials

The synthesized composite materials were treated thermally, based on the results of the previous thermal studies. Composites with MIL-101 support were calcined at 200 °C and 400 °C, and fully characterized. Those with UiO-66 and ZIF-8 supports were calcined at 300 °C and also fully characterized.

For the nomenclature of the calcined materials, the calcination temperature was added. For example, $Au_{25}(SG)_{18}$@MIL-101 calcined at 200 °C, air, 12 h, corresponds to **(MG_{200})**.

V.1. Composites based on MIL-101 support

Since MIL-101 is stable up to 200 °C, **(MG)**, **(MC)** and **(MA)** were calcined at 200 °C under air for 12 h, resulting in **(MG_{200})**, **(MC_{200})** and **(MA_{200})** respectively. PXRD diffractograms of the non-calcined and calcined $Au_{25}(SR)_{18}$@MIL-101 systems at 200° C are presented (**Figure 4-17**) and showed no differences when compared to those of **(MG)**, **(MC)**, **(MA)**, meaning that the MOFs were stable upon thermal treatment at 200 °C. No peaks due to bulk gold were observed.

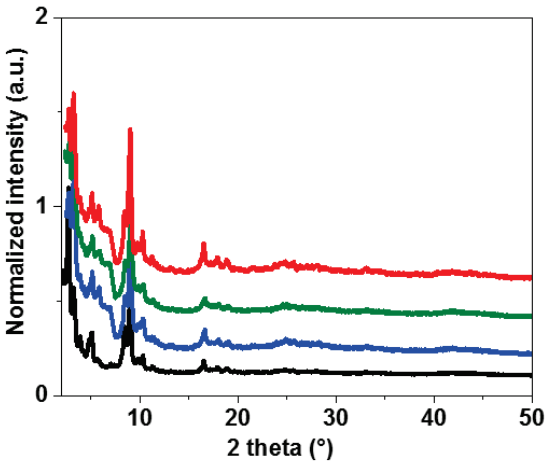

Figure 4-17 PXRD diffractograms of non-calcined $Au_{25}(SR)_{18}$@MIL-101 (black) and calcined $Au_{25}(SR)_{18}$@MIL-101 at 200 °C/air/12 h/10 °C.min^{-1}. **(MG_{200})** (blue), **(MC_{200})** (green) and **(MA_{200})** (red).

N_2 adsorption analyses were performed and showed that the adsorption-desorption isotherms and the corresponding BET surface area have been almost unchanged after the treatment at 200 °C, pointing out that the porosity is preserved and the pores are not blocked. The data are presented in **Figure 4-18** and **Table 4-3.** The BET surface areas of (**MG_{200}**), (**MC_{200}**) and (**MA_{200}**), became a bit higher than those of (**MG**), (**MC**) and (**MA**).

As mentioned before, the nanoclusters can not enter into the pores of MOFs, they can be located on the pores openings, blocking them and leading to slight decrease in the BET surface area of the MOF upon tGNCs deposition. This was noticeable when comparing the BET surface area of the MOFs intact (mentioned in **chapter 3**), and those upon tGNCs deposition. Upon thermal treatment, slight increase in the BET surface area was observed when calcination was performed at 200 °C, maybe this temperature is better in activating the MIL-101 leading to slight increase in the area (the activation of intact MIL-101 was done at 150 °C during 8 h). This confirms that the MIL-101 supports were stable upon tGNCs deposition followed by calcination at 200 °C for 12h under air, as already noticed by PXRD results.

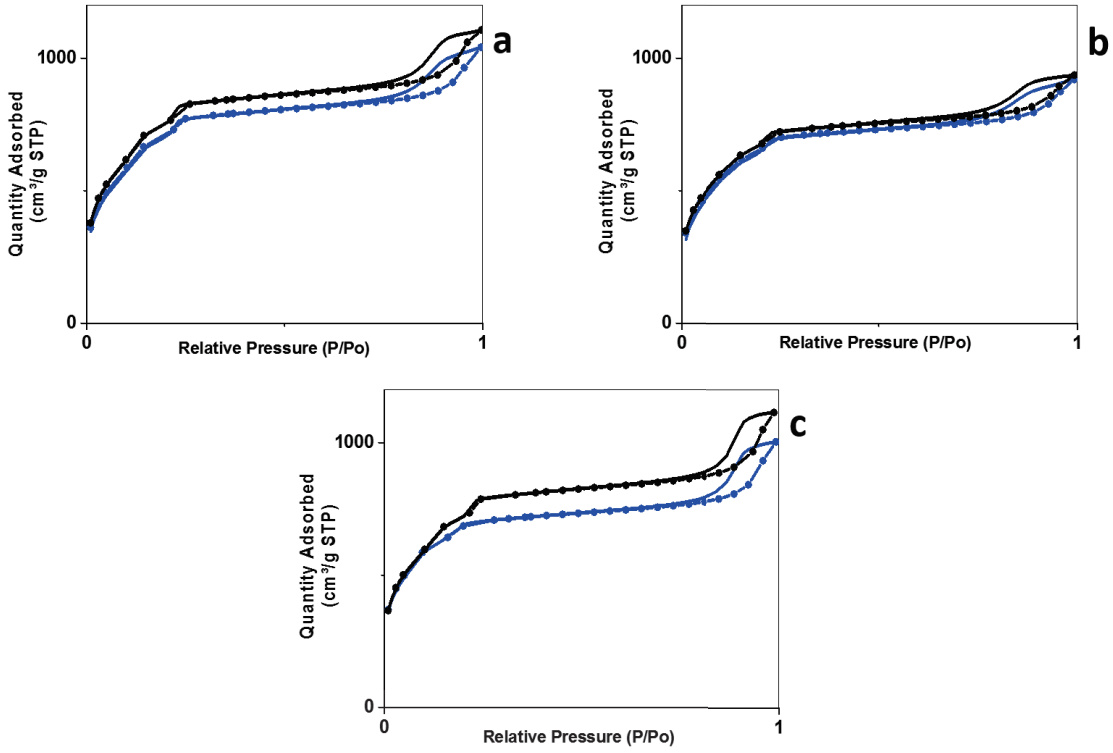

Figure 4-18 N_2 adsorption – desorption isotherms of non- calcined composite materials (blue) and their corresponding calcined derivatives at 200 °C (black). (a) (**MG_{200}**), (b) (**MC_{200}**) and (c) (**MA_{200}**).

Table 4-3 BET surface area of composite materials before and after being calcination.

	S_{BET} (composite materials) $m^2.g^{-1}$	S_{BET} (calcined composite materials) $m^2.g^{-1}$	
(MG)	2600	2800	**(MG_{200})**
(MC)	2400	2500	**(MC_{200})**
(MA)	2300	2700	**(MA_{200})**

In general, supported gold thiolate clusters are known to grow when calcined at high temperature, except when they are inserted in a porous material, such as SBA-15 [140], or loaded with a very small quantity of nanoclusters [142]. Based on that, the choice of the support is very important to be able to control the size of the tGNCs, especially after thermal treatments. As mentioned previously, the synthesized $Au_{25}(SR)_{18}$ are supported over the surface of MOFs, so they are not confined within their pores. The probability of sintering was higher, but we suggested that the nanoparticles size of MOFs will enhance the dispersion of tGNCs and limit their sintering.

TEM analysis was done for non-calcined composite materials, and for those calcined at 200 °C and 400 °C. Sample **(MG)** exhibited homogeneous nanoclusters of average size of 1.1 nm ± 0.3 nm. After calcination at 200 °C/ 12 h/ air with a rate of 10 °C.min^{-1}, the mean particle size in **(MG_{200})** became 9.0 nm ± 1.7 nm (**Figure 4-19**), due to sintering. Same case for **(MA)** which exhibited homogeneous clusters of size 1.6 nm ± 0.5 nm, and became 6.0 nm ± 1.5 nm within **(MA_{200}) (Figure 4-20)**. The growth of the nanoclusters was also observed for **(MC_{200})** to 6.0 nm ± 1.8 nm (**Figure 4-21**).

Following the calcination at 400 °C/ 12h/ air with a rate of 10 °C.min^{-1}, and upon the decomposition of MIL-101 into Cr_2O_3 nanoparticles, the gold nanoparticles have undergone further growth, to an average size of 10 nm ± 1 nm within **(MG_{400})**, 10.9 nm ± 2.4 nm for **(MA_{400})** and 11.8 nm ± 2.7 nm for **(MC_{400})**.

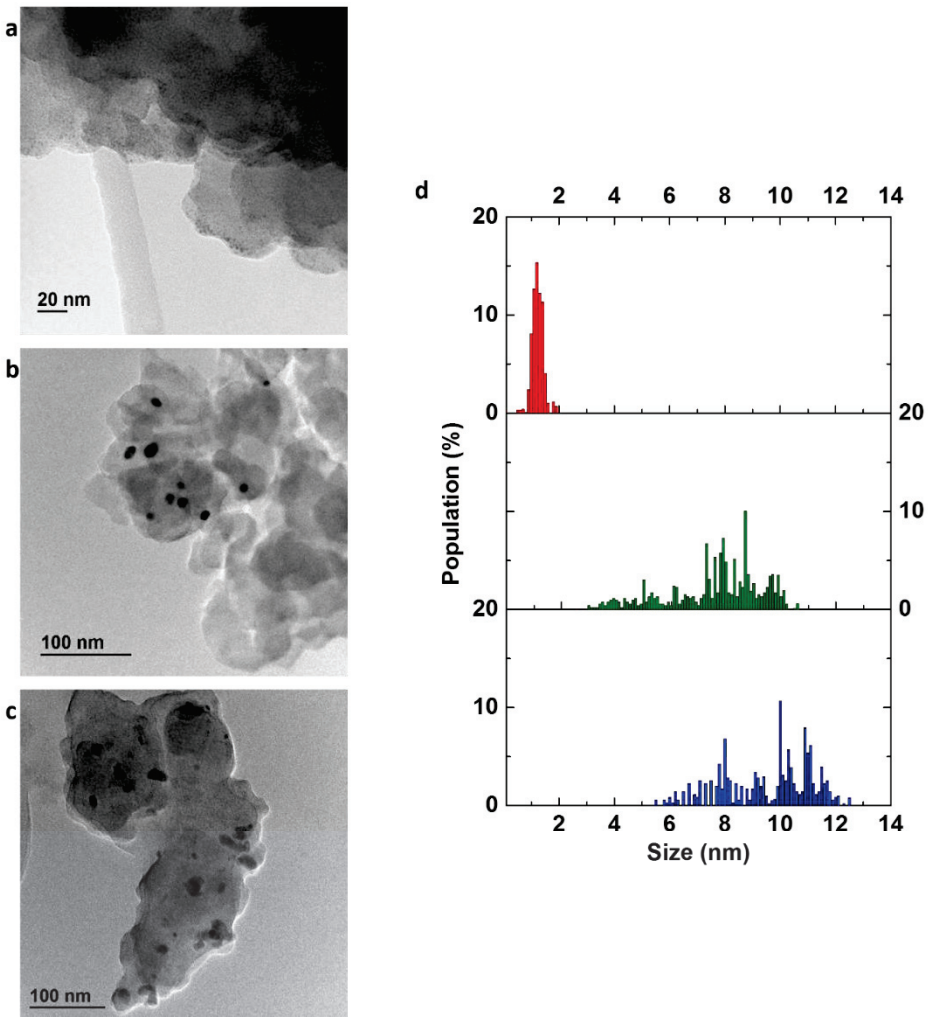

Figure 4-19 TEM images of (a) **(MG)**, (b) **(MG$_{200}$)** and (c) **(MG$_{400}$)**. (d) Average size distribution of **(MG)** in red, **(MG$_{200}$)** in green and **(MG$_{400}$)** in blue.

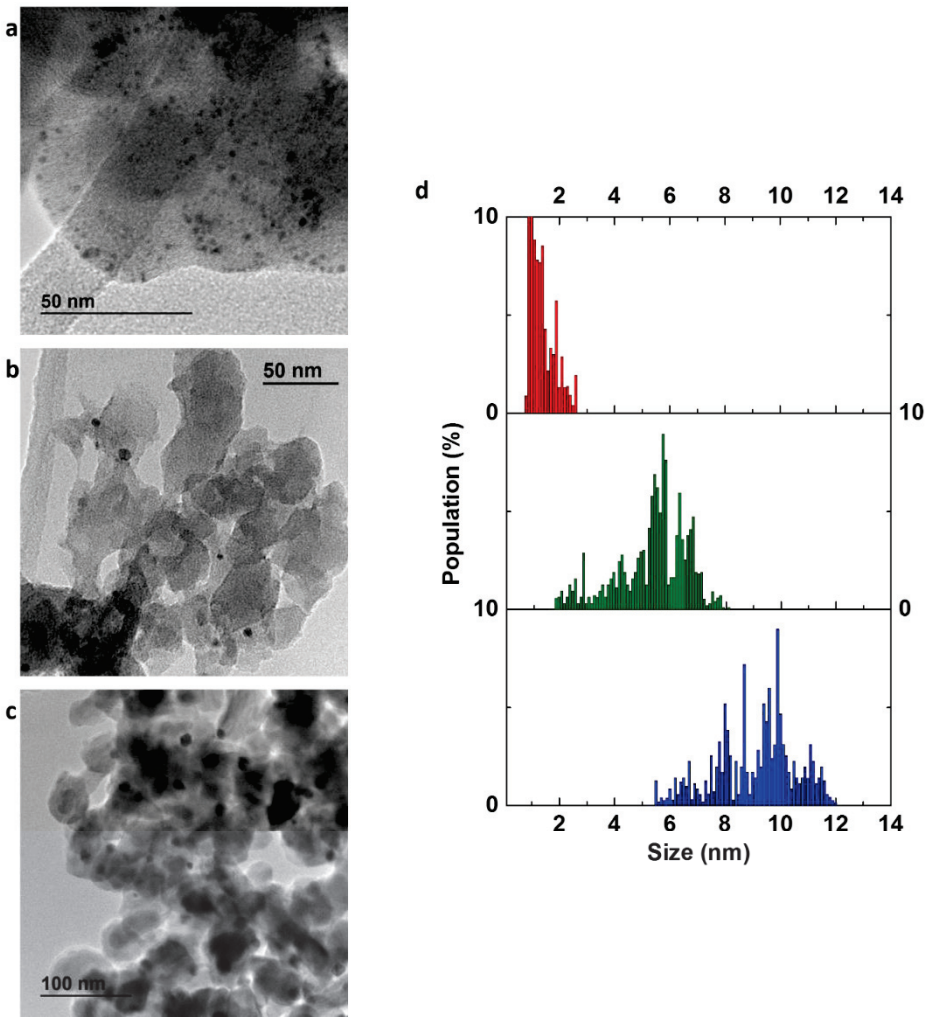

Figure 4-20 TEM images of (a) **(MA)**, (b) **(MA_{200})** and (c) **(MA_{400})**. (d) Average size distribution of **(MA)** in red, **(MA_{200})** in green and **(MA_{400})** in blue.

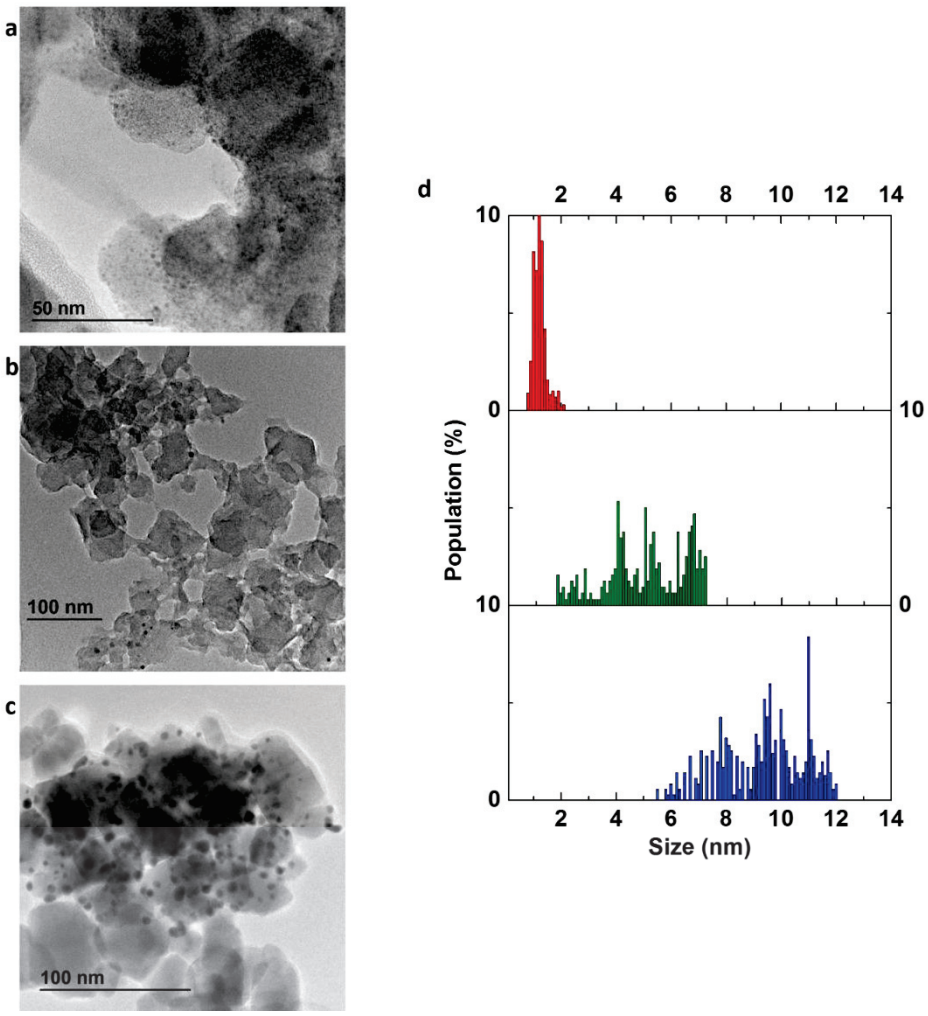

Figure 4-21 TEM images of (a) **(MC)**, (b) **(MC_{200})** and (c) **(MC_{400})**. (d) Average size distribution of **(MC)** in red, **(MC_{200})** in green and **(MC_{400})** in blue.

V.2. Composites based on UiO-66 and ZIF-8 supports

(UG), (UA) (ZG) and **(ZA)** were calcined at 300 °C under air for 12 h, resulting in **(UG_{300})**, **(UA_{300}), (ZG_{300})** and **(ZA_{300}),** respectively. No difference was observed between the diffractograms of the non-calcined and the calcined composite materials, confirming the stability of UiO-66 and ZIF-8, in addition to the absence of bulk gold **Figure 4-22**.

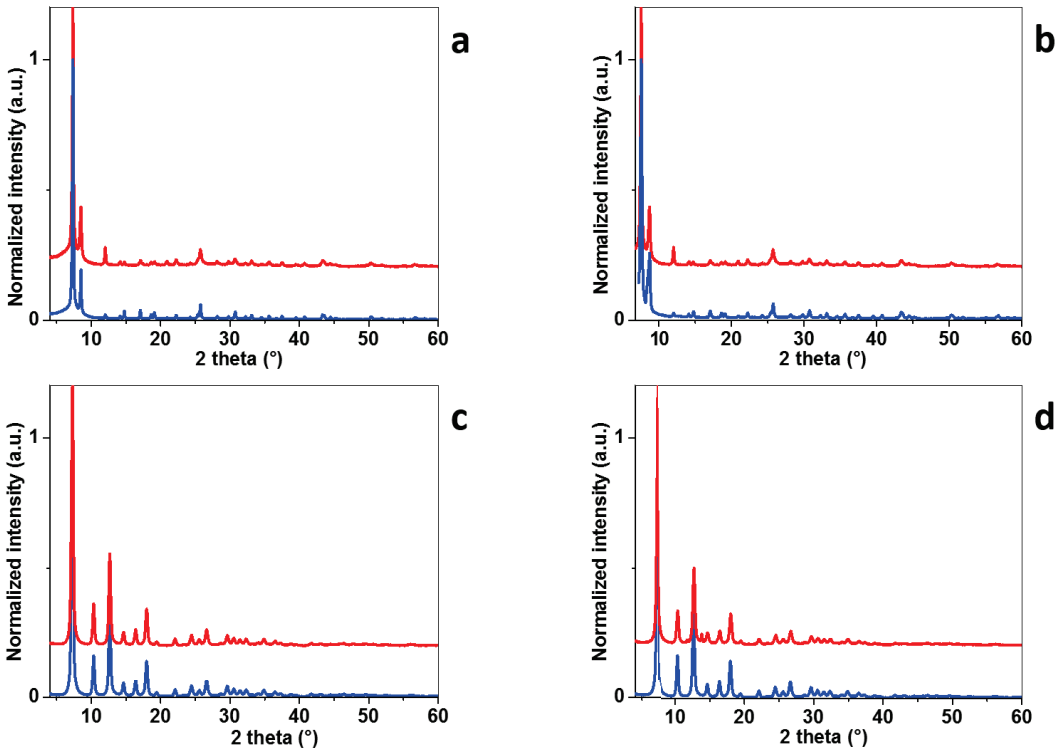

Figure 4-22 PXRD diffractograms of (a) **(UG)** (blue) and **(UG_{300})** (red), (b) **(UA)** (blue) and **(UA_{300})** (red), (c) **(ZG)** (blue) and **(ZG_{300})** (red) and (d) **(ZA)** (blue) and **(ZA_{300})** (red).

In the cases of **(UG_{300})**, **(UA_{300})**, **(ZG_{300})** and **(ZA_{300}),** the N_2 adsorption results aligned with those of MIL-101 based composites, where the BET surface area increased a bit after calcination **Figure 4-23** and **Table 4-4**, again because of higher temperature compared to that used before to activate the MOFs (150 °C during 8 h).

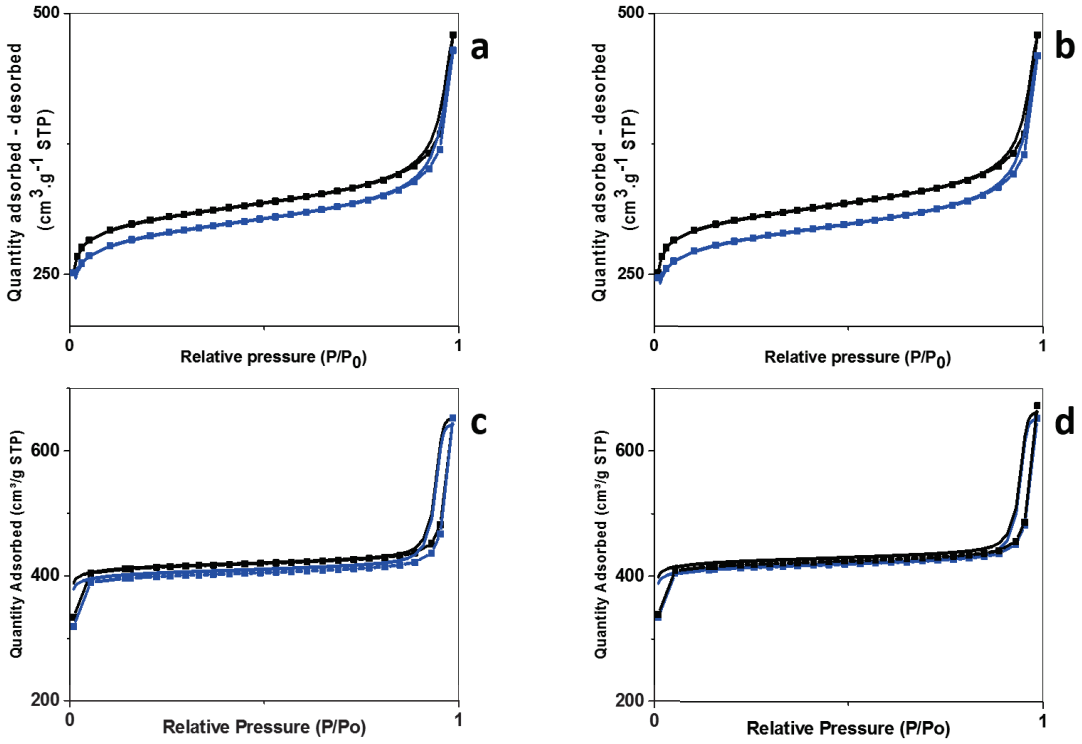

Figure 4-23 N_2 adsorption – desorption isotherms of (a) **(UG)** (blue) and **(UG_{300})** (black), (b) **(UA)** (blue) and**(UA_{300})** (black), (c) **(ZG)** (blue) and **(ZG_{300})** (black) and (d) **(ZA)** (blue) and **(ZA_{300})** (black).

Table 4-4 BET surface area of composite materials before and after calcination.

	S_{BET} (composite materials) $m^2.g^{-1}$	S_{BET} (calcined composite materials) $m^2.g^{-1}$	
(UG)	1250	1350	**(UG_{300})**
(UA)	1200	1250	**(UA_{300})**
(ZG)	1100	1250	**(ZG_{300})**
(ZA)	1200	1300	**(ZA_{300})**

TEM analyses for UiO-66 based composite material **(UG)** exhibited homogeneous clusters of size of 2 nm ± 2.8 nm. After calcination at 300 °C/ 12 h/ air with rate 10 °C.min^{-1}, the mean particle size in **(UG_{300})** was 5.9 nm ± 2.1 nm **Figure 4-24**. As the case of MIL-101 support, sintering of tGNCs supported on UiO-66 also occurred upon calcination.

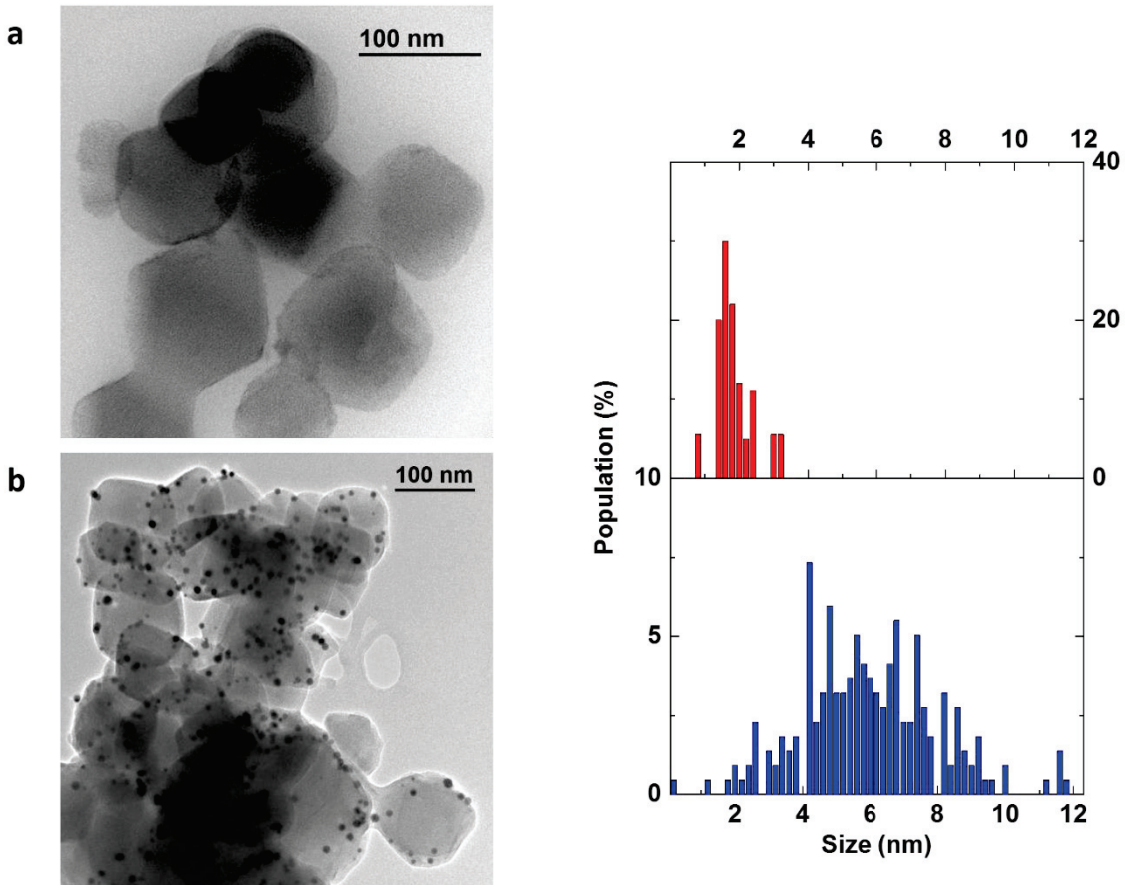

Figure 4-24 TEM images of (a) **(UG)** and (b) **(UG_{300})**. (c) Average size distribution of **(UG)** in red and **(UG_{300})** in blue.

TEM analysis for ZIF-8 based composite material **(ZG)** exhibited clusters of size 1.8 nm ± 1.76 nm. After calcination at 300 °C/ 12 h/ air with rate 10 °C.min^{-1}, the mean particle size in **(ZG_{300})** was 4.8 nm ± 2.4 nm **Figure 4-25**. Again sintering occurred.

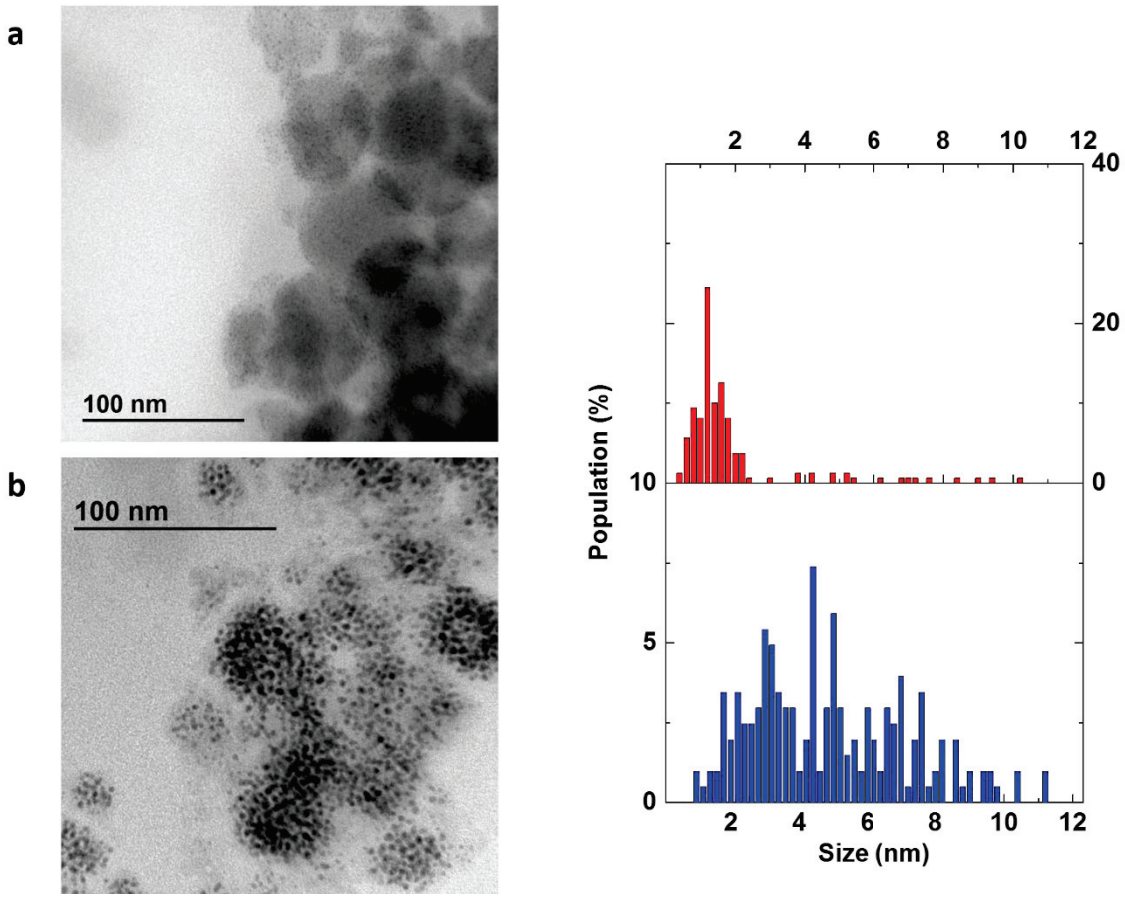

Figure 4-25 TEM images of (a) **(ZG)** and (b) **(ZG_{300})**. (c) Average size distribution of **(ZG)** in red and **(ZG_{300})** in blue.

The formation of Au Nps of size ≥ 5 nm was observed with the three types of MOFs. Considering that gold nanoparticles are active for a size less than 5 nm, no catalytic acivity was expected for these composite materials, though, some tests were done.

VI Catalysis

The catalytic abilities of non-calcined and some partially calcined composite materials were assessed through three different reactions. Glucose conversion (in water), benzyl alcohol selective oxidation (in toluene) and furfural oxidative esterification (in methanol). All reactions were performed in oxidative conditions, in order to evaluate the role of tGNCs and that of the MOF support.

(MG) and **(MG_{200})** were tested for sugars conversion (glucose and fructose) and for selective benzyl alcohol oxidation. No or weak activity was observed, as expected. To test the composites calcined at higher temperatures, it was necessary to move to UiO-66 and

ZIF-8 based composite materials. For that **(UG)**, **(UG_{300})**, **(ZG)** and **(ZG_{300})** were chosen to be tested for furfural oxidative esterification, in base free conditions to be sure that the MOFs will not decompose.

VI.1. **Sugar oxidation**

(MG) and **(MG_{200})** were tested for the reactivity of glucose and fructose in H_2O at 140 °C under O_2 **Scheme 4-1** and **Scheme 4-2**, to check wether the obtained gold nanoparticles are active, and wether the activity obtained by using only MIL-101 (described in **chapter 3**) will be modified. For both conversions, **(MG)** and **(MG_{200})** showed comparable results as those obtained with MIL-101 alone. Below, the results only after using **(MG_{200})** catalyst are presented.

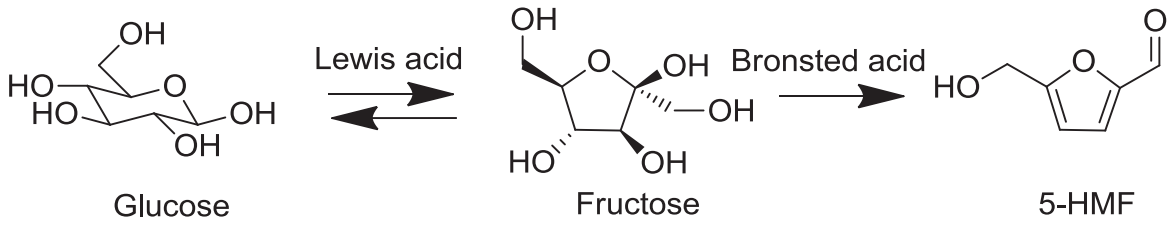

Scheme 4-1 Glucose conversion using (MG_{200}).

Under oxidative conditions and at 140 °C, 12 % of glucose were converted into fructose (3 %) and 5-HMF (9 %) without a catalyst. In the presence of **(MG_{200})**, the conversion of glucose increased to 58 %, producing fructose (18 %) and 5-HMF (10 %) **Figure 4-26**. Traces (<2 %) of formic acid, acetic acid and lactic acid were detected, but no gluconic acid, as we could expect due to the presence of Au. Consequently, the composite was only able to isomerize glucose into fructose, originating from the catalytic activity of the MOFs, as shown previously in chapter 3.

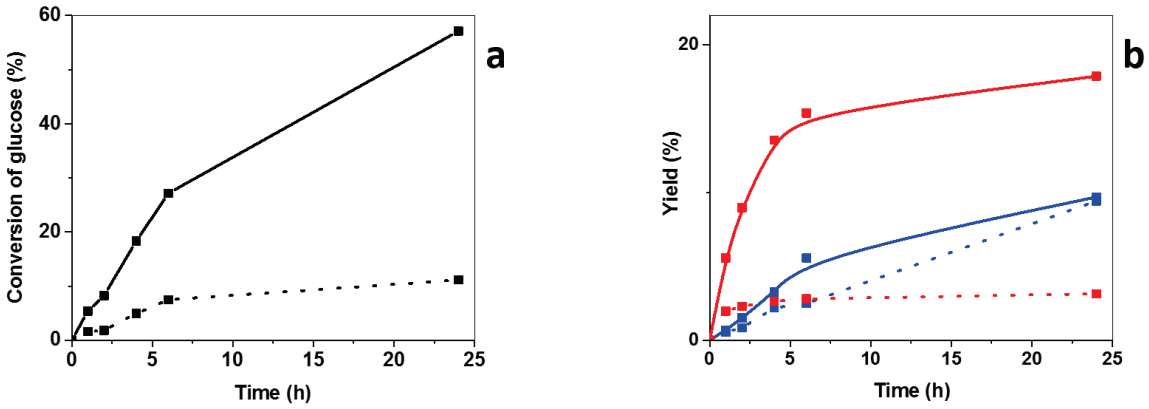

Figure 4-26 (a) presents the conversion of glucose (black) with and without catalyst at 140 °C. (b) presents the yields of fructose (red) and 5-HMF (blue) obtained with and without catalyst at 140°C. Dotted lines (no catalyst), solid lines (with catalyst).

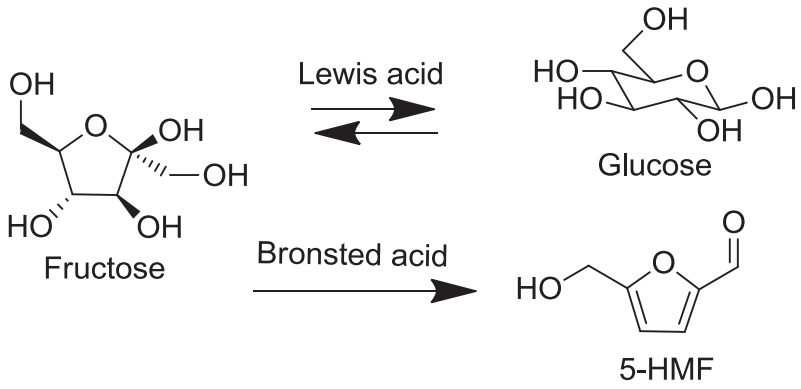

Scheme 4-2 Fructose conversion using **(MG_{200})**.

The reverse reaction was also assessed starting with fructose. At 140 °C, 65 % of fructose were converted into glucose (0.9 %) and 5-HMF (12 %) without a catalyst, while with **(MG_{200}),** the conversion of fructose increased into 76 %, producing glucose (7 %) and 5-HMF (14 %) **Figure 4-27**. Traces (< 2 %) of formic acid, acetic acid and lactic acid were detected.

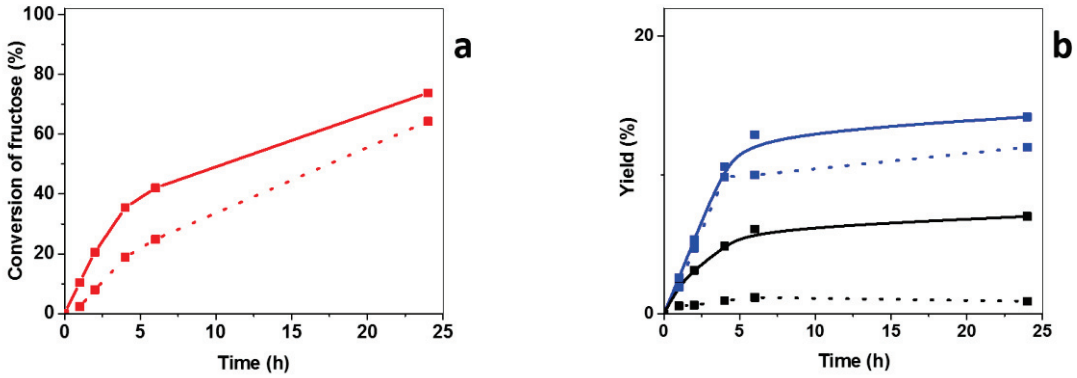

Figure 4-27 (a) presents the conversion of fructose (red) with and without catalyst at 140 °C. (b) presents the yields of glucose (black) and 5-HMF (blue) obtained with and without catalyst at 140 °C. Dotted lines (no catalyst), solid lines (with catalyst).

This means that similar behavior for the conversion of glucose and fructose were observed using **(MG_{200})** when compared to the activity of MIL-101 alone, described in **chapter 3**. No oxidation reaction took place, only isomerization with some production of 5-HMF (certainly produced due to temperature only) occurred due to the presence of Lewis acid sites. So, gold nanoparticles had no activity in such reactions. Therefore, we tested the activity of **(MG)** and **(MG_{200})** on benzyl alcohol oxidation, a probably less demanding reaction.

VI.2. Benzyl alcohol oxidation

Benzyl alcohol (BnOH) oxidation toward benzaldehyde (Bnald) **Scheme 4-3**, was a reaction previously used in our group to test the activity of $Au_{25}(ATP)_{18}$ supported over SBA-15. The fully defunctionalized clusters showed full conversion of benzyl alcohol into benzaldehyde in toluene at 80 °C with a base (Cs_2CO_3) and under atmospheric conditions [140]. The same conditions were applied using **(MG)** and **(MG_{200}).**

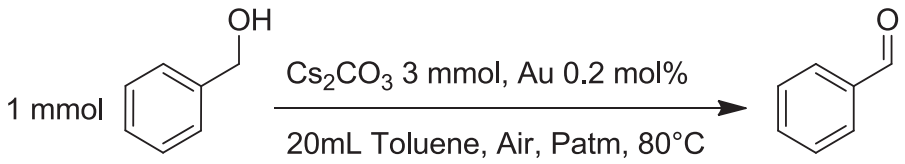

Scheme 4-3 Benzyl alcohol oxidation.

The non-calcined composite material **(MG)** possessed no activity, no conversion of

benzyl alcohol and no products appeared. The partially calcined one **(MG$_{200}$)** showed weak activity, 6 % conversion of benzyl alcohol with 100 % selectivity toward benzaldehyde **Figure 4-28**. This aroused the following hypotheses: (i) despite an existing activity, the supported tGNCs should be calcined at higher temperature to be clearly active, which is not possible with MIL-101 being the support and (ii) the MIL-101 is not a good support because it causes the sintering of the clusters and the formation of big gold nanoparticles that are not anymore active in oxidation reactions.

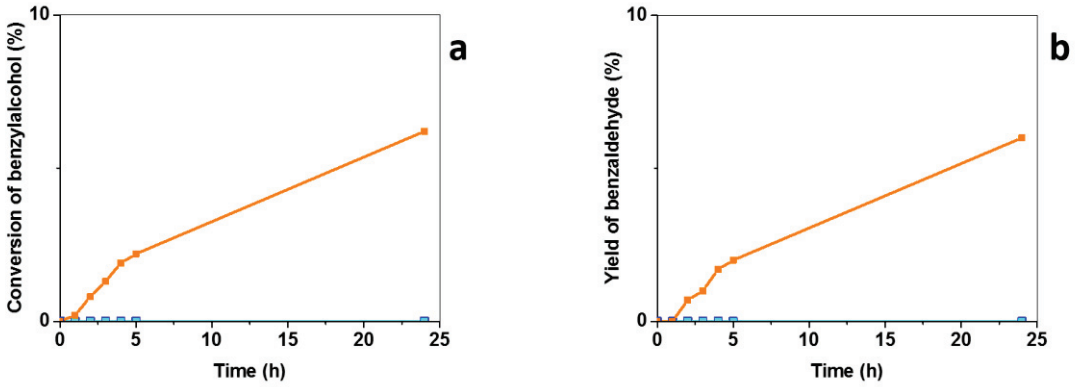

Figure 4-28 (a) presents the conversion of BnOH and (b) presents the yield of benzaldehyde. No catalyst (blue), using **(MG)** (aqua) and using **(MG$_{200}$)** (orange).

For further studies, the composites based on UiO-66 and ZIF-8 supports, calcined at 300 °C for 12 h under air were tested for furfural oxidative esterification.

VI.3. **Furfural oxidative esterification**

This reaction (**Scheme 4-4**) was tested using **(UG)**, **(ZG)**, **(UG$_{300}$)** and **(ZG$_{300}$)** in methanol (see **chapter 2** for the detailed conditions). The non-calcined **(UG)** and **(ZG)**, in addition to the partially calcined ones at 300 °C/ 10 °C.min^{-1} for only 4 h , showed no activity. **(ZG$_{300}$)** also after being calcined for 12h was also not active. The only active composite material was **(UG$_{300}$)** calcined at 300 °C/ 10 °C.min^{-1} for 12 h and having gold particles size of 5.9 nm ± 2 nm.

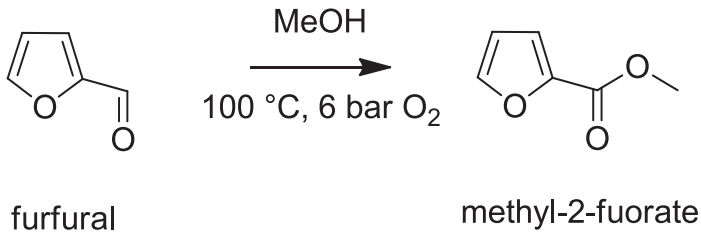

Scheme 4-4 Oxidative esterification of furfural into methyl-2-furoate.

Figure 4-29 a shows that furfural conversion reached approximately completition (67 %) after 46 h using **(UG_{300})**, accompanied with the production of 2-(dimethoxymethyl) furan (30.6 %) and methyl-2-furoate (6.5 %) under base free conditions. The formation of 2-(dimethoxymethyl) furan dominated over oxidative esterification (the latter is due to the activity of gold nanoparticles). The activity of the composite material using **(UG_{300})** differed from that of UiO-66 which under the same conditions resulted in 75 % conversion of furfural into 2-(dimethoxymethyl) furan (100 % selectivity) **Figure 3-25**. This means that the presence of gold affected the properties of UiO-66 and the kinetics toward the 2-(dimethoxymethyl) furan formation. In **Figure 4-29 b**, under base conditions, **(UG_{300})** resulted in 100 % conversion of furfural after 46 h, with 97 % yield of methyl-2-furoate and 3 % of 2-(dimethoxymethyl) furan. This means that Na2CO3 suppressed the acetal production and so enhanced the selectivity toward methyl-2-furoate.

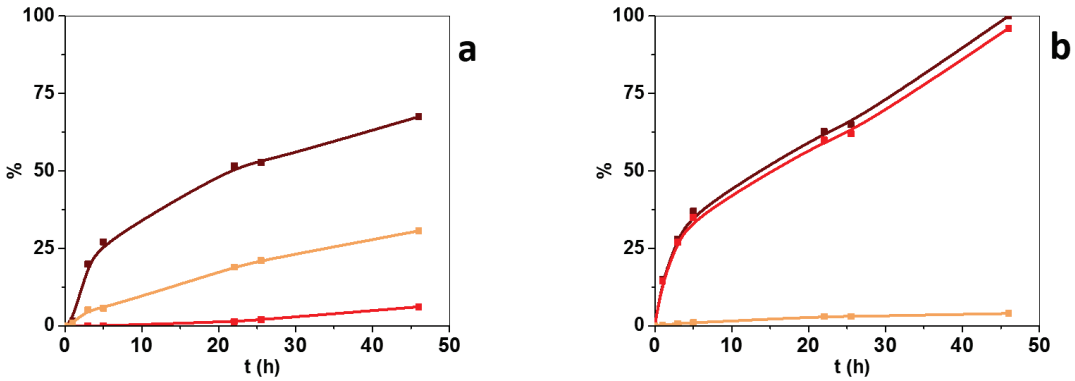

Figure 4-29 (a) presents the conversion of furfural (wine) and yields of methyl-2-furoate (red) and 2-(dimethoxymethyl) furan (orange) using **(UG_{300})** under base free conditions. (b) presents the same transformation using Na_2CO_3 as base.

The observation using a base aligns with a previous report [234], where Au/UiO-66 of

Au Nps size ≤ 5 nm, produced hemi acetal as an intermediate for the production of methyl-2-furoate, whereas the acetal was a byproduct.

Unfortunately, **(UG_{300})** was not tested for several cycles because the support (UiO-66) was not stable after being tested under basic conditions. Following the catalytic test, the PXRD of the collected catalyst showed that the support (UiO-66) was transformed into a new product having mixed crystalline and amorphous phases **Figure 4-30**.

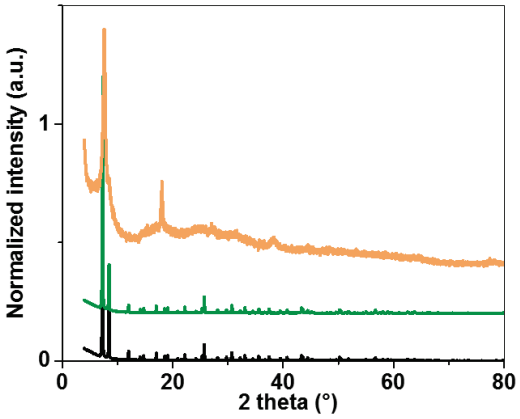

Figure 4-30 PXRD patterns of UiO-66 (black), UG300 (green) and collected catalyst after furfural transformation using a base (orange).

VII Conclusion

The first composite materials coupling MOFs and thiolate gold clusters are reported and fully characterized. Nevertheless, the studies showed that upon calcination of the composite materials, in order to remove the thiolate ligands, the clusters grew and sintered for the three types of MOFs. Despite the growth, **(UG_{300})** showed activity in the oxidative esterification of furfural toward methyl-2-furoate under base conditions.

To test separately the activity of $Au_{25}(SR)_{18}$, it was decided to move to a more classical and stable support, chemically and thermally stable, certainly more suitable to defunctionalize clusters. ZrO_2 was chosen as a support for $Au_{25}(SG)_{18}$. The next chapter describes the synthesis and catalytic activities of non-calcined and calcined $Au_{25}(SG)_{18}@ZrO_2$. Its catalytic application will be determined through benzyl alcohol oxidation and furfural oxidative esterification.

Chapter 5

Thermal control of the defunctionalization of Au_{25}(SG:Glutathione)$_{18}$ supported over zirconia catalysts for oxidation reactions

I. Introduction

$Au_{25}(SR)_{18}$ thiolate-protected gold nanoclusters, being promising materials for catalysis, have been supported on different types of MOFs to assess the synergy between both counterparts in catalysis (**chapter 4)**. $Au_{25}(SG)_{18}$@UiO-66 calcined at 300 °C for 4 h showed synergy in furfural oxidative esterification, but with sintering of the clusters resulting in 4.8 nm ± 2.4 nm Au Nps. For that reason, we chose to support the tGNCs on more conventional support, ZrO_2 (zirconia). The interest in using ZrO_2 comes from its high physical and chemical stability, along with its ability to form nanoparticles for high dispersion of the gold nanoclusters. Such approach made the controlled partial and total thermal defunctionalization of tGNCs within $Au_{25}(SG)_{18}$@ZrO_2 possible, along with studying the defunctionalization effect of the catalyst on the activity and selectivity in heterogeneously catalyzed reactions.

In this chapter, a brief literature overview highlighting the use of Au Nps supported on ZrO_2 for the oxidation of benzyl alcohol and furfural is described. The synthesis of new $Au_{25}(SG)_{18}$@ZrO_2 composite material is discussed, then the controlled thermal defunctionalization produces partial and total defunctionalized composites. The importance of the calcination temperature on catalytic activity is described. Benzyl alcohol oxidation toward benzaldehyde and the parameters influencing the progression of the oxidative transformation of furfural in methanol were investigated.

II Literature overview

ZrO_2, TiO_2 and CeO_2 are known as good supports for Au Nps, possessing all amphoteric properties (acid-base properties). Au Nps@ZrO_2 presented below (parts II.1 and II.2), Au Nps@TiO_2 [244, 245] and Au Nps@CeO_2 [246] have been active in alcohols oxidation. An interesting report concerning the comparison of the behavior of Au Nps supported over ZrO_2, TiO_2 or CeO_2 for furfural oxidation, showed the effectiveness of ZrO_2 at the level of Au dispersion and catalytic activity, which dominated over TiO_2 and CeO_2 supports (described below in part II.2).

In **chapter 1**, the uses of $Au_{25}(SR)_{18}$@TiO_2 and $Au_{25}(SR)_{18}$@CeO_2 for styrene and CO oxidation reactions are cited. $Au_{25}(SR)_{18}$@ZrO_2 composite material has never been synthesized before this work. Therefore, based on all these facts, we decided to valorize for the first time the activity of $Au_{25}(SR)_{18}$@ZrO_2 catalyst for benzyl alcohol and furfural transformations.

II.1. Au@ZrO_2 catalysts for benzyl alcohol oxidative dehydrogenation and oxidative esterification

The valorization of benzyl alcohol, a biogenic source produced mainly by fruits and flowers, is of high importance. One route in its selective oxidation results in benzaldehyde, a valuable product in pharmaceuticals, agro-chemistry and fragrance industries. Another route results in alkyl benzoates. Some examples are cited in the literature for Au nanoparticles@ZrO_2 systems dealing with such transformations and have been highlighted below. Some reports targeted benzaldehyde, while others targeted alkyl benzoates, in both cases starting from benzyl alcohol **Scheme 5-1**.

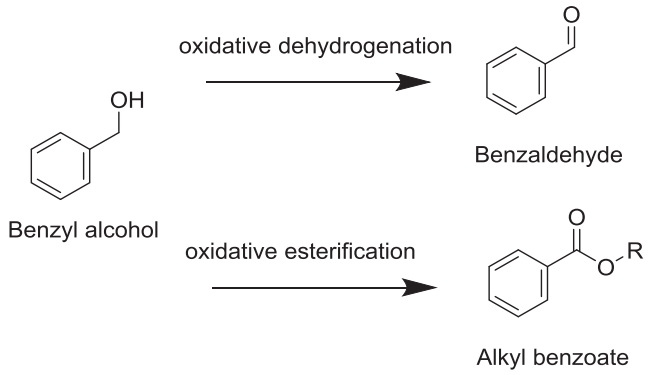

Scheme 5-1 Benzyl alcohol oxidative dehydrogenation and oxidative esterification.

Table 5-1 summarizes the characteristics of different Au@ZrO_2 catalysts, used for benzyl alcohol oxidation toward benzaldehyde or alkyl benzoate. The reaction conditions with the corresponding conversion and yield are mentioned too.

Wei et al. described the activity of Au@ZrO_2 in benzyl alcohol esterification, under ambient temperature and pressure conditions, using Cs_2CO_3 as a base. The synthesis was done by mixing ZrO_2 with $HAuCl_4$ precursor in water, followed by $NaBH_4$ reduction and HCl addition for precipitation, resulting in Au particles over ZrO_2 having a size between 4-7 nm. The drawbacks were leaching and sintering after the catalytic test. They assessed other supports too, TiO_2 and CeO_2, with the latter being of same efficiency as ZrO_2 but also undergoing leaching and sintering [247] (entry 1). Comparable results were reported by Cui et al. who did the same catalyst synthesis and catalytic test with similar reaction conditions, but no recyclability tests were done [248] (entry 2). Choudhary et al. reported homogeneous deposition-precipitation synthetic method for Au@ZrO_2 catalyst, using urea as precipitating agent. Calcination was done under air at 400 °C, resulting in 4.5 nm average Au particles size. Tert-butyl hydrogen peroxide was used as oxidizing agent of benzyl alcohol at 95 °C in solvent free conditions, but the catalyst was not selective. Both products, benzaldehyde and benzyl benzoate were observed [249] (entry 3). The same catalyst with O_2 as oxidizing agent showed 100 % selectivity to benzaldehyde but with uncomplete conversion [250] (entry 4). Therefore, the dispersion of Au and its average particle size depends on the synthetic method (precipitating agent, reducing agent, calcination temperature etc.). The support itself also determines the nature of gold species deposited, Au(0), Au(I) or Au(III), which controls the catalytic activities [250].

As already discussed in **chapter 1,** $Au_{25}(SR)_{18}$ tGNCs, for benzyl alcohol oxidation, should be defunctionalized to be active, in order to generate $Au^{\delta+}$ or $Au^{(0)}$ species. The presence of a base is also a nessecity, thus the reaction is able to provide high selectivity under ambient conditions of temperature and pressure. If benzaldehyde is targeted, alcohols should not be the reaction medium, toluene is be a better substituent [140].

Table 5-1 Different Au@ZrO_2 catalysts for benzyl alcohol selective oxidation to benzaldehyde **(entry 4)**, and for benzyl alcohol oxidative esterification to methyl-2-benzoate **(entries 1 and 2)** and to benzyl-2-benzoate **(entry 3)**.

Entry	Au (%)	Au average size (nm)	n BnOH (mmol)	n Au (µmol)	Base: n base (mmol)	Solvent: v (ml)	Atmosphere	T (°C)	t (h)	BnOH conversion (%)	Bnald yield (%)	Ester: yield (%)	Reference
1	2.1	4-7	2	3.8	Cs_2CO_3:0.2	MeOH:5	ambient	25	6	100	-	99	[247]
2	2.7	2-7	0.5	5.5	KOH:0.5	MeOH:10	ambient	30	24	95	-	95	[248]
3	0.3	4.5	52	7.6	-	-	TBHP	95	2	59.5	48.5	11	[249]
4	3	4.5	29	15.2	-	-	O_2	130	5	50.6	44	-	[250]

II.2. Au@ZrO_2 catalysts for furfural oxidative esterification

The valorization of furfural, a chemical produced at industrial scale from biomass, is of increasing importance in the development of the bio-based economy. The oxidative esterification of furfural to alkyl-2-furoates **Scheme 5-2** is a valorization route giving compounds finding applications in the fine chemical industry as flavors or flagrance.

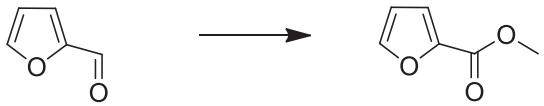

Scheme 5-2 Oxidative esterification of furfural into methyl-2-furoate.

Table 5-2 summarizes different catalysts characteristics, reaction conditions with the conversion and yield results for furfural oxidative esterifications.

Signoretto and Manzoli and co. have been very active in the furfural oxidative esterification [251-256]. They studied the gold nanosize effect on furfural conversion. Au was added by deposition-precipitation method using NaOH, then calcined at different temperatures ranginging between 180 °C and 600 °C. Calcination at 180 °C resulted in 1.68 ± 0.38 nm Au particles size, whereas sintering occurred after calcination at 600 °C resulting in 4.49 ± 1.35 nm particles. Best catalytic activity was recorded for Au@ZrO_2 calcined at 180 °C (entry 2), whereas for the one calcined at 600 °C, only 40 % of furfural conversion in methyl-2-furoate with the acetal being a byproduct was observed [253]. They particularly noticed the superiority at the level of activity, selectivity and stability for ZrO_2 as support for Au Nps compared to CeO_2 and TiO_2. This good activity is due to the high molar ratio of surface Au that are able to activate molecular oxygen, in addition to the best Au dispersion in the case of ZrO_2 that enhanced the conversion of furfural [254].

Table 5-2 Different Au@ZrO_2 catalysts for furfural oxidative esterification to Methy-2-furoate (MF).

Entry	Au (%)	Au average size (nm)	n Furfural (mmol)	n Au (µmol)	Base	Solvent: v (ml)	Atmosphere: Pressure (bar)	T (°C)	t (h)	Furfural conversion (%)	MF yield (%)	Reference
1	1.5	2.7	38	7.6	-	MeOH: 150	O_2:6	120	3	100	98	[251]
2	1.5	1.68	38	7.6	-	MeOH: 150	O_2:6	120	1.5	98	98	[253]
3	1	2.3	38	5	-	MeOH: 150	O_2:6	120	1.5	82	75.5	[254]

III $Au_{25}(SG)_{18}@ZrO_2$ composite materials

III.1. Synthesis

$Au_{25}(SG)_{18}$ synthesis and ZrO_2 preparation were described in **chapter 2**. $Au_{25}(SG)_{18}$ characterizations were described in **chapter 4**. ZrO_2 has ~ 50 nm particle size.

$Au_{25}(SG)_{18}$ cluster deposition was performed using a wet impregnation method. Gold clusters, with a mass of 10 mg corresponding to a theoretical loading of 1 wt % Au, and 500 mg of support (ZrO_2 nanoparticles) were dispersed in 5 ml of water, swirled, and left for 15 min. The prepared catalyst $Au_{25}(SG)_{18}@ZrO_2$ (ZrG) was recovered by centrifugation (4000 rpm, 10 min) after the addition of small amounts of ethanol, and was followed by drying under air.

Calcination was performed on **(ZrG)**. Around 100 mg of compounds were heated under air at 200 °C for 4 h, 300 °C for 4 h and 400 °C for 12 h at a rate of 2 °C/min, resulting in **(ZrG_{200})**, **(ZrG_{300})** and **(ZrG_{400})** respectively.

III.2. Catalyst characterization

III.2.1. Powder X-ray diffraction

The powder X-ray diffraction pattern of of ZrO_2 indicated the presence of two crystallographic phases, monoclinic and tetragonal **Figure 5-1**, the monoclinic being the dominant one as usual.

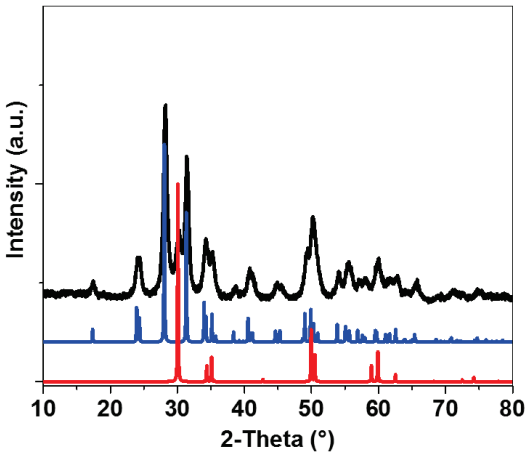

Figure 5-1 Powder X Ray diffraction patterns of synthesized ZrO_2 (black) and simulated monoclinic (blue) and tetragonal (red) phases of ZrO_2.

The composite material $Au_{25}(SG)_{18}@ZrO_2$ (0.7 % Au), before and after being calcined at different temperatures (200, 300 and 400 °C) to gradually remove the ligands, induced a change in color from beige for $Au_{25}(SG)_{18}@ZrO_2$ to pink for the calcined samples. Nevertheless, the PXRD patterns of the obtained materials showed no change from the ZrO_2 diagrams and no indication of reflection of bulk gold **Figure 5-2**.

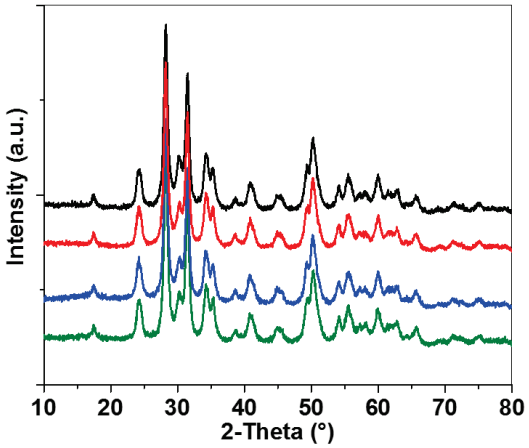

Figure 5-2 Powder X Ray diffraction patterns of $Au_{25}(SG)_{18}@ZrO_2$ after calcination at 400 °C for 12 h under air (red), calcination at 300 °C for 4 h under air (blue), calcination at 200 °C for 4 h under air (green), and ZrO_2 support alone (black).

These observations mean that there is no modification of the support and that the

quantity of gold is too low to be detected.

III.2.2. Thermogravimetric analysis for the thermal control of the defunctionalization

Thermal studies of the materials were done by thermogravimetric analysis (TGA) under air on pure $Au_{25}(SG)_{18}$ gold clusters, gold clusters deposited on ZrO_2 and ZrO_2 alone. Studies in (chapter 4) **Figure 4-14**, shows that 17.0 %, 40.0 % and 53 % of the total weight of $Au_{25}(SG)_{18}$ were lost, corresponding to 32.0 %, 75.0 % and 100 % of thiolate ligands after calcination at 200, 300 and 400 °C, respectively. It is interesting to note that the complete calcination of the ligands at 400 °C is reached after almost 8 h of heating, suggesting that a heating ramp of at least 8 hours is required to completely remove the glutathione molecules from the gold surface.

For the TGA of the ZrO_2 support, 2.5 % weight loss was observed at low temperature that corresponds to water traces. After the deposition of 1 wt % Au using $Au_{25}(SG)_{18}$ on ZrO_2, a first weight loss of 2.4 % was observed and a second weight loss of 1.5 % from 250 °C was also seen and fitted well with the decomposition of the glutathione molecules **Figure 5-3**.

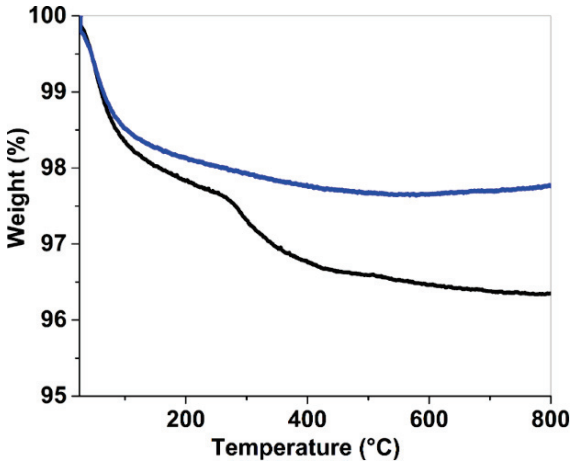

Figure 5-3 TGA experiments on $Au_{25}(SG)_{18}$ deposited on ZrO_2 (black) and ZrO_2 alone (blue) carried out under air at 10 °C/min.

III.2.3. Transmission electron microscopy

TEM images showed that the ZrO_2 particles have a diameter of around 50 nm. This technique was also used to monitor the thiolate gold nanocluster size when impregnated,

before and after calcination **Figure 5-4**.

Sample **(ZrG)** exhibited homogeneous clusters of size 1.6 ± 0.3 nm **Figure 5-4** (**a,e)**, being close to the expected Au_{25} diameter estimated from the crystal structure (1 nm). For (ZrG_{200}) the mean particle size was 1.6 ± 0.7 nm and approximately the same for **(ZrG_{300})** at 1.7 ± 0.5 nm **Figure 5-4 (b,c,e)**. For **(ZrG_{400})**, the particle size increased to 2.0 ± 0.7 nm, which is due to the sintering Au_{25} gold cores **Figure 5-4 (d,e)**.

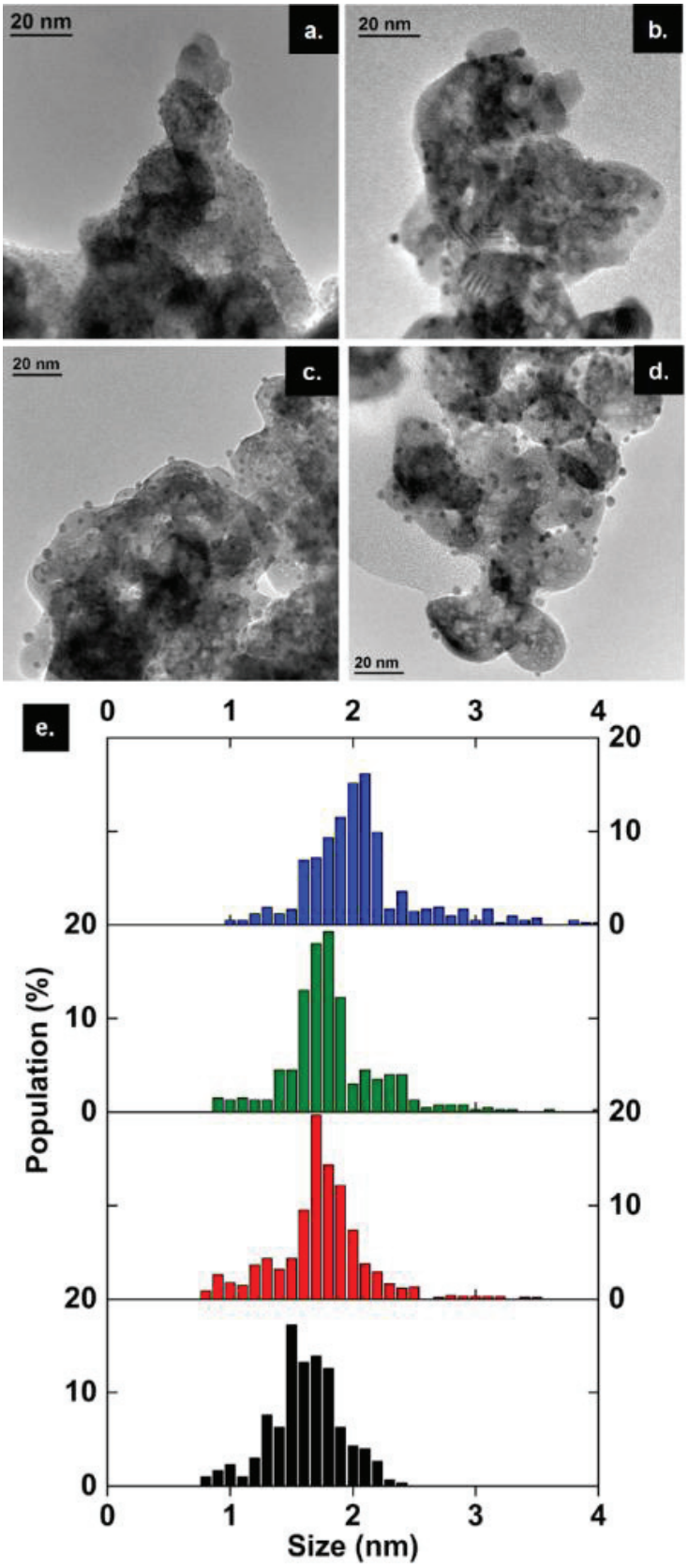

Figure 5-4 TEM images of $Au_{25}(SG)_{18}@ZrO_2$ (Au 0.7 wt %) (a) before calcination, sample **(ZrG)**, (b) calcined at 200 °C for 4 h under air, sample **(ZrG_{200})**, (c) calcined at 300 °C for 4 h under air, sample **(ZrG_{300})**, and (d) calcined at 400 °C for 12 h under air, sample **(ZrG_{400})**, and (e) the size distribution of the composites – **(ZrG)** in black, **(ZrG_{200})** in red, **(ZrG_{300})** in green and **(ZrG_{400})** in blue.

As mentioned in the **chapter 1**, supported gold thiolate clusters are known to grow when calcined at high temperature, except when they are inserted in a porous material, such as SBA-15, or loaded with a very small quantity of clusters. Here we note that the gold nanoparticles maintain a diameter of around 2 nm or below, with a narrow size distribution, upon calcination at temperatures up to 400 °C with 0.7 wt % of Au loading, even in a non porous support.

III.2.4. **XPS analysis**

Figure 5-5 shows the high resolution photoelectron spectra of $Au_{25}(SG)_{18}$ supported on ZrO_2 from Au_{4f}, before and after calcination at 200 °C, 300 °C and 400 °C. For **(ZrG)**, the $4f_{7/2}$ and $4f_{5/2}$ binding energies of gold were at 84.7 and 88.4 eV, respectively. The $4f_{7/2}$ peak location is very close to the published one for glutathione based $Au_{25}(SR)_{18}$, 84.8 eV [257]. These values indicate that gold has a δ+ state. The $4f_{7/2}$ and $4f_{5/2}$ binding energies of gold in the case of **(ZrG_{200})** were at 84.7 and 88.2 eV, very similar to the values before calcination. Following the calcination at 300 °C, the $4f_{7/2}$ and $4f_{5/2}$ binding energies of gold shifted to 84.0 and 87.7 eV, while after calcination at 400 °C, they have been equal to 83.9 and 87.6 eV, respectively. These values are very close to the $4f_{7/2}$ and $4f_{5/2}$ binding energies of Au(0). This means that after the remove of the thiolate ligands, the dominant oxidation state of gold was (0).

The N_{1s} and S_{2p} regions were also examined **Figure 5-6**. The peak of N_{1s} of **(ZrG)** at 399.7 eV is assigned to free amino groups or to (N-C) bonds, both mainly found in the glutathione ligand. After calcination at 200 °C, The peak was also detected, which means that glutathione parts having amino functionalities were still present. Moreover, in **(ZrG_{300})** and **(ZrG_{400})**, no peak related to the binding energy of N_{1s} was observed, indicating the absence of amino groups **Figure 5-6 (a)**. The S_{2p} binding energy was located at 163.4 eV in the case of **(ZrG)**, and is typical of thiolated ligands (from 163.2 to 163.4 eV) [257]**.** This is related to (Au-S) and showed that the sulfur atoms were not oxidized. This peak was of very weak intensity in **(ZrG_{200})** and absent in **(ZrG_{300})** and **(ZrG_{400})**, proving the bond cleavage between Au and S upon calcination **Figure 5-6 (b)**.

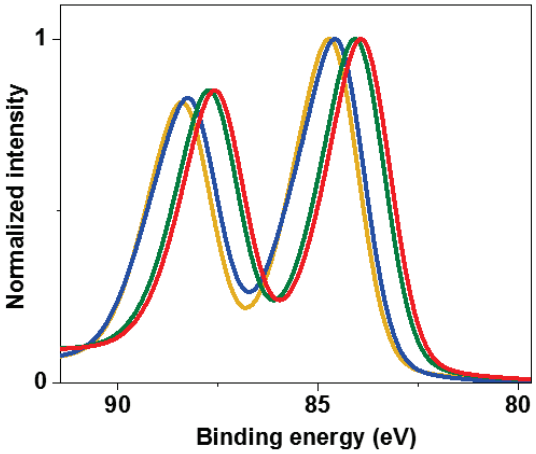

Figure 5-5 XPS analyses of $Au_{25}(SG)_{18}$ nanoclusters supported over ZrO_2 from Au_{4f}. Non-calcined **(ZrG)** (orange), **(ZrG_{200})** (blue), **(ZrG_{300})** (green) and **(ZrG_{400})** (red).

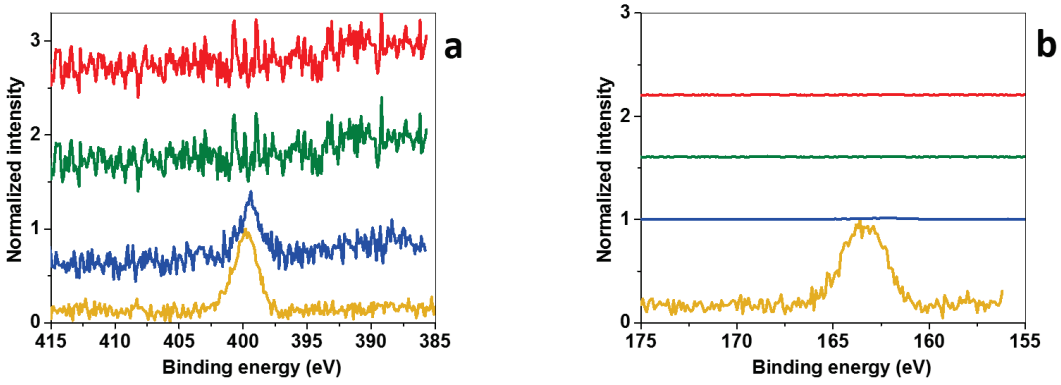

Figure 5-6 XPS analyses of $Au_{25}(SG)_{18}$ nanoclusters supported over ZrO_2 **(ZrG)** (orange), **(ZrG_{200})** (blue), **(ZrG_{300})** (green) and **(ZrG_{400})** (red). (a) from N_{1s} and (b) from S_{2p}.

IV Application of $Au_{25}(SG)_{18}$@ZrO_2 as catalyst for different oxidation reactions

IV.1. Benzyl alcohol oxidation reaction

The catalytic activity of $Au_{25}(SG)_{18}$@ZrO_2, calcined at different temperatures, was studied for the oxidative dehydrogenation of benzyl alcohol to benzaldehyde **Scheme 5-3**.

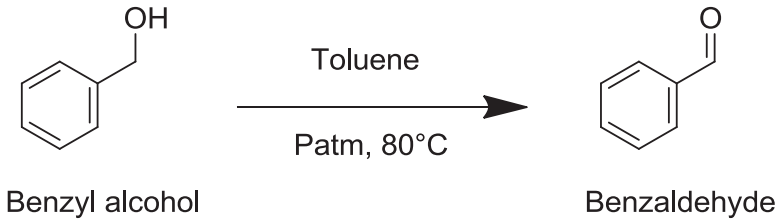

Scheme 5-3 Benzyl alcohol oxidative dehydrogenation under standard conditions.

IV.1.1. **Influence of the calcination temperature on the catalytic performance**

Before observing the influence of calcination of thiolates on the activity of the gold catalysts, a blank reaction, in addition to a reaction with the support alone were performed to confirm the catalytic activity of the gold catalyst. Since there was no benzyl alcohol conversion and no formation of benzaldehyde in both cases, it was deduced that the reaction conditions, such as temperature or atmospheric O_2 did not have any role in the oxidation reaction, in the absence of Au.

$Au_{25}(SG)_{18}@ZrO_2$ **(ZrG)** was inactive and unable to oxidize benzyl alcohol to benzaldehyde. Despite the well-dispersed, homogenously the small-sized gold particles, as seen from the TEM image **Figure 5-4 (a)** and the size distribution graph **Figure 5-4 (e)**, their catalytic activity was likely to be affected by the presence of the thiolate ligands. The same behavior was observed for the untreated $Au_{25}(SPhNH_2)_{17}$@SBA-15, which did not show any activity for benzyl alcohol oxidation [140]. For **(ZrG_{200})**, 64 % of the thiolate ligands remained, and benzyl alcohol conversion reached 50 % after 12 h with an initial turn over frequency (TOF) of 10 h^{-1}, which was very low compared to that of **(ZrG_{300})**. Indeed, the latter had 46 % of the thiolate ligands remaining and only 1.5 h were needed to reach 50 % conversion with a TOF = 261 h^{-1}, showing that the partial calcination had improved the catalyst activity. For **(ZrG_{400})**, for which no thiolate ligands remained, 2.4 h were needed to reach 50 % conversion with a TOF = 123 h^{-1} **Figure 5-7** and **Table 5-3**.

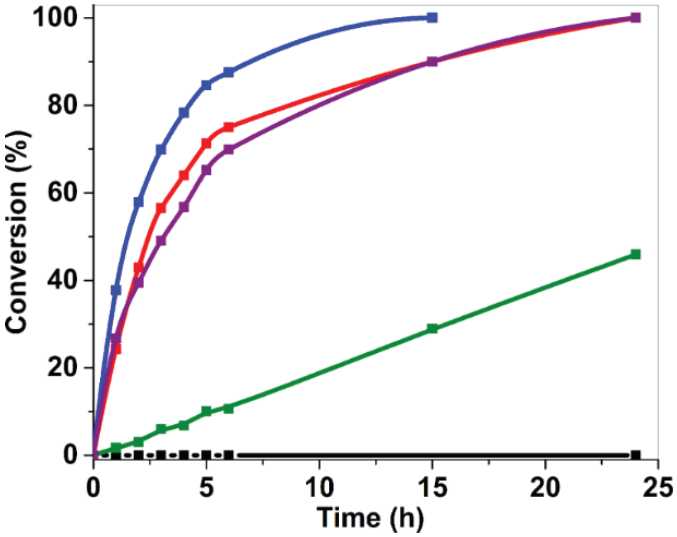

Figure 5-7 Monitoring over time of benzyl alcohol oxidative dehydrogenation conversion with $Au_{25}(SG)_{18}@ZrO_2$ before calcination (black), after calcination at 200 °C for 4 h under air, (ZrG_{200}) (green), at 300 °C for 4 h under air, (ZrG_{300}) (blue), at 400 °C for 12 h under air, (ZrG_{400}) (red) and compared to AuNP@ZrO_2 (purple).

Table 5-3 Catalytic performance of $Au_{25}(SG)_{18}@ZrO_2$ based catalysts (2 µmol Au) in the oxidative dehydrogenation of benzyl alcohol in toluene at 80 °C (1 atm of air): 25 %, 50 % and 90 % conversion times (t), benzaldehyde selectivity at half conversion (Sel 50 %), turn over frequency (TOF) and gold particle size measured by TEM before the catalytic test. ND: Not determined.

	Catalyst	$t_{25\%}$ (h)	$t_{50\%}$ (h)	$t_{90\%}$ (h)	$Sel_{50\%}$ (%)	TOF (h^{-1})	Average AuNPs diameter (nm)
(ZrG)	$Au_{25}(SG)_{18}@ZrO_2$	ND	ND	ND	ND	/	1.6 ± 0.3 nm
(ZrG_{200})	**(ZrG)** calcined at 200 °C	6	12	22	80	10	1.6 ± 0.7 nm
(ZrG_{300})	**(ZrG)** calcined at 300 °C	0.6	1.5	7	94	261	1.7 ± 0.5 nm
(ZrG_{400})	**(ZrG)** calcined at 400 °C	1	2.5	15	100	123	2 ± 0.7 nm
(R)	Au Nps@ZrO_2	1	3	15	100	144	2.7 ± 1.5 nm

The increase in catalytic activity from **(ZrG)** to **(ZrG_{200})** and the highest TOF (261 h^{-1}) in the case of **(ZrG_{300})**, is explained by the increase of defunctionalization of the supported thiolate clusters, which triggered the catalytic activity. However, the decrease in catalytic activity of **(ZrG_{400})**, with a lower TOF value (123 h^{-1}), though it was fully defunctionalized, is related to the sintering of the gold nanoparticles, where bigger 2.0 ± 0.7 nm particles were observed on the TEM images. This means that both the defunctionalization and the particle size affect the catalytic activity of the composite material. A balance between both is required to have maximum activity, as in **(ZrG_{300})** triggering gold activity and keeping small sized particles at 1.7± 0.5 nm. Therefore, partially calcined clusters did not inhibit high catalytic activity. In contrast, it was enhanced.

Concerning the selectivity at 50 % ($Sel_{50\%}$) conversion toward benzaldehyde, an increase with the increase of calcination temperature was observed for compound **(ZrG)**. The $Sel_{50\%}$ for **(ZrG_{200})** was 80 %, less than that of **(ZrG_{300})**, 94 %, which was also lower than the $Sel_{50\%}$ of **(ZrG_{400}),** 100 % **Table 5-3**. This means that having pure gold without any organic ligand is necessary to have high selectivity toward benzaldehyde, but still the partially calcined composite material **(ZrG_{300})**, with comparable selectivity of 94 %, to **(ZrG_{400})** resulted in the best activity with highest TOF = 261 h^{-1}.

(ZrG) catalytic performance was compared to a catalyst synthesized by the deposition-precipitation method of gold nanoparticles on ZrO_2 nanoparticles, compound **(R)**. The average particle size of **(R)**, measured by TEM images, was 2.7 ± 1.5 nm, higher than that of the gold particles obtained in **(ZrG_{400})** after full calcination **Figure 5-8**. Compound **(R)** showed 50 % conversion of benzyl alcohol in 3 h, a value close to that obtained with **(ZrG_{400})**, having slightly higher initial TOF (144 h^{-1}). They both reached 90 % conversion after 15 h. This showed that when gold nanoparticles have a diameter more than 2 nm, they act in a similar catalytic manner (Both **(ZrG_{400})** and **(R)** had $Sel_{50\%}$ equal to 100 %), but still have slower catalytic activity compared to the partially calcined composite material **(ZrG_{300}) Table 5-3**.

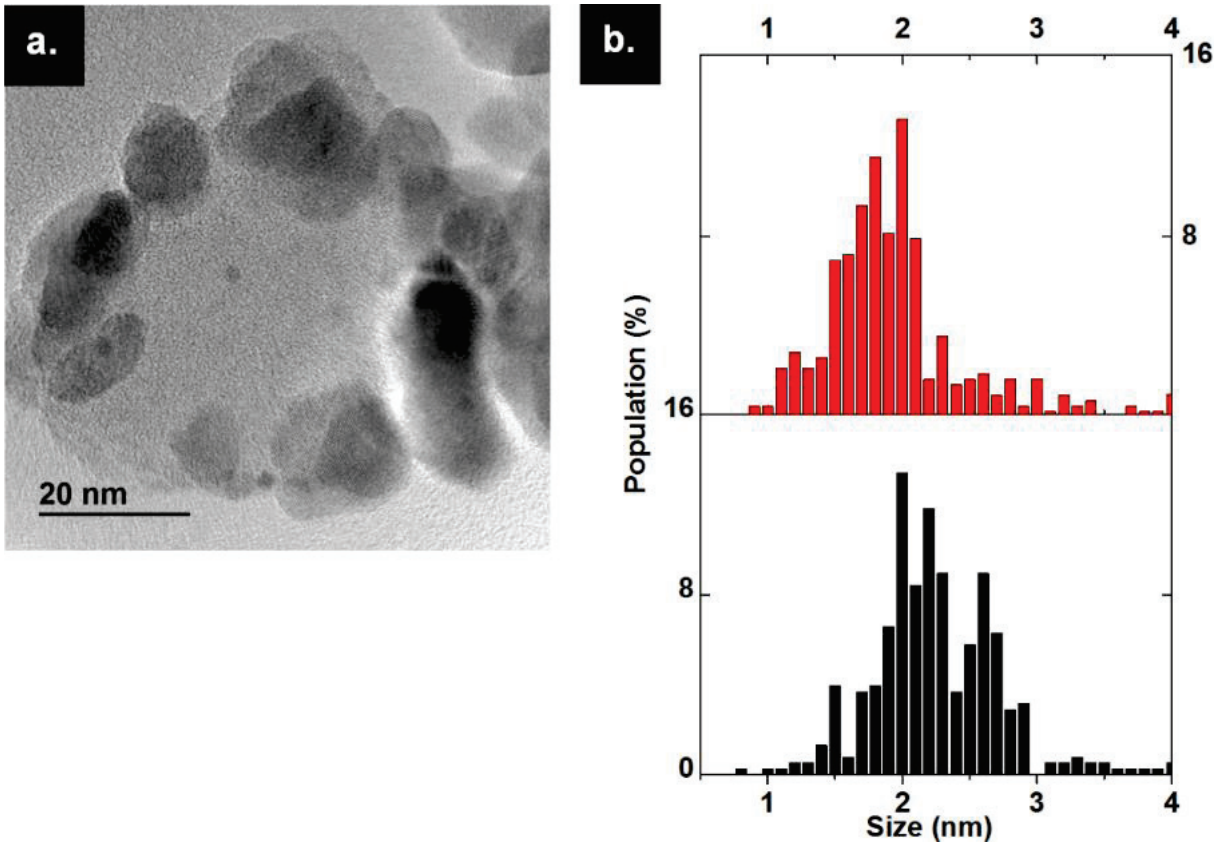

Figure 5-8 (a) TEM image of AuNps@ZrO_2 prepared by the deposition-precipitation method **(R)**. (b) Comparison of size distribution of $Au_{25}(SG)_{18}$@ZrO_2 calcined at 400 °C for 12 h under air **(ZrG_{400})** in red and AuNps@ZrO_2 **(R)** in black.

Compared to previously cited studies **(chapter 1)**, $Au_{25}(SC_{12}H_{25})_{18}$ supported on hierarchically porous carbon nanosheets and $Au_{25}(SPhNH_2)_{17}$ supported on SBA-15, both calcined at 400 °C, showed 67 % and 68 % of selectivity for benzaldehyde, respectively. Thus, the 100 % selectivity for benzaldehyde of $Au_{25}(SG)_{18}$ over ZrO_2 when calcined at 400 °C may result from the different compositions of the clusters or the effect of the type of support that can be involved in the oxidation mechanism or their different morphologies, as porous materials for the carbon nanosheets and silica, and nanoparticles for ZrO_2.

IV.1.2. **Influence of the reaction temperature on the catalytic performance**

In general, the oxidation of benzyl alcohol is performed under harsh conditions of temperature and pressure without a catalyst [258]. Gold-based catalysts perform this oxidation under milder conditions [259]. The reaction using **(ZrG_{300})**, was performed at two different temperatures, 60 °C and 80 °C, with all other experimental conditions being

the same. Such relatively low temperatures showed no thermal conversion of benzyl alcohol without catalyst. The conversion curves clearly showed that the increase of the temperature of 20 °C favors the benzyl alcohol conversion **Figure 5-9**. At 60 °C, the time necessary to reach 50 % conversion was 3 h, whereas it was 1.5 h at 80 °C. Besides, the $Sel_{50\%}$ increased from 75 % to 94 % with temperature, suggesting that the faster the reaction rate, the higher the benzaldehyde selectivity **Table 5-4**.

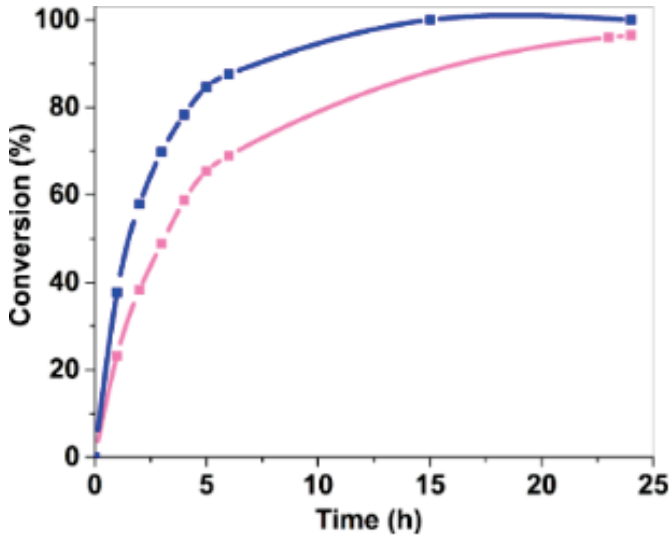

Figure 5-9 Monitoring over time of benzyl alcohol oxidative reaction with $Au_{25}(SG)_{18}@ZrO_2$ calcined at 300 °C for 4 h under air **(ZrG_{300})** at 60 °C (pink), and at 80 °C (blue).

Table 5-4 Catalytic performance of **(ZrG_{300})** catalyst (2 µmol Au) in the oxidative reaction of benzyl alcohol in toluene at 80 °C and 60 °C (1 atm of air): 25 %, 50 % and 90 % conversion time (*t*), benzaldehyde selectivity at half conversion ($Sel_{50\%}$) and turn over frequency (TOF).

	Reaction temperature (°C)	**$t_{25\%}$ (h)**	**$t_{50\%}$ (h)**	**$t_{90\%}$ (h)**	**$Sel_{50\%}$ (%)**	TOF (h^{-1})
(ZrG_{300})	80	0.6	1.5	6.8	94	261
(ZrG_{300})	60	1.2	3	16	75	101

IV.1.3. **Recyclability of the catalyst**

The recyclability of **(ZrG_{300})**, the catalyst that showed the highest TOF value in the

oxidative dehydrogenation of benzyl alcohol, was tested by adding a new portion of benzyl alcohol to the reaction mixture after each cycle. It was observed that after each run, the catalytic stability decreased, giving full conversion in the first cycle **$(ZrG_{300})^1$**, 87.0 % conversion in the second cycle **$(ZrG_{300})^2$** and 70.0 % in the third cycle **$(ZrG_{300})^3$**, after 24 h of reaction **Figure 5-10**. This decrease in the catalytic activity is explained by particle aggregation and sintering with time. The particle size after the third cycle in **$(ZrG_{300})^3$** was 2.8 ± 0.8 nm **Figure 5-11**. No Au was detected in the liquid mixture at the end of the three cycles.

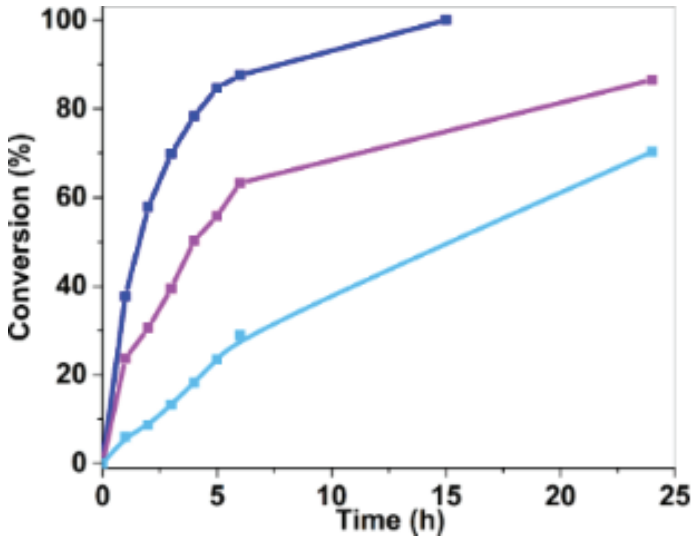

Figure 5-10 Monitoring over time of benzyl alcohol oxidative dehydrogenation conversion for successive additions of 1 mmol BnOH in the reaction medium (each reaction was carried out during 24 h) using **(ZrG_{300})** as a catalyst. **$(ZrG_{300})^1$** represents the conversion (%) while using the catalyst for the first cycle (blue), **$(ZrG_{300})^2$** for the second cycle (pink) and **$(ZrG_{300})^3$** for the third cycle (cyan).

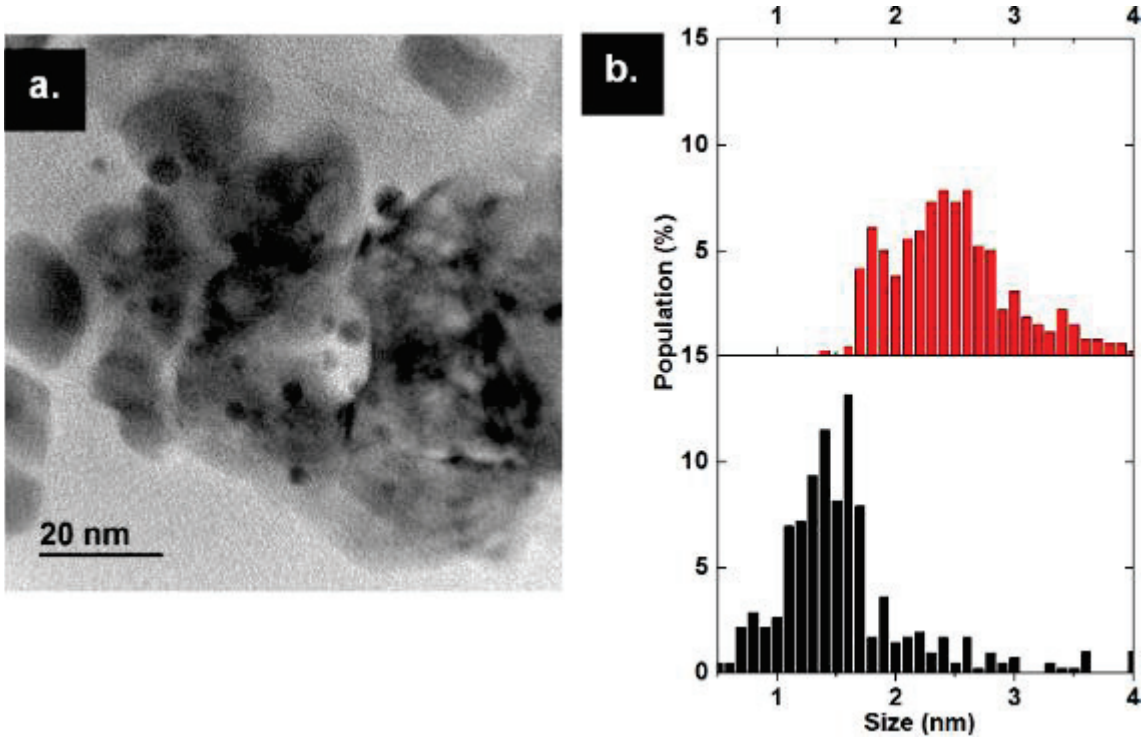

Figure 5-11 (a) TEM image of **$(ZrG_{300})^3$** after the third catalytic cycle. (b) Comparison of the size distribution of **$(ZrG_{300})^3$** in red and **(ZrG_{300})** before the catalytic test in black.

IV.2. **Furfural oxidative esterification reaction**

IV.2.1. **Catalytic protocol**

The catalytic activity of $Au_{25}(SG)_{18}@ZrO_2$, non-calcined and calcined at different temperatures, was studied in a different type of reaction, the oxidative esterification of furfural into methyl-2-furoate **Scheme 5-4**.

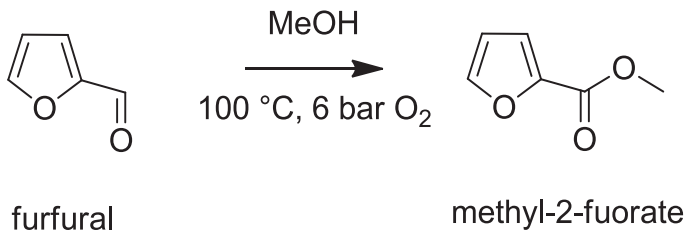

Scheme 5-4 Oxidative esterification of furfural into methyl-2-furoate.

IV.2.2. **Influence of the amount of Au**

The influence of the amount of Au was assessed by performing the reaction in the presence of 0.5 µmol and 1 µmol of Au in the absence of a base. With 0.5 µmol, the overall transformation was accomplished after 5 h, while it needed 4 h when 1 µmol was used

Figure 5-12. Therefore, the amount of Au had limited influence at the total rate of the reaction. 1 µmol of Au was chosen for gold amount for next reactions.

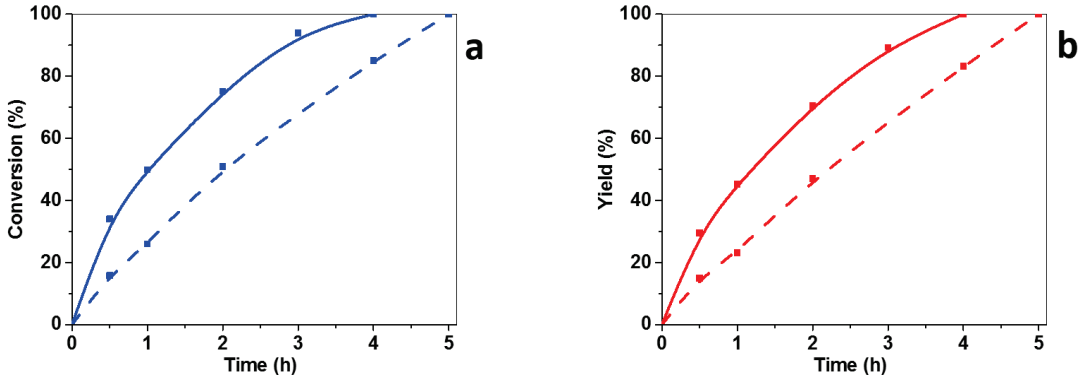

Figure 5-12 (a) Conversion of furfural and (b) yield of methyl-2-furoate with 0.5 µmol of Au (dashed line) and with 1 µmol of Au (line).

IV.2.3. **Influence of O_2**

Furfural oxidative esterification was performed in the absence of base (Na_2CO_3), with O_2 pressure (6 bar) and without O_2 pressure (reaction was performed under ambient air) to assess the influence of O_2 on the transformation. 100 % selectivity was observed with or without O_2, but for the latter, the conversion was limited to 55 % even after running the reaction over 24 h. This means that ambient air pressure is not sufficient and O_2 pressure is essential for complete conversion in 4 h **Figure 5-13**.

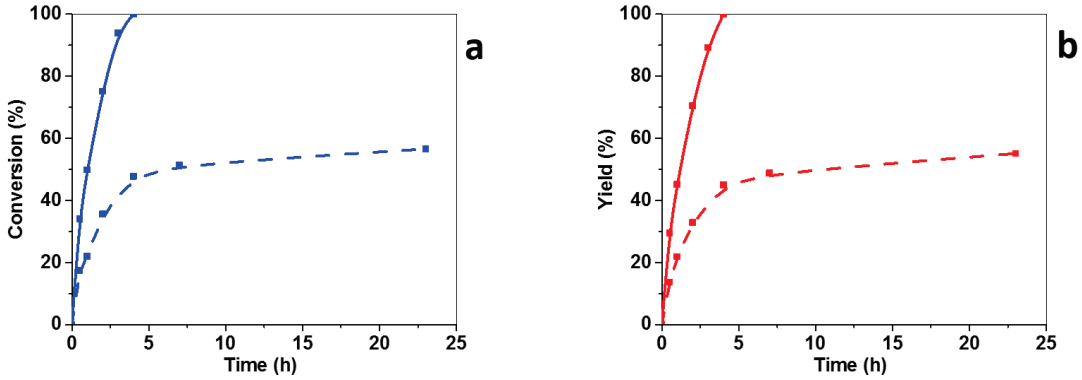

Figure 5-13 (a) Conversion of furfural and (b) yield of methyl-2-furoate with O_2 (line) and without O_2 (dashed line).

IV.2.4. **Influence of a base**

In the following part, 1 µmol Au and O_2 (6 bars) pressure were used. The presence and absence of a base (Na_2CO_3) was evaluated. Without a base, the conversion was complete after 4 h with 100 % selectivity toward methyl-2-furoate (TOF = 210 h^{-1}). A base allowed a slightly faster reaction and product formation was complete after 3h (TOF = 361 h^{-1}) **Figure 5-14**.

The results obtained here are completely in line with those reported in the literature with other Au/ZrO_2 [253, 256], or more recently Au/UiO-66 [260] and Au/CMK-3 [261] catalysts, in similar conditions, particularly involving less that 1 wt% Au/furfural and most of the time in the absence of base.

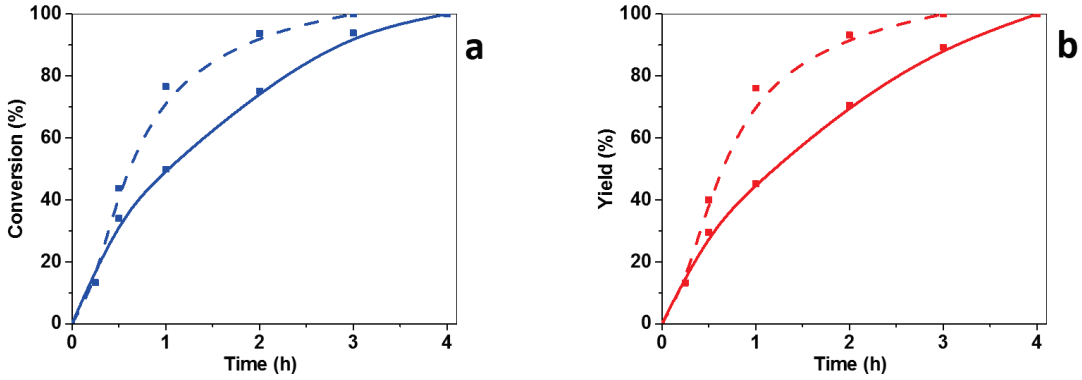

Figure 5-14 (a) Conversion of furfural and (b) yield of methyl-2-furoate without base (line) and with Na_2CO_3 75mg (0.33 mol equiv./furfural) (dashed line), using **(ZrG_{400})**.

IV.2.5. **Influence of the calcination temperature on catalytic performance**

The previously described reactions were realized after calcination of the nanocomposite catalyst at 400 °C allowing complete SG ligands removing [262]. When the reaction was performed with a material calcined at 300 °C [262], similar results were obtained with or without a base **Figure 5-15**, compared to **Figure 5-14.**

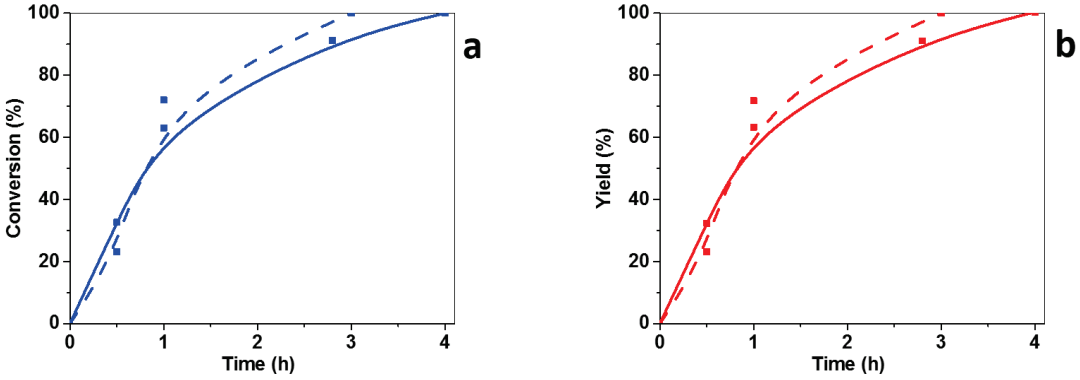

Figure 5-15 (a) Conversion of furfural and (b) yield of methyl-2-furoate without base (line) and with Na_2CO_3 75 mg (0.33 mol equiv./furfural) (dashed line), **using (ZrG_{300})**.

Based on what preceeded, total calcination is not a condition for complete conversion of furfural into methyl-2-furoate, and Au size showed limited effect on this transformation. As long as Au is active and able to activate O_2, furfural oxidative esterification works successfully [253, 255]. This results are in contrast with what we observed previously for benzyl alcohol oxidation, where partially calcined with smaller Au particles size catalyst**, (ZrG_{300})**, was the best catalyst.

For the partially calcined catalyst at 200 °C (64 % of ligand on the Au clusters), no activity was observed for furfural conversion, even with the use of a base (data not presented). Otherwise, **(ZrG_{200})** was slightly active for benzyl alcohol oxidation.

The influence of calcination temperature (also meaning the presence or absence of thiolate ligands) was not conclusive in this case. Calcination extent enhanced benzyl alcohol oxidation, but not the furfural oxidative esterification. Reaction mechanisms are not the same. Benzyl alcohol oxidation proceeds with a first step of dehydrogenative oxidation into benzaldehyde, probably affected by the amphoteric properties (acidic and basic properties) of zirconia.

IV.2.6. **Using higher FF concentration**

In this section, the initial concentration of furfural was multiplied by 10 while using the same amount of catalyst in order to increase the production of desired compound.

Performing the reaction under base free conditions and at 100 °C led to incomplete

furfural conversion even after 24 h. Two products were obtained, methyl-2-fuorate and dimethyl acetal of furfural **Figure 5-16**. According to the literature, the obtained acetal, in contrast to the hemiacetal, is a co-product and not an intermediate towards methyl-2-furoate, and it is stable during the reaction. In our case, the conversion of furfural reached stability after 5 h, whereas methyl-2-furoate continued to be produced. In parallel, methyl-2-furoate was consumed, showing that it is an intermediate for methyl-2-furoate formation [263]. The formation of this acetal was reported in the literature to be obtained with catalysts with Au particles size > 4 nm [264], or due to the Lewis acidity of zirconia [265]. Actually, this acetal was only observed when working with high furfural concentration (10 g/kg). This probably means that the Au/furfural ratio was not sufficient for total furfural conversion into methyl-2-furoate and so Au sites are blocked. Based on that, dimethyl acetal formation can be considered as a side reaction occurring at the Lewis acid sites of zirconia.

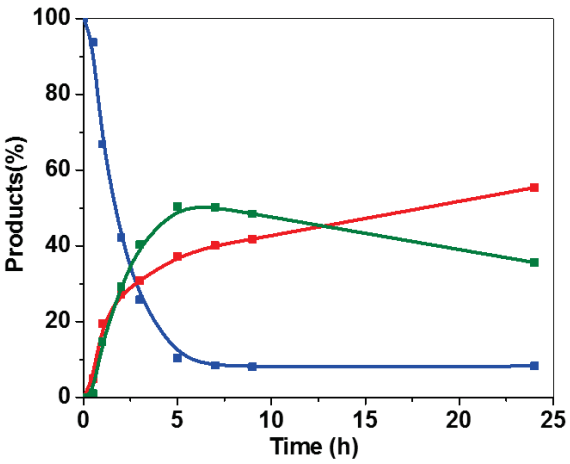

Figure 5-16 Percentage of remaining furfural (1 wt % in methanol) in (blue), yield of methyl-2-furoate in (red) and dimethyl acetal of furfural in (green) at 100 °C in the absence of base.

Performing the reaction at 120 °C increased the selectivity to methyl-2-fuorate, but did not block the formation of the acetal **Figure 5-17**.

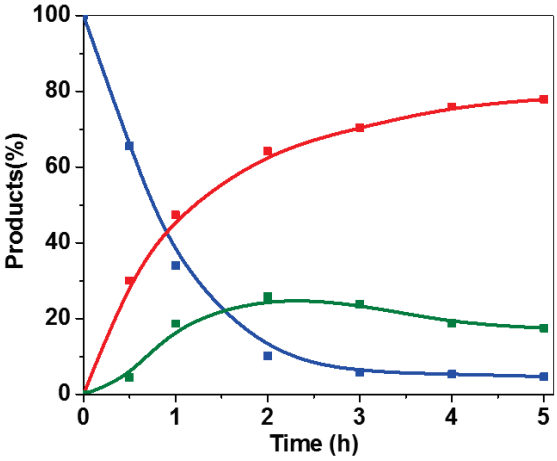

Figure 5-17 Percentage of remaining furfural (1 wt % in methanol) in (blue), yield of methyl-2-furoate in (red) and dimethyl acetal of furfural in (green) at 120 °C in the absence of base.

To prove our hypothesis, a base was used. The presence of the base neutralizes the acid sites of zirconia, so the production of the acetal should not be observed, and it was the case. Only methyl-2-furoate was produced, but with longer reaction time for complete furfural conversion and methyl-2-furoate formation, due to the lower catalyst/furfural ratio **Figure 5-18**.

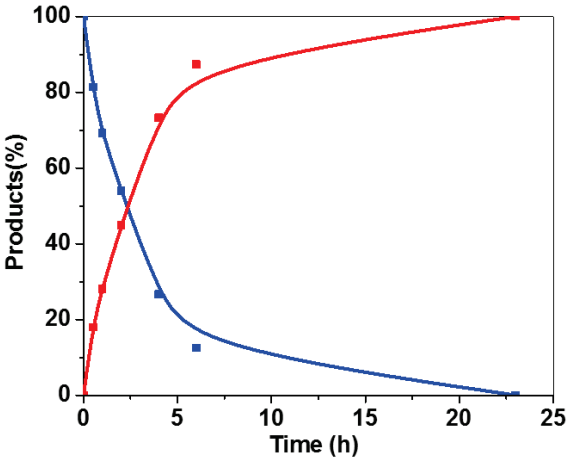

Figure 5-18 Percentage of remaining furfural (1 wt % in methanol) in (blue) and yield of methyl-2-furoate in (red) at 100 °C in the presence of base.

IV.2.7. **Recyclability of the catalyst**

Furfural oxidative esterification was done using furfural (0.1 % in MeOH), with 1 µmol Au using (ZrG_{400}) and no base, at 100 °C and under 6 bars O_2. The results in **Figure 5-19 (a)** showed reproducible results as described before, with complete conversion after 4 h and 100 % selectivity toward methyl-2-furoate. This reaction was considered as **run 1**.

The catalyst was recovered after the first cycle and labelled **(C1)**. **(C1)** was analyzed by TGA and showed no organic materials adsorbed onto it. Based on that, recycling of the catalyst was done without calcination and reproducible results were observed **Figure 5-19 (b)**. This was considered as **run 2**. **(C2)** was reused for **run 3** again without washing and activation. After 4 h, 94 % conversion was observed which reached completition after 5 h. Always 100 % selectivity to methyl-2-furoate was observed.

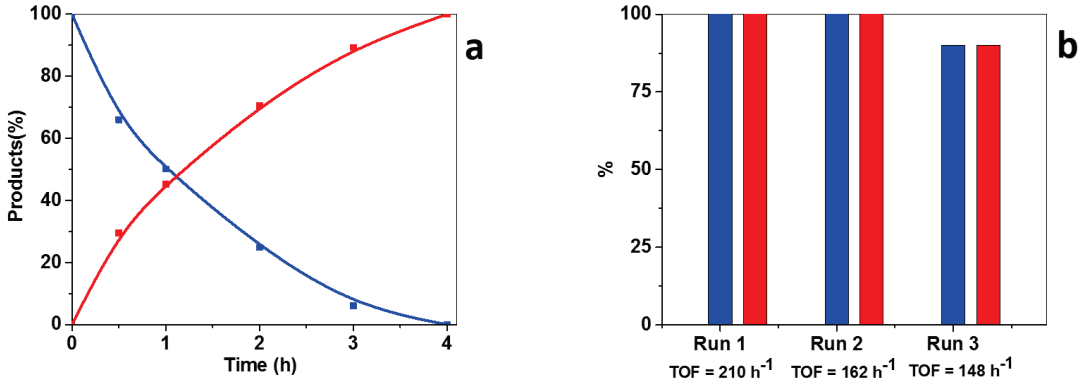

Figure 5-19 Furfural oxidative esterification to methyl-2-furoate. Percentage of remaining furfural (blue), yield of methyl-2-furoate in (red) and yield of acetal of furfural in (green). (a) Cycle one and (b) data collected after 4 h during recyclability tests in three runs .

IV.2.8. **Reactivity of different substrates using same catalytic conditions**

Substrates, other than furfural, were used under the same optimized reaction conditions of furfural oxidative esterification (substrate (0.1 % in MeOH), 1 µmol Au amount using **(ZrG_{400})**, 100 °C, 6 bar O_2, 700 rpm), to figure out if the catalyst activity has the same behavior toward different substrates. Benzyl alcohol and furfuryl alcohol were used.

IV.2.8.1. **Benzyl alcohol**

Reaction with benzyl alcohol worked well. Complete conversion in 2 h with 100 % selectivity toward methyl-2-benzoate **Figure 5-20**. This shows that when compared to the results obtained previously [262], the product from benzyl alcohol oxidation, using the same catalyst **(ZrG_{400})**, can be tuned based on the reaction conditions.

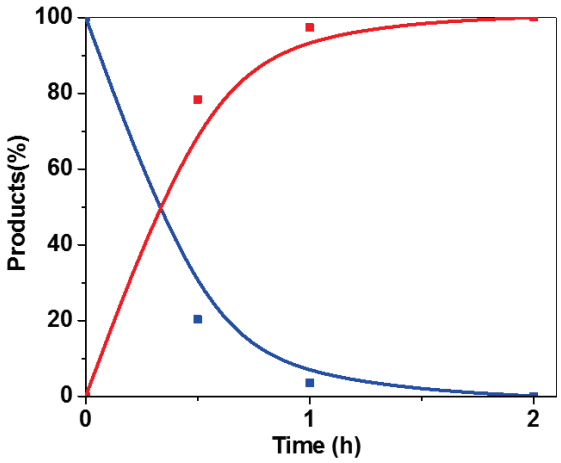

Figure 5-20 Benzyl alcohol oxidative esterification in methanol. Percentages of the remaining of benzyl alcohol (blue), and yield of methyl-2-benzoate (red).

IV.2.8.2. **Furfuryl alcohol**

Reaction with furfuryl alcohol **Figure 5-21**, resulted in 30 % conversion after 24 h, with the production of furfural (9 %) after 6 h. Methyl-2-furoate started to be produced after 2 h of reaction, while the acetal of furfural appeared after 6 h. When the 6 h were passed, the furfural yield decreased with further increase in methyl-2-furoate and acetal, reaching 15 % and 10 % respectively after 24 h. The remained furfural was 5 % at the end of the reaction. This showed that, first step oxidation from furfuryl alcohol to furfural occurred. Then furfural started to be transformed to methyl-2-furoate in the first 6 h where both products yields was increasing. After 6 h, the acetal production from furfural occurred. The furfural was consumed in two pathways, so its yield was seen to decrease with time, with parallel production of methyl-2-furoate and acetal with the continuous conversion of furfuryl alcohol.

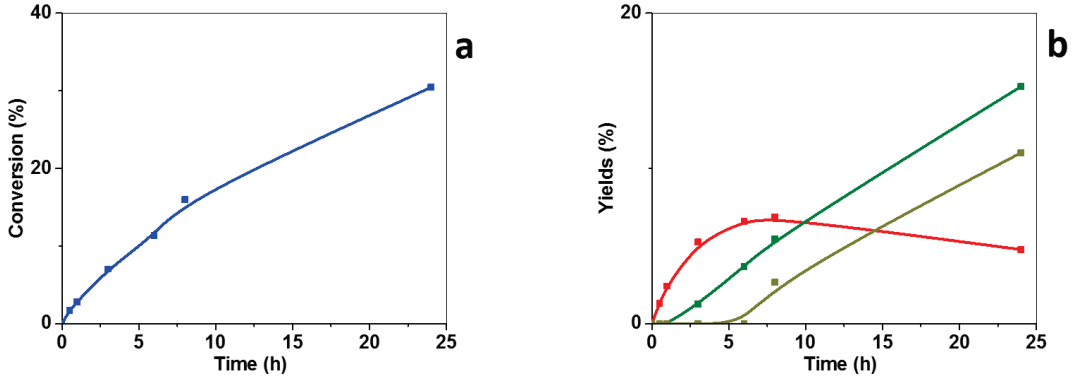

Figure 5-21 (a) Conversion of furfuryl alcohol in (blue). (b) Yields of furfural (red), methyl-2-furoate (green) and acetal (dark yellow).

V Conclusion

$Au_{25}(SG)_{18}$ clusters were successfully supported on ZrO_2 nanoparticles. The new materials are active as catalysts, after activation, in the oxidative dehydrogenation of benzyl alcohol to benzaldehyde and furfural oxidative esterification to methyl-2-furoate. The effect of the calcination temperature was studied by subsequent calcination steps under different conditions. For partial defunctionalization, activation at 200 °C and 300 °C for 4 h was done under air, whereas the treatment at 400 °C for 12 h resulted in the complete removal of the thiolate ligands. The influence of the presence of thiolate ligands and the size of the particles was clearly observed during benzyl alcohol conversion but not furfural transformation. This study confirmed that the activity and selectivity of supported $Au_{25}(SG)_{18}$ clusters are highly efficient for oxidation reactions carried out under mild conditions, and most importantly do not require the complete removal of the thiolate ligands.

General conclusions and perspectives

The goal of this project was to assess the catalytic properties of thiolate-protected gold nanoclusters deposited on MOFs, for oxidative reactions.

First, the reactivity of MIL-101, UiO-66 and ZIF-8 MOFs was studied for sugars transformation, showing mainly isomerization due to the Lewis acid character of these materials. However, no oxidation products were obtained. Also furfural reactivity was investigated, where the production of 2-dimethoxy methyl furan was observed. With UiO-66, possessing the highest value of Lewis acidity, direct acetal formation was observed.

Then, several composites based on tGNCs@MOFs were prepared and fully characterized. A particular attention was paid to their thermal stability, in order to control the tGNCs defunctionalization, which is necessary for catalytic reactivity. Thermal studies revealed that tGNCs can be partially defunctionalized at 200 °C (case of MIL-101), and at 300 °C (cases of UiO-66 and ZIF-8). However, these thermal treatments resulted in increase of Au particles size. Globally, the presence of tGNCs had no impact on the catalytic reactions of sugars. Nevertheless, for different kinds of reactions, $Au_{25}(SG)_{18}$@MIL-101 calcined at 200 °C for 12 h showed weak activity for benzyl alcohol oxidation in toluene, while $Au_{25}(SG)_{18}$@UiO-66 calcined at 300 °C for 12 h showed activity toward furfural oxidative esterification using a base, with a synergy between UiO-66 and the Au Nps. As a conclusion, though limited defunctionalization of tGNCs is available when they are supported on UiO-66, **UG_{300}** composite catalyst is efficient for oxidative esterification with base. Controlled thermal defunctionalization for partially and totally defunctionalized $Au_{25}(SG)_{18}$ has been possible when supported over ZrO_2, due to the better chemical and thermal stability of the latter. The best results and catalytic performances resulted by the partially calcined $Au_{25}(SG)_{18}$@ZrO_2 at 300 °C/4 h. This composite material showed an average particle size distribution of 1.7 nm after 53 % remove of the thiolate ligands. In that case, 100 % conversion of benzyl alcohol with 100 % selectivity toward benzaldehyde were obtained in toluene under mild conditions of temperature and atmospheric pressure. Good performances were also observed in the case of furfural oxidative esterification in methanol. Complete conversion within 4h

toward 100 % 2-methyl furoate, in base free conditions, at 100 °C and 6 bars O_2, during at least 3 consecutive cycles.

To assess the activity of MOFs based composites, it may be better to focus on gas phase transformations, rather than liquid phase ones. CO oxidation could be a suitable reaction, for tGNCs being well known for this transformation, even without defunctionalization [145-147]. We already did some tests using $Au_{25}(SG)_{18}@ZrO_2$ composites. ZrO_2 as pure support was inactive for CO oxidation. Non-calcined $Au_{25}(SG)_{18}@ZrO_2$ was active at 120 °C with a rate of CO_2 production of $0.5*10^3$ $\mu mol_{CO2}.g^{-1}.s^{-1}$ and the activity was stable for 1000min**.** Calcined $Au_{25}(SG)_{18}@ZrO_2$ at 200 °C for 4 h showed higher activity than the non-calcined at 120 °C, where the activity was constant during 1000 min with a higher rate of $3.25*10^3$ $\mu mol_{CO2}.g^{-1}.s^{-1}$. Its activity was tested at lower temperatures (30 °C and 80 °C), it showed activity but with lower rates of $0.1*10^3$ $\mu mol_{CO2}.g^{-1}.s^{-1}$ and $0.3*10^3$ $\mu mol_{CO2}.g^{-1}.s^{-1}$, respectively. The partial defunctionalisation at 200 °C may be the reason that triggered better activity at 120 °C. $Au_{25}(SG)_{18}@ZrO_2$ calcined at 400 °C, showed high activity even at ambient temperature (30 °C), with a high rate of $75*10^6$ $\mu mol_{CO2}.g^{-1}.s^{-1}$.

Different types of MOFs with Brønsted acid groups (ex: MIL-101-SO_3H and UiO-66-SO_3H) may be better supports especially for biomass transformations.

Starting from furfuryl alcohol to form methyl-2-furoate is one of the major perspectives. Then using 5-HMF as a starting substrate would be of high importance to produce furan dicarboxylic acid (FDCA). This approach, if it would be successful, will open the doors to start grom C-6 sugar (Glucose) and target FDCA, using a composite material ($Au_{25}(SR)_{18}$@MOF) having Brønsted acid and oxidative properties.

Annex A

Starting materials and physio-chemical characterizations for synthesized compounds

I. Starting materials

Table A-1 reports the commercial compounds used as precursors for all materials synthesis. It also shows the reagents used as substrates in the catalytic tests as well as the standards for chromatography calibrations. All compounds, unless 4-aminothiophenol, were used without any further purification. 4-aminothiophenol was sublimated two times prior to use.

Table A-1 List of commercial products used.

	Compound	Chemical Formula	Supplier	Purity/%
Precursors for thiolate gold nanoclusters preparation	**Gold(III) chloride trihydrate**	$HAuCl_4.3H_2O$	Sigma-Aldrich	≥ 99,9
	Sodium borohydride	$NaBH_4$	Sigma-Aldrich	99,9
	Lithium borohydride (2 M in THF)	$LiBH_4$	Sigma-Aldrich	N.I.
	Captopril	$C_9H_{15}NO_3S$	Alfa Aesar	N.I.
	4-aminothiophenol	C_6H_7NS	Alfa Aesar	97
	Glutathione	$C_{10}H_{17}N_3O_6S$	Alfa Aesar	>98
	Tetaoctylammonium bromide	$[CH_3(CH_2)_7)_4NBr$	Sigma-Aldrich	98
Precursors for supports preparation	**Zinc nitrate hexahydrate**	$Zn(NO_3)_2.6H_2O$	Sigma-Aldrich	≥ 99,9
	2-Methyl imidazole	$C_4H_6N_2$	Sigma-Aldrich	99
	Zirconium (IV) chloride	$ZrCl_4$	Sigma-Aldrich	99,9
	Terephthalic acid	$C_8H_6O_4$	Sigma-Aldrich	98
	Chromium (III) nitrate nonahydrate	$Cr(NO_3)_3.9H_2O$	Sigma-Aldrich	≥ 99,9
	Zirconium hydroxide	$Zr(OH)_4$	Sigma-Aldrich	97
Substrates for catalytic tests and calibrations	**Benzyl alcohol**	$C_6H_5CH_2OH$	Sigma-Aldrich	99,8
	Benzaldehyde	C_7H_6O	Sigma-Aldrich	≥ 99
	Dodecane	$C_{12}H_{26}$	Sigma-Aldrich	≥ 99
	Furfural	$C_5H_4O_2$	Sigma-Aldrich	99
	Methyl-2-furoate	$C_6H_6O_3$	Alfa Aesar	98
	Glucose	$C_6H_{12}O_6$	Sigma-Aldrich	≥ 99,5
	Fructose	$C_6H_{12}O_6$	Sigma-Aldrich	≥ 99
	Xylose	$C_5H_{10}O_5$	Sigma-Aldrich	≥ 99
	Butyric acid	$C_4H_8O_2$	Sigma-Aldrich	≥ 99

If not mentioned, all characterizations were performed at IRCELYON.

II Elemental analysis

The chemical analysis was obtained by ICP-OES to access the actual metal content deposited on the support, and to detect any leaching of the active species into the reaction solution during catalytic tests.

Gold amount was measured on an ICP-OES ACTIVA spectrometer (HORIBA Jobin Yvon) and the obtained gold content of different synthesized composite materials are summarized in **Table A-2**.

Table A-2 ICP analysis of Au content within the different composite materials.

$Au_{25}(SR)_{18}$@support	**Au content (%)**
(MG): $Au_{25}(SG)_{18}$@MIL-101	0.3
(MC): $Au_{25}(Capt)_{18}$@MIL-101	0.6
(MA): $Au_{25}(ATP)_{18}$@MIL-101	0.5
(UG): $Au_{25}(SG)_{18}$@UIO-66	0.9
(UA): $Au_{25}(ATP)_{18}$@UIO-66	0.5
(ZG): $Au_{25}(SG)_{18}$@ZIF-8	0.99
(ZA): $Au_{25}(ATP)_{18}$@ZIF-8	1.07
(ZrG): $Au_{25}(SG)_{18}$@ZrO_2	0.7

III Textural analysis

The textural analysis of a material gives the surface area (SBET) expressed in $m^2.g^{-1}$, pore size and distribution. The SBET is related to the mass of the degassed solid used during the analysis, and is based on nitrogen adsorption / desorption isotherm at 77 K (liquid nitrogen). Nitrogen adsorption is a physisorption, where weak Van der Waals interactions take place between the adsorbent (material) and adsorbate (N_2 gas). The adsorption energy Ea between the adsorbent and the adsorbate is in this case, is close to the liquefaction energy E_1 of the N_2 gas.

The BET specific surface area of the samples was determined by N_2 physisorption at -196 °C, using an ASAP 2020 Micromeritics apparatus. Prior to the measurements, catalysts were activated at 150 °C for at least 7 h under an ultrahigh vacuum (10^{-4} mbar) to eliminate adsorbed gases and molecules (H_2O, CO_2, alcohols or DMF). The analysis is usually done on ~ 50 mg of a product.

The isothermal adsorption/desorption equilibria are represented by the amount of

adsorbed N_2 molecules as a function of the equilibrium pressure of the cell. The shape of the isotherm provides information about the nature and shape of the pores. For metal-organic frameworks, the rapid increase in the adsorbed value at low relative pressure indicates the presence of microporosity (same case in both isotherms in **Figure A-0-1**. The left isotherm, representing MIL-101 (Cr), shows two peaks (inclinations) around (P/P_0 = 0.25) indicating the presence of mesopores. The BET surface area of MIL-101 is 2700 $m^2.g^{-1}$ while that of ZIF-8 is 1300 $m^2.g^{-1}$ (approximately doubled in the case of MIL-101). This was reflected by the maximum quantity adsorbed (1120 $cm^3.g^{-1}$ for MIL-101 and 650 $cm^3.g^{-1}$ for ZIF-8). The further high increase in the quantity adsorbed in the case of ZIF-8 at high relative pressure is an indication about the presence of mesopores.

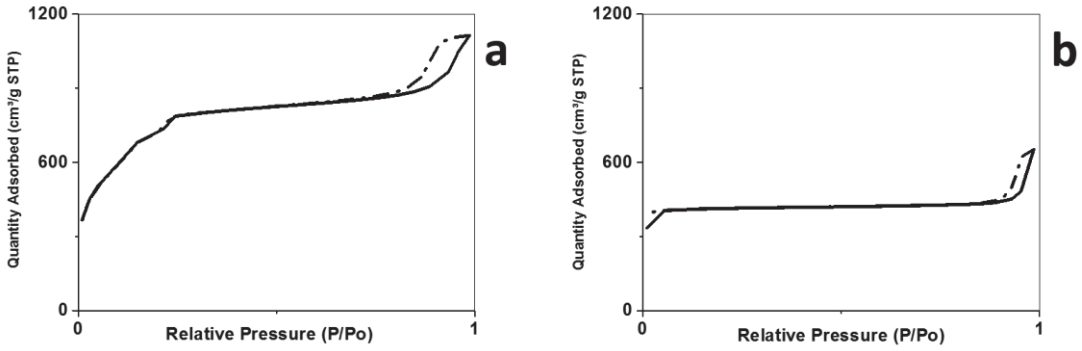

Figure A-0-1 N_2 adsorptio (line) and desorption (dash) isotherms of (a) MIL-101 and (b) ZIF-8.

IV Powder X-ray diffraction (PXRD)

Powder X-ray diffraction is a basic characterization technique of materials, used to identify the nature of crystalline phases present in a solid and to determine the mean crystallite size of each phase present in the sample. This method is mainly applied to materials containing a large volume of matter of high crystallinity. The crystallized phases can then be identified by comparison with a reference file (JCPDS file, Joint Committee on Powder Diffraction Standards).

IV.1. Equipment

XRD analyses were performed on a Bruker Advance Diffractometer D8A25 equipped with a nickel filter, a copper tube ($\lambda_{K\alpha\,(Cu)}$ = 1.54184 Å) and a multi-channel fast detector

(LynxEye 192 channels an active length of 2.947°). Low-angle diffractograms are recorded between 2θ = 0.45° and 7 ° (25 min for low-angle analysis). The high-angle diffractograms are recorded between 2θ = 4° and 80° (28 min for high-angle analysis).

IV.2. Determination of crystallite sizes

With heterogeneous catalysts, it is possible to estimate the mean crystallite size (dM) using the Debye-Scherrer relation **Equation A-1** from the half-width of the XRD broadening peak in a diffraction pattern.

Equation A-1

$$dM = 0.9\,\lambda / \beta \cos \Theta$$

With:

dM: size of the crystallites (nm)

λ: X-ray wavelength (λCu = 1.54184 Å)

Θ: Bragg angle (degree)

β: Line broadening at half-maximum of diffraction peak, in radians.

However, if the metal particles are too small (< 5 nm) and well dispersed, the signals are not observed. If they are visible, it is possible to use the Debye-Scherrer formula to determine the mean crystallite sizes.

When the crystallite size or concentration decreases (after deposition), the lines of diffraction decrease in intensity and widen and there may be overlap of neighboring lines. Debye-Scherrer's method in such case is imprecise. The Rietveld method described by Young et al. is used instead to estimate the crystallite size [266].

V Thermogravimetric Analysis (TGA)

Thermogravimetric Analysis (TGA) of materials is commonly used to provide quantitative information on the weight loss of a sample with temperature increases and about the thermal stability of a compound under oxidizing (Air) or inert (N_2, Argon) atmosphere. The thermograms provide information on decomposition reactions and allow to determine the temperature ranges in which various solvents and organic groups

are eliminated. Thanks to this analysis, we can calculate the loss of mass due to organic groups grafted on the surface. In the case of thiolate gold nanoclusters, the mass losses observed under air correspond directly to those of the ligands (and any solvents / gases adsorbed) constituting the organic mass of the solid with bulk gold as the remaining solid.

The thermogravimeter used was a TGA / DSC STARe system from Mettler Toledo. About 3 mg of product were introduced into a 70 µl alumina crucible and heated from 25 °C to 800 °C at a rate of 10 °C·min^{-1} under a flow of air or nitrogen (30 ml·min^{-1} + 20 ml·min^{-1} balance).

VI Thermogravimetric Analysis coupled to micro gas chromatography (TGA-µGC)

This technique is used to determine the nature of gases elaborated during thermal treatment of a material. It was used for MIL-101 to make sure that the washing and desorption treatment after the synthesis were efficient (no gases related to MeOH and DMF were detected). The µ-GC has a shorter column compared to normal GC. It allows the separation of light molecules (H_2O, O_2, NH_3, DMF, MeOH etc).

VII Infrared spectroscopy (IR)

The infrared spectra of the compounds were recorded on a Vector spectrometer 22 Fourier Transform Brucker (FT-IR) using KBr disks of samples. These are recorded in transmittance in the wavenumber area from 4000 cm^{-1} to 400 cm^{-1}.

VIII Transmission Electron Microscopy (TEM)

Transmission electron microscopy (TEM) is a technique for material characterization at the nanoscale. It allows the direct size and morphology observation of previously deposited nanoparticles on a microscopy grid. Samples can be prepared by direct deposition on a microscopy grid, being suspended in ethanol (grinding then kept in an ultrasonic bath for few minutes). A drop of the solution is deposited on a copper grid covered with a carbon film and the grid is then left to dry.

From microscopy snapshots, we can determine the average particle size and size distribution of nanoparticles, if the number of particles observed is sufficient (at least

200).

The microscopy used was a JEOL 2010 F. It is equipped with a LaB6 filament (electron source), accelerated at a voltage of 200 kv. The resolution is 0.19 nm and can reach a magnification up to 800 kv. The equipment is under a high vacuum (< 10^{-6} mbar) and is also equipped with an Oxford Link Isis EDX microanalysis system (Energy Dispersive X-ray spectroscopy) used to determine the local composition of catalysts with a special resolution lower than 5 nm, thanks to the energy dispersion of the re-emitted photons.

Particle sizes and corresponding size distributions were determined using ImageJ image processing software [267].

IX Scanning electron microscopy (SEM)

SEM images were obtained with FEI Quanta 250 FEG scanning electron microscope, samples were mounted on stainless pads and sputtered with Au/Pd alloy to prevent charging during observation.

X X-ray photoelectron spectroscopy (XPS)

X-ray photoelectron spectroscopy (XPS) is a quantitative technique for analyzing the surface chemistry (~ 10 nm deep) of a material. XPS measures the elemental composition, chemical and electronic states (eg. oxidation state) of a metal within a material.

XPS was performed using monochromatized AlKα X-ray source (hν = 1486.6 eV) on a AXIS Ultra DLD KRATOS Apparatus. The XPS spectrum was obtained by plotting the number of photoelectrons emitted as a function of their binding energy. The energy of these photoelectrons is characteristic of the atoms, orbitals as well as the electronic environment from which the electron is emitted. In a study, few milligrams of a material are placed within the enclosure under ultrahigh vacuum (P < 10^{-9} mbar) then bombarded by the X-ray source. X-ray material generates photoelectrons which are then detected by an analyzer measuring their kinetic energies.

XI Mass spectrometry (MS)

The ionization source we used to characterize gold clusters was the electrospray source coupled flight time (ESI-MS). In this ionization method, the sample to be analyzed was

dissolved and then injected directly into the nebulizer, then ionized in the evaporation chamber. It is a gentle ionization method, which allows the production of protonated, multi-protonated or cationized ions in positive mode, which allows the generation of deprotonated ions, multi-deprotonated or anionized ions in negative mode.

ESI-MS measurements have been done at Lyon university common center of Mass Spectrometry (CCSM). Mass spectra have been recorded in a positive mode on a hybrid quadrupole/flight time spectrometer (MicroTOFQII, Bruker Daltonics, Bremen) with an electrospray ionization source (ESI). The flow of gas spray (N_2) is set at 0.6 bar and the capillary voltage at 4.5 kV. Sweet conditions of ion transfer have been used to keep clusters intact during this step. The solutions (~ 1 $g.L^{-1}$) were dispersed and injected at a speed of 180 $\mu l \cdot h^{-1}$ in a solvent mixture (MeOH/ CH_2Cl_2/ water: 45/ 40/ 15). The analysis has been carried out over the range of 800 Th to 5000 Th and the calibration have been performed with cesium iodide (Agilen). Some extended spectra (800 Th at 10,000 Th) were recorded, but beyond 5000 Th, the accuracy of the measurement is not sufficient.

XII Ultraviolet-visible spectroscopy (UV-Vis)

It is based on using ultraviolet and near visible spectral regions to characterize the absorption or reflection abilities of compounds. When the light crosses the sample, the latter undergoes electronic transitions leading to absorption peaks at specific wavelengths. Valence electronic transitions between molecular orbitals absorb radiation in the visible ($400 > \lambda > 800$nm) and ultraviolet ($200 > \lambda > 400$ nm) domains. These peaks are always characteristic to the analyzed compound.

The sample was dissolved in a solvent and diluted according to Beer-Lambert Law. In the case of $Au_{25}(SG)_{18}$, the powder was dissolved in water, and 2 characteristic peaks at 450 nm and 670 nm were observed, indicating that the $Au_{25}(SR)_{18}$ cluster is obtained [45].

The UV-Vis spectrometer was an Agilent 8453, equipped with deuterium and tungsten lamp light sources for trouble-free maintenance.

XIII TPD-NH_3

The instrument used was TGA 92-12 SETARAM. The sample was placed in platinium crucible. The method was programmed to increase the temperature from 25 °C to 150 °C

(3 °C.min^{-1}) for desorption step, then stabilize at 80 °C, at which the ammonia adsorption takes place.The pretreatment takes place under helium flow. 1 % NH_3/He bottle is used.

Annex B

Analysis of reaction mixtures

Catalytic reactions were performed in 50 ml autoclave, equipped with a 150 bar pressure gauge, a 100 bar safety rupture disk and a thermocouple (in direct contact with the reaction mixture). The seal between the tank and the top was ensured by a Teflon® ring. The autoclave was heated by an electrical heating jacket with electric control. A magnetic stirrer drives a magnetic bar agitation. Addition of gas was also possible and sampling from the liquid phase was possible through a tube dipping **Scheme B-1**.

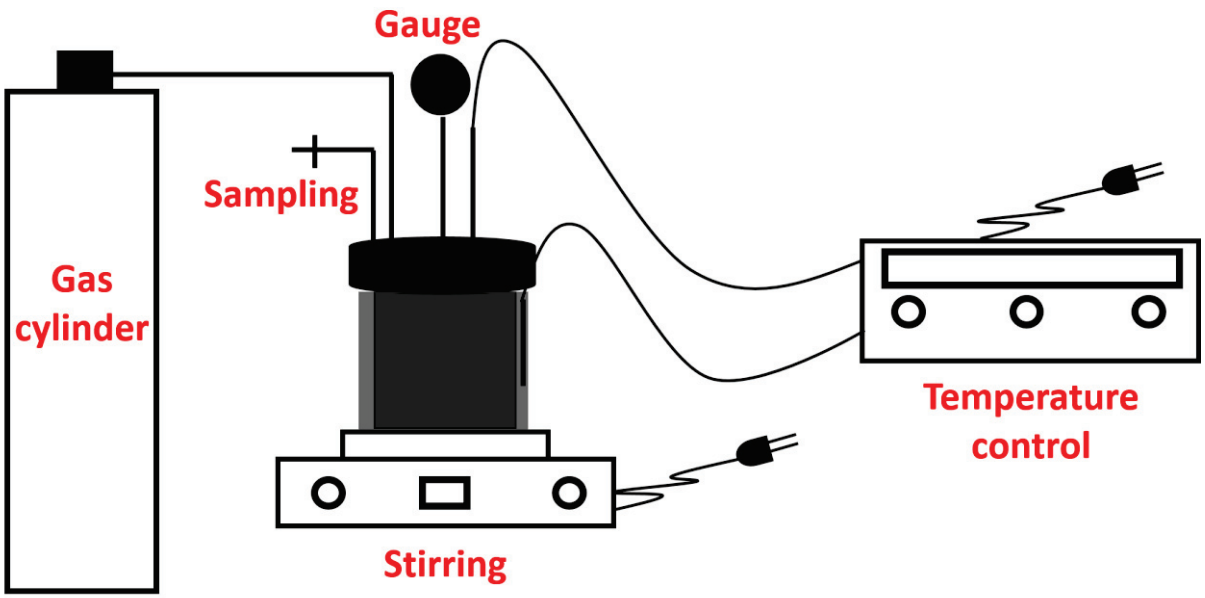

Scheme B-1 Catalytic setup.

The analysis of the reaction mixtures was done using High performance liquid chromatography (HPLC) and Gas chromatography (GC) depending the solvent used and on the products to be analyzed.

I High performance liquid chromatography (HPLC)

Liquid reaction samples were analyzed on a Shimadzu LC 20A HPLC connected to a refractive index detector (RID-10A). The separation of the products was achieved using a CORGEL 107H column maintained at 40 °C. A solution of H_2SO_4 (0.005 N) in ultra-pure ELGA water was used as a mobile phase at a flow rate of 0.6 $ml.min^{-1}$. The products (glucose, fructose, xylose, xylulose and 5-hyroxymethylfuran) were identified by their retention time in comparison with available standards.

II Gas chromatography (GC)

Products of benzyl alcohol oxidation and furfural oxidative esterification, [benzyl alcohol (BA), benzaldehyde (Bald), furfural (Fal), furfuryl alcohol (FA) methyl-2-furoate (MF), 2-(dimethoxy) methyl furan (MMF)], were analyzed on a Shimadzu GC-2010 PLUS system equipped with a flame ionization detector. CP8843- WCOT Fused Silica, CP-Wax 52 CB 30 m x 0.25 µm column was used for separating the products. The carrier gas was N_2, the injector and detector temperatures were 220 °C and 250 °C respectively.

Annex C

Calculations

I Calculation protocol before synthesis of composite materials

During the impregnation of $Au_{25}(SR)_{18}$ on different supports, we first fixed the quantity of support we want to use, in addition to the theoretical percentage of gold we want to impregnate on the support (1 wt% of gold). The mass of gold needed was calculated by using the equation of the weight percentage of gold to be impregnated (%Au), presenting the mass ratio of gold in the tGNC to the mass of the used support **Equation C-1**.

Equation C-1

$$\text{wt\% Au} = \frac{m \text{ of Au in the tGNC}}{m \text{ of the used support}} * 100$$

Moreover, TGA analysis reveals the exact percentage of gold in the used thiolate nanocluster (wt% Au_{tGNC}). $\%Au_{tGNC}$ is the mass ratio of Au in the nanocluster to the total tGNC mass. Having the wt% Au_{tGNC} from TGA, and the mass of gold from **Equation C-1**, the mass of the tGNC needed is calculated from **Equation C-2**:

Equation C-2

$$\text{wt\%Au}_{\text{tGNC}} = \frac{m \text{ of Au in the tGNC}}{m \; of \; tGNC} * 100$$

Impregnation method was used for the preparation of different composite materials. Maximum 500 mg of the support (MOFs or ZrO_2) were used. The amount of $Au_{25}(SR)_{18}$ was calculated according to the previous description.

II Calculation protocol before catalytic tests

In the catalytic reactions, specific amount of gold was used (1 µmol or 2 µmol) depending on each test. The calculation of the mass of the composite material (used as catalyst) corresponding to 1 µmol or 2 µmol of pure gold was calculated as following:

- Mass of gold that corresponds to the specific number of µmols, corresponds to the wanted µmols multiplied by the molar mass of atomic gold **Equation C-3**.

Equation C-3

$$m\,Au = n\,(\mu mol) * 197$$

- Experimental gold content in the composite material (known from ICP analysis) is the massic ratio between the mass of gold needed from **Equation C-3** and the mass of the composite material (the mass of catalyst to be used in the reaction) **Equation C-4**.

Equation C-4

$$\%\ \boldsymbol{Au}\ \text{tGNC from ICP analysis} = \frac{\boldsymbol{m}\ \text{Au}}{\boldsymbol{m}\ \text{catalyst}} * \mathbf{100}$$

III Calculations related for the analysis of the reaction mixtures after catalytic tests

The samples taken during the catalytic test were analyzed by different analytical techniques. Chromatographic analysis allows us to follow the concentration of substrates, identify and quantify the formed products. The correlation coefficient associated with each commercially available compound was established by external calibration according to **Equation C-5**:

Equation C-5

$$A = K.\ C$$

With:

A: Area of the compound at a given molar concentration

K: Correlation coefficient of the compound

C: Molar concentration of the compound ($mol.L^{-1}$)

The samples were diluted several times before being analyzed by HPLC and GC. For the non-commercial products, K was estimated.

The described set of analysis allows us to plot the evolution of substrates and products

concentrations as function of time, to calculate the conversions, yields and carbon-based selectivities, as well as the TOF (Turn Over Frequency) of the reaction.

The substrate conversion at time t was calculated from **Equation C-6**.

Equation C-6

$$(\%)Conversion = \frac{C0\ substrate - Ct\ substrate}{C0\ substrate} * 100$$

With:

C_0 substrate: Initial concentration of substrate ($g.kg^{-1}$)

C_t substrate: Concentration of substrate at time t ($g.kg^{-1}$)

The products yield at time t was calculated from **Equation C-7**:

Equation C-7

$$(\%)yield = \frac{nt\ product}{n0\ substrate} * 100$$

With:

n_t product: Number of mol of the formed product at t (mol)

n_0 substrate: Initial number of mol of the substrate at t_0 (mol)

The selectivity toward a product was calculated according to **Equation C-8**:

Equation C-8

$$(\%)S\ p = \frac{yield}{conversion} * 100$$

The turn over frequency of the reaction was calculated using **Equation C-9**:

Equation C-9

$$TOF\ (h\text{-}1) = \frac{n0\ substrate\ -\ nt\ substrate}{n\ of\ Au * time}$$

With:

n_0 substrate: Initial number of mol of substrate (mmol)

n_t substrate: Number of mol of substrate at time t (mmol)

n of Au: Number of mol of Au present in the catalyst (mmol)

t: Time at which the TOF is calculated (h)

References

1. Miao, M.; Brgoch, J.; Krishnapriyan, A.; Goldman, A.; Kurzman, J. A.; Seshadri, R., On the stereochemical inertness of the auride lone pair: initio studies of AAu (A = K, Rb, Cs). *Inorg. Chem.* **2013,** *52*, 8183-8189.
2. Leary, K.; Bartle, N., A new oxidation state of gold: The preparation and some properties of $[AuF]^-$ Salts. *Chem. commun.* **972,** *15*, 903-904.
3. Faraday, M., The Bakerian lecture-experimental relations of gold (and other metals) to light. *Phil. Trans. R. Soc.* **1857,** *147*, 145-181.
4. Graham, T., Liquid diffusion applied to analysis. *Phil. Trans. R. Soc.* **1861,** *151*, 183-224.
5. Eustis, S.; El-Sayed, M. A., Why gold nanoparticles are more precious than pretty gold: Noble metal surface plasmon resonance and its enhancement of the radiative and nonradiative properties of nanocrystals of different shapes. *Chem. Soc. Rev.* **2006,** *35*, 209–217.
6. Staples, R. J.; Grant, T.; Jr, J. P. F., Structure of trichloro(triphenylphosphine)gold(III), $AuCl_3\{P(C_6HS)_3$. *A. Acta Crystallogr., Sect. C: Cryst. Struct.Commun.* **1994,** *50*, 39-40.
7. Haruta, M.; Kobayashi, T.; Sano, H.; Yamada, N., Novel gold catalysts for the oxidation of carbon monoxide at a temperature far below 0 °C. *Chem. Lett.* **1987,** *16*, 405.
8. Yonzon, C. R.; Stuart, D. A.; Zhang, X.; McFarland, A. D.; Haynes, C. L.; Van Duyne, R. P., Towards advanced chemical and biological nanosensors-An overview. *Talanta* **2005,** *67*, 438-448.
9. Jin, R., Quantum sized thiolate-protected gold nanoclusters. *Nanoscale* **2010,** *2*, 343-362.
10. Schmid, G.; Schmid, G.; Pfeil, R.; Boese, R.; Bandermann, F.; Meyer, S.; Calis, G. H. M.; Vandervelden, W. A., $Au_{55}[P(C_6H_5)_3]_{12}Cl_6^-$ in goldcluster ungewohnlicher Grofie. *Chem. Ber. Recl.* **1981,** *114*, 3634-3642.
11. Li, H.; Li, L.; Pedersen, A.; Gao, Y.; Khetrapal, N.; Jonsson, H.; Zeng, X. C., Magic-number gold nanoclusters with diameters from 1 to 3.5 nm: relative stability and catalytic activity for CO oxidation. *Nano. Lett.* **2015,** *15*, 682-688.
12. Pichugina, D. A.; Kuzmenko, N. E.; Shestakov, A. F., Ligand-protected gold clusters: the structure, synthesis and applications. *Russ. Chem. Rev.* **2015,** *84*, 1114-1144.
13. Maity, P.; Xie, S.; Yamauchi, M.; Tsukuda, T., Stabilized gold clusters: from isolation toward controlled synthesis. *Nanoscale* **2012,** *4*, 4027-4037.
14. Goodman, J. L.; Petersson, E. J.; Daniels, D. S.; Qiu, J. X.; Schepartz, A., Biophysical and structural characterization of a robust octameric peptide bundle. *J. Am. Chem. Soc.* **2007,** *129*, 14746-14751.
15. Ertl, G., Reactions at surfaces: from atoms to complexity (Nobel Lecture). *Angew. Chem. Int. Ed. Engl.* **2008,** *47*, 3524-3535.
16. Somorjai, G. A.; Park, J. Y., Concepts, instruments, and model systems that enabled the rapid evolution of surface science. *Surf. Sci.* **2009,** *603*, 1293-1300.
17. Velden, J. W. A. V. D.; Bour, J. J.; Bosmax, W. P.; Xoordik, J. H., Synthesis and X-ray crystal structure determination of the cationic gold cluster compound $[Au_8(PPh_3)_7](NO_3)_2$. *J. Chem. Soc. Chem. Commun.* **1981**, 1218-1219.
18. Briant, C. E.; Hall, K. P.; Wheeler, A. C.; Mingos, D. M. P., Structural characterisation of $[Au_{10}Cl_3(PCy_2Ph)_6](NO_3)$ (Cy=cyclohexyl) and the development of a structural principle for high nuclearity gold clusters. *J. Chem. Soc. Chem. Commun.* **1984**, 248-250.
19. Mcpartlin, M.; Maso, R., Novel cluster complexes of gold(0)-gold(I), *Chem. Commun.* **1969**, 334.
20. Teo, B. K.; Shi, X.; Zhang, H., Pure gold cluster of 1:9:9:1:9:9:1 layered structure: A novel 39-metal-atom cluster $[(Ph_3P)_{14}Au_{39}Cl_6]Cl_2$ with an interstitial gold atom in a hexagonal antiprismatic cage. *J. Am. Chem. Soc.* **1992,** *114*, 2743-2745.

21. Schmid, G., The relevance of shape and size of Au_{55} clusters. *Chem. Soc. Rev.* **2008,** *37*, 1909-1930.
22. Bellon, B. P. L.; Cariati, F.; Manaserro M.; Naldini, L.; Sanso, M., Novel gold clusters: Preparation, properties, and X-ray structure determination of salts of octakis(triarylphosphine)enneagold, [Au_9L_8]X_3. *Chem. Commun.* **1971**, 1423-1424.
23. Laupp, M.; Strahle, J., [$(Ph_3PAu)_6$(dppeAu_2)$(AuCl)_4$Pd] an icosahedral Au_{12} Cluster with a central Pd atom. *Angew. Chem. Int. Ed. Engl.* **1994,** *33*, 207-209.
24. Jin, R.; Zhu, Y.; Qian, H., Quantum-sized gold nanoclusters: bridging the gap between organometallics and nanocrystals. *Chem. Eur. J.* **2011,** *17*, 6584-6593.
25. Pei, Y.; Zeng, X. C., Investigating the structural evolution of thiolate protected gold clusters from first-principles. *Nanoscale* **2012,** *4*, 4054-4072.
26. Kurashige, W.; Yamaguchi, M.; Nobusada, K.; Negishi, Y., Ligand-induced stability of gold nanoclusters: thiolate versus selenolate. *J. Phys. Chem. Lett.* **2012,** *3*, 2649-2652.
27. Yee, C. K.; Ulman, A.; Ruiz, J. D.; Parikh, A.; White, H.; Rafailovich, M., Alkyl selenide- and alkyl thiolate-functionalized gold nanoparticles: chain packing and bond nature. *Langmuir* **2003,** *19*, 9450-9458.
28. Meng, X.; Xu, Q.; Wang, S.; Zhu, M., Ligand-exchange synthesis of selenophenolate-capped Au_{25} nanoclusters. *Nanoscale* **2012,** *4*, 4161-4165.
29. Kurashige, W.; Yamazoe, S.; Kanehira, K.; Tsukuda, T.; Negishi, Y., Selenolate-protected Au_{38} nanoclusters: isolation and structural characterization. *J. Phys. Chem. Lett.* **2013,** *4*, 3181-3185.
30. Maity, P.; Wakabayashi, T.; Ichikuni, N.; Tsunoyama, H.; Xie, S.; Yamauchi, M.; Tsukuda, T., Selective synthesis of organogold magic clusters Au_{54}(C triple bond CPh)$_{26}$. *Chem. Commun.* **2012,** *48*, 6085-6087.
31. Maity, P.; Tsunoyama, H.; Yamauchi, M.; Xie, S.; Tsukuda, T., Organogold clusters protected by phenylacetylene. *J. Am. Chem. Soc.* **2011,** *133*, 20123-20125.
32. Kang, X.; Chong, H.; Zhu, M., $Au_{25}(SR)_{18}$: the captain of the great nanocluster ship. *Nanoscale* **2018,** *10*, 10758-10834.
33. Brust, M.; Walker, M.; Bethell, D.; Schiffrin, D. J.; Whyman, R., Synthesis of thiol-derivatised gold nanoparticles in a two-phase liquid-liquid system. *J. Chem. Soc. Chem. Commun.* **1994**, 801-802.
34. Whetten, R. L.; Khoury, J. T.; Alvarez, M. M.; Murthy, S.; Vezmar, I.; Wang, Z. L.; Stephens, P. W.; Cleveland, C. L.; Luedtke, W. D.; Landman, U., Nanocrystal gold molecules. *Adv. Mater.* **1996**, 428-433.
35. Schaaff, T. G.; Shafigullin, M. N.; Khoury, J. T.; Vezmar, I.; Whetten, R. L.; Cullen, W. G.; First, P. N., Isolation of smaller nanocrystal Au molecules: robust quantum effects in optical spectra. *J. Phys. Chem. B* **1997**, 7885-7891.
36. Arnold, R. J.; Reilly, J. P., High-resolution time-of-flight mass spectra of alkanethiolate-coated gold nanocrystals. *J. Am. Chem. Soc.* **1998,** *120*, 1528-1532.
37. Schaaff, T. G.; Knight, G.; Shafigullin, M. N.; Borkman, R. F.; Whetten, R. L., Isolation and selected properties of a 10.4 kDa gold:glutathione cluster compound. *J. Phys. Chem. B* **1998,** *102*, 10643-10646.
38. Schaaff, T. G.; Whetten, R. L., Giant gold-glutathione cluster compounds: Intense optical activity in metal-based transitions. *J. Phys. Chem. B* **2000,** *104*, 2630-2641.
39. Negishi, Y.; Nobusada, K.; Tsukuda, T., Glutathione-protected gold clusters revisited: Bridging the gap between gold(I)-thiolate complexes and thiolate-protected gold nanocrystals. *J. Am. Chem. Soc.* **2005,** *127*, 5261-5270.
40. Donkers, R. L.; Lee, D.; Murray, R. W., Synthesis and isolation of the molecule-like cluster $Au_{38}(PhCH_2CH_2S)_{24}$. *Langmuir* **2004,** *20*, 1945-1952.

41. Tracy, o. B.; Kalyuzhny, G.; Crowe, M. C.; Balasubramanian, R.; Choi, J. P.; Murray, R. W., Poly(ethylene glycol) ligands for high-resolution nanoparticle mass spectrometry. *J. Am. Chem. Soc.* **2007,** *129*, 6706-6707.
42. Price, R. C.; Whetten, R. L., All-aromatic, nanometer-scale, gold-cluster thiolate complexes. *J. Am. Chem. Soc.* **2005,** *127*, 13750-13751.
43. Heaven, M. W.; Dass, A.; White, P. S.; Holt, K. M.; Murray, R. W., Crystal structure of the gold nanoparticle $[N(C_8H_{17})_4][Au_{25}(SCH_2CH_2Ph)_{18}]$. *J. Am. Chem. Soc.* **2008,** *130*, 3754-3755.
44. Zhu, M.; Lanni, E.; Garg, N.; Bier, M. E.; Jin, R., Kinetically controlled, high-yield synthesis of Au_{25} clusters. *J. Am. Chem. Soc.* **2008,** *130*, 1138-1139.
45. Zhu, M.; Aikens, C. M.; Hollander, F. J.; Schatz, G. C.; Jin, R., Correlating the crystal structure of a thiol-protected Au_{25}cluster and optical properties. *J. Am. Chem. Soc.* **2008,** *130*, 5883–5885.
46. Wu, Z.; Suhan, J.; Jin, R., One-pot synthesis of atomically monodisperse, thiol-functionalized Au_{25} nanoclusters. *J. Mater. Chem.* **2009,** *19*, 622-626.
47. Parker, J. F.; Weaver, J. E.; McCallum, F.; Fields-Zinna, C. A.; Murray, R. W., Synthesis of monodisperse $[Oct_4N^{(+)}][Au_{25}(SR)_{18}^{(-)}]$ nanoparticles, with some mechanistic observations. *Langmuir* **2010,** *26*, 13650-13654.
48. Qian, H.; Jin, R., Controlling nanoparticles with atomic precision: The case of $Au_{144}(SCH_2CH_2Ph)_{60}$. *Nano. Lett.* **2009,** *9*, 4083-4087.
49. Lavenn, C.; Albrieux, F.; Bergeret, G.; Chiriac, R.; Delichere, P.; Tuel, A.; Demessence, A., Functionalized gold magic clusters: $Au_{25}(SPhNH_2)_{17}$. *Nanoscale* **2012,** *4*, 7334-7337.
50. Xie, J.; Zheng, Y.; Ying, J. Y., Protein-directed synthesis of highly fluorescent gold nanoclusters. *J. Am. Chem. Soc.* **2009,** *131*, 888–889.
51. Kumar, S.; Jin, R., Water-soluble $Au_{25}(Capt)_{18}$ nanoclusters: synthesis, thermal stability, and optical properties. *Nanoscale* **2012,** *4*, 4222-4227.
52. Zeng, C.; Chen, Y.; Das, A.; Jin, R., Transformation chemistry of gold nanoclusters: from one stable size to another. *J. Phys. Chem. Lett.* **2015,** *6*, 2976-2986.
53. Woehrle, G. H.; Warner, M. G.; Hutchison, J. E., Ligand Exchange Reactions Yield Subnanometer, Thiol-stabilized gold particles with defined optical transitions. *J. Phys. Chem. B* **2002,** *106*, 9979-9981.
54. Shichibu, Y.; Negishi, Y.; Tsukuda, T.; Teranishi, T., Large-scale synthesis of thiolated Au_{25} clusters via ligand exchange reactions of phosphine-stabilized Au_{11} clusters. *J. Am. Chem. Soc.* **2005,** *127*, 13464-13465.
55. McKenzie, L. C.; Zaikova, T. O.; Hutchison, J. E., Structurally similar triphenylphosphine-stabilized undecagolds, $Au_{11}(PPh_3)_7Cl_3$ and $[Au_{11}(PPh_3)_8Cl_2]Cl$, exhibit distinct ligand exchange pathways with glutathione. *J. Am. Chem. Soc.* **2014,** *136*, 13426-13435.
56. Tracy, J. B.; Crowe, M. C.; Parker, J. F.; Hampe, O.; Fields-Zinna, C. A.; Dass, A.; Murray, R. W., Electrospray ionization mass spectrometry of uniform and mixed monolayer nanoparticles: $Au_{25}[S(CH_2)_2Ph]_{18}$ and $Au_{25}[S(CH_2)_2Ph]_{18-x}(SR)_x$. *J. Am. Chem. Soc.* **2007,** *129*, 16209-16215.
57. Devadas, M. S.; Kwak, K.; Park, J.-W.; Choi, J.-H.; Jun, C.-H.; Sinn, E.; Ramakrishna, G.; Lee, D., Directional electron transfer in chromophore-labeled quantum-sized Au_{25} clusters: Au_{25} as an electron donor. *J. Phys. Chem. Lett.* **2010,** *1*, 1497-1503.
58. Shibu, E. S.; Muhammed, M. A. H.; Tsukuda, T.; Pradeep, T., Ligand exchange of $Au_{25}SG_{18}$ leading to functionalized gold clusters: spectroscopy, kinetics, and luminescence. *J. Phys. Chem. C* **2008,** *112*, 12168–12176.
59. Ni, T. W.; Tofanelli, M. A.; Phillips, B. D.; Ackerson, C. J., Structural basis for ligand exchange on $Au_{25}(SR)_{18}$. *Inorg. Chem.* **2014,** *53*, 6500-6502.
60. Zeng, C.; Li, T.; Das, A.; Rosi, N. L.; Jin, R., Chiral structure of thiolate-protected 28-gold-atom nanocluster determined by X-ray crystallography. *J. Am. Chem. Soc.* **2013,** *135*, 10011-10013.
61. Zeng, C.; Liu, C.; Chen, Y.; Rosi, N. L.; Jin, R., Gold-thiolate ring as a protecting motif in the $Au_{20}(SR)_{16}$ nanocluster and implications. *J. Am. Chem. Soc.* **2014,** *136*, 11922-11925.

62. Zeng, C.; Qian, H.; Li, T.; Li, G.; Rosi, N. L.; Yoon, B.; Barnett, R. N.; Whetten, R. L.; Landman, U.; Jin, R., Total structure and electronic properties of the gold nanocrystal $Au_{36}(SR)_{24}$. *Angew. Chem. Int. Ed. Engl.* **2012,** *51*, 13114-13118.
63. Das, A.; Liu, C.; Zeng, C.; Li, G.; Li, T.; Rosi, N. L.; Jin, R., Cyclopentanethiolato-protected $Au_{36}(SC_5H_9)_{24}$ nanocluster: crystal structure and implications for the steric and electronic effects of ligand. *J. Phys. Chem. A* **2014,** *118*, 8264-8269.
64. Das, A.; Li, T.; Li, G.; Nobusada, K.; Zeng, C.; Rosi, N. L.; Jin, R., Crystal structure and electronic properties of a thiolate-protected Au_{24} nanocluster. *Nanoscale* **2014,** *6*, 6458-6462.
65. Zeng, C.; Chen, Y.; Kirschbaum, K.; Appavoo, K.; Sfeir, M. Y.; Jin, R., Structural patterns at all scales in a nonmetallic chiral $Au_{133}(SR)_{52}$ nanoparticle. *Sci. Adv.* **2015,** *1*, e1500045.
66. Schaaff, T. G.; Whetten, R. L., Controlled etching of Au:SR cluster compounds. *J. Phys. Chem. B* **1999,** *103*, 9394-9396.
67. Demers, L. M.; Mirkin, C. A.; Mucic, R. C.; Reynolds, R. A.; Letsinger, R. L.; Elghanian, R.; Viswanadham, G., A fluorescence-based method for determining the surface coverage and hybridization efficiency of thiol-capped oligonucleotides bound to gold thin films and nanoparticles. *Anal. Chem.* **2000,** *72*, 5535-5541.
68. Liu, X.; Wu, Y.; Li, S.; Zhao, Y.; Yuan, C.; Jia, M.; Luo, Z.; Fu, H.; Yao, J., Quantum-size-effect accommodation of gold clusters with altered fluorescence of dyes. *RSC Adv.* **2015,** *5*, 30610-30616.
69. Yu, Y.; Luo, Z.; Yu, Y.; Lee, J. Y.; Xie, J., Observation of cluster size growth in CO-directed synthesis of $Au_{25}(SR)_{18}$ nanoclusters. *ACS Nano.* **2012,** *6*, 7920–7927
70. Yu, Y.; Chen, X.; Yao, Q.; Yu, Y.; Yan, N.; Xie, J., Scalable and precise synthesis of thiolated $Au_{10–12}$, Au_{15}, Au_{18}, and Au_{25} nanoclusters via pH controlled CO reduction. *Chem. Mater.* **2013,** *25*, 946-952.
71. Yuan, X.; Zhang, B.; Luo, Z.; Yao, Q.; Leong, D. T.; Yan, N.; Xie, J., Balancing the rate of cluster growth and etching for gram-scale synthesis of thiolate-protected Au_{25} nanoclusters with atomic precision. *Angew. Chem. Int. Ed. Engl.* **2014,** *53*, 4623-4627.
72. Yuan, X.; Yu, Y.; Yao, Q.; Zhang, Q.; Xie, J., Fast synthesis of thiolated Au_{25} nanoclusters via protection-deprotection method. *J. Phys. Chem. Lett.* **2012,** *3*, 2310-2314.
73. Lavenn, C.; Albrieux, F.; Tuel, A.; Demessence, A., Synthesis, characterization and optical properties of an amino-functionalized gold thiolate cluster: $Au_{10}(SPh\text{-}p NH_2)_{10}$. *J. Colloid Interface Sci.* **2014,** *418*, 234.
74. Wiseman, M. R.; Marsh, P. A.; Bishop, P. T.; Brisdon, B. J.; Mahon, M. F., Homoleptic gold thiolate catenanes. *J. Am. Chem. Soc.* **2000,** *122*, 12598-12599.
75. Zhu, M.; Qian, H.; Jin, R., Thiolate-protected Au_{20} clusters with a large energy gap of 2.1 eV. *J. Am. Chem. Soc.* **2009,** *131*, 7220–7221.
76. Zhu, X.; Jin, S.; Wang, S.; Meng, X.; Zhu, C.; Zhu, M.; Jin, R., One-pot synthesis of phenylmethanethiolate-protected $Au_{20}(SR)_{16}$ and $Au_{24}(SR)_{20}$ nanoclusters and insight into the kinetic control. *Chem. Asian J.* **2013,** *8*, 2739-2745.
77. Zhu, M.; Qian, H.; Jin, R., Thiolate-protected $Au_{24}(SC_2H_4Ph)_{20}$ nanoclusters: Superatoms or Not? *J. Phys. Chem Lett.* **2010,** *1*, 1003-1007.
78. Crasto, D.; Barcaro, G.; Stener, M.; Sementa, L.; Fortunelli, A.; Dass, A., $Au_{24}(SAdm)_{16}$ nanomolecules: X-ray crystal structure, theoretical analysis, adaptability of adamantane ligands to form $Au_{23}(SAdm)_{16}$ and $Au_{25}(SAdm)_{16}$, and its relation to $Au_{25}(SR)_{18}$. *J. Am. Chem. Soc.* **2014,** *136*, 14933-14940.
79. Chen, Y.; Liu, C.; Tang, Q.; Zeng, C.; Higaki, T.; Das, A.; Jiang, D. E.; Rosi, N. L.; Jin, R., Isomerism in $Au_{28}(SR)_{20}$ nanocluster and stable structures. *J. Am. Chem. Soc.* **2016,** *138*, 1482-1485.
80. Crasto, D.; Dass, A., Green gold: $Au_{30}(S\text{-}t\text{-}C_4H_9)_{18}$ molecules. *J. Phys. Chem. C* **2013,** *117*, 22094-22097.

81. Crasto, D.; Malola, S.; Brosofsky, G.; Dass, A.; Hakkinen, H., Single crystal XRD structure and theoretical analysis of the chiral $Au_{30}S(S\text{-}t\text{-}Bu)_{18}$ cluster. *J. Am. Chem. Soc.* **2014,** *136*, 5000-5005.
82. Yang, H.; Wang, Y.; Edwards, A. J.; Yan, J.; Zheng, N., High-yield synthesis and crystal structure of a green Au_{30} cluster co-capped by thiolate and sulfide. *Chem. Commun.* **2014,** *50*, 14325-14327.
83. Dass, A.; Jones, T.; Rambukwella, M.; Crasto, D.; Gagnon, K. J.; Sementa, L.; De Vetta, M.; Baseggio, O.; Aprà, E.; Stener, M.; Fortunelli, A., Crystal structure and theoretical analysis of green gold $Au_{30}(S\text{-}tBu)_{18}$ nanomolecules and their relation to $Au_{30}S(S\text{-}tBu)_{18}$. *J. Phys. Chem. C* **2016,** *120*, 6256-6261.
84. Higaki, T.; Liu, C.; Zeng, C.; Jin, R.; Chen, Y.; Rosi, N. L.; Jin, R., Controlling the atomic structure of Au_{30} nanoclusters by a ligand-based strategy. *Angew. Chem. Int. Ed. Engl.* **2016,** *55*, 6694-6697.
85. Qian, H.; Eckenhoff, W. T.; Zhu, Y.; Pintauer, T.; Jin, R., Total structure determination of thiolate-protected Au_{38} nanoparticles. *J. Am. Chem. Soc.* **2010,** *132*, 8280–8281.
86. Liu, C.; Li, T.; Li, G.; Nobusada, K.; Zeng, C.; Pang, G.; Rosi, N. L.; Jin, R., Observation of body-centered cubic gold nanocluster. *Angew. Chem. Int. Ed. Engl.* **2015,** *54*, 9826-9829.
87. Chen, Y.; Zeng, C.; Kauffman, D. R.; Jin, R., Tuning the magic size of atomically precise gold nanoclusters via isomeric methylbenzenethiols. *Nano. Lett.* **2015,** *15*, 3603-3609.
88. Qian, H.; Zhu, Y.; Jin, R., Isolation of ubiquitous $Au_{40}(SR)_{24}$ clusters from the 8 kDa gold clusters. *J. Am. Chem. Soc.* **2010,** *132*, 4583–4585.
89. Knoppe, S.; Boudon, J.; Dolamic, I.; Dass, A.; Burgi, T., Size exclusion chromatography for semipreparative scale separation of $Au_{38}(SR)_{24}$ and $Au_{40}(SR)_{24}$ and larger clusters. *Anal. Chem.* **2011,** *83*, 5056-5061.
90. Zeng, C.; Chen, Y.; Liu, C.; Nobusada, K.; Rosi, N. L.; Jin, R., Gold tetrahedra coil up: Kekule-like and Ddouble helical super- structures. *Sci. Adv.* **2015,** *1*, e1500425.
91. Tsunoyama, H.; Negishi, Y.; Tsukuda, T., Chromatographic isolation of "missing" Au_{55} clusters protected by alkanethiolates. *J. Am. Chem. Soc.* **2006,** *128*, 6036-6037.
92. Tsunoyama, R.; Tsunoyama, H.; Pannopard, P.; Limtrakul, J.; Tsukuda, T., MALDI mass analysis of 11 kDa gold clusters protected by octadecanethiolate ligands. *J. Phys. Chem. C* **2010,** *114*, 16004–16009.
93. Qian, H.; Jin, R., Synthesis and electrospray mass spectrometry determination of thiolate-protected $Au_{55}(SR)_{31}$ nanoclusters. *Chem. Commun.* **2011,** *47*, 11462-11464.
94. Zeng, C.; Chen, Y.; Li, G.; Jin, R., Magic Size $Au_{64}(S\text{-}c\text{-}C_6H_{11})_{32}$ nanocluster protected by cyclohexanethiolate. *Chem. Mater.* **2014,** *26*, 2635−2641.
95. Nimmala, P. R.; Yoon, B.; Whetten, R. L.; Landman, U.; Dass, A., $Au_{67}(SR)_{35}$ nanomolecules: characteristic size-specific optical, electrochemical, structural properties and first-principles theoretical analysis. *J. Phys. Chem. A* **2013,** *117*, 504-517.
96. Li, G.; Zeng, C.; Jin, R., Thermally robust $Au_{99}(SPh)_{42}$ nanoclusters for chemoselective hydrogenation of nitrobenzaldehyde derivatives in water. *J. Am. Chem. Soc.* **2014**, *136*, 3673-3679.
97. Jadzinsky, P. D.; Calero, G.; Ackerson, C. J.; Bushnell, D. A.; Kornberg, R. D., Structure of a thiol monolayer–protected gold nanoparticle at 1.1 Å resolution. *Science* **2007,** *318*, 430-433.
98. Negishi, Y.; Sakamoto, C.; Ohyama, T.; Tsukuda, T., Synthesis and the origin of the stability of thiolate-protected Au_{130} and Au_{187} clusters. *J. Phys. Chem. Lett.* **2012,** *3*, 1624-1628.
99. Tang, Z.; Robinson, D. A.; Bokossa, N.; Xu, B.; Wang, S.; Wang, G., Mixed dithiolate durene-DT and monothiolate phenylethanethiolate protected Au_{130} nanoparticles with discrete core and core-ligand energy states. *J. Am. Chem. Soc.* **2011,** *133*, 16037-16044.
100. Chen, Y.; Zeng, C.; Liu, C.; Kirschbaum, K.; Gayathri, C.; Gil, R. R.; Rosi, N. L.; Jin, R., Crystal Structure of Barrel-Shaped Chiral $Au_{130}(p\text{-MBT})_{50}$ Nanocluster. *J. Am. Chem. Soc.* **2015,** *137*, 10076-10079.

101. Jupally, V. R.; Dharmaratne, A. C.; Crasto, D.; Huckaba, A. J.; Kumara, C.; Nimmala, P. R.; Kothalawala, N.; Delcamp, J. H.; Dass, A., $Au_{137}(SR)_{56}$ nanomolecules: composition, optical spectroscopy, electrochemistry and electrocatalytic reduction of CO_2. *Chem. Commun.* **2014,** *50*, 9895-9898.
102. Zeng, C.; Chen, Y.; Kirschbaum, K.; Lambright, K. J.; Jin, R., Emergence of hierarchical structural complexities in nanoparticles and their assembly. *Science* **2016,** *354*, 1580-1584.
103. Sakthivel, N. A.; Theivendran, S.; Ganeshraj, V.; Oliver, A. G.; Dass, A., Crystal structure of faradaurate-279: $Au_{279}(SPh\text{-}tBu)_{84}$ plasmonic nanocrystal molecules. *J. Am. Chem. Soc.* **2017,** *139*, 15450-15459.
104. Kumara, C.; Zuo, X.; Cullen, D. A.; Dass, A., Faradaurate-940: Synthesis, mass spectrometry, electron microscopy, high-energy X-ray diffraction, and X-ray scattering study of $Au_{\sim 940\pm 20}(SR)_{\sim 160\pm 4}$ nanocrystals. *ACS Nano.* **2014,** *8*, 6431–6439.
105. Walter, M.; Akola, J.; Lopez-Acevedo, O.; Jadzinsky, P. D.; Calero, G.; Ackerson, C. J.; Whetten, R. L.; Gronbeck, H.; Hakkinen, H., A unified view of ligand-protected gold clusters as superatom complexes. *Proc. Natl. Acad. Sci. U. S. A.* **2008,** *105*, 9157-9162.
106. Wyrwas, R. B.; Alvarez, M. M.; Khoury, J. T.; Price, R. C.; Schaaff, T. G.; Whetten, R. L., The colours of nanometric gold. *Eur. Phys. J. D* **2007,** *43*, 91-95.
107. Hakkinen, H., Atomic and electronic structure of gold clusters: understanding flakes, cages and superatoms from simple concepts. *Chem. Soc. Rev.* **2008,** *37*, 1847-1859.
108. Fernando, A.; Weerawardene, K. L.; Karimova, N. V.; Aikens, C. M., Quantum mechanical studies of large metal, metal oxide, and metal chalcogenide nanoparticles and clusters. *Chem. Rev.* **2015,** *115*, 6112-6216.
109. Das, A.; Liu, C.; Byun, H. Y.; Nobusada, K.; Zhao, S.; Rosi, N.; Jin, R., Structure determination of $[Au_{18}(SR)_{14}]$. *Angew. Chem. Int. Ed. Engl.* **2015,** *54*, 3140-3144.
110. Jung, J.; Kang, S.; Han, Y. K., Ligand effects on the stability of thiol-stabilized gold nanoclusters: $Au_{25}(SR)_{18}^-$, $Au_{38}(SR)_{24}$, and $Au_{102}(SR)_{44}$. *Nanoscale* **2012,** *4*, 4206-4210.
111. Akola, J.; Walter, M.; Whetten, R. L.; Ha¨kkinen, H.; Gro¨nbeck, H., On the structure of thiolate-protected Au_{25}. *J. Am. Chem. Soc. 2008* **2008,** *130*, 3756-3757.
112. Zhu, M.; Eckenhoff, W. T.; Pintauer, T.; Jin, R., Conversion of anionic $[Au_{25}(SCH_2CH_2Ph)_{18}]^-$ cluster to charge neutral cluster via air oxidation. *J. Phys. Chem. C* **2008,** *112*, 14221–14224.
113. Das, A.; Li, T.; Nobusada, K.; Zeng, C.; Rosi, N. L.; Jin, R., Nonsuperatomic $[Au_{23}(SC_6H_{11})_{16}]^-$ nanocluster featuring bipyramidal Au_{15} kernel and trimeric $Au_3(SR)_4$ motif. *J. Am. Chem. Soc.* **2013,** *135*, 18264-18267.
114. Jin, R.; Zeng, C.; Zhou, M.; Chen, Y., Atomically precise colloidal metal nanoclusters and nanoparticles: Fundamentals and opportunities. *Chem. Rev.* **2016,** *116*, 10346-10413.
115. Li, G.; Jin, R., Atomically precise gold nanoclusters as new nodel catalysts. *Acc. Chem. Res.* **2013,** *46*, 1749–1758
116. Liu, P.; Qin, R.; Fu, G.; Zheng, N., Surface coordination chemistry of metal nanomaterials. *J. Am. Chem. Soc.* **2017,** *139*, 2122-2131.
117. Zhang, J.; Li, Z.; Huang, J.; Liu, C.; Hong, F.; Zheng, K.; Li, G., Size dependence of gold clusters with precise numbers of atoms in aerobic oxidation of d-glucose. *Nanoscale* **2017,** *9*, 16879-16886.
118. Cook, A. W.; Jones, Z. R.; Wu, G.; Scott, S. L.; Hayton, T. W., An organometallic Cu_{20} nanocluster: Synthesis, characterization, immobilization on silica, and "click" chemistry. *J. Am. Chem. Soc.* **2018,** *140*, 394-400.
119. Zhao, S.; Jin, R.; Abroshan, H.; Zeng, C.; Zhang, H.; House, S. D.; Gottlieb, E.; Kim, H. J.; Yang, J. C.; Jin, R., Gold nanoclusters promote electrocatalytic water oxidation at the nanocluster/$CoSe_2$ interface. *J. Am. Chem. Soc.* **2017,** *139*, 1077-1080.
120. Li, M. B.; Tian, S. K.; Wu, Z., Catalyzed formation of alpha,beta-unsaturated ketones or aldehydes from propargylic acetates by a recoverable and recyclable nanocluster catalyst. *Nanoscale* **2014,** *6*, 5714-5717.

121. Gao, Y.; Shao, N.; Pei, Y.; Zeng, X. C., Icosahedral crown gold nanocluster $Au_{43}Cu_{12}$ with high catalytic activity. *Nano. Lett.* **2010,** *10*, 1055-1062.
122. Kauffman, D. R.; Alfonso, D.; Matranga, C.; Ohodnicki, P.; Deng, X.; Siva, R. C.; Zeng, C.; Jin, R., Probing active site chemistry with differently charged Au_{25}^{q} nanoclusters (q = −1, 0, +1). *Chem. Sci.* **2014,** *5*.
123. Shivhare, A.; Chevrier, D. M.; Purves, R. W.; Scott, R. W. J., Following the thermal activation of $Au_{25}(SR)_{18}$ clusters for catalysis by X-ray absorption spectroscopy. *J. Phys. Chem. C* **2013,** *117*, 20007-20016.
124. Chen, H.; Liu, C.; Wang, M.; Zhang, C.; Li, G.; Wang, F., Thermally robust silica-enclosed Au $_{25}$ nanocluster and its catalysis. *Chinese J. Catal.* **2016,** *37*, 1787-1793.
125. Sudheeshkumar, V.; Shivhare, A.; Scott, R. W. J., Synthesis of sinter-resistant Au@silica catalysts derived from Au_{25} clusters. *Catal. Sci. Technol.* **2017,** *7*, 272-280.
126. Zhu, Y.; Wu, Z.; Gayathri, C.; Qian, H.; Gil, R. R.; Jin, R., Exploring stereoselectivity of Au_{25} nanoparticle catalyst for hydrogenation of cyclic ketone. *J. Catal.* **2010,** *271*, 155-160.
127. Negishi, Y.; Mizuno, M.; Hirayama, M.; Omatoi, M.; Takayama, T.; Iwase, A.; Kudo, A., Enhanced photocatalytic water splitting by $BaLa_4Ti_4O_{15}$ loaded with approximately 1 nm gold nanoclusters using glutathione-protected Au_{25} clusters. *Nanoscale* **2013,** *5*, 7188-7192.
128. Li, G.; Abroshan, H.; Liu, C.; Zhuo, S.; Li, Z.; Xie, Y.; Kim, H. J.; Rosi, N. L.; Jin, R., Tailoring the electronic and catalytic properties of Au_{25} nanoclusters via ligand engineering. *ACS Nano* **2016,** *10*, 7998-8005.
129. Li, G.; Liu, C.; Lei, Y.; Jin, R., Au_{25} nanocluster-catalyzed Ullmann-type homocoupling reaction of aryl iodides. *Chem. Commun.* **2012,** *48*, 12005-12007.
130. Li, G.; Jiang, D.-e.; Liu, C.; Yu, C.; Jin, R., Oxide-supported atomically precise gold nanocluster for catalyzing Sonogashira cross-coupling. *J. Catal.* **2013,** *306*, 177-183.
131. Abroshan, H.; Li, G.; Lin, J.; Kim, H. J.; Jin, R., Molecular mechanism for the activation of $Au_{25}(SCH_2CH_2Ph)_{18}$ nanoclusters by imidazolium-based ionic liquids for catalysis. *J. Catal.* **2016,** *337*, 72-79.
132. Chong, H.; Li, P.; Wang, S.; Fu, F.; Xiang, J.; Zhu, M.; Li, Y., Au_{25} clusters as electron-transfer catalysts induced the intramolecular cascade reaction of 2-nitrobenzonitrile. *Sci. Rep.* **2013,** *3*, 3214.
133. Kumar, S. S.; Kwak, K.; Lee, D., Amperometric sensing based on glutathione protected Au_{25} nanoparticles and their pH dependent electrocatalytic activity. *Electroanal.* **2011,** *23*, 2116-2124.
134. Li, J.; Nasaruddin, R. R.; Feng, Y.; Yang, J.; Yan, N.; Xie, J., Tuning the accessibility and activity of $Au_{25}(SR)_{18}$ nanocluster catalysts through ligand engineering. *Chem. Eur. J.* **2016,** *22*, 14816-14820.
135. Yoskamtorn, T.; Yamazoe, S.; Takahata, R.; Nishigaki, J.-i.; Thivasasith, A.; Limtrakul, J.; Tsukuda, T., Thiolate-mediated selectivity control in aerobic alcohol oxidation by porous carbon-supported Au_{25} clusters. *ACS Catal.* **2014,** *4*, 3696-3700.
136. Liu, C.; Lin, S.; Pei, Y.; Zeng, X. C., Semiring chemistry of $Au_{25}(SR)_{18}$: Fragmentation pathway and catalytic active site. *J. Am. Chem. Soc.* **2013,** *135*, 18067-18079.
137. Moulijn, J. A.; van Diepen, A. E.; Kapteijn, F., Catalyst deactivation: is it predictable?: What to do? *Appl. Catal. A.* **2001,** *212*, 3-16.
138. Fang, J.; Li, J.; Zhang, B.; Yuan, X.; Asakura, H.; Tanaka, T.; Teramura, K.; Xie, J.; Yan, N., The support effect on the size and catalytic activity of thiolated Au_{25} nanoclusters as precatalysts. *Nanoscale* **2015,** *7*, 6325-6333.
139. Zhang, B.; Fang, J.; Li, J.; Lau, J. J.; Mattia, D.; Zhong, Z.; Xie, J.; Yan, N., Soft, Oxidative stripping of alkyl thiolate ligands from hydroxyapatite-supported gold nanoclusters for oxidation reactions. *Chem. Asian J.* **2016,** *11*, 532-539.
140. Lavenn, C.; Demessence, A.; Tuel, A., $Au_{25}(SPh\text{-}p NH_2)_{17}$ nanoclusters deposited on SBA-15 as catalysts for aerobic benzyl alcohol oxidation. *J. Catal.* **2015,** *322*, 130-138.

141. Huang, P.; Chen, G.; Jiang, Z.; Jin, R.; Zhu, Y.; Sun, Y., Atomically precise Au_{25} superatoms immobilized on CeO_2 nanorods for styrene oxidation. *Nanoscale* **2013,** *5*, 3668-3672.
142. Liu, Y.; Tsunoyama, H.; Akita, T.; Xie, S.; Tsukuda, T., Aerobic oxidation of cyclohexane catalyzed by size-controlled Au clusters on hydroxyapatite: Size effect in the sub-2 nm regime. *ACS Catal.* **2010,** *1*, 2-6.
143. Lavenn, C.; Demessence, A.; Tuel, A., Atomically well-defined $Au_{25}(SR)_{17/18}$ nanoclusters deposited on silica supports for the aerobic epoxidation of trans-stilbene. *Catal. Today* **2014,** *235*, 72-78.
144. Liu, C.; Zhang, J.; Huang, J.; Zhang, C.; Hong, F.; Zhou, Y.; Li, G.; Haruta, M., Efficient aerobic oxidation of glucose to gluconic acid over activated carbon-supported gold clusters. *ChemSusChem* **2017,** *10*, 1976-1980.
145. Nie, X.; Qian, H.; Ge, Q.; Xu, H.; Jin, R., CO oxidation catalyzed by oxide-supported $Au_{25}(SR)_{18}$ nanoclusters and identification of perimeter sites as active centers. *ACS Nano.* **2012,** *6*, 6014–6022.
146. Wu, Z.; Jiang, D.-e.; Mann, A. K. P.; Mullins, D. R.; Qiao, Z.-A.; Allard, L. F.; Zeng, C.; Jin, R.; Overbury, S. H., Thiolate ligands as a double-edged sword for CO oxidation on CeO_2 supported $Au_{25}(SCH_2CH_2Ph)_{18}$ nanoclusters. *J. Am. Chem. Soc.* **2014,** *136*, 6111-6122.
147. Green, I. X.; Tang, W.; Neurock, M.; Jr., J. T. Y., Spectroscopic observation of dual catalytic sites during oxidation of CO on a Au/TiO_2 catalyst. *Science* **2011,** *333*, 736-739.
148. Habeeb Muhammed, M. A.; Pradeep, T., $Au_{25}@SiO_2$: quantum clusters of gold embedded in silica. *Small* **2011,** *7*, 204-208.
149. Han, N. S.; Kim, D.; Lee, J. W.; Kim, J.; Shim, H. S.; Lee, Y.; Lee, D.; Song, J. K., Unexpected size effect observed in ZnO-Au composite photocatalysts. *ACS Appl. Mater. Interfaces* **2016,** *8*, 1067-1072.
150. Kim, J. K.; Jang, D.-J., Metal-enhanced fluorescence of gold nanoclusters adsorbed onto $Ag@SiO_2$ core–shell nanoparticles. *J. Mater. Chem. C* **2017,** *5*, 6037--6046
151. Luo, Y.; Fan, S.; Yu, W.; Wu, Z.; Cullen, D. A.; Liang, C.; Shi, J.; Su, C., Fabrication of $Au_{25}(SG)_{18}$ -ZIF-8 nanocomposites: A facile strategy to position $Au_{25}(SG)_{18}$ nanoclusters inside and outside ZIF-8. *Adv. Mater.* **2018,** *30*.
152. Sumida, K.; Rogow, D. L.; Mason, J. A.; McDonald, T. M.; Bloch, E. D.; Herm, Z. R.; Bae, T. H.; Long, J. R., Carbon dioxide capture in metal-organic frameworks. *Chem. Rev.* **2012,** *112*, 724-781.
153. Lee, J.; Farha, O. K.; Roberts, J.; Scheidt, K. A.; Nguyen, S. T.; Hupp, J. T., Metal-organic framework materials as catalysts. *Chem. Soc. Rev.* **2009,** *38*, 1450-1459.
154. Nandasiri, M. I.; Jambovane, S. R.; McGrail, B. P.; Schaef, H. T.; Nune, S. K., Adsorption, separation, and catalytic properties of densified metal-organic frameworks. *Coord. Chem. Rev.* **2016,** *311*, 38-52.
155. Zhao, Y.; Song, Z.; Li, X.; Sun, Q.; Cheng, N.; Lawes, S.; Sun, X., Metal organic frameworks for energy storage and conversion. *Energy Storage Mater.* **2016,** *2*, 35-62.
156. Miller, S. E.; Teplensky, M. H.; Moghadam, P. Z.; Fairen-Jimenez, D., Metal-organic frameworks as biosensors for luminescence-based detection and imaging. *Interface Focus* **2016,** *6*, 20160027.
157. Gascon, J.; Corma, A.; Kapteijn, F.; Llabrés i Xamena, F. X., Metal organic framework catalysis: Quo vadis? *ACS Catal.* **2013,** *4*, 361-378.
158. Chen, J.; Shen, K.; Li, Y., Greening the processes of metal-organic framework synthesis and their use in sustainable catalysis. *ChemSusChem* **2017,** *10*, 3165-3187.
159. Devic, T.; Serre, C., High valence 3p and transition metal based MOFs. *Chem. Soc. Rev.* **2014,** *43*, 6097-6115.
160. Cavka, J. H.; Jakobsen, S.; Olsbye, U.; Guillou, N.; Lamberti, C.; Bordiga, S.; Lillerud, K. P., A new zirconium inorganic building brick forming metal organic frameworks with exceptional stability. *J. Am. Chem. Soc.* **2008,** *130*, 13850–13851.

161. Yang, C.; Kaipa, U.; Mather, Q. Z.; Wang, X.; Nesterov, V.; Venero, A. F.; Omary, M. A., Fluorous metal-organic frameworks with superior adsorption and hydrophobic properties toward oil spill cleanup and hydrocarbon storage. *J. Am. Chem. Soc.* **2011,** *133*, 18094-18097.
162. Yuan, S.; Feng, L.; Wang, K.; Pang, J.; Bosch, M.; Lollar, C.; Sun, Y.; Qin, J.; Yang, X.; Zhang, P.; Wang, Q.; Zou, L.; Zhang, Y.; Zhang, L.; Fang, Y.; Li, J.; Zhou, H. C., Stable metal-organic frameworks: Design, synthesis, and applications. *Adv. Mater.* **2018,** *30*, e1704303.
163. Sun, X.; Dong, S.; Wang, E., Coordination-induced formation of submicrometer-scale, monodisperse, spherical colloids of organic-inorganic hybrid materials at room temperature. *J. Am. Chem. Soc.* **2005,** *127*, 13102-13103.
164. Oh, M.; Mirkin, C. A., Chemically tailorable colloidal particles from infinite coordination polymers. *Nature* **2005,** *438*, 651-654.
165. Rieter, W. J.; Pott, K. M.; Taylor, K. M. L.; Lin, W., Nanoscale coordination polymers for platinum-based anticancer drug delivery. *J. Am. Chem. Soc.* **2008,** *180*, 11584–11585.
166. Li, Y. S.; Bux, H.; Feldhoff, A.; Li, G. L.; Yang, W. S.; Caro, J., Controllable synthesis of metal-organic frameworks: From MOF nanorods to oriented MOF membranes. *Adv. Mater.* **2010,** *22*, 3322-3326.
167. Haque, E.; Khan, N. A.; Park, J. H.; Jhung, S. H., Synthesis of a metal-organic framework material, iron terephthalate, by ultrasound, microwave, and conventional electric heating: a kinetic study. *Chem. Eur. J.* **2010,** *16*, 1046-1052.
168. Wang, S.; McGuirk, C. M.; d'Aquino, A.; Mason, J. A.; Mirkin, C. A., Metal-organic framework nanoparticles. *Adv. Mater.* **2018,** *30*, e1800202.
169. Schaate, A.; Roy, P.; Godt, A.; Lippke, J.; Waltz, F.; Wiebcke, M.; Behrens, P., Modulated synthesis of Zr-based metal-organic frameworks: from nano to single crystals. *Chem. Eur. J.* **2011,** *17*, 6643-6651.
170. Hu, M.; Furukawa, S.; Ohtani, R.; Sukegawa, H.; Nemoto, Y.; Reboul, J.; Kitagawa, S.; Yamauchi, Y., Synthesis of prussian blue nanoparticles with a hollow interior by controlled chemical etching. *Angew. Chem. Int. Ed. Engl.* **2012,** *51*, 984-988.
171. Prestipino, C.; Regli, L.; Vitillo, J. G.; Bonino, F.; Damin, A.; Lamberti, C.; Zecchina, A.; Solari, P. L.; Kongshaug, K. O.; Bordiga, S., Local structure of framework Cu(II) in HKUST-1 metallorganic framework: Spectroscopic characterization upon activation and interaction with adsorbates. *Chem. Mater.* **2006,** *18*, 1337-1346.
172. Areán, C. O.; Cabello, C. P.; Palomino, G. T., Infrared spectroscopic and thermodynamic study on hydrogen adsorption on the metal organic framework MIL-100(Sc). *Chem. Phys. Lett.* **2012,** *521*, 104-106.
173. Fe´rey, G.; Mellot-Draznieks, C.; C. Serre, F. M.; Dutour, J.; Surble´, S.; Margiolaki, I., A Chromium terephthalate–based solid with unusually large pore volumes and surface area. *Science* **2005,** *309*, 2040-2042.
174. Vandichel, M.; Hajek, J.; Vermoortele, F.; Waroquier, M.; De Vos, D. E.; Van Speybroeck, V., Active site engineering in UiO-66 type metal–organic frameworks by intentional creation of defects: a theoretical rationalization. *CrystEngComm* **2015,** *17*, 395-406.
175. Sen, R.; Saha, D.; Koner, S., Controlled construction of metal-organic frameworks: hydrothermal synthesis, X-ray structure, and heterogeneous catalytic study. *Chem. Eur. J.* **2012,** *18*, 5979-5986.
176. Juan-Alcañiz, J.; Ramos-Fernandez, E. V.; Lafont, U.; Gascon, J.; Kapteijn, F., Building MOF bottles around phosphotungstic acid ships: One-pot synthesis of bi-functional polyoxometalate-MIL-101 catalysts. *J. Catal.* **2010,** *269*, 229-241.
177. Zhang, Y.; Degirmenci, V.; Li, C.; Hensen, E. J., Phosphotungstic acid encapsulated in metal-organic framework as catalysts for carbohydrate dehydration to 5-hydroxymethylfurfural. *ChemSusChem* **2011,** *4*, 59-64.

178. Ponomareva, V. G.; Kovalenko, K. A.; Chupakhin, A. P.; Dybtsev, D. N.; Shutova, E. S.; Fedin, V. P., Imparting high proton conductivity to a metal-organic framework material by controlled acid impregnation. *J. Am. Chem. Soc.* **2012,** *134*, 15640-15643.
179. Vermoortele, F.; Ameloot, R.; Alaerts, L.; Matthessen, R.; Carlier, B.; Fernandez, E. V. R.; Gascon, J.; Kapteijn, F.; De Vos, D. E., Tuning the catalytic performance of metal–organic frameworks in fine chemistry by active site engineering. *J. Mater. Chem.* **2012,** *22*.
180. DeCoste, J. B.; Demasky, T. J.; Katz, M. J.; Farha, O. K.; Hupp, J. T., A UiO-66 analogue with uncoordinated carboxylic acids for the broad-spectrum removal of toxic chemicals. *New J. Chem.* **2015,** *39*, 2396-2399.
181. Akiyama, G.; Matsuda, R.; Sato, H.; Takata, M.; Kitagawa, S., Cellulose hydrolysis by a new porous coordination polymer decorated with sulfonic acid functional groups. *Adv. Mater.* **2011,** *23*, 3294-3297.
182. Hwang, Y. K.; Hong, D. Y.; Chang, J. S.; Jhung, S. H.; Seo, Y. K.; Kim, J.; Vimont, A.; Daturi, M.; Serre, C.; Ferey, G., Amine grafting on coordinatively unsaturated metal centers of MOFs: consequences for catalysis and metal encapsulation. *Angew. Chem. Int. Ed. Engl.* **2008,** *47*, 4144-4148.
183. Gascon, J.; Aktay, U.; Hernandezalonso, M.; Vanklink, G.; Kapteijn, F., Amino-based metal-organic frameworks as stable, highly active basic catalysts. *J. Catal.* **2009,** *261*, 75-87.
184. Bernt, S.; Guillerm, V.; Serre, C.; Stock, N., Direct covalent post-synthetic chemical modification of Cr-MIL-101 using nitrating acid. *Chem. Commun.* **2011,** *47*, 2838-2840.
185. Hartmann, M.; Fischer, M., Amino-functionalized basic catalysts with MIL-101 structure. *Micropor. Mesopor. Mater.* **2012,** *164*, 38-43.
186. Jiang, J.; Yaghi, O. M., Brønsted acidity in metal-organic frameworks. *Chem. Rev.* **2015,** *115*, 6966-6997.
187. Kang, Y.-S.; Lu, Y.; Chen, K.; Zhao, Y.; Wang, P.; Sun, W.-Y., Metal–organic frameworks with catalytic centers: From synthesis to catalytic application. *Coord. Chem. Rev.* **2019,** *378*, 262-280.
188. Kaye, S. S.; Long, J. R., Matrix isolation chemistry in a porous metal-organic framework: Photochemical substitutions of N_2 and H_2 in $Zn_4O[(\eta6\text{-}1,4\text{-Benzenedicarboxylate})Cr(CO)_3]_3$. *J. Am. Chem. Soc.* **2008,** *130*, 806-807.
189. Corma, A.; Garcia, H.; Llabres i Xamena, F. X., Engineering metal organic frameworks for heterogeneous catalysis. *Chem. Rev.* **2010,** *110*, 4606-4655.
190. Denny, M. S., Jr.; Parent, L. R.; Patterson, J. P.; Meena, S. K.; Pham, H.; Abellan, P.; Ramasse, Q. M.; Paesani, F.; Gianneschi, N. C.; Cohen, S. M., Transmission electron microscopy reveals deposition of metal oxide coatings onto metal-organic frameworks. *J. Am. Chem. Soc.* **2018,** *140*, 1348-1357.
191. Kim, C. R.; Uemura, T.; Kitagawa, S., Inorganic nanoparticles in porous coordination polymers. *Chem. Soc. Rev.* **2016,** *45*, 3828-3845.
192. Dhakshinamoorthy, A.; Garcia, H., Catalysis by metal nanoparticles embedded on metal-organic frameworks. *Chem. Soc. Rev.* **2012,** *41*, 5262-5284.
193. Dhakshinamoorthy, A.; Asiri, A. M.; Garcia, H., Metal organic frameworks as versatile hosts of Au nanoparticles in heterogeneous catalysis. *ACS Catal.* **2017,** *7*, 2896-2919.
194. Sabo, M.; Henschel, A.; Fröde, H.; Klemm, E.; Kaskel, S., Solution infiltration of palladium into MOF-5: synthesis, physisorption and catalytic properties. *J. Mater. Chem.* **2007,** *17*.
195. Henschel, A.; Gedrich, K.; Kraehnert, R.; Kaskel, S., Catalytic properties of MIL-101. *Chem. Commun.* **2008**, 4192-4194.
196. El-Shall, M. S.; Abdelsayed, V.; Khder, A. E. R. S.; Hassan, H. M. A.; El-Kaderi, H. M.; Reich, T. E., Metallic and bimetallic nanocatalysts incorporated into highly porous coordination polymer MIL-101. *J. Mater. Chem.* **2009,** *19*, 7625–7631.

197. Rasero-Almansa, A. M.; Corma, A.; Iglesias, M.; Sánchez, F., Post-functionalized iridium–Zr-MOF as a promising recyclable catalyst for the hydrogenation of aromatics. *Green Chem.* **2014,** *16*, 3522-3527.
198. Zhu, J.; Wang, P. C.; Lu, M., Selective oxidation of benzyl alcohol under solvent-free condition with gold nanoparticles encapsulated in metal-organic framework. *Appl. Catal. A* **2014,** *477*, 125-131.
199. Liu, H.; Liu, Y.; Li, Y.; Tang, Z.; Jiang, H., Metal-organic framework supported gold nanoparticles as a highly active heterogeneous catalyst for aerobic oxidation of alcohols. *J. Phys. Chem. C* **2010,** *114*, 13362–13369.
200. Jiang, H.-L.; Liu, B.; Akita, T.; Haruta, M.; Sakurai, H.; Xu, Q., Au@ZIF-8: CO oxidation over gold nanoparticles deposited to metal-organic framework. *J. Am. Chem. Soc.* **2009,** *131*, 11302–11303.
201. Jayaramulu, K.; Geyer, F.; Schneemann, A.; Kment, S.; Otyepka, M.; Zboril, R.; Vollmer, D.; Fischer, R. A., Hydrophobic metal-organic frameworks. *Adv. Mater.* **2019**, e1900820.
202. Cliffe, M. J.; Wan, W.; Zou, X.; Chater, P. A.; Kleppe, A. K.; Tucker, M. G.; Wilhelm, H.; Funnell, N. P.; Coudert, F.-X.; Goodwin, A. L., Correlated defect nanoregions in a metal–organic framework. *Nat. Commun.* **2014,** *5*.
203. Hinde, C. S.; Webb, W. R.; Chew, B. K.; Tan, H. R.; Zhang, W. H.; Hor, T. S.; Raja, R., Utilisation of gold nanoparticles on amine-functionalised UiO-66 (NH_2-UiO-66) nanocrystals for selective tandem catalytic reactions. *Chem. Commun.* **2016,** *52*, 6557-6560.
204. Li, Y.; Liu, Y.; Gao, W.; Zhang, L.; Liu, W.; Lu, J.; Wang, Z.; Deng, Y.-J., Microwave-assisted synthesis of UiO-66 and its adsorption performance towards dyes. *CrystEngComm* **2014,** *16*, 7037-7042.
205. Kandiah, M.; Nilsen, M. H.; Usseglio, S.; Jakobsen, S.; Olsbye, U.; Tilset, M.; Larabi, C.; Quadrelli, E. A.; Bonino, F.; Lillerud, K. P., Synthesis and stability of tagged UiO-66 Zr-MOFs. *Chem. Mater.* **2010,** *22*, 6632-6640.
206. Dhakshinamoorthy, A.; Santiago-Portillo, A.; Asiri, A. M.; Garcia, H., Engineering UiO-66 metal organic framework for heterogeneous catalysis. *ChemCatChem* **2019,** *11*, 899-923.
207. Serre, C.; Millange, F.; Thouvenot, C.; Nogue, M.; Marsolier, G.; Louer, D.; Ferey, G., Very large breathing effect in the first nanoporous chromium(III)-based solids: MIL-53 or $Cr^{III}(OH)\{O_2C\text{-}C_6H_4\text{-}CO_2\}\{HO_2C\text{-}C_6H_4\text{-}CO_2H\}_x,H_2O_y$. *J. Am. Chem. Soc.* **2002,** *124*, 13519-13526.
208. Férey, G.; Serre, C.; Mellot-Draznieks, C.; Millange, F.; Surblé, S.; Dutour, J.; Margiolaki, I., A hybrid solid with giant pores prepared by a combination of targeted chemistry, simulation, and powder diffraction. *Angew. Chem. Int. Ed. Engl.* **2004,** *116*, 6456-6461.
209. Jhung, S. H.; Lee, J. H.; Yoon, J. W.; Serre, C.; Férey, G.; Chang, J. S., Microwave synthesis of chromium terephthalate MIL-101 and its benzene sorption ability. *Adv. Mater.* **2007,** *19*, 121-124.
210. Demessence, A.; Horcajada, P.; Serre, C.; Boissiere, C.; Grosso, D.; Sanchez, C.; Ferey, G., Elaboration and properties of hierarchically structured optical thin films of MIL-101(Cr). *Chem. Commun.* **2009**, 7149-7151.
211. Herbst, A.; Janiak, C., MOF catalysts in biomass upgrading towards value-added fine chemicals. *CrystEngComm* **2016,** *19*, 4092-4117.
212. Bhattacharjee, S.; Chen, C.; Ahn, W.-S., Chromium terephthalate metal–organic framework MIL-101: synthesis, functionalization, and applications for adsorption and catalysis. *RSC Adv.* **2014,** *4*, 52500-52525.
213. Park, K. S.; Ni, Z.; Cote, A. P.; Choi, J. Y.; Huang, R.; Uribe-Romo, F. J.; Chae, H. K.; O'Keeffe, M.; Yaghi, O. M., Exceptional chemical and thermal stability of zeolitic imidazolate frameworks. *Proc. Natl. Acad. Sci.* **2006,** *103*, 10186–10191.
214. Srivastava, M.; Roy, P. K.; Ramanan, A., Hydrolytically stable ZIF-8@PDMS core–shell microspheres for gas–solid chromatographic separation. *RSC Adv.* **2016,** *6*, 13426-13432.

215. Banerjee, R.; Phan, A.; Wang, B.; Knobler, C.; Furukawa, H.; O'Keeffe, M.; Yaghi, O. M., High-throughput synthesis of zeolitic imidazolate frameworks and application to CO_2 capture. *Science* **2008,** *319*, 939-943.
216. Pan, Y.; Liu, Y.; Zeng, G.; Zhao, L.; Lai, Z., Rapid synthesis of zeolitic imidazolate framework-8 (ZIF-8) nanocrystals in an aqueous system. *Chem. Commun.* **2011,** *47*, 2071-2073.
217. Cho, H.-Y.; Kim, J.; Kim, S.-N.; Ahn, W.-S., High yield 1-L scale synthesis of ZIF-8 via a sonochemical route. *Micropor. Mesopor. Mater.* **2013,** *169*, 180-184.
218. Martinez Joaristi, A.; Juan-Alcañiz, J.; Serra-Crespo, P.; Kapteijn, F.; Gascon, J., Electrochemical synthesis of some archetypical Zn^{2+}, Cu^{2+}, and Al^{3+} metal organic frameworks. *Cryst. Growth Des.* **2012,** *12*, 3489-3498.
219. Beldon, P. J.; Fabian, L.; Stein, R. S.; Thirumurugan, A.; Cheetham, A. K.; Friscic, T., Rapid room-temperature synthesis of zeolitic imidazolate frameworks by using mechanochemistry. *Angew. Chem. Int. Ed. Engl.* **2010,** *49*, 9640-9643.
220. Bhattacharjee, S.; Jang, M.-S.; Kwon, H.-J.; Ahn, W.-S., Zeolitic imidazolate frameworks: Synthesis, functionalization, and catalytic/adsorption applications. *Catal. Surv. Asia* **2014,** *18*, 101-127.
221. Dorneles de Mello, M.; Tsapatsis, M., Selective Glucose-to-fructose isomerization over modified zirconium UiO-66 in alcohol media. *ChemCatChem* **2018,** *10*, 2417-2423.
222. Valekar, A. H.; Cho, K.-H.; Chitale, S. K.; Hong, D.-Y.; Cha, G.-Y.; Lee, U. H.; Hwang, D. W.; Serre, C.; Chang, J.-S.; Hwang, Y. K., Catalytic transfer hydrogenation of ethyl levulinate to γ-valerolactone over zirconium-based metal–organic frameworks. *Green Chem.* **2016,** *18*, 4542-4552.
223. Chia, M.; Dumesic, J. A., Liquid-phase catalytic transfer hydrogenation and cyclization of levulinic acid and its esters to gamma-valerolactone over metal oxide catalysts. *Chem. Commun.* **2011,** *47*, 12233-12235.
224. Tang, X.; Chen, H.; Hu, L.; Hao, W.; Sun, Y.; Zeng, X.; Lin, L.; Liu, S., Conversion of biomass to γ-valerolactone by catalytic transfer hydrogenation of ethyl levulinate over metal hydroxides. *Appl. Catal. B.* **2014,** *147*, 827-834.
225. He, J.; Li, H.; Lu, Y.-M.; Liu, Y.-X.; Wu, Z.-B.; Hu, D.-Y.; Yang, S., Cascade catalytic transfer hydrogenation–cyclization of ethyl levulinate to γ-valerolactone with Al–Zr mixed oxides. *Appl. Catal. A* **2016,** *510*, 11-19.
226. Akiyama, G.; Matsuda, R.; Sato, H.; Kitagawa, S., Catalytic glucose isomerization by porous coordination polymers with open metal sites. *Chem. Asian J.* **2014,** *9*, 2772-2777.
227. Herbst, A.; Janiak, C., Selective glucose conversion to 5-hydroxymethylfurfural (5-HMF) instead of levulinic acid with MIL-101Cr MOF-derivatives. *New J. Chem.* **2016,** *40*, 7958-7967.
228. Tsilomelekis, G.; Orella, M. J.; Lin, Z.; Cheng, Z.; Zheng, W.; Nikolakis, V.; Vlachos, D. G., Molecular structure, morphology and growth mechanisms and rates of 5-hydroxymethyl furfural (HMF) derived humins. *Green Chem.* **2016,** *18*, 1983-1993.
229. Chatterjee, A.; Hu, X.; Lam, F. L.-Y., Towards a recyclable MOF catalyst for efficient production of furfural. *Catal. Today* **2018,** *314*, 129-136.
230. Murillo, B.; Zornoza, B.; de la Iglesia, O.; Téllez, C.; Coronas, J., Chemocatalysis of sugars to produce lactic acid derivatives on zeolitic imidazolate frameworks. *J. Catal.* **2016,** *334*, 60-67.
231. Aijaz, A.; Xu, Q., Catalysis with metal nanoparticles immobilized within the pores of metal-organic frameworks. *J. Phys. Chem. Lett.* **2014,** *5*, 1400-1411.
232. Dhakshinamoorthy, A.; Alvaro, M.; Garcia, H., Aerobic oxidation of benzylic alcohols catalyzed by metal–organic frameworks assisted by TEMPO. *ACS Catal.* **2010,** *1*, 48-53.
233. Ishida, T.; Nagaoka, M.; Akita, T.; Haruta, M., Deposition of gold clusters on porous coordination polymers by solid grinding and their catalytic activity in aerobic oxidation of alcohols. *Chem. Eur. J.* **2008,** *14*, 8456-8460.

234. Ning, L.; Liao, S.; Liu, X.; Guo, P.; Zhang, Z.; Zhang, H.; Tong, X., A regulatable oxidative valorization of furfural with aliphatic alcohols catalyzed by functionalized metal-organic frameworks-supported Au nanoparticles. *J. Catal.* **2018,** *364*, 1-13.
235. Kim, D.-W.; Kim, H.-G.; Cho, D.-H., Catalytic performance of MIL-100 (Fe, Cr) and MIL-101 (Fe, Cr) in the isomerization of endo- to exo-dicyclopentadiene. *Catal. Commun.* **2016,** *73*, 69-73.
236. Zhou, F.; Lu, N.; Fan, B.; Wang, H.; Li, R., Zirconium-containing UiO-66 as an efficient and reusable catalyst for transesterification of triglyceride with methanol. *J. Energy Chem.* **2016,** *25*, 874-879.
237. Pan, Y.; Yuan, B.; Li, Y.; He, D., Multifunctional catalysis by Pd@MIL-101: one-step synthesis of methyl isobutyl ketone over palladium nanoparticles deposited on a metal-organic framework. *Chem. Commun.* **2010,** *46*, 2280-2282.
238. Zhu, M.; Srinivas, D.; Bhogeswararao, S.; Ratnasamy, P.; Carreon, M. A., Catalytic activity of ZIF-8 in the synthesis of styrene carbonate from CO_2 and styrene oxide. *Catal. Commun.* **2013,** *32*, 36-40.
239. Bernstein, E. F.; Brown, D. B.; Schwartz, M. D.; Kaidbey, K.; Ksenzenko, S. M., The polyhydroxy acid gluconolactone protects against ultraviolet radiation in an in vitro model of cutaneous photoaging. *Dermatol. Surg.* **2004,** *30*, 189–196.
240. Choudhary, V.; Pinar, A. B.; Sandler, S. I.; Vlachos, D. G.; Lobo, R. F., Xylose isomerization to xylulose and its dehydration to furfural in aqueous media. *ACS Catal.* **2011,** *1*, 1724-1728.
241. Dapsens, P. Y.; Mondelli, C.; Jagielski, J.; Hauert, R.; Pérez-Ramírez, J., Hierarchical Sn-MFI zeolites prepared by facile top-down methods for sugar isomerisation. *Catal. Sci. Technol.* **2014,** *4*.
242. Paniagua, M.; Saravanamurugan, S.; Melian-Rodriguez, M.; Melero, J. A.; Riisager, A., Xylose isomerization with zeolites in a two-step alcohol-water process. *ChemSusChem* **2015,** *8*, 1088-1094.
243. Guo, R.; Murray, R. W., Substituent effects on redox potentials and optical gap energies of molecule-like $Au_{38}(SPhX)_{24}$ nanoparticles. *J. Am. Chem. Soc.* **2005,** *127*, 12140-12143.
244. Martra, G., Lewis acid and base sites at the surface of microcrystalline TiO_2 anatase: relationships between surface morphology and chemical behaviour. *Appl. Catal. A* **2000,** *200*, 275–285.
245. Sudarsanam, P.; Mallesham, B.; Durgasri, D. N.; Reddy, B. M., Physicochemical and catalytic properties of nanosized Au/CeO_2 catalysts for eco-friendly oxidation of benzyl alcohol. *J. Ind. Eng. Chem.* **2014,** *20*, 3115-3121.
246. Vivier, L.; Duprez, D., Ceria-based solid catalysts for organic chemistry. *ChemSusChem* **2010,** *3*, 654-678.
247. Wei, H.; Li, J.; Yu, J.; Zheng, J.; Su, H.; Wang, X., Gold nanoparticles supported on metal oxides as catalysts for the direct oxidative esterification of alcohols under mild conditions. *Inorg. Chim. Acta.* **2015,** *427*, 33-40.
248. Cui, W.; Jia, M.; Ao, W.; Zhaorigetu, B., Selective oxidative esterification of alcohols on Au/ZrO_2 catalyst under ambient conditions. *Reac. Kin. Mech. Catal.* **2013,** *110*, 437-448.
249. Choudhary, V. R.; Dumbre, D. K.; Bhargava, S. K., Oxidation of benzyl alcohol to benzaldehyde by tert-Butyl hydroperoxide over nanogold supported on TiO_2 and other transition and rare-earth metal oxides. *Ind. Eng. Chem. Res.* **2009,** *48*, 9471-9478.
250. Choudhary, V. R.; Dumbre, D. K., Supported nano-gold catalysts for epoxidation of styrene and oxidation of benzyl alcohol to benzaldehyde. *Top. Catal.* **2009,** *52*, 1677-1687.
251. Signoretto, M.; Menegazzo, F.; Contessotto, L.; Pinna, F.; Manzoli, M.; Boccuzzi, F., Au/ZrO_2: an efficient and reusable catalyst for the oxidative esterification of renewable furfural. *Appl. Catal. B.* **2013,** *129*, 287-293.
252. Signoretto, M.; Menegazzo, F.; Trevisan, V.; Pinna, F.; Manzoli, M.; Boccuzzi, F., Investigation on the stability of supported gold nanoparticles. *Catalysts* **2013,** *3*, 656-670.

253. Pinna, F.; Olivo, A.; Trevisan, V.; Menegazzo, F.; Signoretto, M.; Manzoli, M.; Boccuzzi, F., The effects of gold nanosize for the exploitation of furfural by selective oxidation. *Catal. Today* **2013,** *203*, 196-201.
254. Menegazzo, F.; Signoretto, M.; Pinna, F.; Manzoli, M.; Aina, V.; Cerrato, G.; Boccuzzi, F., Oxidative esterification of renewable furfural on gold-based catalysts: Which is the best support? *J. Catal.* **2014,** *309*, 241-247.
255. Manzoli, M.; Menegazzo, F.; Signoretto, M.; Marchese, D., Biomass Derived Chemicals: Furfural oxidative esterification to methyl-2-furoate over gold catalysts. *Catalysts* **2016,** *6*.
256. Menegazzo, F.; Fantinel, T.; Signoretto, M.; Pinna, F.; Manzoli, M., On the process for furfural and HMF oxidative esterification over Au/ZrO_2. *J. Catal.* **2014,** *319*, 61-70.
257. Shibu, E. S.; Radha, B.; Verma, P. K.; Bhyrappa, P.; Kulkarni, G. U.; Pal, S. K.; Pradeep, T., Functionalized Au_{22} clusters: Synthesis, characterization, and patterning. *ACS Appl. Mater. Interfaces* **2009,** *1*, 2199-2210.
258. Sheldon, R. A.; Arends, I. W. C. E.; ten Brink, G.-J.; Dijksman, A., Green, Catalytic Oxidations of alcohols. *Acc. Chem. Res.* **2002,** *35*, 774-781.
259. Sharma, A. S.; Kaur, H.; Shah, D., Selective oxidation of alcohols by supported gold nanoparticles: recent advances. *RSC Adv.* **2016,** *6*, 28688-28727.
260. Ning, L.; Liao, S.; Liu, X.; Guo, P.; Zhang, Z.; Zhang, H.; Tong, X., A regulatable oxidative valorization of furfural with aliphatic alcohols catalyzed by functionalized metal-organic frameworks-supported Au nanoparticles. *J. Catal.* **2018,** *364*, 1-13.
261. Radhakrishnan, R.; Thiripuranthagan, S.; Devarajan, A.; Kumaravel, S.; Erusappan, E.; Kannan, K., Oxidative esterification of furfural by Au nanoparticles supported CMK-3 mesoporous catalysts. *Appl. Catal., A* **2017,** *545*, 33-43.
262. Shahin, Z.; Ji, H.; Chiriac, R.; Essayem, N.; Rataboul, F.; Demessence, A., Thermal control of the defunctionalization of supported Au_{25}(glutathione)$_{18}$ catalysts for benzyl alcohol oxidation. *Beilstein J Nanotechnol* **2019,** *10*, 228-237.
263. Casanova, O.; Iborra, S.; Corma, A., Biomass into chemicals: One pot-base free oxidative esterification of 5-hydroxymethyl-2-furfural into 2,5-dimethylfuroate with gold on nanoparticulated ceria. *J. Catal.* **2009,** *265*, 109-116.
264. Pinna, F.; Olivo, A.; Trevisan, V.; Menegazzo, F.; Signoretto, M.; Manzoli, M.; Boccuzzi, F., The effects of gold nanosize for the exploitation of furfural by selective oxidation. *Catal. Today* **2013,** *203*, 196-201.
265. Menegazzo, F.; Fantinel, T.; Signoretto, M.; Pinna, F.; Manzoli, M., On the process for furfural and HMF oxidative esterification over Au/ZrO_2. *J. Catal.* **2014,** *319*, 61-70.
266. Young, R. A., The Rietveld Method. *International Union of Crystallography Monographs on Crystallography 5; Oxford Science Publications* **1995**.
267. Rasband, W. S. ImageJ; U. S. National Institutes of Health, Bethesda, Maryland, USA, http://imagej.nih.gov/ij/,. **1997-2014**

Scientific contributions

Published papers

Zahraa Shahin, Hyewon Ji, Rodica Chiriac, Nadine Essayem, Franck Rataboul, Aude Demessence*; Thermal control of the defunctionalization of supported Au_{25}(glutathione)$_{18}$ catalysts for benzyl alcohol oxidation Beilstein J. Nanotechnol.,* **2019***, 10,* 228-237

Paulina A Kobielska, Richard Telford, Jemma Rowlandson, Mi Tian, Zahraa Shahin, Aude Demessence, Valeska P. Ting, Sanjit Nayak, *Polynuclear Complexes as Precursor Templates for Hierarchical Microporous Graphitic Carbon: An Unusual ApproachACS Appl. Mater. Interfaces,* **2018***, 10,* 25967−25971

On going work

Zahraa Shahin, Mahado Said-Ahmed, Rodica Chiriac, Franck Rataboul, Aude Demessence*; Oxidative esterification of furfural by Au thiolate clusters supported on zirconia (writing in progress).*

Conferences

August 2019: EuropaCat International conference, Aachen – Germany / Poster communication

July 2018: Gold International conference, Paris – France / Oral communication

July 2018: SCF congress, Montpellier – France / Oral communication

June 2018: SCF journée Rhone Alpes Journey, Lyon – France / Oral communication

December 2017: Catbior conference, Lyon - France/ Poster communication

May 2017: Gecom Concoord conference, Forges-les-Eaux – France / Oral communication